

8-26-2020

Designing a More Effective MRI Contrast Agent: Investigation into Various Functionalization Strategies for Targeted Imaging

Lauren Nicole Rust
Portland State University

Follow this and additional works at: https://pdxscholar.library.pdx.edu/open_access_etds

 Part of the [Chemistry Commons](#)

Let us know how access to this document benefits you.

Recommended Citation

Rust, Lauren Nicole, "Designing a More Effective MRI Contrast Agent: Investigation into Various Functionalization Strategies for Targeted Imaging" (2020). *Dissertations and Theses*. Paper 5610.
<https://doi.org/10.15760/etd.7482>

This Dissertation is brought to you for free and open access. It has been accepted for inclusion in Dissertations and Theses by an authorized administrator of PDXScholar. Please contact us if we can make this document more accessible: pdxscholar@pdx.edu.

Designing a More Effective MRI Contrast Agent: Investigation into Various
Functionalization Strategies for Targeted Imaging

by

Lauren Nicole Rust

A dissertation submitted in partial fulfillment of the
requirements for the degree of

Doctor of Philosophy
in
Chemistry

Dissertation Committee:
Mark Woods, Chair
Jason Podrabsky
Robert Strongin
David Stuart

Portland State University
2020

Magnetic resonance imaging (MRI) is a medical imaging technique that provides high-resolution images used for diagnostic medicine while maintaining a superior safety profile compared to other radiative techniques. The administration of gadolinium-based contrast agents (GBCAs) improves the diagnostic power of MRI and have been used clinically for over three decades. Although GBCAs are effective at improving the contrast in the image, their detection limits are high and require a large dose to generate an observable effect. This high dose is the consequence of the current available designs of clinical GBCAs; their structures are not tuned to generate optimal efficacy. Efficacy of GBCAs is defined as relaxivity; how effectively the agent increases the T_1 relaxation rate constant of protons on water. The isoelectric structure of the f -orbitals of Gd^{3+} yields it an effective relaxivity agent. However, Gd^{3+} is toxic and insoluble *in vivo*, and is therefore bound as a low molecular weight hydrophilic chelate. The ligand which forms the most kinetically inert and safest GBCA is 1,4,7,10-tetraazacyclododecane-1,4,7,10-tetraacetate (DOTA).

Parameters defined by Solomon, Bloembergen, and Morgan (SBM) describe different factors that influence relaxivity of a GBCA. Two of which have been demonstrated to dramatically influence efficacy: chelate tumbling and water exchange rates. A drawback to current ligand systems are low molecular weight; relaxivity increases with slower tumbling chelates. Current GBCAs have a tumbling rate that is much too rapid to achieve high relaxivities. Secondly, while this value is predominating, it is difficult to ascertain the contribution of other SBM parameters. It had been originally hypothesized that to improve relaxivity, water exchange rate needs to be fast. However, research in our

group has demonstrated that a chelate which exchanges water too rapidly suffers from a reduction in its hydration state. The implication of this reduction in hydration state on relaxivity has yet to be fully appreciated.

The importance of the influence of SBM parameters on relaxivity is realized when advancements in GBCA technology are applied. The non-specific nature of GBCAs means they cannot directly diagnose pathology. One promising approach to reduce detection limits by increasing specificity *in vivo* is through bifunctional chelators (BFCs). These ligands have two components: a metal chelating group to bind gadolinium (DOTA), and a reactive moiety that couples with a targeting vector to bind desired biological receptors. This allows for defined bioaccumulation *in vivo*, resulting in improved diagnostics and lower detection limits. But with several BFCs available commercially, each positioning the vector attachment differently on the DOTA scaffold, the ideal scaffold for BFC design while including the influence of SBM is yet to be established.

The three most common strategies of targeting vector attachment are off the tetraaza macrocycle, through a monoamide pendant arm, or off an α -carbon on the acetate pendant arm. A thorough investigation of these three strategies was explored herein, in which BFC precursors were synthesized, and their structures analyzed relaxometrically. It was found that the attachment strategy significantly impacted water exchange parameters and molecular tumbling, which in turn greatly influenced relaxivity. The experiments conducted herein presented compelling new evidence in the way we define water exchange and hydration state. Studies into derivatives of the macrocycle substituted chelate NB-DOTA presented the impact an extremely rapidly exchanging chelate has on hydration state and its effect on relaxivity. Synthesis and analysis of a new tetra α -carbon substituted

chelate, DOTFA, yielded an exceedingly high relaxivity, as well as an interesting and novel impact on water exchange; there is strong evidence that DOTFA chelates exchange water in a mechanism that is not purely dissociative. Finally, studies into amide substituted chelates provided the expected low relaxivity associated with slow water exchange. Yet, it was demonstrated that changing the type of coordinating monoamide pendant arm, water exchange can be tuned to slightly more optimal values. These systematic studies provided novel insight how the most effective targeted GBCA can be designed, synthesized, and analyzed, as well as presented new evidence into the impact functionalization strategies have on relaxometric values.

Dedication

This thesis is dedicated to the strong women in my life who inspire me daily. Dr. Jenn Finders, my best friend since childhood, who blazed the trail in pursuing a PhD. Your strength, brilliance, and compassion has been a constant source of inspiration to me, and I am so lucky to call you my bestie. Karley Maier, my science soul-sister, your emotional and scientific support, love, and friendship have meant the world to me, I would not be finishing this PhD without you! Linda Moholt, the first person who told me there are no limitations to becoming whomever I want to be when I grow up. Mom, your fearless and confident approach to life has made me realize the person I want to be is you! “Here’s to strong women, may we know them, may we be them, may we raise them.” – Unknown.

Acknowledgements

Professor Mark Woods, for being an advisor who challenged me to becoming the best scientist I could be. Your dedication to producing the highest quality science has left an indelible mark on me, and I hope that I can continue to grow towards that level.

Professors Jason Podrabsky, Robert Strongin, and David Stuart, for being a dedicated and supportive committee throughout the entire PhD process and for the constructive discussions regarding my work.

Professor Mauro Botta and collaborators at the University of Eastern Piedmont, for NMRD and ^{17}O -NMR analyses of all my chelates, and invaluable instruction in interpretation of data.

Professor Ed Valente at University of Portland, for crystal structure analysis and interpretation.

Dr. Katie Payne, for teaching me the ropes, for being a constant source of support throughout this whole process, and for your friendship! I am so grateful for all your help, and proud to say so much of my work is owed to you.

Woods Group members past and present, Joe Armstrong, Dr. Annah Farashishiko, Shelby Kuykendall, Karley Maier, Sam Mumford, Lexy Newberry, Dr. Katie Payne, and Jackie Slack, for providing such a wonderful environment for scientific discussion, and fun!

Decatur Foster, Professor Marilyn Mackiewicz, Karley Maier, Professor Theresa McCormick, and Irving Rettig, and all members of WiSTEM, this club has been one of the most amazing, inspiring, and important parts of my PhD experience.

Portland State University, Oregon Health & Sciences University, National Institutes of Health, and the Nation Science Foundation, for funding.

Dr. Hayden Winter, our friendship is founded in challenging each other to become better scientists, and I am so grateful for that! Also, our love of cats, fancy coffee drinks, and baking has made the difficulty of a PhD process to be much more bearable!

My friends and colleagues in the Chemistry Department, our department feels like a family, and although a PhD is a difficult process, knowing I have the support of so many of you has made it a great experience.

Dan Rust, the love of my life, father of cats, thank you for supporting me through every step of this process, from triumphs to emotional breakdowns, your steadfast encouragement is the reason I am graduating. You make this process worth it!

My amazing family and friends, your unwavering support, enthusiasm, and optimism that I can do this means the world to me! This process really takes a village, and I would not be defending without each and every one of you. I love you all!

Table of Contents

Abstract	i
Dedication	iv
Acknowledgements	v
List of Tables	xiv
List of Figures	xviii
List of Equations	xxiv
List of Schemes	xxv
CHAPTER 1. Introduction.....	1
1.1. Medical Imaging History	1
1.1.1. Introduction.....	1
1.1.2. Comparison of Imaging Modalities	2
1.1.3. Multi-Modal Imaging Technologies	9
1.1.4. Summary	11
1.2. Magnetic Resonance Imaging (MRI).....	12
1.2.1. Generating Contrast	12
1.2.2. Amplifying the Signal Produced – The Spin Echo.....	15
1.3. MRI Contrast Agents (CAs)	19
1.3.1. Non gadolinium-based Contrast Agents	20

1.3.2. Gadolinium Based Contrast Agents (GBCAs)	22
1.4. SBM Theory and Relaxivity	26
1.4.1. Measurable Parameters of SBM Theory	30
1.4.2. Interdependent Nature of SBM.....	31
1.4.3. Rotational Correlation Time (τ_R)	32
1.4.4. Water Exchange Lifetime (τ_M)	34
1.4.5. Activation Volume (ΔV^\ddagger)	36
1.4.6. Characteristic Correlation Time of Dipole-Dipole (τ_C)	38
1.4.7. Mean Square ZFS Energy (Δ^2), Relaxation Rate Time Constant for the Modulation of the Transient ZFS (τ_V), and Electron Spin Relaxation Time (T_{1e}) ...	39
1.4.8. Hydration Number (q) and Lanthanide-Proton Distance (r_{GdH}).....	41
1.4.9. Conclusions.....	42
1.5. Coordination Geometries and Regioisomerism in DOTA and DOTA-Derived Chelates.....	43
1.5.1. Coordination Geometries of DOTA.....	43
1.5.2. Substitution on the DOTA Scaffold.....	46
1.6. Bifunctional Chelators (BFCs)	48
1.6.1. Attachment Strategies	49
1.7. Scope of This Work	50

CHAPTER 2. Macrocycle Substituted Chelates.....	52
2.1. Chelates Undergoing Extremely Fast Dissociative Water Exchange	52
2.2. The impact of r_{GdH} on τ_{R}	55
2.3. Regioisomerism in Macrocycle Substituted Chelates.....	56
2.4. Relaxometric Analysis of the Corner and Side Isomers of GdNB-DOTA	59
2.5. Relaxometric Analysis of the Corner and Side Isomers of GdNB-DOTMA	63
2.6. Exploration into Self-Association of the Side Isomer of GdNB-DOTA	64
2.6.1. T_1 -Relaxation Studies on GdNB-DOTA	65
2.6.2. Attempt of an Amino-Substituted Chelate (GdAB-DOTA).....	65
2.6.3. ^1H -NMR Experiments on EuNB-DOTA.....	66
2.6.4. Luminescence Studies on NB-DOTA Chelates	66
2.6.5. Curie Relaxation Study on TbNB-DOTA.....	69
2.6.6. Curie Relaxation Approach on TbNB-DOTMA.....	72
2.6.7. The Difference in Exchange Between Corner and Side Isomers.....	76
2.7. Conjugation with a Biphenyl Moiety – Implications as a Bioconjugate	77
2.8. Conclusions.....	82
CHAPTER 3. Comparison of Three Functionalization Strategies	84
3.1. Building a Better Bifunctional Chelator	84
3.2. Synthesis of Monoamide Attachment Strategy Chelates.....	88

3.2.1. Synthesis of Nitro-Substituted Monoamide Chelates	88
3.2.2. Synthesis of Biphenyl-Substituted Monoamide Chelates	89
3.3. Synthesis of α -Carbon Pendant Arm Attachment Strategy Chelates	91
3.3.1. Synthesis of Nitro-Substituted α -Carbon Pendant Arm Chelates	91
3.3.2. Synthesis of Biphenyl-Substituted α -Carbon Pendant Arm Chelates	97
3.4. Analysis of the Three Nitro-Substituted Chelates	97
3.5. Analysis of the Three Biphenyl-Substituted Chelates	105
3.5.1. Critical Micelle Concentration Studies	105
3.5.2. Incorporation into Poly- β -Cyclodextrin	114
3.6. Conclusions and Future Directions	117
CHAPTER 4. Tetra α -Carbon Substitution: Synthesis & Relaxometry	119
4.1. Substitution on the α -Carbon Pendant Arm of DOTA	119
4.2. Properties of α -Carbon Pendant Arm Substituted Chelates	120
4.2.1. Stereochemistry of α -Carbon Pendant Arm Substituted DOTA Derivatives	121
4.2.2. Water Exchange Kinetics.....	123
4.2.3. Relaxivity of α -Substituted Chelates	124
4.3. Synthetic Strategy of Tetra α -Carbon Substituted Chelates	124
4.3.1. Attempted Synthesis of DOT ⁱ PrA.....	126
4.3.2. Attempted Synthesis of DOT ⁱ BuA Chelates.....	129

4.3.3. Comparing the Isopropyl and Isobutyl Substitution Strategies	132
4.3.4. Synthesis of DOTFA Chelates	134
4.4. Analysis of LnDOTFA Chelates.....	135
4.4.1. Structural Analysis of DOTFA Chelates	135
4.4.2. Relaxometric Analysis of GdDOTFA	137
4.4.3. Lifting the Barrier of τ_R	142
4.5. Conclusions and Future Directions.....	150
CHAPTER 5. Tetra α -Carbon Substitution: Crystal Structures of DOTFA Chelates....	153
5.1. Introduction.....	153
5.2. Crystallization and Structural Analysis of LnDOTFA Chelates.....	156
5.2.1. Crystallization	156
5.2.2. Crystal Structure Hydration	157
5.2.3. Water Exchange Mechanism via Crystal Structure Analysis	164
5.3. Racemization in DOTFA Chelates	166
5.3.1. Chiral Shift Reagent Study on the Bromoacetate Alkylating Agent	168
5.3.2. α_D Measurements in DOTFA	169
5.3.3. Synthesis and Analysis of Racemic EuDOTFA	169
5.4. Conclusions.....	172
CHAPTER 6. Other Chelates of Interest: DO3A-Monoamides	174

6.1. Monoamides in Medicine and Research	174
6.1.1. Background	174
6.1.2. Properties of Amides as GBCAs.....	175
6.1.3. Chemical Exchange Saturation Transfer	178
6.1.4. Bimodal Agents and Bifunctional Chelators	179
6.2. Synthesis of Monoamide Chelates.....	180
6.3. Analysis of the Monoamide Chelates	182
6.4. Conclusions and Future Directions	187
CHAPTER 7. Experimental.....	190
7.1. General Procedural Remarks	190
7.2. Synthesis, purification, and characterization of Chapter 2 Complexes	191
7.2.1. Synthesis of TbNB-DOTMA S-SSSS Corner and Side Isomers.....	191
7.3. Synthesis, purification, and characterization of Chapter 3 Complexes	196
7.3.1. DO3A tert-Butyl Esters Synthesis	196
7.3.2. Synthesis of DO3A-NBAM derivatives	198
7.3.3. DO3A-BPAM Derivatives.....	203
7.3.4. Synthesis of DOTA-NF Derivatives.....	207
7.3.5. Synthesis of DOTA-BP Derivatives	212
7.4. Synthesis, purification, and characterization of Chapter 4 Complexes	216

7.4.1. Methyl (R)-2-bromo-2-phenylacetate (4-1).....	216
7.4.2. Tetramethyl 2, 2', 2'', 2'''-(1, 4, 7, 10-tetraazacyclododecane-1, 4, 7, 10-tetrayl) (2 S, 2'S, 2''S, 2'''S)-tetrakis (2-phenylacetate) (Me ₄ -DOTFA)	217
7.4.3. (2 S, 2'S, 2''S, 2'''S)-2, 2', 2'', 2'''-(1, 4, 7, 10-tetraazacyclododecane-1, 4, 7, 10-tetrayl) tetrakis (2-phenylacetic acid) (H ₄ -DOTFA)	218
7.4.4. Ln(III)-(2 S, 2'S, 2''S, 2'''S)-2, 2', 2'', 2'''-(1, 4, 7, 10-tetraazacyclododecane-1, 4, 7, 10-tetrayl) tetrakis (2-phenylacetate) from lanthanide chloride salts (LnDOTFA)	219
7.5. Synthesis, purification, and characterization of Chapter 5 Complexes	220
7.5.1. General Remarks.....	220
7.5.2. Ln(III)-(2 S, 2'S, 2''S, 2'''S)-2, 2', 2'', 2'''-(1, 4, 7, 10-tetraazacyclododecane-1, 4, 7, 10-tetrayl) tetrakis(2-phenylacetate) (LnDOTFA)	221
7.5.3. Synthesis of Racemic EuDOTFA	223
7.6. Synthesis, purification, and characterization of Chapter 6 Complexes	226
7.6.1. General Remarks.....	227
7.6.2. Synthesis of Aniline Derived Monoamides	227
7.6.3. Synthesis of Benzylamine Derived Monoamides	231
7.6.4. Synthesis of Dibenzylamine Derived Monoamides.....	235
References.....	240
Appendix.....	257

List of Tables

Table 1.1. Clinically relevant linear derived GBCAs.	23
Table 1.2. Clinically relevant macrocyclic GBCAs.....	24
Table 1.3. Thermodynamic stabilities and metal – ligand dissociation constants for clinically relevant GBCAs.	26
Table 1.4. SBM parameters that determine relaxivity (r_1).....	30
Table 2.1. Values of τ_R generated by fitting different values of r_{GdH} to the NMRD profile of MS-325	56
Table 2.2. Calculated relaxometric values from the fitted ^{17}O -NMR R_{2p} and NMRD profiles of GdNB-DOTA, at 298 K.....	61
Table 2.3. Selected fitted relaxometric values for the four isomers of GdNB-DOTMA..	64
Table 2.4. Stern-Volmer quenching constants for the luminescence lifetime and emission lifetime for NB-DOTA Corner and Side.	68
Table 2.5. Terbium – proton distances (r_{TbH}) and rotational correlation times (τ_R) for TbNB-DOTA Corner and Side using the Curie-spin mechanism.	71
Table 2.6. Estimated τ_R values for TbNB-DOTMA <i>S</i> -SSSS Corner TSAP and Side TSAP from the Curie relaxation analysis of the 1H -NMR spectra.....	75
Table 2.7. Relaxometric values from the fitted NMRD profiles of the Corner and Side isomers of GdBP-DOTA below the CMC.....	80
Table 2.8. Critical micelle concentrations, micelle diameters, and relaxivities from the NMRD profiles of GdBP-DOTA Corner and Side above the CMC	81

Table 3.1. Multi-variable approach to synthesis of the protected ligand (3-4) percent product formation after 24- and 48-hour reaction times.	95
Table 3.2. Structures of the parent complex EuDOTA and the three substitution strategies with their percent of SAP coordination geometry.	98
Table 3.3. Calculated relaxometric values from the fitted ^{17}O -NMR R_{2p} and NMRD profiles of GdDOTA, GdNB-DOTA, GdDO3A-NBAM, and GdDOTA-NF	100
Table 3.4. CMC, micelle diameters, and relaxivities above their respective CMCs for GdBP-DOTA Corner and Side isomers, and GdDO3A-BPAM.....	109
Table 3.5. Calculated relaxometric values from the fitted ^{17}O -NMR R_{2p} and NMRD profiles of GdBP-DOTA Corner and Side isomers, and GdDO3A-BPAM, below their respective CMCs	110
Table 3.6. Relaxometric data from the fitted ^{17}O -NMR and NMRD profiles of GdDO3A-BPAM above its CMC value	111
Table 3.7. Calculated relaxometric values from the fitted ^{17}O -NMR R_{2p} and NMRD profiles of GdBP-DOTA Corner, GdBP-DOTA Side, and GdDO3A-BPAM incorporated with poly- β -cyclodextrin.....	115
Table 3.8. Mathematical determination of the binding affinity on the change in relaxation rate constant (ΔR_1)	117
Table 4.1. Comparison of the three leaving group strategies for alkylating cyclen with an ^iPr methyl ester after four days of reacting.	128
Table 4.2. ESI-MS reaction monitoring of tetra $\text{Me}_4\text{-DOT}^i\text{BuA}$ formation compared with di- and tri-alkylated species	131

Table 4.3. Comparison of the two leaving group strategies for alkylating cyclen with an ⁱ Bu methyl ester after four days of reacting.....	132
Table 4.4. Comparing two leaving group strategies for the alkylation of cyclen with an ⁱ Pr or ⁱ Bu methyl ester with their highest percentage of tetra-alkylated after the reaction was stopped.....	134
Table 4.5. Calculated relaxometric values from the fitted ¹⁷ O-NMR R_{2p} and NMRD profiles of GdDOTA, GdDOTMA, and GdDOTFA.....	138
Table 4.6. Selected data for GdDOTFA bound with β -cyclodextrin and poly- β -cyclodextrin.....	143
Table 4.7. The binding affinity of GdDOTFA to HSA and the relaxivity of the bound chelate to HSA	148
Table 5.1. Calculated values from crystallographic data for chelates of DOTFA.....	160
Table 5.2. α_D values for products in each synthetic step of DOTFA chelate synthesis.	169
Table 6.1. Selected relaxometric properties of linear and macrocyclic chelates, comparison of amide containing and non-amide containing complexes.....	177
Table 6.2. Coordination geometry ratios for amide-containing chelates.....	184
Table 7.1. RP-HPLC purification method for LnNB-DOTMA chelates.....	194
Table 7.2. RP-HPLC purification method for LnDO3A-NBAM chelates.	202
Table 7.3. RP-HPLC purification method for LnDO3A-BPAM chelates.	207
Table 7.4. RP-HPLC method used for nitrophenyl containing ligands.....	210
Table 7.5. RP-HPLC method for nitrophenyl containing chelates.	211
Table 7.6. RP-HPLC method to purify biphenyl containing chelates.	216

Table 7.7. RP-HPLC purification method for LnDOTFA chelates. 220

Table 7.8. RP-HPLC purification method of LnDO3A-Monoamide Chelates. 227

List of Figures

Figure 1.1. Dual-modal imaging performed on a 58-year-old male patient with nasopharyngeal carcinoma.....	10
Figure 1.2. Rotating frame depiction of the two relaxation mechanisms that occur in an NMR experiment.	13
Figure 1.3. Pulse sequence to obtain an MR image. 90° and 180° refer to RF pulses of that strength. TE is the echo time, and TR is the repetition time.....	15
Figure 1.4. Pulse sequence techniques used to alter TR and TE to result in T_1 -weighted (T_1 -W), T_2 -weighted (T_2 -W), and Proton Density (PD) images.....	19
Figure 1.5. T_2 -weighed image, T_1 -weighted image, and T_1 -weighted image with gadolinium-based contrast agent administered.....	20
Figure 1.6. Mn derived contrast agents.....	21
Figure 1.7. Relaxivity (r_1) is defined by SBM parameters as described in Equations 1.3 – 1.10.....	29
Figure 1.8 When other SBM parameters are fixed, the influence of the water exchange lifetime (τ_M) and rotational correlation time (τ_R) on relaxivity (r_1) are realized.	32
Figure 1.9 Water exchange mechanism continuum with relevant gadolinium complexes based on their activation volumes (ΔV_0^\ddagger).....	38
Figure 1.10. [3, 3, 3, 3] ring conformations of 1, 4, 7, 10-tetraazacyclododecane (cyclen).	43
Figure 1.11. The four possible coordination isomers of GdDOTA. Interconversion between SAP and TSAP is achieved through arm rotation and ring inversion.....	44

Figure 1.12. Side profiles of the two coordination geometries of DOTA chelates	45
Figure 1.13. Possible regio- and coordination isomers of substituted DOTA chelates.	47
Figure 1.14. The strategy for biological targeting of a BFC.....	49
Figure 1.15. The three main attachment strategies for a targeting vector.....	50
Figure 2.1. The dissociative water exchange mechanism described herein.	53
Figure 2.2. Dale structures of the four coordination geometries of GdNB-DOTA.	57
Figure 2.3. RP-HPLC chromatogram of the separation of the Corner and Side isomers of GdNB-DOTA monitored at $\lambda = 270$ nm.....	58
Figure 2.4. Dale structures of the four coordination geometries of GdNB-DOTMA.....	59
Figure 2.5. Temperature dependence of ^{17}O transverse relaxation rate constants of the Corner and Side isomers of GdNB-DOTA. NMRD profiles of the Corner and Side isomers of GdNB-DOTA recorded at three temperatures.....	60
Figure 2.6. Relaxivities (r_1) of GdNB-DOTA Corner and Side isomers at different concentrations and temperatures.....	65
Figure 2.7. The most shifted axial proton (ax^S) dependence on the transverse relaxation rate of TbNB-DOTA Corner SAP, Side SAP, and Side TSAP at three magnetic field strengths, 9.4 T, 11.5 T, and 14.1 T at 298 K. $G = 10^{-4}$ T.....	71
Figure 2.8. Analysis of the most shifted axial (ax^S) protons of TbNB-DOTMA (<i>S</i> -SSSS) Corner and Side isomers. ^1H -NMR spectra of the most shifted ax^S protons of the two regioisomers. Field dependence of the transverse relaxation rate constant of the most shifted ax^S protons of the Corner and Side regioisomers.....	74

Figure 2.9. DFT modeling calculations of the distortion of the macrocyclic cage in GdNB-DOTA Corner, and Side	76
Figure 2.10. Dynamic light scattering (DLS) distribution of the micelles formed by the Corner and Side isomers of GdBP-DOTA.....	78
Figure 2.11. NMRD Profiles at 298 K of GdBP-DOTA Corner below the CMC, and above the CMC; Side below the CMC, and above the CMC.....	79
Figure 3.1. Point of attachment of a targeting vector on a DOTA-based BFC; off the macrocycle, through a monoamide pendant arm, or on the α -carbon of a pendant arm ..	85
Figure 3.2. The three nitro-substituted macrocyclic chelates analyzed in Section 3.4.1..	87
Figure 3.3. The three biphenyl-substituted macrocyclic chelates analyzed in Section 3.4.2.	87
Figure 3.4. Relaxivity as a function of magnetic field strength (NMRD profile) of GdDO3A-NBAM, and the temperature dependence of the reduced ^{17}O NMR transverse relaxation rate, and chemical shift measured at 67.8 MHz.....	99
Figure 3.5. Relaxivities and rotational correlation times of the four chelates examined herein, compared to the parent structure, GdDOTA, at 20 MHz and 298 K.	102
Figure 3.6. NMRD Profiles of GdDO3A-BPAM below and above its CMC	106
Figure 3.7. Determination of the critical micelle concentration (CMC) of GdBP-DOTA Corner, Side, and GdDO3A-BPAM	108
Figure 3.8. NMRD profiles of GdBP-DOTA Corner, GdBP-DOTA Side, and GdDO3A-BPAM above their respective CMC values, at 298 K.	110

Figure 3.9. Temperature dependence of relaxivity for GdDO3A-BPAM below the CMC and above the CMC	112
Figure 3.10. Longitudinal relaxation rates for the three chelates GdBP-DOTA Corner, GdBP-DOTA Side, and GdDO3A-BPAM as a function of concentration of poly- β -cyclodextrin, at 298 K and 20 MHz.....	114
Figure 3.11. Fitted NMRD profiles of GdBP-DOTA Corner, GdBP-DOTA Side, and GdDO3A-BPAM conjugated with poly- β -cyclodextrin, at 298 K.....	115
Figure 4.1. Common pendant arm α -substituted ligands.....	120
Figure 4.2. The four possible stereoisomers of GdDOTMA.	122
Figure 4.3. Retrosynthetic pathway to various α -carbon substituted pendant arm chelates with potential chiral amino acid starting materials.	125
Figure 4.4. The three tetra-substituted ligand systems studied, tetra-isopropyl (H_4 -DOT ⁱ PrA), tetra-isobutyl (H_4 -DOT ⁱ BuA), and tetra-phenyl (H_4 -DOTFA)	126
Figure 4.5. Coordination geometry mole fractions for LnDOTA, LnDOTMA, and LnDOTFA.....	137
Figure 4.6. ¹ H-NMRD profiles of GdDOTFA at 283 K, 298 K, and 310 K and pH 6.6; temperature dependence of the transverse ¹⁷ O water relaxation rate (R_{2p}) at 67.8 MHz and pH 6.6.....	139
Figure 4.7. The observed longitudinal relaxation rate of water (R_1) as a function of concentration of β -cyclodextrin or poly- β -cyclodextrin in a solution of GdDOTFA [0.18 mM] at 20 MHz and 298 K.....	143

Figure 4.8. The change in partial heat capacity (ΔC_p) as a function of temperature for the binding of GdDOTFA with plasma, and the change in partial heat capacity as a function of temperature of pure plasma.....	145
Figure 4.9. When other SBM parameters are optimized, the influence of the water exchange lifetime (τ_M) and rotational correlation time (τ_R) on relaxivity (r_1) are realized	146
Figure 4.10. The observed longitudinal relaxation rate of water (R_1) as a function of concentration of human serum albumin in a solution of GdDOTFA [0.09 mM] at 20 MHz and 298 K.....	147
Figure 5.1. Side view depiction of the d/c ratio and the O-Ln-O torsion angle. Top view depiction of the O ₄ and N ₄ areas, and the torsion angle of the antiprism, α . The NCCN angle, carboxylates and substituents removed for clarity.	156
Figure 5.2. Later lanthanide crystal structures of DOTFA chelates: DyDOTFA (●), ErDOTFA, TmDOTFA, YbDOTFA. YbDOTFA is the only structure that crystallized without an apical water coordinated.	157
Figure 5.3. Metal-water distances versus lanthanide ionic radius for DOTFA chelates.	158
Figure 5.4. Ionic radii calculated for each chelate of DOTFA. The gray and blue lines are calculated CNs of the lanthanide	161
Figure 5.5. Calculated coordination numbers for each chelate of DOTFA based on water-lanthanide distance.....	162
Figure 5.6. Lanthanide ionic radius as a function of O-Ln-O angle for LnDOTFA.....	163
Figure 5.7. Ionic radius as a function of d/c ratio for LnDOTFA.....	164
Figure 5.8. Simulated ¹ H-NMR spectrum of racemic EuTCE-DOTA.	167

Figure 5.9. $^1\text{H-NMR}$ spectra of 4-1 and 4-1 with the chiral shift reagent	168
Figure 5.10. Zoomed in section of the $^1\text{H-NMR}$ spectrum of Racemic EuDOTFA. The axial protons in this region show the predominance of the homochiral (<i>RRRR/SSSS</i>) conformation in the large TSAP peak at ~18 ppm, and the smaller SAP peak at ~50 ppm.	172
Figure 6.1. Active coupling of <i>N</i> -hydroxysuccinimide ester with a terminal amine to form an amide and <i>N</i> -hydroxysuccinimide.....	174
Figure 6.2. The structures of two clinically available MRI contrast agents containing amides. Omniscan TM (gadodiamide), and OptiMARK [®] (gadoversetamide).....	175
Figure 6.3. The three monoamide containing chelates explored herein. ($\text{Ln} = \text{Eu}, \text{Gd}, \text{Yb}$).	180
Figure 6.4. Axial proton regions of the macrocycle in the $^1\text{H-NMR}$ spectra of Yb complexes of DO3A-Dibenzylamide, DO3A-Phenylamide, and DO3A-Benzylamide.	183
Figure 6.5. Aromatic proton regions in the $^1\text{H-NMR}$ spectra of Yb complexes of DO3A-Dibenzylamide, DO3A-Phenylamide, and DO3A-Benzylamide	185
Figure 6.6. The superposition of the crystal structures of the <i>p</i> -OMe derivative of TmTetra-phenylamide and the <i>p</i> -Me derivative of GdTetra-benzylamide on a heat map of the magnetic field induced by the paramagnetic Ln^{3+} ion. In each case two pendant arms of the chelate and any aromatic substituents are not shown for clarity. The magnetic field is assumed to be perfectly axial with the principal magnetic axis aligned along the Ln-OH_2 bond (if present). Red regions correspond to a downfield shift for Ln^{3+} and blue regions correspond to upfield shifts in the $^1\text{H-NMR}$	186

List of Equations

Equation 1.1. The definition of Larmor frequency	12
Equation 1.2. The determination of signal intensity (S) from a pulse sequence	17
Equation 1.3. Definition of T_1 relaxation rate of bulk water	28
Equation 1.4. Observed solvent relaxation rate ($1/T_{1, \text{obs}}$).....	28
Equation 1.5. Longitudinal proton relaxation time of water (T_{1M})	28
Equation 1.6. DD contribution to T_1 relaxation	28
Equation 1.7. SC contribution to T_1 relaxation.....	28
Equation 1.8. Characteristic correlation time of the DD interaction (τ_C)	29
Equation 1.9. Characteristic correlation time of the SC interaction (τ_e).....	29
Equation 1.10. Field dependent paramagnetic electron spin relaxation time of zero field splitting interactions (T_{1e}^{ZFS}).....	29
Equation 1.11. Debye-Stokes equation for τ_R	33
Equation 1.12. The water exchange mechanism.....	37
Equation 2.1. The Curie-spin mechanism contribution to transverse relaxation rate.....	70
Equation 3.1. Equation to determine critical micelle concentration.....	109
Equation 3.2. The measured difference in relaxation rate	117
Equation 5.1. Calculation to determine the ionic radius (I.R.)	159
Equation 7.1. Determination of mass of potassium carbonate to add to the DO3A ¹ Bu ester HBr salt to effectively neutralize.	197

List of Schemes

Scheme 2.1. Chelation of NB-DOTA with terbium chloride.	69
Scheme 2.2. Synthesis of TbNB-DOTMA <i>S</i> -SSSS.....	73
Scheme 2.3. Synthesis of target chelate, GdBP-DOTA from IB-DOTA.	77
Scheme 3.1. Total synthesis of LnDO3A-NBAM Chelates..	89
Scheme 3.2. Synthesis of LnDO3A-BPAM Chelates.....	90
Scheme 3.3. Proposed synthetic strategy of DOTA-NF.....	92
Scheme 3.4. Synthesis of ethyl 2-bromo-2-(4-nitrophenyl)acetate (3-3)	93
Scheme 3.5. Total synthesis of LnDOTA-NF chelates.....	96
Scheme 3.6. Synthesis of LnDOTA-BP chelates.....	97
Scheme 4.1. Proposed synthetic strategy for the tetra-isopropyl protected ligand.....	126
Scheme 4.2. Synthesis of ⁱ Pr Methyl Ester Arms	129
Scheme 4.3. Proposed synthetic pathway for LnDOT ⁱ BuA chelates.	130
Scheme 4.4. Synthesis of Me ₄ -DOT ⁱ BuA.....	132
Scheme 4.5. Total synthesis of LnDOTFA chelates.....	135
Scheme 5.2. Synthesis of racemic EuDOTFA.....	171
Scheme 6.1. Total synthesis of LnDO3A-Monoamide chelates.....	182
Scheme 7.1. Synthesis of methyl (<i>R</i>)-2-(((trifluoromethyl)sulfonyl)oxy)propanoate (2-1).	191
Scheme 7.2. Synthesis of protected methyl ester ligand (Me ₄ -NB-DOTMA <i>S</i> -SSSS, 2-2)	192
Scheme 7.3. Synthesis of ligand <i>S</i> -SSSS H ₄ -NB-DOTMA.....	193

Scheme 7.4. Synthesis of <i>S</i> -SSSS TbNB-DOTMA	194
Scheme 7.5. Synthesis of DO3A- <i>tert</i> -butyl esters.	196
Scheme 7.6. Synthesis of 2-bromo- <i>N</i> -(4-nitrobenzyl) acetamide (3-1).....	198
Scheme 7.7. Synthesis of the protected ligand (3-2)	199
Scheme 7.8. Synthesis of the ligand DO3A-NBAM	200
Scheme 7.9. Chelation of the ligand DO3A-NBAM	201
Scheme 7.10. Synthesis of DO3A-ABAM.	203
Scheme 7.11. Synthesis of DO3A-IBAM.....	204
Scheme 7.12. Synthesis of DO3A-BPAM.....	205
Scheme 7.13. Chelation of the ligand DO3A-BPAM.....	206
Scheme 7.14. Synthesis of ethyl 2-bromo-2-(4-nitrophenyl) acetate (3-3).	207
Scheme 7.15. Synthesis of the protected ligand (3-4)	208
Scheme 7.16. Synthesis of the ligand DOTA-NF.....	209
Scheme 7.17. Chelation of DOTA-NF with lanthanide chlorides	210
Scheme 7.18. Reduction of DOTA-NF.....	212
Scheme 7.19. Synthesis of DOTA-IF	213
Scheme 7.20. Synthesis of DOTA-BP	214
Scheme 7.21. Chelation of DOTA-BP.....	215
Scheme 7.22. Two-step synthesis of methyl (<i>R</i>)-2-bromo-2-phenylacetate (4-1).....	216
Scheme 7.23. Synthesis of Me ₄ -DOTFA	217
Scheme 7.24. Synthesis of H ₄ -DOTFA.	218
Scheme 7.25. Synthesis of LnDOTFA	219

Scheme 7.26. Synthesis of LnDOTFA from corresponding lanthanide triflates, chlorides, and oxides	221
Scheme 7.27. Synthesis of DL-methyl 2-bromo-2-phenylacetate (6-1).	223
Scheme 7.28. Synthesis of the protected ligand Racemic Me ₄ -DOTFA	224
Scheme 7.29. Synthesis of Racemic H ₄ -DOTFA	225
Scheme 7.30. Synthesis of Racemic EuDOTFA.	226
Scheme 7.31. Synthesis of 2-bromo- <i>N</i> -phenylacetamide (6-1).	227
Scheme 7.32. Synthesis of the protected ligand (6-2)	228
Scheme 7.33. Synthesis of DO3A-Phenylamide	229
Scheme 7.34. Synthesis of LnDO3A-Phenylamide	230
Scheme 7.35. Synthesis of <i>N</i> -benzyl-2-bromoacetamide (6-3).	231
Scheme 7.36. Synthesis of the protected ligand (6-4)	232
Scheme 7.37. Synthesis of the ligand DO3A-Benzylamide	233
Scheme 7.38. Synthesis of LnDO3A-Benzylamide.....	233
Scheme 7.39. Synthesis of <i>N,N</i> -dibenzyl-2-bromoacetamide (6-5).	235
Scheme 7.40. Synthesis of the protected ligand (6-6)	236
Scheme 7.41. Synthesis of the ligand DO3A-Dibenzylamide	237
Scheme 7.42. Synthesis of LnDO3A-Dibenzylamide	238

CHAPTER 1

INTRODUCTION

1.1. Medical Imaging History

1.1.1. Introduction

Before the invention of imaging technology, diagnostic medicine was based on a patient's symptoms and a physician's ability to decipher disease from the presented signs. This changed in 1895 when German physicist Dr. Wilhelm Röntgen discovered the X-ray, and for the first time physicians were able to peer inside the human body without the aid of a scalpel.¹ This invaluable advancement ignited a new field of medical technology in which physicians looked towards modalities that glean anatomy without invasive surgery.

In 1942 utilizing technology created by Pierre Curie in 1880, neurologist Karl Dussik used ultrasonic waves to generate the first image of a human brain. This imaging modality was perfected by physicist John Wild in the late 1940s and ultrasound has remained largely unchanged to this day.

The next major leap in medical imaging was in the field of nuclear medicine. In 1960 physician William Oldendorf filed for the first patent entitled "Radiant Energy Apparatus for Investigating Selected Areas of the Interior of Objects Obscured by Dense Material" and subsequently published his findings in 1961.^{2,3} Then in 1967, electrical engineer Sir Godfrey Hounsfield invented the first computed axial tomography (CAT) scanner used clinically.

In 1971, physician Raymond Damadian published a seminal paper in *Science* which described the differentiation between healthy and malignant tissue based on relaxation times in nuclear magnetic resonance spectroscopy (NMR).⁴ Two years later, chemist Dr. Paul Lauterbur was able to translate the data provided by NMR into an image.⁵ Combining the important discoveries by Damadian and Lauterbur, physicist Dr. Peter Mansfield employed the use of gradients, which resulted in the first practical method for magnetic resonance (MR) imaging in humans.⁶ These discoveries led to the first MR image generated in 1977, and a Nobel prize for Lauterbur and Mansfield.

The field of nuclear medicine was expanded with the advent of positron emission tomography (PET). This imaging modality detects gamma rays from radioactive decay of an injected radioactive tracer. Following the foundational research into radioisotopes by the Manhattan Project, many scientists sought to develop radioactive materials that were inert to humans. In 1975, graduate student Louis Sokoloff developed a radioactive 2-deoxyglucose, a competitive inhibitor for glucose-6-phosphate, utilizing ^{14}C and the first radiotracer for imaging was born.⁷ Sokoloff expanded his research with the development of [^{18}F]fluoro-2-deoxy-D-glucose (FDG), which remains as the most clinically used radiotracer. This allowed physicians to glean insight into metabolic processes, in addition to the generation of discrete images.

1.1.2. Comparison of Imaging Modalities

While there are many benefits to the myriad of imaging techniques a physician has available, each has their own set of inherent drawbacks. Comparing these modalities helps

to understand the advantages and limitations of each, as well as determining which imaging technique works best for each purpose.

1.1.2.1. X-ray

X-ray imaging is an inexpensive and accessible modality that does not require specialized building setup. Furthermore, new technology has allowed X-ray imaging to be portable, thus allowing diagnosticians to image in a variety of settings. X-rays are a type of electromagnetic radiation, where the high energy of an X-ray photon is transferred to any electrons it encounters. This interaction results in the atom ejecting the energized electron, resulting in a net positive charge on the atom, thus X-ray radiation is termed ionizing radiation. Although the energy transfer and electron ejection results in a destabilization of the molecular structure of the object the X-ray hits, infrequent short exposure to X-ray radiation does not generally result in long lasting detrimental effects.

The amount of X-ray radiation an object can absorb is dependent on its density and atomic makeup. High atomic number containing matter will absorb X-rays more easily because there is a higher probability of an encounter with an electron. Thus, dense matter such as bone, which is primarily composed of calcium, will absorb X-rays better than soft tissue which is primarily constituted of lower atomic number elements. As a result, X-ray is an excellent modality for analyzing the skeleton, and not very effective at differentiating against soft tissue. Another limitation of this imaging modality is that it only analyzes the patient from a two-dimensional configuration. When taking an X-ray, the area being imaged is placed against a photographic or fluorescent film. The X-ray is passed through the afflicted area; dense material absorbs the X-ray radiation, preventing the X-rays from

hitting the film. The X-rays pass through the soft tissue and are deposited on the film, turning it black.

X-ray can also employ the use of a contrast enhancing agent, typically a compound which contains high atomic elements such as barium or iodine. This allows for certain anatomical information that is typically dark on the image to appear bright. Thus, features such as the circulatory system or digestive tract can be imaged with good detail. However, neither of these contrast agents are specific; they either circulate through the bloodstream non-specifically or travel through the digestive tract *via* peristalsis, and thus cannot directly diagnose pathology.

1.1.2.2. Ultrasound

Ultrasound imaging has the benefit of being inexpensive, extremely portable, and simple to use. Ultrasound devices are transducers comprised of piezoelectric crystals that vibrate when an electrical current is applied through the crystal array. This vibration results in the generation of high frequency ultrasonic waves. When ultrasonic waves are emitted into the body, they encounter tissues of different densities, resulting in characteristic vibrational echoes that are detected by the transducer. The signals of these echoes are measured based on the time it takes for them to travel back to the transducer. The varied signals are then translated into electrical currents that are computationally resolved into a colorimetric spectrum. The color spectrum produced is like that of MRI, where strong signals are encoded as bright and weak signals are encoded as dark. The differentiation in color intensity is what gives rise to the image produced. A major benefit to ultrasound is its ability to display real-time motion, such as that of a heart valve opening, or movement

of fluid, by exploiting the Doppler effect. This allows diagnosticians to determine physiological information that is typically missed in many other imaging modalities. The main drawback to ultrasound imaging is its inability to image past a certain depth. Because ultrasound utilizes the movement of sound waves the transducer does not have high enough sensitivity to detect waves that travel deep into the body. As a result, deeper tissues and organs cannot be imaged. Patients who have a large amount of subcutaneous fat are also poor candidates for ultrasound for this reason.

Contrast agents in ultrasound are limited due to the nature of the imaging modality. The main source of improving contrast in ultrasound is implementing microbubbles; these are insoluble gas cores made up of fluorinated compounds enveloped in an insoluble material, typically a lipid or polymer. They facilitate the enhancement of the acoustic contrast ratio in the generated image and are used primarily in cardiological imaging. Ultrasound can move, expand, or divide microbubbles through insonation, which requires their stability to be robustly studied. As a result, microbubbles have been thoroughly evaluated to ensure patient safety.⁸

There has been research in recent years to increase the utility of microbubbles by implementing them as therapeutic agents. Ultrasound can control the oscillation of the microbubbles to alter the walls of blood vessels, which would facilitate the delivery of a therapeutic drug.⁹ Although preliminary studies are promising, there are limitations to this technology; microbubbles cannot overcome the flow of blood through the cardiovascular system, resulting in dissipation of the drug. There has been research to increase specificity of microbubbles, by altering the chemical surface of the encapsulating material. However,

efforts to create a stable, uniform, specific material is still underway. Most importantly, the extremely low resolution observed in ultrasound imaging cannot be overcome regardless of the specificity of the targeted agent.

1.1.2.3. CT

Computed tomography (CT) is a high sensitivity imaging modality that alleviates the major limitation of X-ray imaging: inability to spatially resolve images. CT operates under the same principle as X-ray imaging; however, it utilizes a rotating source of X-rays, generated from a tungsten ring. A continuous source of X-rays is simultaneously received through a detection ring that also encircles the patient. This allows for cross-sectional slices of the body to be imaged. These images can then be computationally rendered through projection-reconstruction to create a three-dimensional image and allows physicians to glean detailed anatomical information that a traditional X-ray does not provide. A major benefit of this modality is the speed with which images are produced. X-rays are detected instantaneously, and a full CT imaging session can take less than 10 minutes. The images generated are perpendicular to the patient's body, and thus CT is sometimes referred to as computational axial tomography (CAT). The major limitation to this imaging modality is the same as X-ray: the patient is being exposed to ionizing radiation and at a higher exposure rate due to the ring of X-rays being shot at the patient. The amount of radiation a patient is exposed to is not minimal, and CT imaging is typically performed to monitor progress of treatment. Thus, the patient could receive multiple scans in a short period of time, increasing their ionizing radiation exposure.

Contrast agents are commonly used during CT image acquisition. The most used contrast agent in CT is an iodinated compound; typically, an aromatic organic structure decorated with multiple iodine atoms. Although these agents are quite effective at increasing the contrast on the image, they require a high dose to be effective, in the range of 30 g – 50 g of organo-iodine per dose.¹⁰ The high detection limits of iodinated contrast agents means that the structure in which iodine is bound must be robust, as excess free iodine can cause irreversible damage to the endocrine system.¹¹ Secondly, it has been reported that iodinated contrast agents, even when effectively bound in their organic frameworks, can trigger an allergic response in up to 14% of patients.¹⁰ With dose and toxicity aside, a major issue within the use of iodinated CT agents is their lack of specificity. They are typically used to enhance circulatory imaging; however, they do not selectively highlight areas of damage or distress, thus it is up to the radiologist to carefully analyze the image to diagnose pathology.

1.1.2.4. PET

Positron emission tomography (PET) utilizes a radionuclide-labeled sugar, to monitor metabolism inside a tumor cell. Once the radiopharmaceutical is taken up by the tumor, the radioactive component decays and emits a positron. The positron then collides with an electron, and the annihilation event results in the emission of two photons of γ -radiation emitted in opposite directions. The relative position of the emitted γ particles can then be detected in a circular detector around the patient, to highlight important metabolic information.

One major benefit to PET imaging is its ability to examine metabolism inside tumor cells and other soft tissues by monitoring the uptake of the radiopharmaceutical. This allows for PET to be a quantitative imaging modality that directly diagnoses pathology. However, there are some drawbacks to this imaging methodology. Like CT, the PET decay of the radiotracer results in the patient being exposed to ionizing radiation; albeit a much lower dose than that produced in X-ray or CT imaging. Unlike CT, the mechanism of a PET scan does not provide anatomical information. Secondly, certain patients are unable to undergo PET imaging; those who are pregnant or diabetic are contraindicated, due to risk associated with exposure to a radioactive material or a sugar-containing substance, respectively. Another major drawback to PET is the extremely low resolution of the images produced by this modality. Although PET is considered a high sensitivity modality due to the mechanism of detecting photons, the images produced are difficult to interpret. Thus, PET has the ability to monitor metabolic activity that could potentially provide important information about pathology; however, the resolution is much lower than that of CT or MRI. Lastly, PET imaging is expensive, requires specialized equipment, and a dedicated lab-space capable of synthesizing and disposing of the radiotracer.

1.1.2.5. MRI

Magnetic Resonance Imaging (MRI) is a unique diagnostic tool in that it provides high resolution images without exposing the patient to ionizing radiation like its X-ray, CT, and PET counterparts. The mechanism of action for MRI is the same principle as NMR: a large external magnet is utilized to align the orientation of the magnetic vector of an NMR-active nucleus. The external field perturbs the magnetic moments of these nuclei

so the net magnetic vector aligns with a slight bias in the orientation of the magnetic field. Once aligned, the system is not static; the net magnetic vector precesses about the applied magnetic field at a rate specific to the nucleus in question. However, the signal generated by this precession of spins is of a much lower magnitude than that of the applied magnetic field and is therefore unable to be detected. Thus, through a series of radiofrequency pulses, the bulk magnetic moment is translated to the transverse plane where the signal can be detected by receiver coils. The primary difference from NMR to MRI is the utilization of gradient magnetic fields which encode spatial resolution of the signal to generate an image.

Although MRI is an excellent tool to differentiate between tissue types, the time it takes for nuclei to relax to equilibrium results in low temporal resolution. Furthermore, MRI is limited in its ability to image metabolic processes. Another drawback to current MRI practices is the cost; because scanners utilize superconducting magnets, they need to be cooled to near absolute zero to reduce electrical resistance. This requires the use of liquid cryogenics, which are finite resources, to maintain the superconducting nature of the magnet. Finally, the cost associated with maintaining, and the facilities required to house MRIs are limiting factors for many hospitals and medical centers. Because MRIs are permanent fixtures in these settings, their utility is limited to mostly urban centers.

1.1.3. Multi-Modal Imaging Technologies

Combining two advanced imaging modalities allows physicians to glean greater insight into the pathology of disease. PET imaging provides important metabolic information but suffers from resolution and is therefore unable to provide anatomical information. CT and MR can generate in high resolution images of anatomy, but do not

provide the metabolic information of PET. There is a great demand for combining a metabolic imaging modality with an anatomical one. Thus, PET-CT and PET-MRI are the predominant multimodal imaging modalities. The differences in the dual images they produce are shown in Figure 1.1.

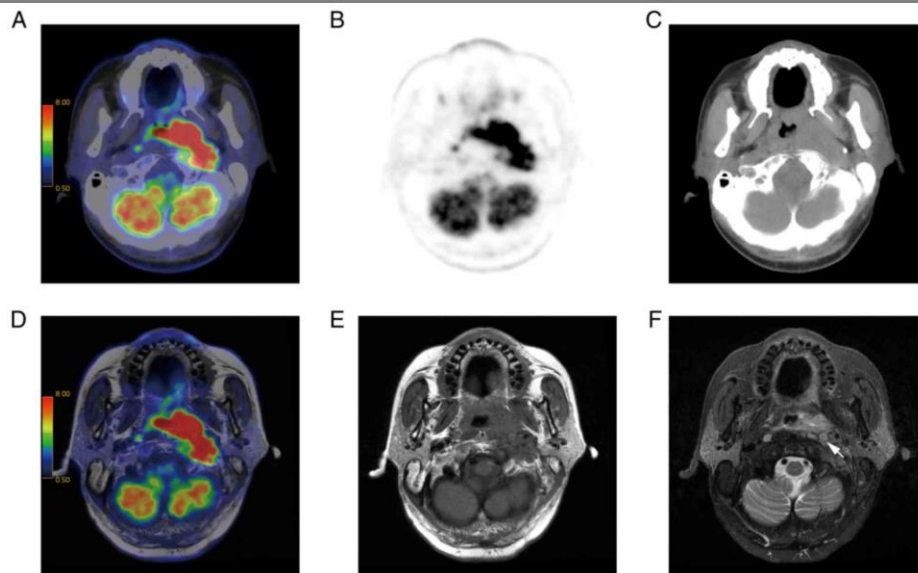


Figure 1.1. Dual-modal imaging performed on a 58-year-old male patient with nasopharyngeal carcinoma. (A) PET/CT dual image. (B) PET image (C) CT image (D) T_1 -weighted PET/MR dual image. (E) T_1 -weighted image. (F) T_2 -weighted image.¹²

The dual-modal technology of PET-CT allows for metabolic and anatomical information to be obtained simultaneously.¹³ Because CT is an advanced form of X-ray imaging, it provides highly detailed images of bone and other dense material. However, one major drawback to a dual-modal PET-CT scan is the high dose of ionizing radiation: both the CT scanner and PET radiotracer result in the production of ionizing radiation, thus increasing the patient's exposure. Yet, this dual imaging modality has become increasingly popular for physicians who need information on a metabolic process with high resolution

images. PET-CT continually proves utility due to its lower cost in comparison with MR imaging, and quick acquisition time. Conversely, PET-MRI is an attractive dual-modal imaging modality due to reduced patient exposure to ionizing radiation. A major advantage of a dual PET-MRI is its ability to take simultaneous images in one session.¹⁴ This allows for real-time imaging of a metabolic process, while maintaining the high-resolution imaging power of MRI. Secondly, a combined imaging probe can be utilized to act as a radiotracer as well as contrast agent. One drawback of PET-MRI is its inability to effectively image dense material such as bone. Another detriment of PET-MRI is the expense associated with imaging.

1.1.4. Summary

The individual and combined imaging techniques presented each have their inherent benefits as well as drawbacks. No one imaging modality has a major advantage over another in current clinical practice. The major goal in the future of medical imaging is to develop tools that provide more specific information about pathology. Currently, each modality can overcome high detection limits, low sensitivity, or poor resolution by implementing a contrast enhancing agent, yet none of these agents facilitate direct diagnosis. Thus, the field needs a modality that provides high resolution images, low detection limits while maintaining a superior safety profile.

1.2. Magnetic Resonance Imaging (MRI)

1.2.1. Generating Contrast

The weak magnetic field of the earth causes any nucleus with an odd number of protons, neutrons, or both, to have a net magnetic moment. These moments, or spins, are randomly positioned in space with no bias towards any orientation. However, when they are placed in an external magnetic field such as an NMR or MRI, the external field induces a bias in the net magnetic moment according to the Boltzmann distribution of individual spins. The distribution of spins is nearly split between aligning with (α -state), or against (β -state) the applied magnetic field, with only parts per one million more spins aligned with the lower energy α -state. This slight excess of bias of spin distribution is the result of the field frequency of the NMR being much higher than the net magnetic field of the earth and generates the net magnetic moment (M_z) that is probed in an NMR experiment.

$$\omega_0 = -\gamma B_0$$

Equation 1.1. The definition of Larmor frequency in which ω_0 is the Larmor frequency in $\text{rad}\cdot\text{s}^{-1}$, γ is the gyromagnetic ratio of the nucleus, and B_0 is the magnetic field strength.

B_0 causes M_z to precess at a specific frequency called Larmor as shown in Equation 1.1. The gyromagnetic ratio, γ , is a specific property of the nucleus and affects the rate of Larmor precession, which is linearly dependent on field strength. To glean information about the chemical environment, torque is applied to M_z via an excitation radiofrequency (RF) pulse (B_1) at the Larmor frequency of the nucleus being probed. This transfers the magnetization into the transverse plane where the precession of M_z produces a signal. Once

the RF pulse is turned off, the spins will return to equilibrium through two simultaneously occurring mechanisms.

Once the RF pulse is turned off, the spins lose coherence across the transverse plane, where they no longer act as a bulk property (M_{xy}) but decay into individual spins; this is caused by local magnetic fields generated by spins on each other, B_{loc} . Concurrently, they will return to alignment with B_0 . The loss of coherence is denoted transverse relaxation (characterized by the time constant T_2) and occurs faster than the return to the z-axis, called longitudinal relaxation (denoted by the time constant T_1). These processes are described in Figure 1.2.

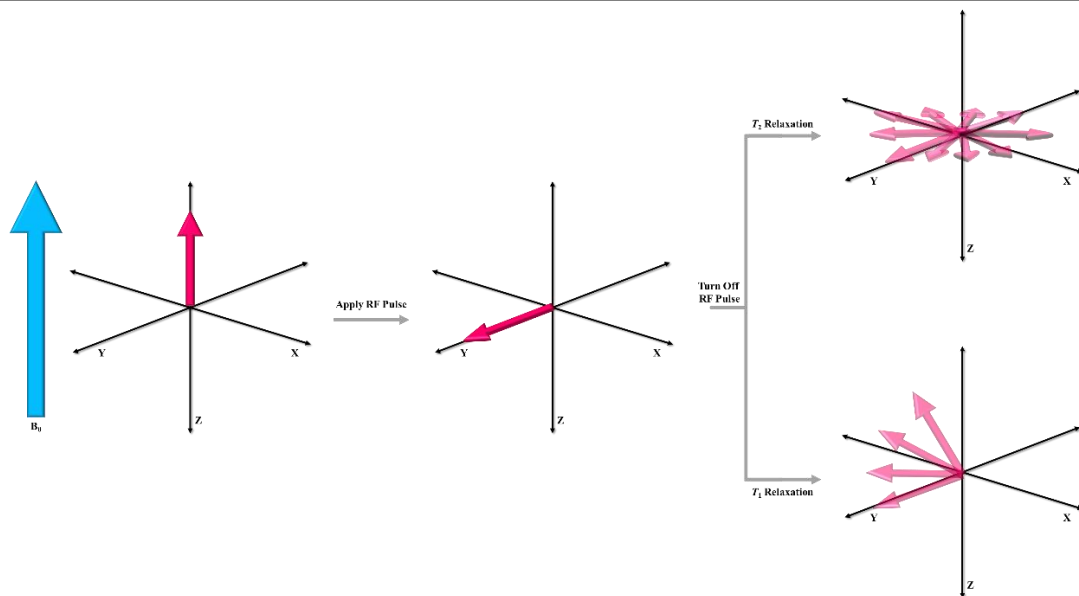


Figure 1.2. Rotating frame depiction of the two relaxation mechanisms that occur in an NMR experiment. The magnetic sum of spins is depicted as a bulk property, large pink arrow, and are aligned with the applied magnetic field, B_0 . After a RF pulse is applied, the spins are tilted into the transverse plane. Once the pulse is turned off, the spins lose coherence (T_2 relaxation), and return to alignment with B_0 (T_1 relaxation).

Once the RF pulse is turned off, the simultaneous relaxation mechanisms result in a loss of signal generated by the magnetic flux in the form of a free induction decay (FID). The FID then goes through a receiver coil where it is amplified. This amplified signal is then digitized to convert the FID signal into a series of data points. Through a Fourier transform, these data points are converted to a frequency spectrum for an NMR experiment.

An MRI scan utilizes the same principles as an NMR experiment; however, there are some major differences in data acquisition. With a spin quantum number of $\frac{1}{2}$, the hydrogen nucleus has a small magnetic moment that will generate a weak signal in an NMR experiment. Thus, it is important to have a high concentration of nuclei to probe to generate a strong signal. In the context of MRI, the protons of water provide the greatest signal; the human body is approximately 60% water, and with two hydrogen atoms per water molecule, it is the most abundant NMR-active nucleus to probe. However, the water molecules within the human body are all in vastly different chemical environments and these environments impart different magnetic characteristics that can be exploited to allow for differentiation in the image contrast produced.

To maximize the effect of signal intensity differences, an MRI scan employs the use of three magnetic field gradients. The orientation of the slice selection gradient determines the plane of the image, which allows for specific area in the anatomy to be selected for the image along the x-, y-, and z-axes. Each slice has a thickness and contains volume, so each cross-sectional image is comprised of all three axes, denoted as voxels. A phase encoding gradient is applied to the slice along one axis to cause the B_{loc} of each region of the slice to be different, and once turned off, cause each section of spins to be out

of phase. Finally, a frequency encoding gradient is applied to the slice along the opposite axis to change each voxel to have a different rate of precession. What results is a slice with each voxel producing a signal in which the frequency and phase are unique. Each voxel is assigned a grayscale value based on the strength of its B_{loc} signal. A strong signal, arising from quickly relaxing material appears bright, and a weak signal appears dark.

1.2.2. Amplifying the Signal Produced – The Spin Echo

To maximize the contrast generated in an MR image, different pulse sequences can be implemented to weight the relaxation rate of one tissue type versus another. The pulse sequence used in an MR image is slightly different than that produced in an NMR experiment. A spin-echo pulse sequence is typical of an MR imaging pulse sequence: it applies two consecutive RF pulses, producing a spin echo rather than an FID. This process allows for the dephasing that occurs during transverse relaxation to be refocused to generate a stronger signal. A spin echo pulse sequence is described in Figure 1.3, where the time between each 90° excitation pulse is called the repetition time (TR), and the time between the 90° pulse and the echo produced is called the echo time (TE). To maximize the contrast generated in an image, TE and TR are altered.

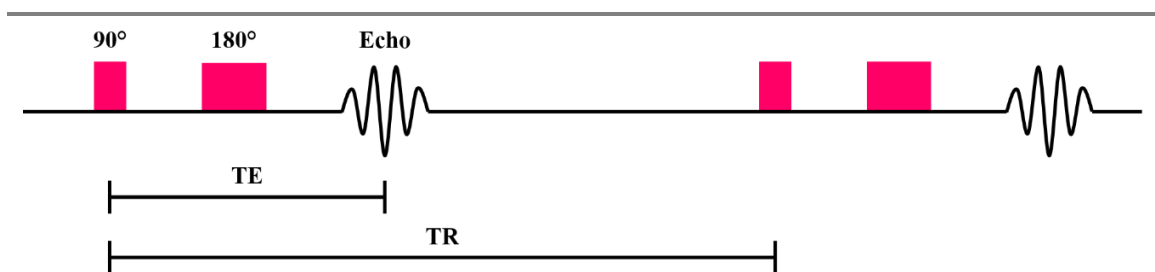


Figure 1.3. Pulse sequence to obtain an MR image. 90° and 180° refer to RF pulses of that strength. TE is the echo time, and TR is the repetition time.

The T_1 relaxation time for free-flowing water is approximately 3 – 4 s, and its T_2 relaxation time is slightly shorter. The different chemical environments of water *in vivo* lead to different relaxation properties: these differences in relaxation time constants are exploited in designing an MR spin echo pulse sequence.

1.2.2.1. Echo Time (TE)

The time between the 90° pulse and maximum height of the echo (TE) can be manipulated in the echo pulse sequences to alter the signal sensitivity to transverse relaxation, which is deemed T_2^* in MR imaging due to complications caused by field inhomogeneity, magnetic susceptibility in the human body, and the gradients required for spatial resolution. Nevertheless, when TE is much shorter than the T_2 of the desired tissue being imaged, the spins are effectively rephased and thus transverse relaxation effects are minimized. But when TE is much longer than tissue T_2 , the spins dephase and cannot be effectively refocused: the differing T_2^* relaxations occurring in two different tissues are amplified and this allows for different color assignments in the image. A short TE typically refers to a value that is much shorter than T_2 , whereas a long TE is $\sim 3 - 5$ times greater than T_2 .

1.2.2.2. Repetition Time (TR)

The time between 90° pulses (TR) can also be shortened or lengthened to amplify or minimize the effect of local differences in longitudinal relaxation. If TR is made several times longer than the T_1 of the tissue being imaged, then the nuclei have time to completely return to equilibrium along the Zeeman alignment, thus two tissues with differing T_1 values

will not be exaggerated. Conversely, if TR is made short, tissues with short T_1 values will relax to equilibrium faster than those with a longer T_1 . This means that more signal will be obtained with longer T_1 values; the differences in T_1 relaxation in two different tissues is emphasized. As with TE, a short TR refers to a value that is much shorter than T_1 , whereas a long TR is $\sim 3 - 5$ times greater than T_1 .

1.2.2.3. Weighted Imaging

Favoring one relaxation process over another is known as weighting, and it is the result of altering TR, TE, or both. Altering TR mostly impacts T_1 effects, whereas the major influence on T_2 effects is altering TE. These effects on signal intensity are described in Equation 1.2.

$$S = K[H](1 - e^{-TR/T_1})e^{-TE/T_2}$$

Equation 1.2. The determination of signal intensity (S) from a pulse sequence where K is a scaling factor, $[H]$ is the proton density.

Dense stationary tissue such as fat and protein will return to equilibrium along B_0 quickly and will therefore appear bright on the T_1 -weighted image. Free flowing tissue such as cerebrospinal fluid (CSF) and edema retain transverse magnetization longer, and return to equilibrium along B_0 more slowly, resulting in a weak signal that translates to a dark color in a T_1 -weighted image. A short TR and short TE results in a T_1 -weighted image as shown in Figure 1.4 Top Left.

In contrast, a T_2 -weighted imaging pulse sequence has greater time between pulses and nuclei with a short T_2 lose coherence completely. Free flowing tissue that loses

coherence quickly, such as CSF and edema will result in a strong signal and appear bright on the image, where dense stationary tissue like fat and protein dephase slowly and appear dark. A long TR and long TE results in a T_2 -weighted image as shown in Figure 1.4 Bottom Right.

The last type of echo pulse sequence that is relevant clinically is proton density (PD). Because shortening TE minimizes T_2 effects, and lengthening TR minimizes T_1 effects, an echo pulse sequence that employs short TE and long TR results in a PD image. This sequence is used to determine the actual density of protons in a tissue. As a result, CSF as well as fat provide a high signal in PD imaging, whereas cartilage produces a low signal. This is highlighted in Figure 1.4 Top Right.

It is possible to use a spin echo pulse sequence that employs a long TE and short TR. However, this would result in poor signal from T_1 as well as T_2 effects. This is because a short TR maximizes T_1 effects and minimizes T_2 effects, whereas a long TE maximizes T_2 effects and minimizes T_1 effects, essentially canceling out the weighted advantage of both. This is shown in Figure 1.4 Bottom Left.

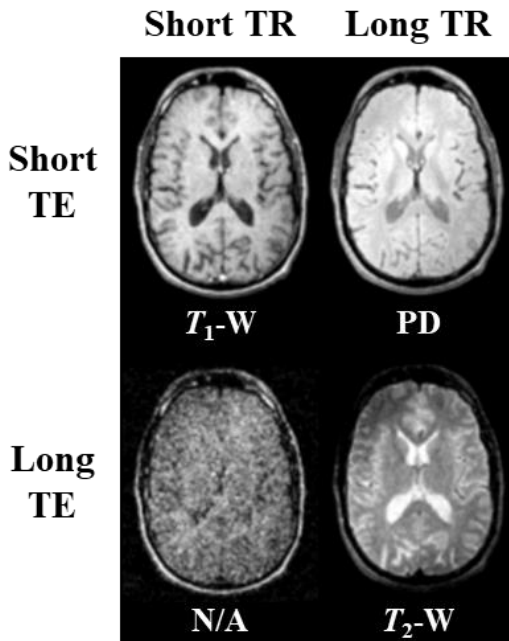


Figure 1.4. Pulse sequence techniques used to alter TR and TE to result in T_1 -weighted (T_1 -W), T_2 -weighted (T_2 -W), and Proton Density (PD) images.¹⁵

1.3. MRI Contrast Agents (CAs)

To improve the diagnostic power of MRI, physicians can employ a contrast enhancing agent (CA). Within a biological system, a contrast agent works by binding free water molecules and shortening their T_1 , or T_2 relaxation time constant. All contrast agents shorten both T_1 and T_2 , but the implementation of weighted imaging favors one relaxation process over another and the most used contrast agents are T_1 -enhancing agents. After interacting with a water molecule and effectively reorienting the magnetic moment of those proton nuclei, the molecule will exchange with the bulk. This process is repeated resulting in the transfer of relaxation to the bulk water. In a T_1 -weighted image, protons that relax quickly will appear bright on an image and those that relax slowly will appear dark. The

differences between a T_1 -weighted image with and without contrast is highlighted in Figure 1.5. It is the difference of the increased relaxation rate of the water molecules that is highlighted in an image enhanced by contrast.

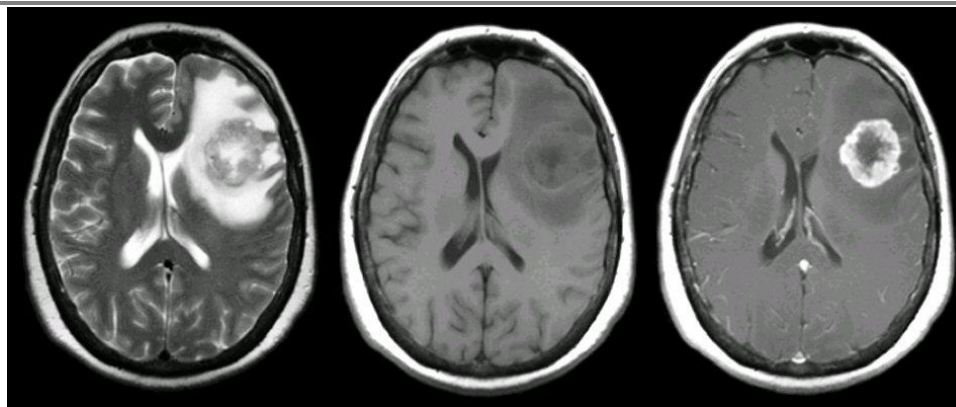


Figure 1.5. T_2 -weighted image (Left), T_1 -weighted image (Center), and T_1 -weighted image with gadolinium-based contrast agent administered (Right).¹⁶

1.3.1. Non gadolinium-based Contrast Agents

1.3.1.1. Iron-Based Superparamagnetic Agents

Superparamagnetic nanoparticles of iron (II) oxide have been used clinically as contrast enhancing agents. Iron oxide nanoparticles have a large magnetic moment, which allows them to shorten both T_1 and T_2 relaxation times of surrounding water molecules. However, they are typically used as T_2^* agents, and their relaxation enhancement of bulk water results in negative contrast observed on the image.¹⁷ Clinical iron (II) oxide nanoparticle agents vary in size from 4 – 4000 nm in diameter. This size discrepancy allows for agents to be used in different applications from MR angiography to digestive tract enhancement.¹⁸ Due to the reactivity of a transition metal-based contrast agent, the nanoparticles are coated in a biocompatible layer, typically comprised of a polymeric sugar

derivative. These coatings vary in size and composition and all help to prevent aggregation of the particles once injected into the bloodstream. Although multiple iron (II) oxide nanoparticles have been approved clinically as contrast enhancing agents, they have fallen out of favor due to anaphylactic side effects experienced by patients and a lack of contrast specificity.¹⁹ Currently, all iron (II) oxide nanoparticle MRI contrast agents have been discontinued.

1.3.1.2. Manganese Paramagnetic Agents

Both the II and III oxidation states of manganese have a paramagnetic $3d$ subshell and have been shown to increase the T_1 relaxation rate of water *in vivo*. However, inorganic solution of Mn^{2+} were shown to be extremely toxic in initial studies and as a result only one chelate of Mn^{2+} is approved clinically, a chelate of dipyridoxal diphosphate (DPDP) (known as Mangafodipir and Teslascan™ clinically), Figure 1.6 Left.²⁰ There has been some research into encapsulating $MnCl_2$ into liposomes, or chelating Mn^{2+} into a ligand such as ethylenediaminetetraacetic acid (EDTA) and imbed the chelate into a lipid bilayer. However, it was shown that free Mn^{2+} was released from both of these systems, thus reducing their utility.²⁰

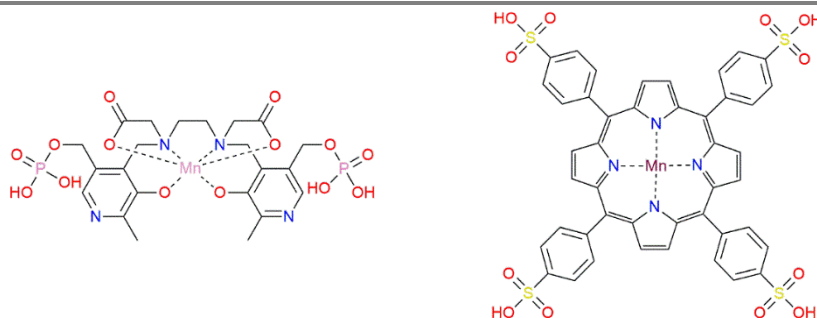


Figure 1.6. Mn derived contrast agents, Mn(II)-DPDP (Left), and Mn(III)-TPPS₄ (Right).

1.3.2. Gadolinium Based Contrast Agents (GBCAs)

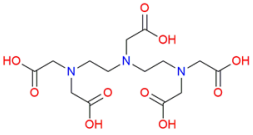
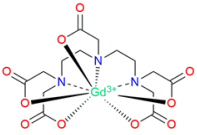
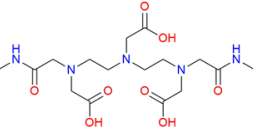
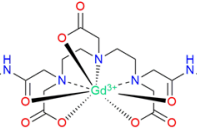
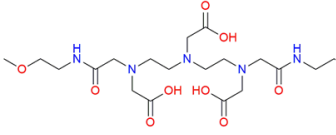
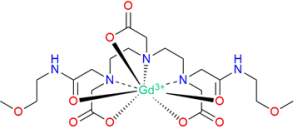
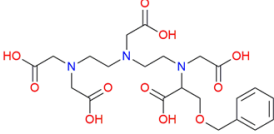
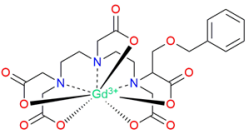
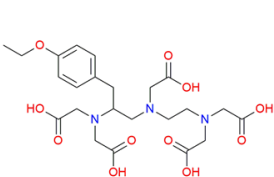
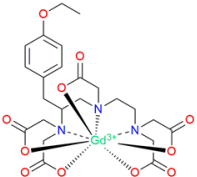
All clinically available contrast agents are complexes of the paramagnetic lanthanide gadolinium (Gd). Due to its isotropic f -shell, Gd^{3+} has an extremely long electronic relaxation time. This, combined with its ability to behave as a Lewis acid and ligate water, makes it an excellent contrast agent. Although gadolinium-based contrast agents (GBCAs) increase both T_1 and T_2 relaxation rates of water, the major difference in signal intensity is observed in a T_1 -weighted image, as highlighted in Figure 1.5.

As a free ion, Gd^{3+} is toxic *in vivo*, displacing Ca^{2+} in bone and disrupting Ca^{2+} dependent biological processes.²¹ Therefore, Gd^{3+} is bound in an organic ligand to ensure its safety as a contrast agent. Lanthanides have a preferred coordination number of 9, thus all ligand systems are designed to be octadentate, leaving one available coordination spot to ligate water and shorten its relaxation time constant. There are two main systems in which a contrast agent ligand is defined: linear, in which a long organic chain wraps around the metal to form a complex; and macrocyclic, a prearranged macrocycle that encapsulates the metal to form a complex.

1.3.2.1. Linear Agents

All linear GBCAs are derivatives of the structure diethylenetriaminepentaacetic acid (DTPA), shown in Table 1.1. The primary differences in these linear agents is the charge of the complex. Most have a 2- charge while the two amide containing derivatives are neutral. These have been developed to reduce osmotic pressure of the agents as aqueous solutions.²²

Table 1.1. Clinically relevant linear derived GBCAs.

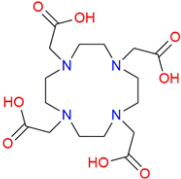
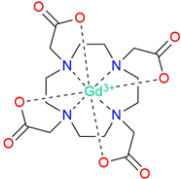
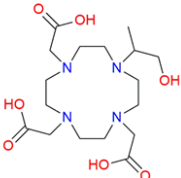
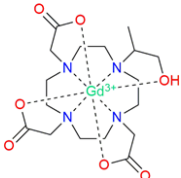
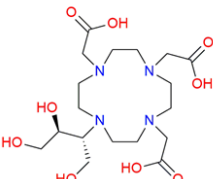
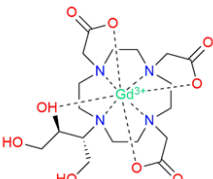
Ligand	Complex	Complex Name	Tradename
		GdDTPA ²⁻	Magnevist®
		GdDTPA-BMA	Omniscan™
		GdDTPA-BMEA	OptiMARK™
		GdBOPTA ²⁻	MultiHance®
		GdEOB-DTPA ²⁻	Eovist® or Primovist®

1.3.2.2. Macrocyclic Agents

The other variety of octadentate ligand structure used to bind gadolinium is the macrocycle. All clinically available macrocyclic contrast agents are derived from dodecane tetraacetic acid (DOTA). The three current clinically approved agents are shown in Table 1.2. Like their linear counterparts, the main difference between these agents is overall complex charge. GdDOTA (Dotarem®) maintains a 1- charge while GdHP-DO3A (ProHance®) and GdDO3A-Butrol (Gadavist®) are neutral. Slight modifications to the

DOTA parent ligand result in the two derivatives, but all three have similar efficacies, pharmacokinetics, and stabilities.

Table 1.2. Clinically relevant macrocyclic GBCAs.

Ligand	Complex	Complex Name	Tradename
		GdDOTA ⁻	Dotarem®
		GdHP-DO3A	ProHance®
		GdDO3A-Butrol	Gadavist®

1.3.2.3. Safety of GBCAs

Although linear agents are commonly used clinically, they are associated with a major limitation. Namely, when evaluating GBCAs for their safety, thermodynamic stability has traditionally been the standard metric. Linear GBCAs perform well thermodynamically, thus it has been assumed that because the energy barrier of dechelation *in vivo* was so high that these chelates remain intact for the duration of the scan and through excretion. However, in 2006 this changed with a publication linking a new disease occurring in renally compromised patients who had received GdDTPA.²³ Coined nephrogenic systemic fibrosis (NSF), it is characterized by the hardening of skin and tissue,

eventually causing fibrosis in organs leading to death. Although GBCA administration is observed in 95% of NSF patients, there has yet to be a defined method of pathophysiology.²⁴ Currently, prevention is the only measure, thus renally compromised patients are dissuaded from contrast enhanced-MRI (CE-MRI).

The discovery of the correlation between NSF and GBCAs mobilized scientists into researching the safety of GBCAs. Because thermodynamics were the key determination of stability, other factors influencing safety were not considered. Both linear and macrocyclic agents are small hydrophilic chelates which are cleared renally, typically in under 4 hours.²⁵ However, if a patient is renally compromised, the chelate will enter hepatic clearance, which can take much longer. Thus, the risk of dechelation is increased if the chelate is not exceedingly kinetically inert. As a result, researchers began to collect data on kinetic inertness as a marker of a superior safety profile, and these values are presented along with their thermodynamic stabilities in Table 1.3.

The data presented in Table 1.3 show that although both the linear and macrocyclic chelates perform similarly thermodynamically, their kinetic inertness constants are significantly different. The high kinetic inertness constants observed in macrocyclic chelates arises from their structure. The macrocyclic effect first described by Desreux, states that the pre-organization of the ligand reduces the entropic penalty on its ligands from coordinating with the metal.²⁶ As a result, macrocyclic derived ligands form much more kinetically inert complexes than their linear counterparts. Thus, macrocyclic agents have a higher propensity to remain chelated for the duration of the scan through excretion, even through alternative clearance modes. Appropriately, the increased kinetic inertness of

macrocyclic derived GBCAs has made their study the primary focus of our group and many MRI researchers around the world.

Table 1.3. Thermodynamic stabilities and metal – ligand dissociation constants for clinically relevant GBCAs.^{27–31}

Ligand	Chelate Name	k_{obs} (s ⁻¹) (0.1 M HCl)	Log K_{GdL}
	GdDTPA ²⁻	1.2×10^{-3}	22.2
	GdDTPA-BMA	$> 20 \times 10^{-3}$	16.85
Linear	GdDTPA-BMEA	$> 2.2 \times 10^{-2}$	16.84
	GdBOPTA ²⁻	0.9×10^{-3}	22.59
	GdEOB-DTPA ²⁻	0.8×10^{-3}	23.5
	GdDOTA ⁻	2.1×10^{-5}	25.3
Macrocyclic	GdHP-DO3A	6.4×10^{-5}	23.8
	GdDO3A-Butrol	2.8×10^{-5}	21.8

1.4. SBM Theory and Relaxivity

Efficacy of a T_1 contrast agent is termed relaxivity (r_1), defined as how effective a GBCA is at increasing the R_1 relaxation rate constant of water as a function of concentration. The higher the relaxivity, the more effective the agent. Relaxivity is described by a series of equations developed by Solomon, Bloembergen, and Morgan, known as SBM theory. Due to the complex nature of relaxivity, these equations attempt to explain the physico-chemical properties of how a contrast agent behaves in solution. Each

of these SBM parameters contribute to relaxivity in different capacities and are collectively called relaxometry. Analyzing relaxometric data requires multiparametric data fitting, and not all SBM parameters can be determined independently. Those parameters are generally fixed to agreed upon values and the choice of those values can influence the values of other obtained during the fitting process. As a result, many of the parameters within the SBM equations are mutually compensatory; changing one value will impact another, and thus complexity arises when determining optimal values for each. With these considerations in mind, SBM theory allows for the extraction of physico-chemical properties of metal chelates and facilitates the probing into their behavior as relaxivity agents. SBM equations describe the dynamic interaction; binding of a water molecule to the lanthanide center, a dipole-dipole interaction between the Gd^{3+} *f*-electrons and the protons on the bound water, the subsequent water exchange with the surrounding bulk through a dissociative ligand exchange process, depicted in Figure 1.7. The SBM equations are shown in Equations 1.3 through 1.10 and will be described in terms of longitudinal (T_1) relaxation.^{29,32}

$$\frac{1}{T_1} = \frac{cq}{55.5} \left(\frac{1}{T_{1M} + \tau_M} \right)$$

Equation 1.3. T_1 relaxation rate of bulk water is defined by the concentration (c), hydration state (q), longitudinal proton relaxation time of water (T_{1M}), and water exchange lifetime (τ_M).

$$\frac{1}{T_{1,\text{observed}}} = \frac{1}{T_{1,d}} + r_1 [\text{Gd}^{3+}]$$

Equation 1.4. Observed solvent relaxation rate ($1/T_{1,\text{obs}}$) is a function of the sum of the relaxation rate of the solvent nuclei without a paramagnetic agent (diamagnetic contribution, $1/T_{1,d}$) and the relaxivity of the paramagnetic agent (r_1) times the concentration of Gd^{3+} .

$$\frac{1}{T_{1M}} = \frac{1}{T_1^{DD}} + \frac{1}{T_1^{SC}}$$

Equation 1.5. Longitudinal proton relaxation time of water (T_{1M}) is governed by the magnetic field dependent dipole-dipole (DD) and scalar or contact (SC) mechanisms.

$$\frac{1}{T_1^{DD}} = \left(\frac{2}{15} \right) \frac{S(S+1)g^2\gamma_H^2\mu_B^2}{r_{\text{GdH}}^6} \left[\frac{7\tau_{C_2}}{(1 + \tau_{C_2}^2\omega_S^2)} + \frac{3\tau_{C_1}}{(1 + \tau_{C_1}^2\omega_H^2)} \right]$$

Equation 1.6. DD contribution to T_1 relaxation is modulated by electron spin (S), electron g factor (g), nuclear gyromagnetic ratio (γ_H), Bohr magnetron (μ_B), electron spin – proton distance (r_{GdH}), electron spin relaxation (τ_C), electron Larmor frequency (ω_S), and nuclear Larmor frequency (ω_H).

$$\frac{1}{T_1^{SC}} = \frac{2S(S+1)}{3} \left(\frac{A}{\hbar} \right)^2 \left(\frac{\tau_{e2}}{1 + \omega_S^2\tau_{e2}^2} \right)$$

Equation 1.7. SC contribution to T_1 relaxation is modulated by electron spin (S), the hyperfine or scalar coupling constant between the electron of the paramagnetic center and proton of the bound water (A/\hbar), electron Larmor frequency (ω_S), and SC correlation time (τ_e).

$$\frac{1}{\tau_C} = \frac{1}{\tau_R} + \frac{1}{T_{1e}} + \frac{1}{\tau_M}$$

Equation 1.8. Characteristic correlation time of the DD interaction (τ_C), is the sum of rotational correlation time (τ_R), longitudinal electron spin relaxation time of the metal (T_{1e}), and water exchange lifetime (τ_M).

$$\frac{1}{\tau_e} = \frac{1}{T_{1e}} + \frac{1}{\tau_M}$$

Equation 1.9. Characteristic correlation time of the SC interaction (τ_e) is the sum of the longitudinal electron spin relaxation time of the metal (T_{1e}), and water exchange lifetime (τ_M).

$$\left(\frac{1}{T_{1e}}\right)^{\text{ZFS}} = \left(\frac{\Delta^2}{50} \tau_V (4S(S+1) - 3)\right) \left(\frac{1}{1 + \omega_S^2 \tau_V^2} + \frac{4}{1 + (4\omega_S^2 \tau_V^2)}\right)$$

Equation 1.10. Field dependent paramagnetic electron spin relaxation time of zero field splitting interactions (T_{1e}^{ZFS}) is defined by the mean square ZFS energy (Δ^2), correlation time for the modulation of the transient ZFS (τ_V), and electron Larmor frequency (ω_S). This equation is only valid when $\tau_V^2 \Delta^2 \ll 1$.

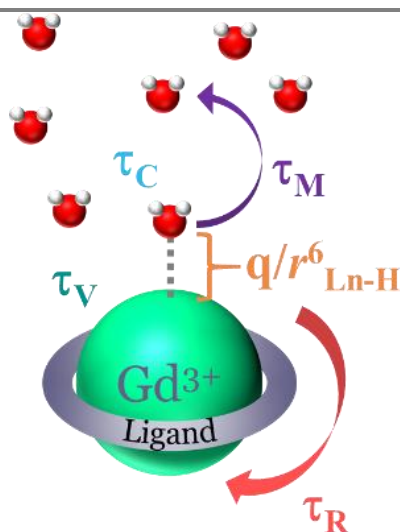


Figure 1.7. Relaxivity (r_1) is defined by SBM parameters as described in Equations 1.3 – 1.10.

1.4.1. Measurable Parameters of SBM Theory

The complicated and interdependent nature of the SBM equations can make it difficult to determine which parameter influences relaxivity the most. However, certain parameters are considered to have the greatest impact on relaxivity; those are described in Table 1.4, along with their measurement technique. The most common method by which SBM parameters are determined is by fitting the data generated from NMRD and ^{17}O -NMR profiles to SBM theory. Nuclear magnetic relaxation dispersion (NMRD) experiments probe the longitudinal relaxation rate of the GBCA as a function of magnetic field strength. ^{17}O -NMR determines the reduced transverse relaxation rate of the quadrupolar $^{17}\text{OH}_2$ as a function of temperature. Both measurements are $[\text{Gd}^{3+}]$ dependent.

Table 1.4. SBM parameters that determine relaxivity (r_1).^{29,32}

SBM Parameter	Units	Definition	Measurement Technique
r_1	$\text{mM}^{-1}\text{s}^{-1}$	Relaxivity	NMRD
τ_R	ps	Rotational correlation time	Fitting of ^{17}O -NMR and NMRD, or Curie relaxation
τ_M	ns	Water exchange lifetime	^{17}O -NMR
ΔV^\ddagger	$\text{cm}^3\text{mol}^{-1}$	Activation volume	Variable pressure NMR
τ_C	ps	Characteristic correlation time of the DD interaction	Fitting of ^{17}O -NMR
$1/T_{1e}$	s	T_1 electron spin relaxation rate of Gd^{3+}	Fitting of NMRD at low fields
τ_V	s^{-1}	Electron spin relaxation time for the modulation of the ZFS interaction	Fitting of NMRD
Δ^2	$\cdot 10^{19} \text{ s}^{-2}$	Mean square ZFS energy	Fitting of NMRD
q	–	Hydration number	Crystal structure evaluation, luminescence lifetimes
r_{GdH}	Å	Gd – proton distance	Assumed from crystal structure evaluation

1.4.2. Interdependent Nature of SBM

Each of the SBM parameters directly influences relaxivity, therefore optimizing one value would not directly improve the efficacy of the chelate. Instead, the contribution of each parameter needs to be considered when building a high relaxivity agent. According to SBM, a rapidly exchanging chelate ($\tau_M \sim 30$ ns) with slower rotation ($\tau_R =$ inverse Larmor frequency of the proton, ~ 20 ns, at low fields) would generate optimal relaxivity values.^{33,34} This can be visualized when SBM parameters are fixed, and fitted to a three dimensional plot, shown in Figure 1.8. This plot showcases the overwhelming influence τ_M and τ_R have on relaxivity. At the bottom of the plot, τ_M and τ_R can be a wide range of values to achieve the same relaxivity. However, as relaxivity increases, the values of τ_M and τ_R become a very narrow range.

Thus, to design the most optimal GBCA, there are very defined values that τ_M and τ_R must be to achieve the highest relaxivity possible. Currently, researchers are seeking to tune the values of τ_M and τ_R to “climb up the mountain”; yet, no major leaps in improving relaxivity have been realized. It is imperative to understand the influence and impact of each SBM parameter on relaxivity to facilitate the most effective agent possible.

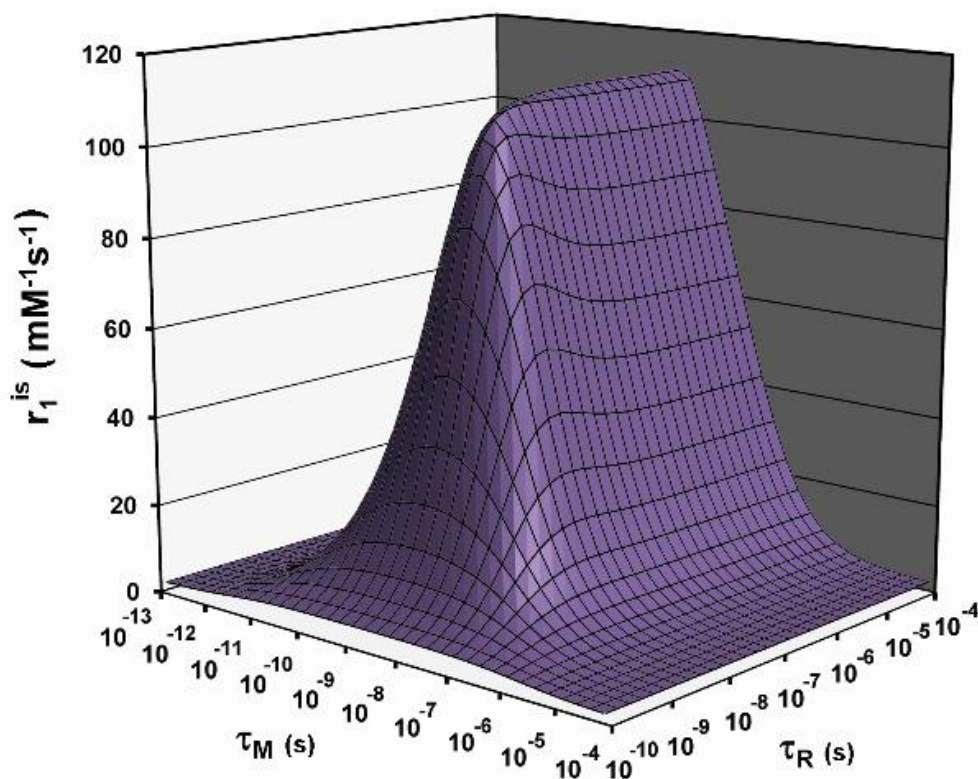


Figure 1.8 When other SBM parameters are fixed, the influence of the water exchange lifetime (τ_M) and rotational correlation time (τ_R) on relaxivity (r_1) are realized. ($B_0 = 0.5$ T, and 298 K)

1.4.3. Rotational Correlation Time (τ_R)

Also described as the tumbling rate, rotational correlation time (τ_R) is specifically defined as the time it takes the chelate to rotate one radian in solution. This value is determined by fitting NMRD profiles to SBM theory. The Debye-Stokes equation is a secondary measure not incorporated into SBM that allows for the mathematical determination for τ_R , Equation 1.11. Although combining SBM and Debye-Stokes provide a semi-accurate description of tumbling, it makes several assumptions. First, the Debye-

Stokes equation is only valid for a spherical molecule, which can be inaccurate for certain chelate systems. Secondly, it is difficult to obtain an exact value for the effective radius, and microviscosity is typically unknown, therefore assumed.

$$\tau_R = \frac{4\pi\eta r_{eff}^3}{3k_B T}$$

Equation 1.11. Debye-Stokes equation for τ_R is dependent on the microviscosity (η), the effective radius (r_{eff}), the Boltzmann constant (k_B), and temperature (T).

A direct determination of τ_R is available through Curie relaxation experiments. This independent measurement technique determines the Curie spin contribution to the transverse relaxation rate of the proton on the coordinated water. It is advantageous because the Curie-contribution is lanthanide specific. However, this method does require certain SBM parameters to be known, so it is primarily used in conjunction with NMRD as a conformational technique to evaluate efficacy of fitting. Secondly, it has been used on non-gadolinium containing lanthanide chelates, and although lanthanides have similar properties, there is significant anisotropy in these chelates that contribute to the measurement.³⁵

When reviewing the SBM equations it is evident that τ_R is the dominating factor influencing relaxivity, illustrated by the mountain plot in Figure 1.8. Yet, there is a major discrepancy between theory and practice for r_1 . Because all current clinically available contrast agents are low molecular weight chelates, they tumble very quickly in solution. Their tumbling rates are on the orders of 10s – 100s of picoseconds, when SBM has dictated

ideal τ_R values should be in the nanosecond range, depending on field. Ideally, the chelate should tumble at the rate of the Larmor frequency of the protons on water. Thus, to improve relaxivity, the barrier of τ_R must be lifted.

The most obvious approach to slowing down molecular tumbling is increasing the size of the chelate. Many efforts are underway to add bulky hydrophobic groups to the ligand structure or bind the chelate in a macromolecule. It has been shown that incorporating a GBCA into a small protein or biomarker can increase the relaxivity by an order of magnitude due to the large reduction in molecular tumbling.³⁶ However, it is important to recognize that when a GBCA is conjugated into a larger system, the traditional SBM approach to molecular tumbling does not apply; local as well as global tumbling must be considered when determining τ_R , because both tumbling rates contribute to r_1 . The Lipari-Szabo approach approximates both contributions of molecular tumbling *via* the addition of a spectral density function to τ_R .³⁷ With bioconjugation of GBCAs becoming rapidly more popular, it is important to understand the impact local and global rotation have on r_1 . Secondly, an accurate method of determining τ_R is essential to fully understand the interplay and dynamics a GBCA undergoes in solution.

1.4.4. Water Exchange Lifetime (τ_M)

In a dissociative exchange mechanism, τ_M has traditionally been defined as the water residence lifetime and was thought to describe the amount of time a water molecule remains bound to the lanthanide center. However, this is an inaccurate description of the water exchange process and does not account for the contribution of the time water spends

unbound to the lanthanide. Instead, τ_M is the inverse of the water exchange rate ($1/k_{ex}$), denoted as the water exchange lifetime. The influence of τ_M on relaxivity is twofold; it determines the efficiency at which the relaxed water molecule exchanges with the bulk, as well as contributes to τ_C , which defines the dipole-dipole interaction between the f -electrons of the lanthanide and the protons on the water molecule.

τ_M is measured directly *via* variable temperature ^{17}O -NMR spectroscopy. The data generated from the ^{17}O -NMR experiment form a bell curve in which there are two water exchange regimes that determine τ_M . The optimal value for τ_M is field dependent, and this value increases as magnetic field increases due to the spectral density function associated with the τ_M contribution to τ_C . As the limiting effect of τ_R is lifted at higher fields (>1 MHz), τ_M begins to become an important factor in determining relaxivity.

Many low molecular weight hydrophilic chelates fall in the fast exchange regime, with GdDOTA having a τ_M of 244 ns.³⁸ However, there is a point in which water exchange is considered too fast, resulting in a negative impact on other SBM parameters. When water exchange gets exceptionally rapid, the time in which a water molecule is not bound becomes significant, resulting in a reduction of hydration state (q/r^6). A chelate with a reduced hydration state will negatively impact relaxivity. The effects of a reduced q/r^6 is explored in Chapter 2.

Another influencing factor on τ_M is the lanthanide ion itself. The lanthanide ionic radius contraction observed across the series, results in a longer metal-water distance.³⁹ The longer bond distance in turn shortens τ_M , resulting in faster exchange. Although we

consider relaxometry in terms of GBCAs, it is important to appreciate the impact a changing ionic radius has on water exchange. Experiments conducted on the same ligand with different lanthanides, show a difference of two orders of magnitude comparing various lanthanide chelates.²⁹ These differences highlight the importance of precise determinations of metal – water distance (r_{L_nH}), in order to generate accurate τ_M values.

1.4.5. Activation Volume (ΔV^\ddagger)

The description of τ_M values does not fully define the entire water exchange event, and thus the mechanism of exchange must be considered. Ligand exchange systems can be either dissociative, interchange, or associative, however it is incorrect to view these processes as discrete. Instead, the exchange process is a continuum, from associative at one end, dissociative on the other with interchange in the center. Thus, various systems can exchange water dissociatively, but have interchange character. The determination of mechanism is *via* the analysis of the activation volume (ΔV^\ddagger). ΔV^\ddagger is defined as the difference between the partial molar volume of the transition state and the reactants.⁴⁰ A dissociative mechanism is the result of a large transition state thus a positive ΔV^\ddagger , whereas a small transition state is observed for an associative mechanism resulting in a negative ΔV^\ddagger .³² Thus, an interchange mechanism would have a ΔV^\ddagger of 0. Because water exchange is on a continuum, chelates with slight positive or negative ΔV^\ddagger values can be considered I_D or I_A , associated with interchange with a dissociative or associative character, respectively. While variable temperature ^{17}O -NMR allows for the experimental

determination of τ_M , variable pressure ^{17}O -NMR experiments gives rise to the determination of ΔV^\ddagger . The water exchange mechanism can be defined by Equation 1.12.

$$\frac{1}{\tau_M} = k_{\text{ex}} = (k_{\text{ex}})_0^T e^{-\frac{\Delta V^\ddagger}{RT}P}$$

Equation 1.12. The water exchange mechanism. Where τ_M is the water exchange lifetime, k_{ex} is the water exchange rate, $(k_{\text{ex}})_0^T$ is the water exchange rate at zero pressure and temperature T , and ΔV^\ddagger is the activation volume in $\text{cm}^3\text{mol}^{-1}$.

Nearly all small molecular weight poly amino carboxylate chelates exchange water through a dissociative mechanism for two reasons. Firstly, all clinically relevant ligands are octadentate; meaning there is only one available site to bind water, thus the relaxed water molecule would need to leave prior to coordinating another. Secondly, the structure of both linear and macrocyclic chelates are rigid; they would require energetically unfavorable rearrangement to accommodate multiple water molecules.

Although all clinically relevant chelates exhibit dissociative exchange, their range of activation volumes indicate that not all chelates exchange water in the same fashion. For example, GdDTPA^{2-} has an activation volume of $12.5 \text{ cm}^3\text{mol}^{-1}$, whereas GdDTPA-BMA has a ΔV_0^\ddagger of $7.3 \text{ cm}^3\text{mol}^{-1}$.⁴¹ Though both these chelates exhibit dissociative exchange, GdDTPA^{2-} has an activation volume nearly double that of GdDTPA-BMA . The introduction of two neutral monoamides to the DTPA structure reduces the electron density around the metal center enough to reduce the activation volume by nearly half. If we view

mechanism as the continuum, GdDTPA-BMA would lie closer to the center of “interchange” than GdDTPA²⁻, as illustrated in Figure 1.9.

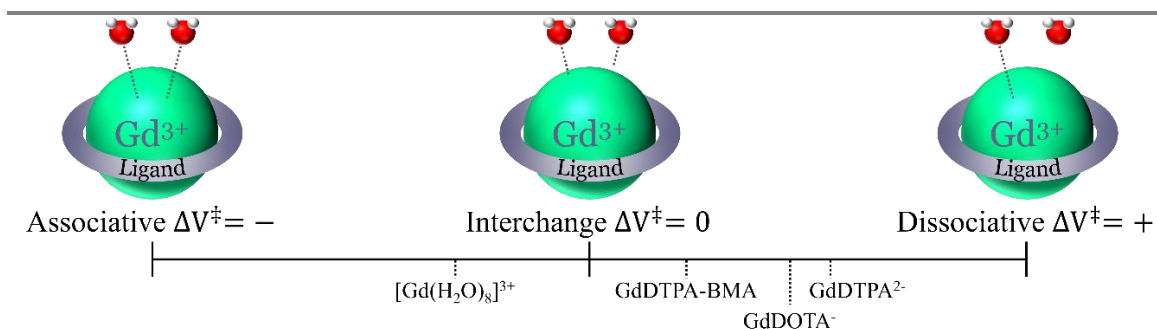


Figure 1.9 Water exchange mechanism continuum with relevant gadolinium complexes based on their activation volumes (ΔV_0^\ddagger). $[\text{Gd}(\text{H}_2\text{O})_8]^{3+}$ $\Delta V_0^\ddagger = -3.3 \text{ cm}^3\text{mol}^{-1}$. GdDOTA^- $\Delta V_0^\ddagger = 10.5 \text{ cm}^3\text{mol}^{-1}$, and GdDTPA^{2-} $\Delta V_0^\ddagger = 12.5 \text{ cm}^3\text{mol}^{-1}$.⁴¹

The lanthanide itself influences the activation volume as well. GdDOTA⁻ has a ΔV_0^\ddagger of $10.4 \text{ cm}^3\text{mol}^{-1}$, however when the Gd is swapped for Eu, the ΔV_0^\ddagger reduces to $-0.5 \text{ cm}^3\text{mol}^{-1}$, thus the chelate changes from a dissociative to an associative mechanism.³ Further analysis shows that upon changing the europium from a 3+ oxidation state to a 2+, the activation volume increases to $0.1 \text{ cm}^3\text{mol}^{-1}$.^{42,43} The combination of a low electronic density around the Eu²⁺ center as well as long metal – water distance contributes to the change from an associative to an interchange mechanism for EuDOTA. These data demonstrate that the ligand structure directly impacts the water exchange mechanism, and thus relaxivity.

1.4.6. Characteristic Correlation Time of Dipole-Dipole (τ_c)

The relaxation rate of the protons of the bound water molecule is directly governed by the fluctuation of the dipole-dipole interaction that occurs when the water molecule

binds to the metal center. This characteristic correlation time of this interaction (τ_C), is dominated by the rotational correlation time (τ_R). Like τ_R , τ_C is considered much too fast according to SBM theory to obtain optimal relaxivity. It has been established that for the highest relaxivity achievable, τ_C must equal the inverse of the Larmor frequency of the proton on the water.²⁹ Thus, efforts are underway to slow tumbling in such a way that τ_C will also be slowed. However, because the Larmor frequency of a nucleus is field dependent, optimizing this value is more complicated than simply slowing molecular tumbling. From Equation 1.8, electron spin relaxation and water exchange lifetime also influence τ_C , and as a result will need to be simultaneously optimized to achieve high relaxivity.

1.4.7. Mean Square ZFS Energy (Δ^2), Relaxation Rate Time Constant for the Modulation of the Transient ZFS (τ_V), and Electron Spin Relaxation Time (T_{1e})

Electronic relaxation can be defined by transient zero field splitting (ZFS) that results from solvent collisions that cause distortions in the chelate.⁴⁴ ZFS results from a variety of mechanisms occurring in solution and in the chelate itself. Ligand field interactions on the *f*-electrons of Gd^{3+} , spin-orbit coupling, and electronic repulsion intermolecularly, all cause the ZFS observed, resulting in electronic relaxation. The mean square ZFS energy (Δ^2) is another parameter that contributes to relaxivity within the subset of electronic relaxation. Its influence in Equation 1.10 is described by the distortions that occur within a complex from a series of electronic interactions. The structure of the ligand

directly defines Δ^2 ; the more rigid the structure, the lesser impact these collisions and interactions have on electronic relaxation and therefore the lower the Δ^2 value.⁴⁵

When water binds to the metal center through the interaction of the Lewis acid metal with the electrons on the oxygen, a dipole-dipole interaction occurs between the metal and the protons on the water molecule. This interaction is modulated *via* the reorientation of the nuclear spin relaxation – electron spin vector of the lanthanide, τ_V . τ_V values are magnetic field dependent and are defined through ZFS interactions.

τ_V influences relaxivity of GBCAs *via* T_{1e} . Electron spin relaxation time (T_{1e}) is defined as the reduction of electron spin magnetization of the lanthanide along B_0 . As a result, this value is also magnetic field dependent. However, the electron spin magnetization decay that occurs in the same direction of the magnetic field is too rapid to be observed experimentally; the $S = 7/2$ spin state of Gd^{3+} results in a multiexponential electronic relaxation.²⁹ Thus, line shape analyses of electron paramagnetic resonance spectra (EPR) allow for the determination of ZFS. Once these data are generated, they can be fitted to Equation 1.10 to determine both τ_V , and Δ^2 . The fitting of these values in turns allows for the determination of T_{1e} .

The impact of electronic spin relaxation and its components are dominating factors on relaxivity at low fields. To optimize relaxivity, the molecular collisions and electronic interactions that occur must be minimized to reduce the influence of electronic relaxivity. This can be achieved through structural manipulation of the ligand by increasing rigidity of the compound as well as increasing the symmetry of the overall complex. Both

approaches help to minimize electronic interactions that cause electronic relaxivity, and thus will increase relaxivity.

1.4.8. Hydration Number (q) and Lanthanide-Proton Distance (r_{GdH})

The hydration number (q) and the lanthanide – proton distance (r_{GdH}) are typically discussed as separate parameters, but because the exact location of the water molecule is unknown, it is more constructive to discuss them in together, as established by Bertini *et. al.*⁴⁶ Equation 1.6 defines the longitudinal relaxation rate of bound water that is attributed to the dipole-dipole interaction of the water molecule protons and the lanthanide center. In this equation, it is shown that this observed relaxation rate has a sixth order dependence on the lanthanide – proton distance (r_{GdH}^6); the spatial strength of the dipole disappears as a cube root, thus the two dipoles are additive and result in a sixth order dependence. The hydration number, or number of water molecules directly bound to the complex, is either 1 or 0 for all octadentate GBCAs. The combination of hydration number and distance results in hydration state, q/r^6 . This value considers not only the number of bound water molecules, but the distance of each molecule.

Hydration number is found through crystal structure analysis, though the utility of this data is limited because solid state does not directly translate mechanisms in solution. Luminescence lifetimes can also be utilized to determine q , however this does not work on Gd^{3+} complexes due to the electronic nature of Gd^{3+} .⁴⁷ The metal – proton distance is an even more difficult value to ascertain. The most common method of determining r_{GdH} is evaluation of the crystal structure of the chelate. However, protons do not appear in the crystallographic data, so their actual location is implicit based on the location of the

coordinated water oxygen. Again, solid state analysis is not a representation of solution state. Horrock's method allows for an accurate determination of hydration state, due to its ability to measure the dipole-dipole interaction. However, difficulty arises when distinguishing the influence of outer sphere water molecules.⁴⁷

1.4.9. Conclusions

Researchers have used SBM theory to calculate that if each SBM parameter is optimized, the highest possible relaxivity of a GBCA is $\sim 100 \text{ mM}^{-1}\text{s}^{-1}$. However, there are some important assumptions in this determination. First, electronic relaxation (T_{1e}) is assumed to be long, the magnetic field strength is fixed to 20 MHz, the temperature is fixed to 298 K, and r_{GDH} is fixed to a short value. Secondly, these assumptions do not account for certain changes that occur when parameters such as water exchange rate become increasingly rapid. Nonetheless, there is a stark difference between calculated SBM theory and clinical practice; current clinically available GBCAs have relaxivities $\sim 5 \text{ mM}^{-1}\text{s}^{-1}$.

In most cases, relaxivity is magnetic field strength and temperature dependent; it decreases with increasing field strength and temperature. It is important to address the current divergence within the field of MRI. Clinically, there has been a push to use MRI instruments at higher and higher magnetic field strengths (1.5 T – 7 T, which equates to 65 MHz – 305 MHz). Although higher magnetic field strengths result in higher resolution images, efficacy of GBCAs dramatically decrease due τ_C of the GBCA modulating much further away from the Larmor frequency of the proton. Thus, we are facing a dichotomy; how do we incorporate the new push for higher magnetic field strengths while maintaining the utility of GBCAs? Secondly, these high magnetic field strengths rely on the non-

renewable resource liquid He to maintain the superconducting nature of the magnet. As a result, although there is a push for higher magnetic field strengths diagnostically, it is possible this He crisis could force clinicians to reduce to lower strength magnets that do not require near absolute zero temperatures. Thus, it is imperative that the contribution of each SBM parameter to relaxivity is recognized and considered to achieve effective GBCAs. Only then can high relaxivity agents be achieved regardless of field strength.

1.5. Coordination Geometries and Regioisomerism in DOTA and DOTA-Derived Chelates

1.5.1. Coordination Geometries of DOTA

The macrocyclic DOTA ligand has some interesting coordination features that need to be discussed to appreciate the function of the resulting chelate. The tetraaza macrocycle ring (cyclen) can adopt multiple conformations; however, studies have shown the symmetrical [3, 3, 3, 3] configuration is the lowest energy conformation.⁴⁸ As a result of the multiple possible conformations, the ring helicity is assigned $\delta\delta\delta\delta$ or $\lambda\lambda\lambda\lambda$ depending on the orientation of the nitrogen atoms in the [3, 3, 3, 3] ring, figure 1.10.

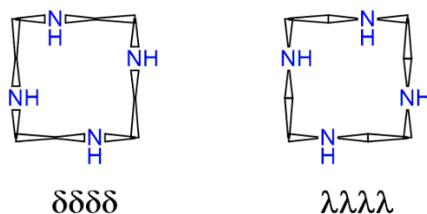


Figure 1.10. [3, 3, 3, 3] ring conformations of 1, 4, 7, 10-tetraazacyclododecane (cyclen).

When acetate arms are introduced to the structure, they also impart their own inherent helicity independent of the helicity of the ring. However, arms bind cooperatively, thus all four pendant arms will adopt the same orientation, denoted Δ or Λ . The combination of ring and arm orientation results in two pairs of enantiomers, as shown in Figure 1.11. These structures interconvert in solution, *via* arm rotation and ring inversion. Once chelated, these structures also exist as two coordination geometries that can be described by the combination of arm and ring helicity; $\Delta(\lambda\lambda\lambda\lambda)$ or $\Lambda(\delta\delta\delta\delta)$ result in a square antiprism (SAP) coordination geometry where $\Delta(\delta\delta\delta\delta)$ or $\Lambda(\lambda\lambda\lambda\lambda)$ result in a twisted square antiprism (TSAP) coordination geometry.

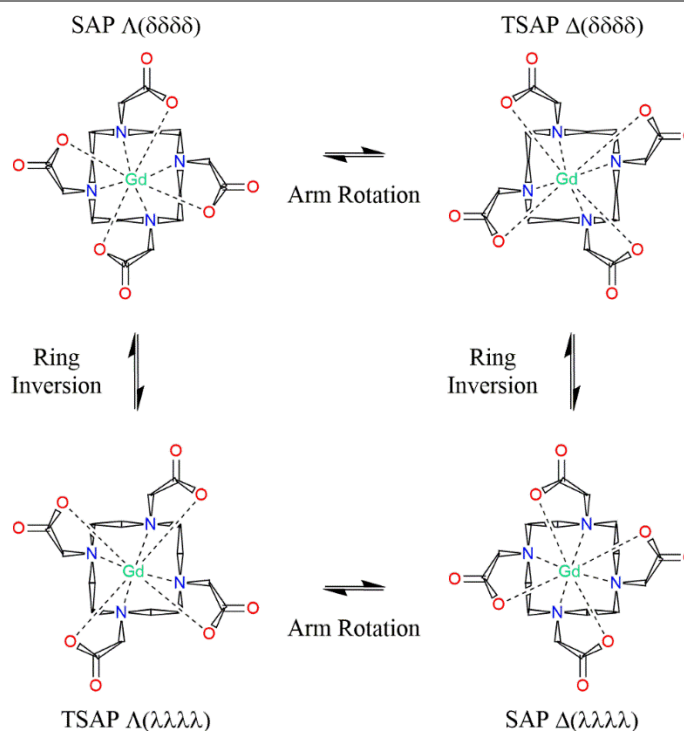


Figure 1.11. The four possible coordination isomers of GdDOTA. Interconversion between SAP and TSAP is achieved through arm rotation and ring inversion.

The impact of SAP and TSAP coordination geometry is more evident when these structures are viewed from the side. The SAP coordination geometry is characterized by its shorter cage height which results in a shorter distance between the nitrogen and oxygen planes. In contrast, the TSAP coordination geometry is defined by its taller cage height, resulting in a longer distance between the two planes, as shown in Figure 1.12. These differences in cage heights result in a dramatic impact on τ_M ; the longer metal – water bond distance sustained by the TSAP coordination geometry results in a k_{ex} that is two orders of magnitude faster than the SAP coordination geometry.⁴⁹ The exchange between SAP and TSAP isomers is slow enough to be observed on the NMR time scale. Although there is interconversion between the two coordination geometries, it has shown that GdDOTA prefers to maintain 85% SAP.⁴²

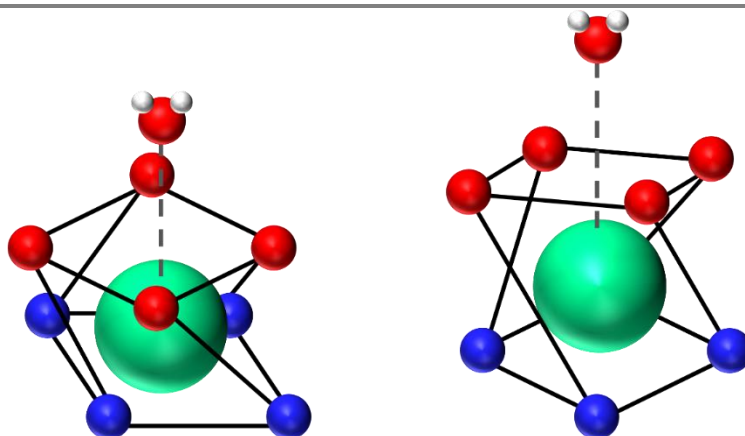


Figure 1.12. Side profiles of the two coordination geometries of DOTA chelates. Square antiprism (SAP, left) and twisted square antiprism (TSAP, right).

1.5.2. Substitution on the DOTA Scaffold

There has been much research into altering the parent DOTA structure to include various moieties to maximize relaxometric properties. The main strategies of modifying the base scaffold is *via* addition of groups on the macrocycle, on one to four α -carbon acetate arms, or replacing a pendant arm with a different coordinating ligand. Depending on the type of moiety, this alters the possible ratio of coordination geometries as well as the changes the interconversion, as shown in the flowchart in Figure 1.13.

The introduction of a benzylic substituent (NB-DOTA) results in two new regioisomers to the structure, in which the moiety is on the corner or side carbon.⁵⁰ A benzylic moiety locks ring inversion, thus interconversion between these two distinct regioisomers is not possible. However, the Corner and Side can interconvert between SAP and TSAP *via* arm rotation. The impact of macrocycle substitution is explored thoroughly in Chapter 2. Substitution on all four α -carbon locks arm rotation, thus interconversion between SAP and TSAP is only achievable through ring inversion. The tetra-methylated DOTA derivative (DOTMA) has been well studied for its unique properties.⁵¹ Other types of tetra-substituted chelates are investigated in Chapters 4 and 5. Combining both arm and ring substitution results in four non-interconverting chelates in solution that can be separated and analyzed independently. An example of this doubly substituted chelate, NB-DOTMA is probed in Chapter 2.

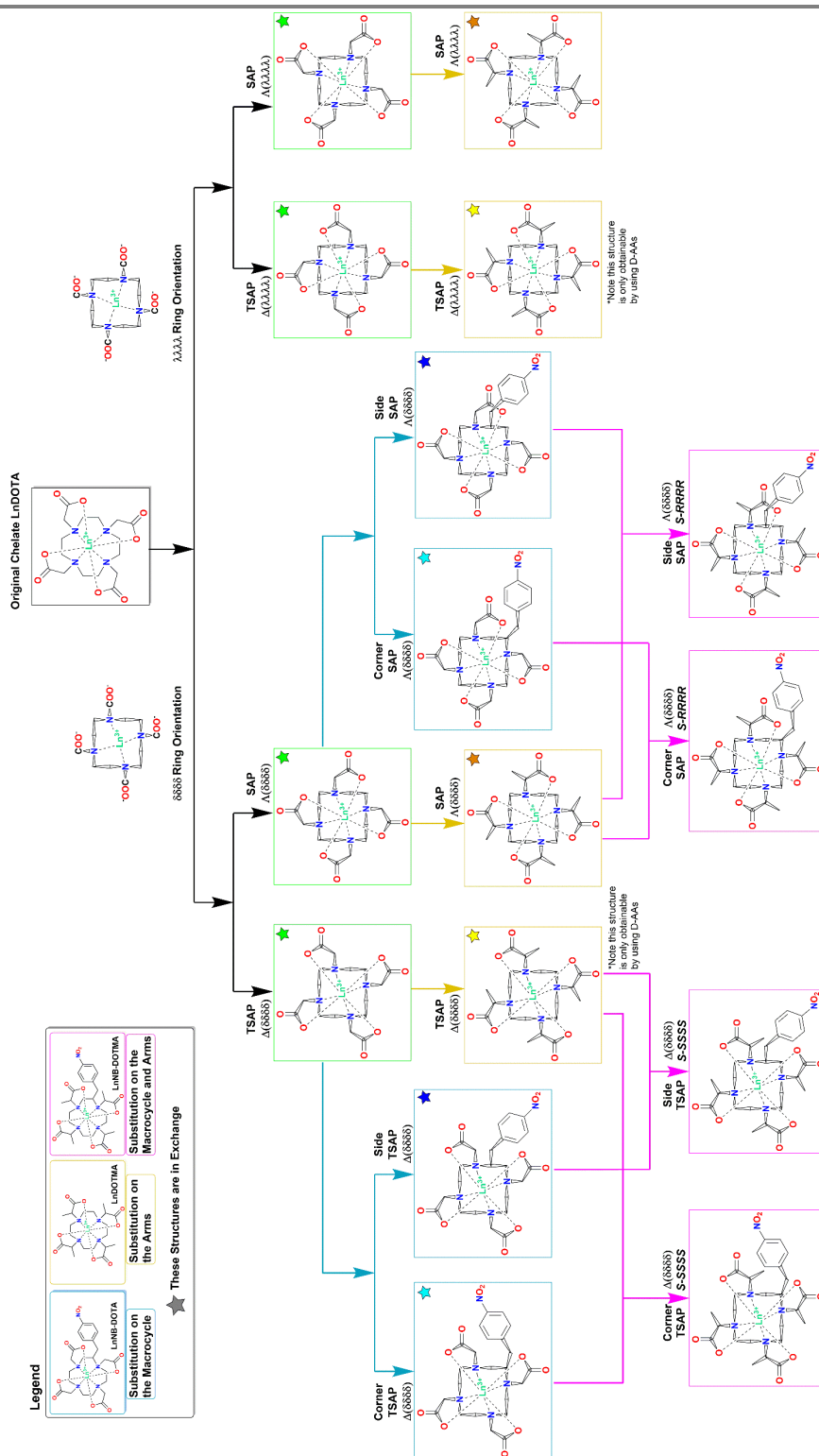


Figure 1.13. Possible regio- and coordination isomers of substituted DOTA chelates.

1.6. Bifunctional Chelators (BFCs)

Bifunctional chelators (BFCs) are ligands for medical applications with two purposes; the first to safely and effectively bind a metal for therapeutic or diagnostic imaging, the second to contain a reactive moiety to bind specifically and selectively to a biological target of interest. One of the earliest known reports of a bifunctional chelator was an ^{111}In complex used to label antibodies.⁵² Since then, BFCs have been primarily used as ligands to sequester a metallic radionuclide that simultaneously bind to a small protein, typically antibodies, for PET and SPECT imaging.⁵³ BFCs have been proposed for use as MRI contrast agents, specifically with the addition of a handle on the structure of a DOTA-derived ligand system.⁵⁴ The incorporation of a targeting vector into the ligand scaffold of DOTA will afford direct target binding. This in turn could lower detection limits due to increasing the specificity of the GBCA. Secondly, a Gd^{3+} based BFC would enable MRI to be a direct diagnostic method, increasing its utility.

Although BFCs have yet to be translated to clinical practice, researchers envisage a ligand system that contains a reactive moiety that can be easily modified for a variety of applications. After modification, this ligand would be chelated, the complex would then be conjugated *via* the targeting vector to a biological molecule of interest, such as a biological ligand. The bioconjugate would be subsequently injected into the patient and the ligand would bind to its relevant receptor, allowing for direct target imaging. This process is depicted in Figure 1.14. There are some important considerations when designing this system, such as the type of targeting vector added to the ligand system, as well as the location of the reactive moiety on the ligand structure.

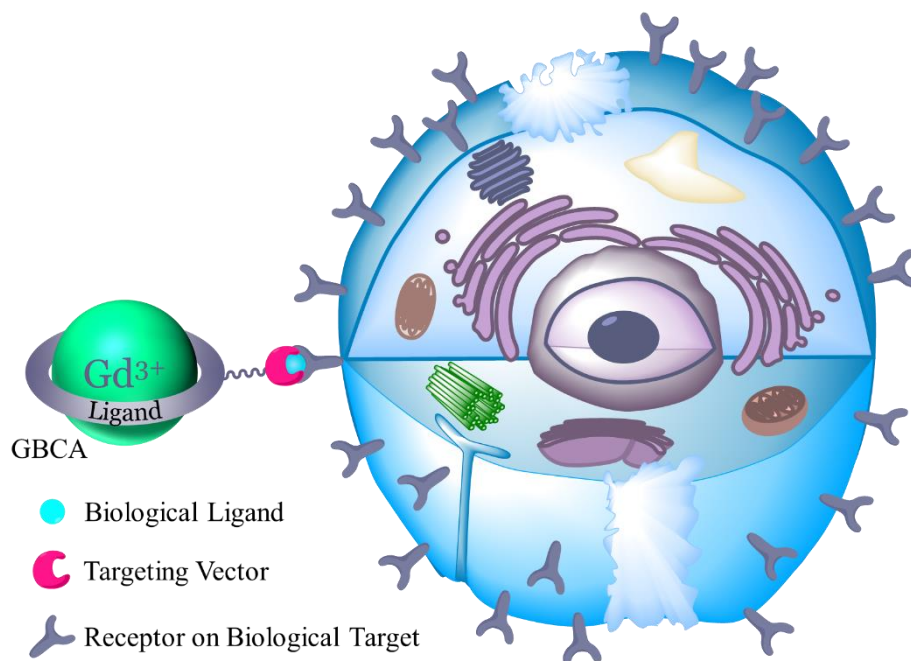


Figure 1.14. The strategy for biological targeting of a BFC.

1.6.1. Attachment Strategies

The increased kinetic robustness of DOTA makes it an ideal scaffold to modify to contain the targeting vector. However, the ideal location of this reactive moiety has yet to be firmly established. The three most synthetically approachable attachment strategies of the targeting vector are: off the macrocycle, through a pendant arm such as a monoamide, or on the α -carbon of a pendant arm. These three strategies are shown in Figure 1.15. Examples of these three substituted chelates have been established in literature, however, there has yet to be a thorough examination of their utility as potential BFCs for MRI.

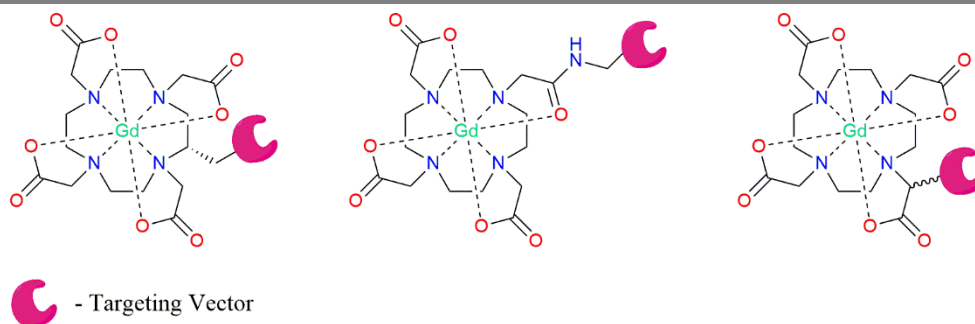


Figure 1.15. The three main attachment strategies for a targeting vector. **Left:** off the macrocycle, **center:** *via* a monoamide pendant arm, **right:** on the α -carbon of a pendant arm.

Once a group is substituted on the DOTA scaffold, relaxometric parameters are impacted. It has been established that the introduction of a substituent on the macrocycle or on the pendant arms, or, replacing one to four pendant arms to amides changes the relative SAP/TSAP ratio in solution. As established, this dramatically impacts water exchange. The introduction of various substituents on the DOTA scaffold also impacts other SBM parameters which in turn affects relaxivity. To determine which strategy is the most advantageous, there needs to be a systematic and thorough inquiry into the most effective attachment strategy in terms of relaxivity and synthetic ease.

1.7. Scope of This Work

Multiple analogs of each BFC attachment strategy on DOTA have been synthesized and explored for their efficacy within the context of water exchange kinetics and relaxivity. Chapter 2 explores the impact of chelates of NB-DOTA and its derivatives have on relaxivity, water exchange, and hydration state. Chapter 2 also includes an exploration of chelates more rigid tetra-methylated NB-DOTMA chelates and a comparison to its parent NB-DOTA. Chapter 3 compares the three main attachment strategies directly; three

chelates were synthesized of similar molecular weights and hydrodynamic volumes each representing an attachment strategy. These chelates were then converted to pseudo-BFCs through the incorporation of a large biphenyl moiety, and their performances were compared in terms of water exchange and molecular tumbling, and that impact on relaxivity. Chapters 4 & 5 explore the impact of other types of moieties substituted on all four α -carbon pendant arms have on the water exchange mechanism and relaxivity. These chelates were then crystallized to glean further information into their properties. Chapter 6 explores other types of mono-amide containing chelates as potential chemical exchange saturation transfer agents (CEST).

CHAPTER 2

MACROCYCLE SUBSTITUTED CHELATES

2.1. Chelates Undergoing Extremely Fast Dissociative Water Exchange

SBM theory calculations have described a chelate that undergoes fast dissociative water exchange ($\tau_M \sim 20$ ns), will yield the highest relaxivity.⁵⁵ This in turn resulted in new synthetic strategies to yield fast exchanging agents. Yet, the expectedly high relaxivities were not achieved when the barrier of τ_R was lifted, and tumbling was slowed. The reason behind this discrepancy was not made clear until relaxometric data was generated for a new chelate, GdNB-DOTMA, which exists as four discrete isomers in solution that can be studied independently. The TSAP isomer of GdNB-DOTMA allowed for extremely rapid water exchange to be determined and compared directly to its slower exchanging SAP counterpart.

This was further confirmed when a biphenyl moiety was attached to the ligand facilitating a longer τ_R . Our group has demonstrated that the isolated TSAP and SAP coordination isomers of GdBP-DO3MA Corner have vastly different τ_M values.⁵⁶ Although they are both the Corner regioisomer, the SAP coordination geometry has a τ_M value nearly 10 times that of TSAP. The only explanation for these differing τ_M values for the same regioisomer is one in which hydration state is reduced for the extremely rapidly exchanging TSAP isomer.

While theory dictates that a chelate with a rapid dissociative water exchange rate and slow molecular tumbling yields highest calculated relaxivity values, there is a point in

which a chelate exchanges water too quickly, resulting in a detrimental impact on r_1 .⁵⁶ The reason behind this “Goldilocks zone” of dissociative water exchange lies in hydration state, q/r^6 . It has been proposed that a chelate with a very fast dissociative water exchange rate reduces q/r^6 , and is considered to have a reduced hydration state.² Hydration state is a measure of metal-proton distance ($r_{\text{Gd-H}}$) and the number of water molecules directly coordinated to the metal center (q), an approach that more accurately describes the nature of hydration, first implemented by Bertini *et. al.*⁴⁶ Due to the octadentate structure of NB-DOTA, the hydration number, q , of its Gd^{3+} chelate will always equal one. The sixth order dependence of the metal-proton distance on relaxivity arises from the intrinsic nature of the dipole-dipole interaction.

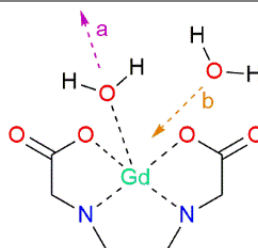


Figure 2.1. The dissociative water exchange mechanism described herein.

If dissociative water exchange is incredibly rapid, the amount of time a water molecule spends coordinated to the metal center might be shorter than the time it spends uncoordinated. Theory dictates that $k_{\text{ex}} = 1/\tau_{\text{M}}$ when the time the water spends uncoordinated with the metal, τ_{off} , is negligible.³² In a dissociative mechanism, the water must leave before a second coordinates, and $q = 1$ means we only need to consider two water molecules, the one coordinated and leaving (H_2O_a) and the one coming in to coordinate (H_2O_b), Figure 2.1. H_2O_a must leave before H_2O_b can coordinate, but we cannot

determine this value experimentally. However, in the fast exchange regime when $\tau_M < 30$ ns, the amount of time H_2O_a spends coordinated is very short. Thus, we can assume that the exchange to H_2O_b is also considerably rapid, yet still an influencing factor on relaxivity. Thus, $k_{ex} \neq 1/\tau_M$, instead τ_{off} contributes to the overall dissociative exchange mechanism. If τ_{off} is now considered a non-negligible value, then we must consider its impact on hydration state.

The process described in Figure 2.1 helps to illustrate the dissociative water exchange mechanism, however it is important to distinguish the behavior of the binding interaction to fully appreciate the relaxation process. The nature of the dipole-dipole interaction does not require the water molecule to be ligated to the metal to feel the effect of relaxation, thus, it is more constructive to think of this process as a matter of metal-water distance rather than “bound” or “unbound”.⁵⁷ Secondly, because q will always equal 1, the more important parameter to consider is that of r_{GdH} . The process described in Figure 2.1 depicts the importance of this distance, to differentiate between the “on” and “off” state.

Because water exchange is rapid, it is difficult to consider these two states independently. Rather, it is more productive to think of hydration as a time averaged value. In any dissociative water exchange process, the time the water is “bound” must be significantly longer than it is “unbound”. However, once exchange becomes increasingly rapid, the contribution of the “unbound” state becomes more significant, resulting in an increase in the time averaged water exchange rate constant. As the time averaged water exchange constant increases, there is an increase in the metal-water distance. Describing

increasingly rapid water exchange as a change in r_{GdH} elucidates the effect extremely rapid water exchange has on chelate hydration.

It is also important to consider the dynamic component of r_{GdH} . Because this value is not a measurably accessible parameter, it is assumed based on solid state crystal structure analysis of the Ln-OH₂ bond. But not only does that not accurately describe the distance from the metal to the proton, it neglects to address the dynamics involved in the water exchange process. Viewing r_{GdH} as a static component rather than a dynamic one is a pitfall in properly understanding water exchange rate. Thus, if we describe the water exchange process as a change in r_{GdH} , we can begin to appreciate how hydration is impacted, and thus better describe the effect seen in these rapidly exchanging chelates.

The resulting impact of these data is unanticipated; the hydration state of a chelate can be reduced by an extremely rapidly exchanging chelate. This limits the highest achievable relaxivity for an extremely rapidly exchanging chelate, because a reduction in hydration state results in a decrease in relaxivity. Two chelates, GdNB-DOTA and GdNB-DOTMA are two multi-isomeric systems that has been identified to undergo extremely rapid dissociative water exchange. These chelates have been prepared by Drs. B. Webber and K. Payne previously in our group, however further analyses of these systems had remained unconducted.

2.2. The impact of r_{GdH} on τ_{R}

As described in Chapter 1, the distance between the lanthanide center and proton of the coordinated water molecule is a difficult parameter to ascertain. It is typically

assumed based on crystallographic data, but in fact is not known. As a result, the value chosen for r_{GdH} is a somewhat arbitrary value, yet its impact is profound on relaxivity and rotation. Muller *et. al.* has demonstrated this interdependent nature of these two values by fitting NMRD profiles to different r_{GdH} values to generate different τ_{R} values, as shown in Table 2.1.⁵⁸ The data in Table 2.1 highlight the importance of choosing the correct value for r_{GdH} ; rotation can vary quite drastically depending on the value chosen. However, due to the difficulty in determining the value for r_{GdH} experimentally, it is more logical to experimentally determine τ_{R} , and allow for r_{GdH} to be determined from fitted data. If τ_{R} is determined experimentally, the value for r_{GdH} can be allowed to wander, and a more accurate description of hydration state can be depicted. However, as described in Chapter 1, independent measurements of τ_{R} can be difficult to ascertain and have some limitations.

Table 2.1. Values of τ_{R} generated by fitting different values of r_{GdH} to the NMRD profile of MS-325 at 310 K.⁵⁸

r_{GdH} (nm)	τ_{R} (ps)
0.285	68
0.290	76
0.295	84
0.3	91
0.31	110

2.3. Regioisomerism in Macrocycle Substituted Chelates

Six years after the debut of NB-DOTA as a potential BFC for MRI, it was found the introduction of the nitrobenzyl substituent on the macrocycle introduced two new regioisomers upon chelation; in which the nitrobenzyl group is situated on the “Corner”

carbon of the macrocycle, or “Side” carbon, as demonstrated by the Dale structures in Figure 2.2.⁵⁹ These two regioisomers are distinct; it is not possible to interconvert between the Corner and Side regioisomers, due to the nitrobenzyl substituent preventing ring inversion.⁶⁰ Research by Payne and Webber has established that the Corner and Side isomers of GdNB-DOTA have different properties.^{50,61} Their different hydrophobicities allows them to be separated *via* RP-HPLC, with a ratio of 75% Corner and 25% Side, as shown in the chromatogram in Figure 2.3, allowing them to be studied independently.⁶²

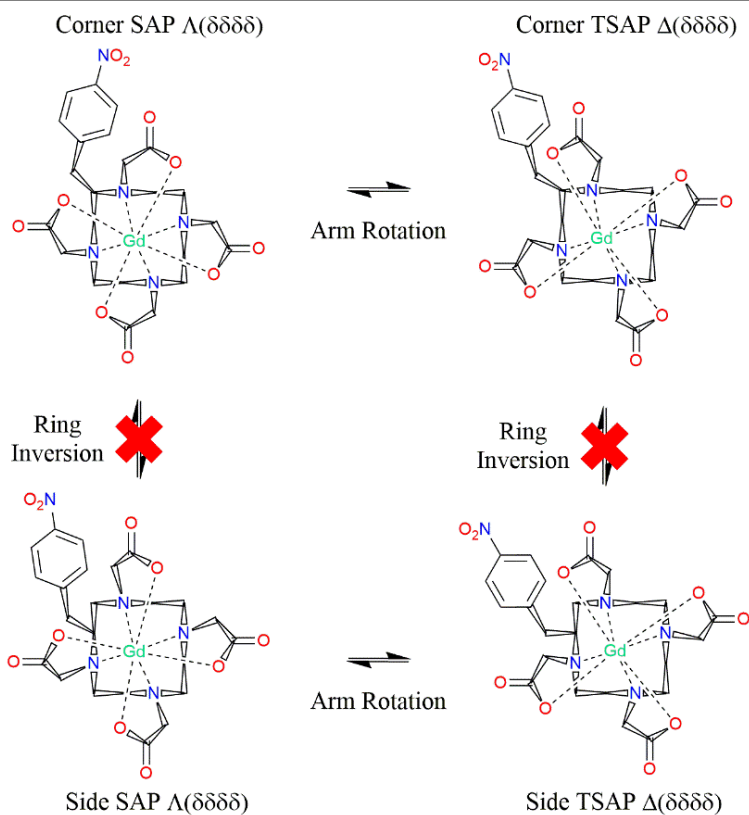


Figure 2.2. Dale structures of the four coordination geometries of GdNB-DOTA.

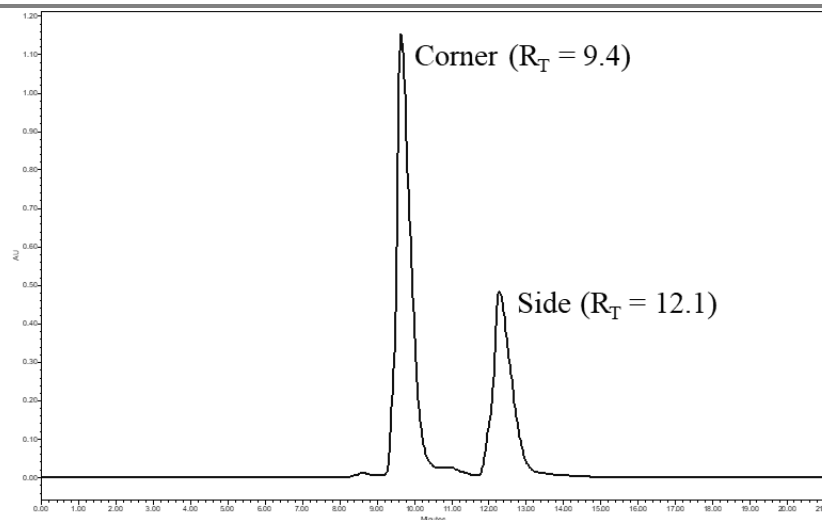


Figure 2.3. RP-HPLC chromatogram of the separation of the Corner and Side isomers of GdNB-DOTA monitored at $\lambda = 270$ nm.

The ratio of SAP and TSAP are also different in NB-DOTA chelates; the Corner is 95% SAP whereas the Side maintains 45% SAP coordination geometry. As a result, water exchange kinetics in the Corner is expected to be much slower in comparison to the Side. Chelates of NB-DOTMA also differentiate into Corner and Side isomers upon chelation. The main difference is the addition of a methyl group substituted on all four α -carbon acetate arms results in four distinct chelates, as shown by their Dale structures, Figure 2.4. This selective substitution affords for the impact coordination geometry as well as regioisomerism has on relaxivity and its corresponding parameters. It is expected that the two TSAP isomers are expected to have extremely rapid water exchange kinetics in comparison with their SAP counterparts.

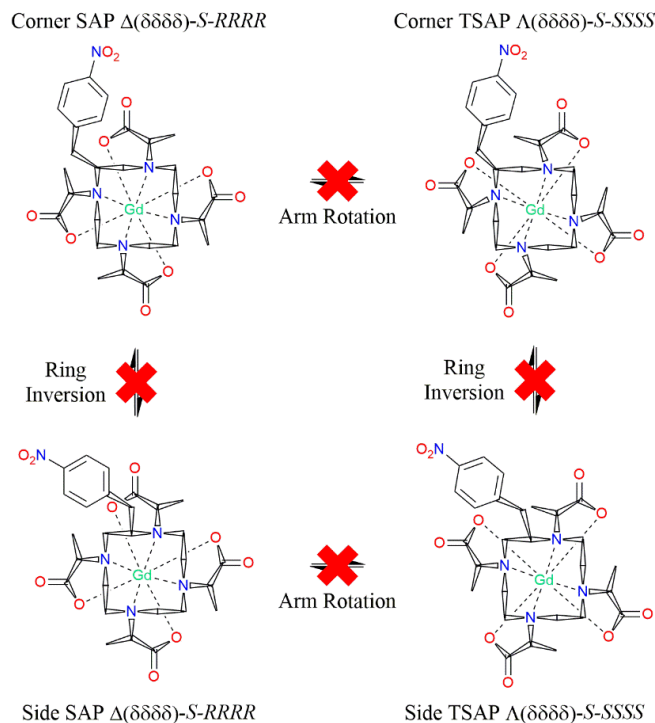


Figure 2.4. Dale structures of the four coordination geometries of GdNB-DOTMA

2.4. Relaxometric Analysis of the Corner and Side Isomers of GdNB-DOTA

GdNB-DOTA was prepared by Dr. K. Payne and relaxometric analysis was conducted by our collaborator, Professor M. Botta at the University of Eastern Piedmont Amedeo Avogadro in Torino, Italy. The transverse relaxation rate constant, R_2 , of ^{17}O was measured for both the Corner and Side of GdNB-DOTA at various temperatures. These data were fitted to SBM theory, and the water exchange lifetimes for both chelates were

determined, Figure 2.5 Top. The relaxivity, r_1 , was measured as a function of magnetic field strength to construct NMRD profiles, Figure 2.5 Bottom.

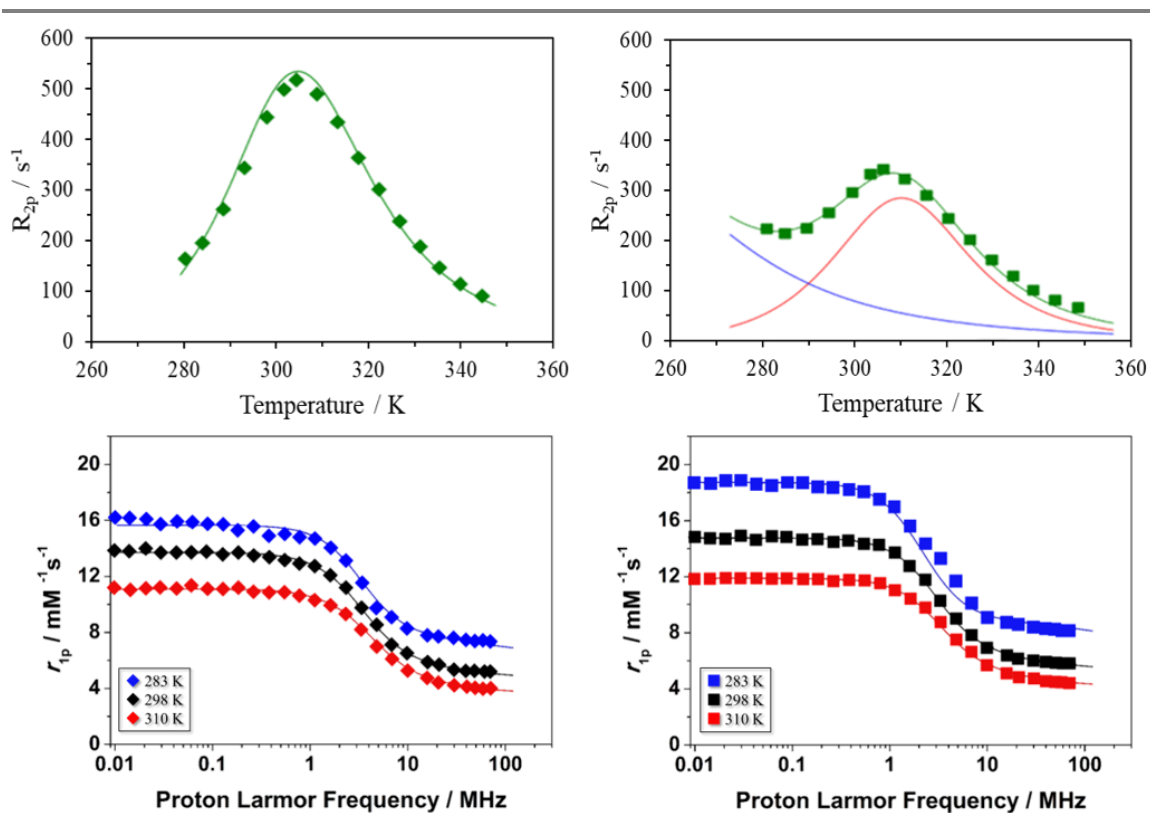


Figure 2.5. Top: Temperature dependence of ^{17}O transverse relaxation rate constants of the Corner (◆) and Side (■) isomers of GdNB-DOTA. **Bottom:** NMRD profiles of the Corner (◆) and Side (■) isomers of GdNB-DOTA recorded at three temperatures.

Fitting the NMRD and VT ^{17}O -NMR data collected to SBM equations allows various physico-chemical parameters associated with the chelate to be determined, these data are shown in Table 2.2.⁶³

Table 2.2. Calculated relaxometric values from the fitted ^{17}O -NMR R_{2p} and NMRD profiles of GdNB-DOTA, at 298 K and 20 MHz from Rust *et. al.*⁶³

Chelate	Corner	Side	
		SAP	TSAP
[Gd] (mM)	8	5.4	6.6
τ_M (ns)	188*		12.4*
		250	7
A/h ($\cdot 10^6 \text{ rad}\cdot\text{s}^{-1}$)	-3.4	-3.5	-3.5
ΔH_M ($\text{kJ}\cdot\text{mol}^{-1}$)	45.7	48.3	28.1
r_{GdH} (\AA)	3.005		3.055
τ_R (ps)	90		120
r_1 ($\text{mM}^{-1}\text{s}^{-1}$)	5.8		6.1
ΔH_R ($\text{kJ}\cdot\text{mol}^{-1}$)	17		16
Δ^2 ($\cdot 10^{19} \text{ s}^{-2}$)	0.86		1.2
τ_V (ps)	19.7		18
ΔH_V ($\text{kJ}\cdot\text{mol}^{-1}$)	1.0		1.0

*Weighted average of SAP and TSAP

The most obvious difference when comparing the Corner and Side is their very different relaxivities. The Side isomer has a higher relaxivity than the Corner. Regioisomers would be expected to exhibit the similar properties, thus the Corner and Side

should have identical relaxivities. This difference could be explained by the fact that the Side isomer has a much higher percentage of TSAP in solution. It has been demonstrated that a high ratio of TSAP can result in extremely rapid dissociative water exchange and produce lower relaxivity.⁵⁶ Reviewing the τ_M values for the Corner and Side, it is confirmed that the Side isomer undergoes rapid dissociative water exchange; its weighted τ_M value is over 10 times shorter than the Corner. The τ_M value of 12.4 ns observed in the Side means that it is undergoing such a rapid dissociative exchange mechanism, that it must experience a reduced hydration state, q/r^6 . However, we do not observe the expected detrimental impact this would have on relaxivity. In fact, it has a higher relaxivity value than that of the Corner. So, we must posit the question, what is facilitating the high relaxivity observed in the Side while simultaneously allowing it to suffer a reduction in q/r^6 ? This explanation must fall in terms of rotational correlation time, τ_R .

The data presented in Table 2.2 show that the Corner isomer tumbles at a faster rate ($\tau_R = 90$ ps) than the Side isomer ($\tau_R = 120$ ps). The Corner and Side are regioisomers; they have identical molecular masses and structures and should therefore have similar hydrodynamic volumes; they should tumble at the same rate in solution. However, the data presented in Table 2.2 suggest otherwise, so either these data were fitted incorrectly or, these two isomers have different properties. In a low-molecular weight chelate exclusively undergoing dissociative water exchange, the predominating influences on relaxivity are τ_R and q/r^6 .⁶⁴ Thus, in order for the Side to have a higher relaxivity than the Corner, it must be tumbling at a slower rate. Otherwise we would observe the impact of a reduction in q/r^6 causing the relaxivity of the Side to be lower than the Corner. This is a result of the

interplay of τ_R and r_{GdH} . TSAP isomers that are in rapid water exchange have demonstrated to have a longer r_{GdH} value.⁵¹ However, the increase in r_{GdH} will result in an increase in τ_R .⁵⁸ A value of 3.1 Å is a justifiable r_{GdH} for a pure TSAP isomer; however this value results in the expected longer τ_R shown in the Side isomer with its higher proportion of TSAP in solution.⁵¹ However, the increase in τ_R experienced by the Side isomer when r_{GdH} is increased is not justified without further exploration into tumbling between the two regioisomers.

2.5. Relaxometric Analysis of the Corner and Side Isomers of GdNB-DOTMA

The four isomers of GdNB-DOTMA were prepared by Drs. B. Webber and K. Payne and analyzed relaxometrically by Professor M. Botta. The relaxometric values determined after fitting the ¹⁷O-NMR and NMRD profiles for the four isomers are shown in Table 2.3. As expected, the τ_M values for the TSAP isomers of both the Corner and Side were much shorter than their SAP counterparts. The reduction of hydration state for these extremely rapidly exchanging chelate results in a reduced relaxivity for both TSAP isomers.

What is most interesting about these data, is the τ_R values for the SAP Corner isomer and both TSAP isomers are nearly identical. However, the longer τ_R value of the SAP Corner isomer results in a longer relaxivity in comparison to the two TSAP isomers, because of the decrease in q/r^6 for both TSAP isomers. One anomaly in these data is the TSAP Side isomer: it has the lowest τ_R values of the four chelates and is shorter than the other TSAP isomer. There are two possible explanations for the short τ_R of the TSAP Side.

Either the interdependent nature of the fitting parameters impacts a change of τ_R , or, the Side isomers behave differently in solution. The most effective means to probe this anomaly is through independent analyses of molecular tumbling.

Table 2.3. Selected fitted relaxometric values for the four isomers of GdNB-DOTMA at 298 K and 20 MHz. Values from Webber *et. al.*⁶⁵

Chelate	SAP S-RRRR		TSAP S-SSSS	
	Corner	Side	Corner	Side
r_1 (mM ⁻¹ s ⁻¹)	6.3 ± 0.1	7.1 ± 0.1	5.9 ± 0.1	5.6 ± 0.1
$^{\dagger}q/r^6$ (nm ⁻⁶)	1372	1372	1127	1127
τ_M (ns)	76 ± 3	61 ± 2	6.6 ± 0.4	5.2 ± 0.3
τ_R (ps)	112 ± 4	134 ± 6	118 ± 5	115 ± 3

[†]Fixed during fitting

2.6. Exploration into Self-Association of the Side Isomer of GdNB-DOTA

A series of experiments were undertaken to develop a thorough understanding of how molecular tumbling impacts hydration and relaxivity in NB-substituted chelates. We hypothesized that for the Side isomer to tumble at a slower rate than the Corner, it must be either forming an aggregate, or self-associating in solution. This would account for the fact that the Side has faster than optimal dissociative water exchange kinetics than the Corner, yet higher relaxivity. We first sought to explore this phenomenon on the two regioisomer chelates of NB-DOTA.

2.6.1. T_1 -Relaxation Studies on GdNB-DOTA

Our first approach in testing this hypothesis to collect variable temperature longitudinal relaxation measurements on the Corner and Side isomers at 20 MHz. T_1 relaxation measurements were taken in triplicate at five different concentrations to generate a curve of r_1 versus temperature. Theoretically, as the concentration of the chelate increases, the likelihood of self-association in the Side would increase, and thus tumbling would be slowed, and we would observe the Side isomer to have a higher relaxivity than the Corner. Our results were inconclusive; there was not a discernable differences in the relaxivities of the Side versus Corner as the concentration was increased, as shown in Figure 2.6. We hypothesize that collecting data at one field strength limited the results.

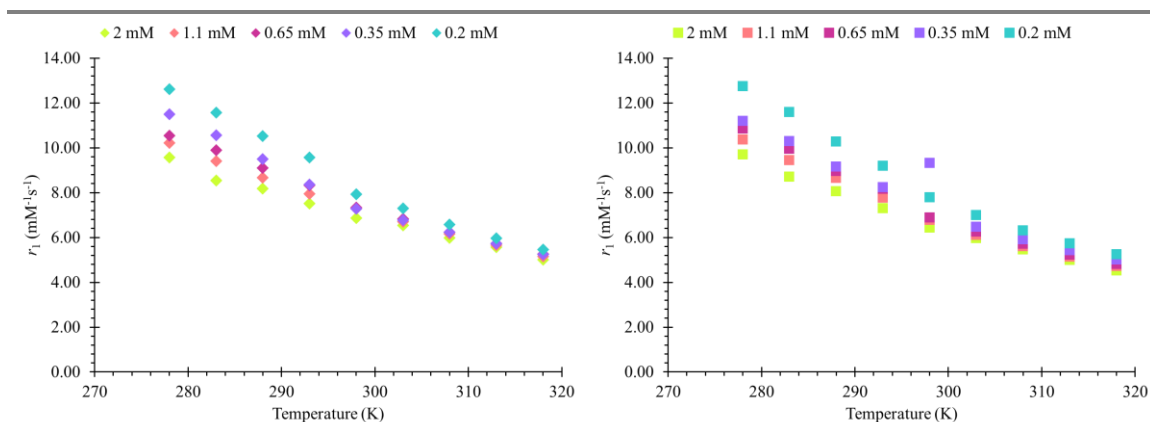


Figure 2.6. Relaxivities (r_1) of GdNB-DOTA Corner (◆) and Side (■) isomers at different concentrations and temperatures.

2.6.2. Attempt of an Amino-Substituted Chelate (GdAB-DOTA)

We hypothesized that reduction of the nitro-substituent to an amino group – converting GdNB-DOTA to GdAB-DOTA, would increase the hydrophilicity of the

benzylic substituent. This would reduce the effect of self-association. Several attempts of isolating pure chelates of GdNB-DOTA Corner and Side were undertaken, however due to the increased hydrophilicity of the amino group, the crude chelate was difficult to separate into regioisomers on the RP-HPLC. Nevertheless, the RP-HPLC method was eventually optimized and samples were sent to our collaborator for analysis, but the NMRD profiles proved inconclusive; the multiparameter influence on relaxivity prevented a definitive determination if tumbling was different between the two.

2.6.3. $^1\text{H-NMR}$ Experiments on EuNB-DOTA

The next set of experiments involved collecting $^1\text{H-NMR}$ spectra of both the Corner and Side isomers of EuNB-DOTA at seven different concentrations of chelate, against a *tert*-butanol internal standard. By collecting spectra at increasing concentrations of chelate, we hypothesized that we would observe a change in shift of the SAP axial proton resonances of the macrocycle. We postulated that the change in shift would be different for the Corner and Side, because if the Side self-associated, the “dimer” would shield these protons and shift them upfield. However, the change in chemical shift of these protons was incredibly minimal (<0.1 ppm in most cases), that we could not confidently draw conclusions from this experiment.

2.6.4. Luminescence Studies on NB-DOTA Chelates

2.6.4.1. Stern-Volmer Experiments: Self-Quenching Study

Previous studies have demonstrated the presence of dimers in solution using Stern-Volmer experiments.^{66,67} These experiments used a Nd^{3+} chelate as a quencher for a Eu^{3+}

chelate. Titrating the Nd^{3+} chelate into a solution of the Eu^{3+} chelate affords Stern-Volmer quenching constants for the luminescent lifetime (K_{SV}^{τ}) and the emission intensity (K_{SV}^{Φ}). K_{SV}^{τ} is largely determined by collisional quenching and therefore should be unaffected by self-association. In contrast, K_{SV}^{Φ} is affected by both collisional and static quenching and is sensitive to self-association. Comparing these two quenching constants can afford an assessment of the extent of self-association.

A sample of NdNB-DOTA Corner was titrated it into a solution of EuNB-DOTA Corner, then the emission intensity and luminescence lifetime of Eu^{3+} was measured. This experiment was then repeated with the Side isomer. These experiments should be conducted at low concentrations to avoid the effects of self-quenching; thus, the first experiment was conducted at $[\text{EuNB-DOTA}] = 10 \mu\text{M}$ and $[\text{NdNB-DOTA}] = 0 - 37 \mu\text{M}$. The determined quenching constants showed there is little to no meaningful difference between them, Table 2.4. However, it is likely that self-association does not occur at the low concentrations at which these experiments were conducted; these experiments were conducted at two orders of magnitude lower than the $^1\text{H-NMR}$ relaxometric experiments and three orders of magnitude lower than the $^{17}\text{O-NMR}$ relaxometric experiments. If self-association is weak, it is reasonable to assume than an effect observable at higher concentrations would be undetected at much lower ones. The Stern-Volmer plot can be seen in the Chapter 2 Appendix. Attempts to run Stern-Volmer experiments at higher concentrations, such as those used in relaxometric studies were frustrated by significant non-linearity in the data, attributed to self-quenching.

Table 2.4. Stern-Volmer quenching constants for the luminescence lifetime and emission lifetime for NB-DOTA Corner and Side.

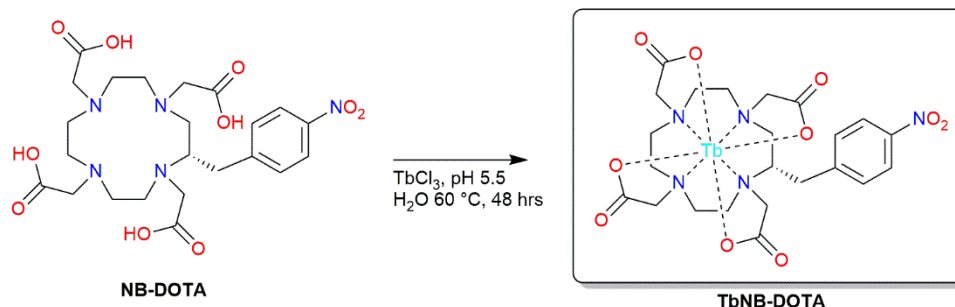
	NB-DOTA Corner	NB-DOTA Side
K_{SV}^{τ} (M ⁻¹)	86.5	117.6
K_{SV}^{Φ} (M ⁻¹)	99.3	99.0

2.6.4.2. Fluorescence and Absorbance Studies

We hypothesized that if the Side self-associates, it will be observable *via* fluorescence or absorbance spectroscopy. This may result in shifts to the emission or absorbance peaks or change their intensity. In order to test this possibility, solutions of GdNB-DOTA Corner and Side were prepared over the following concentrations: 0.2 mM, 0.25 mM, 0.32 mM, 0.4 mM, 0.5 mM, 0.64 mM, 0.8 mM, 1 mM, 1.25 mM, 1.6 mM, and 2 mM. Emission spectra of each solution were collected at $\lambda_{ex} = 270$ nm, 297 nm, and 340 nm. The intensity values from the emission data of the peaks at 597 nm ($\lambda_{ex} = 297$ nm), and 543 nm ($\lambda_{ex} = 270$ nm), were plotted as a function of chelate concentration. Excitation spectra of each solution were collected at $\lambda_{em} = 400$ nm, 535 nm, and 590 nm.

The data from these experiments showed a decrease in intensity as a function of increasing concentration for both Corner and Side isomers. This general trend is an indication of self-quenching of the chelate due to increased molecular collisions. The Side isomer however, decreased in intensity much more rapidly than the Corner with increasing concentration. These results were promising; the Corner and Side behaved differently in both sets of data, but definitive conclusions remained difficult to draw. These spectra can be seen in the Appendix.

2.6.5. Curie Relaxation Study on TbNB-DOTA



Scheme 2.1. Chelation of NB-DOTA with terbium chloride.

The final study into self-association of the Side isomer was a multi-field Curie relaxation experiment. Utilizing this methodology, τ_R can be determined independently, allowing us to confirm that the Corner and Side isomers do indeed tumble at different rates. Chelation of NB-DOTA with terbium chloride was achieved in water at pH 5.5, Scheme 2.1. The Corner and Side regioisomers were separated *via* RP-HPLC, then ¹H-NMR spectra of each were collected at three magnetic field strengths, 9.4 T, 11.5 T, and 14.1 T at 298 K. The Curie-spin mechanism is specific for each lanthanide and contributes to the transverse relaxation rate of a proton. It is dependent on the magnetic field strength (B_0), the metal-proton distance ($r_{\text{Ln-H}}$) and the rotational correlation time. Curie-spin can be defined by equation 2.1.⁶⁸ Assuming the metal-proton distance from crystallographic data, the Curie-spin mechanism allows for the mathematical determination of τ_R of the metal – axial proton vector independently from ¹⁷O-NMR and NMRD at a given temperature. Although this value is not identical to the τ_R determined for the metal – OH₂ vector, it is similar and allows us to compare the values generated from both experiments.

$$\frac{1}{T_2^{\text{Curie}}} = \frac{6}{5} \left(\frac{\mu_0}{4\pi} \right)^2 \frac{\gamma_I^2 \mu_B^4 \mu_{\text{eff}}^4}{(3k_B T)^2 r^6} B_0^2 \left(\frac{\tau_R}{1 + (\omega\tau_R)^2} \right)$$

Equation 2.1. The Curie-spin mechanism contribution to transverse relaxation rate. Where μ_0 is the vacuum permeability, γ_I is the gyromagnetic ratio, μ_B is the Bohr magneton, μ_{eff} is the effective magnetic moment of the lanthanide ion, k_B is the Boltzmann constant, T is the temperature, r is the metal-proton distance, and τ_R is the rotational correlation time.

Evaluation of NMR spectra of the two TbNB-DOTA complexes were completed through an analysis of their most shifted axial proton (ax^S) of the macrocycle ring, as shown in Figure 2.7. Using the metal-proton distance from the crystal structures of TbTCE-DOTA (SAP) and TbDOTMA (TSAP), these data were fit into Equation 2.1 for the determination of τ_R , Table 2.5.^{51,69} The values for r_{LnH} were chosen as a better representation of the Corner and Side chelates. Crystal structures for the terbium complexes for TCE-DOTA and DOTMA exist in primarily the SAP and TSAP coordination geometry, respectively, and allow for a more accurate description of the Corner and Side terbium chelates of NB-DOTA synthesized. Data for TbNB-DOTA Corner SAP was not collected due to the low abundance of this species in solution (5%).

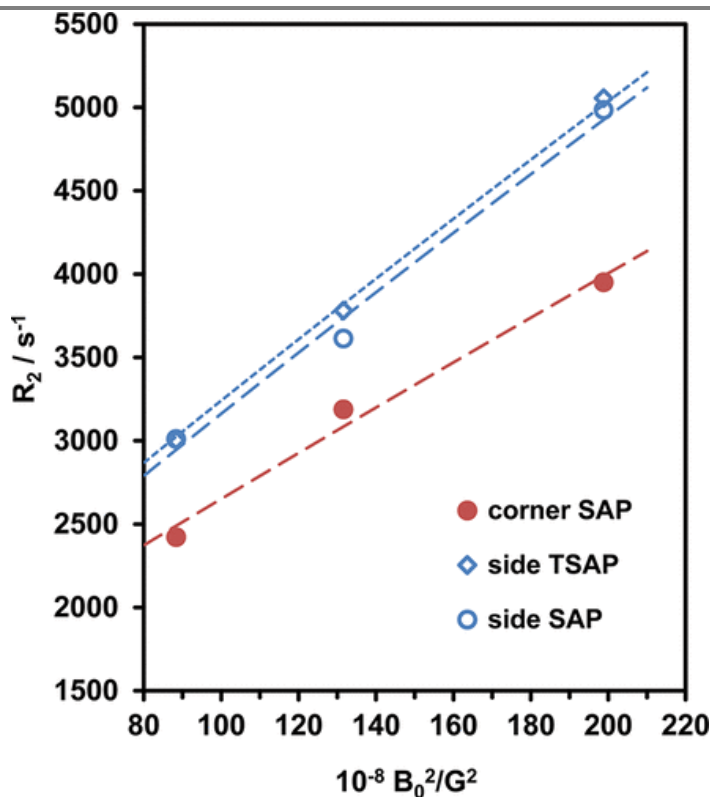


Figure 2.7. The most shifted axial proton (ax^S) dependence on the transverse relaxation rate of TbNB-DOTA Corner SAP (●), Side SAP (○), and Side TSAP (◇) at three magnetic field strengths, 9.4 T, 11.5 T, and 14.1 T at 298 K. $G = 10^{-4}$ T.

Table 2.5. Terbium – proton distances (r_{TbH}) and rotational correlation times (τ_R) for TbNB-DOTA Corner and Side using the Curie-spin mechanism.

Chelate	Corner	Side	
		SAP	TSAP
r_{TbH} (Å)	3.73	3.73	3.69
τ_R (ps)	90 ± 2	125 ± 3	116 ± 1

It is clearly shown that these two chelates, Corner and Side, tumble differently in solution. The values of τ_R obtained with the rotational correlation times generated *via*

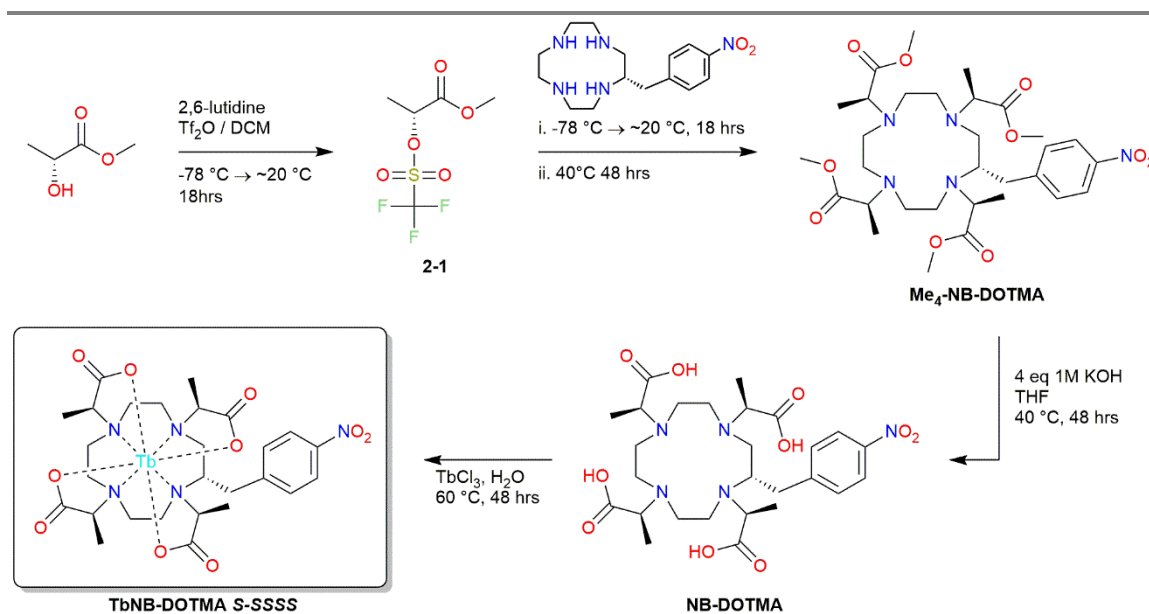
fitting the NMRD profiles (Table 2.3), suggesting the values selected for the metal-proton distance to be accurate. The slower tumbling rate of the Side isomer in comparison to the Corner confirms our hypothesis that the Side self-associates in solution. This slowed rotation would account for its higher relaxivity despite its faster than ideal dissociative water exchange rate and reduced hydration state.

As predicted, these results confirm that the Side isomer suffers from a reduction in hydration state due to its faster than optimal dissociative water exchange kinetics. However, this does not cause the expected negative impact on relaxivity owing to its slower tumbling; in fact, it has one of the highest relaxivities of any low molecular weight macrocyclic chelates. This is in contradiction to established theory that a chelate with a reduced hydration state will have lower than optimal relaxivity. Thus, it seems as if its slower tumbling rate resulting from self-association, compensates for its extremely rapid dissociative water exchange. The interdependent nature of the SBM equations prevents independent probing of each value to determine its impact on relaxivity; a change in one relaxometric value results in an expected change in another. Thus, it is impossible to determine the true impact hydration state has on overall relaxivity without further experimentation.

2.6.6. Curie Relaxation Approach on TbNB-DOTMA

Methyl (*R*)-2-(((trifluoromethyl)sulfonyl)oxy)propanoate (**2-1**) was synthesized from methyl-D-lactate under air- and water-free conditions, with 2,6-lutidine in dichloromethane (-78 °C to ~20 °C). **2-1** was then alkylated on NB-cyclen (purchased from Macrocyclics®) with potassium carbonate and dichloromethane (-78 °C to ~20 °C, 18 hrs;

40 °C, 48 hrs), resulting in an enantiopure ligand (Me₄-NB-DOTMA *S*-SSSS). The ligand was then chelated with TbCl₃ and purified *via* preparatory RP-HPLC to yield two TbNB-DOTMA complexes: Corner *S*-SSSS (TSAP), and Side *S*-SSSS (TSAP), Scheme 2.2.



Scheme 2.2. Synthesis of TbNB-DOTMA *S*-SSSS.

¹H-NMR spectra were collected of TbNB-DOTMA Corner and Side at 2.1 T, 9.4 T, and 14.1 T and 302 K. Analysis of their most shifted axial protons was completed as demonstrated in Aime *et. al.* *via* line-width analysis.³⁵ Because Tb³⁺ chelates of NB-DOTMA are not isochemical to their Gd counterparts, and due to the lack of temperature control on the 90 MHz spectrometer, we cannot allow this analysis to be an exact measurement or comparison to the τ_R values determined *via* NMRD analysis. Therefore, the data presented in Table 2.6 are given without errors and should be treated as general trends and not exact values. However, we can examine the differences observed between the two analyses. Because Tb³⁺ does not have an isotropic *f*-shell, it will exhibit anisotropy

in an external magnetic field, this can give rise to differences in the observed NMR signal, as shown in the line-width analysis in Figure 2.8 Top.

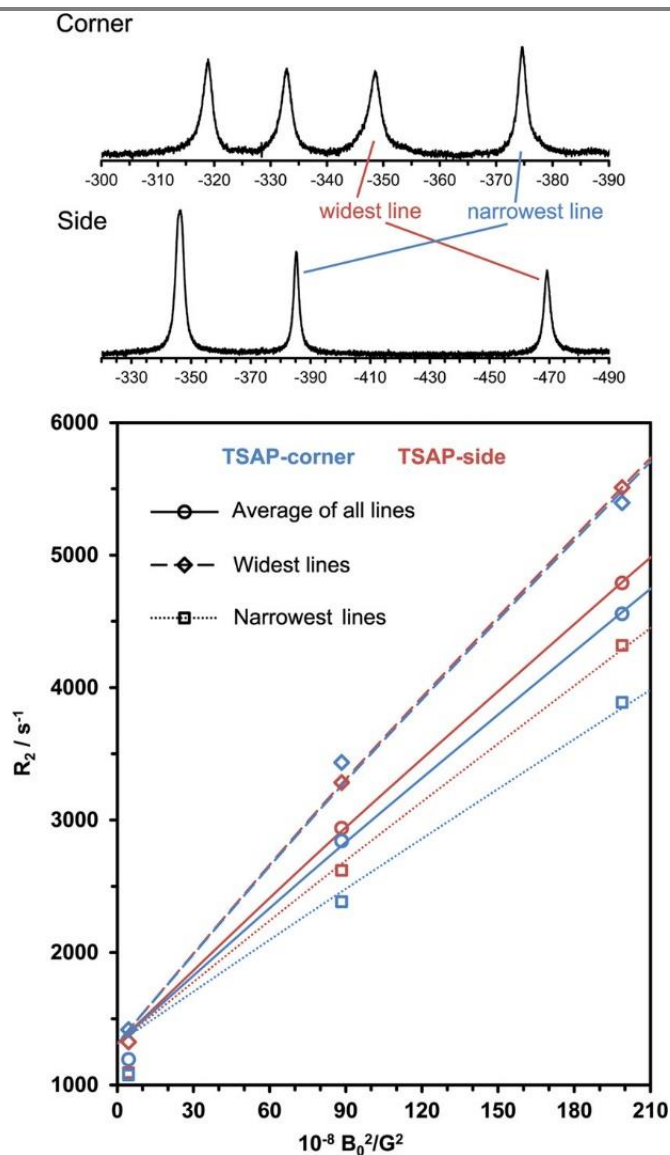


Figure 2.8. Analysis of the most shifted axial (ax^S) protons of TbNB-DOTMA (*S*-SSSS) Corner and Side isomers. **Top:** ¹H-NMR spectra of the most shifted ax^S protons of the two regioisomers. **Bottom:** Field dependence of the transverse relaxation rate constant of the most shifted ax^S protons of the Corner (blue) and Side (red) regioisomers.⁶⁵

The line-width analysis of the two Tb^{3+} complexes showed that the ax^S protons with the widest lines tumble the most slowly, Table 2.6. As expected, the slower molecular tumbling observed corresponds to the higher transverse relaxation rate determined for these protons, Figure 2.8 Bottom. Conversely, the narrowest lines of both Tb^{3+} complexes show that they tumble the fastest, Table 2.6, resulting in a much lower R_2 , Figure 2.8 Bottom. This large difference in anisotropy observed within the line-width analysis coincides with disparate estimated τ_R values in Table 2.6, yet, the general trend when we observe the analysis of the widest versus shortest line τ_R values both depict the Side tumbling more slowly. Furthermore, when the average is taken of all the lines, to reduce the observed anisotropy, the Side isomer still tumbles slower than the Corner. These data, supported by our previous Curie relaxation analysis of NB-DOTA chelates, demonstrate that although the Corner and Side are isomers, they tumble at different rates.⁶³ We were able to publish these findings in 2020.⁶⁵ This independent observation of different molecular tumbling rates of regioisomers is remarkable; their different in solution behavior requires further experimentation.

Table 2.6. Estimated τ_R values for TbNB-DOTMA S-SSSS Corner TSAP and Side TSAP from the Curie relaxation analysis of the ^1H -NMR spectra presented in Figure 2.8.⁶⁵

τ_R (ps)	Corner (TSAP)	Side (TSAP)
Average of All Lines	104.4	112.6
Widest Lines	138.8	139.7
Narrowest Lines	79.3	94.4

Data analyzed using: $T_{1e} = 0.43$ ps, $r_{\text{TbH}} = 3.694$ Å, and $\mu = 9.72$

2.6.7. *The Difference in Exchange Between Corner and Side Isomers*

All the systems studied herein demonstrate the Side isomer exhibiting faster water exchange kinetics. Density functional theory (DFT) can be used to calculate the effect substitution has on the macrocycle ring. DFT calculations collected by our collaborator Dr. T. McCormick show the macrocycle having to distort to accommodate the bulky nitrobenzyl substituent, Figure 2.9. The distortion in the antiprism NCCN torsion angle (α) influences the location of the metal within the cage; the Corner isomer with an α of 68.4° and 66.9° for the Side. Crystallographic data of LnDOTMA chelates demonstrate that dissociative exchange most likely arises from flattening of the macrocycle ring.⁷⁰ The lower α of the Side correlates with the flattening of the macrocycle, and implies the Side isomer distorts in a conformation that is closer to the transition state of exchange. This distortion would reduce the energy barrier to dissociative water exchange, causing the mechanism of exchange to be increasingly rapid.

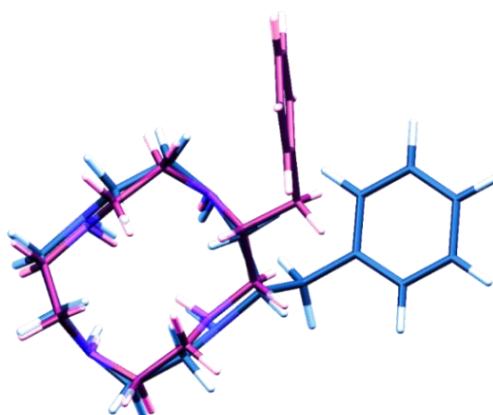
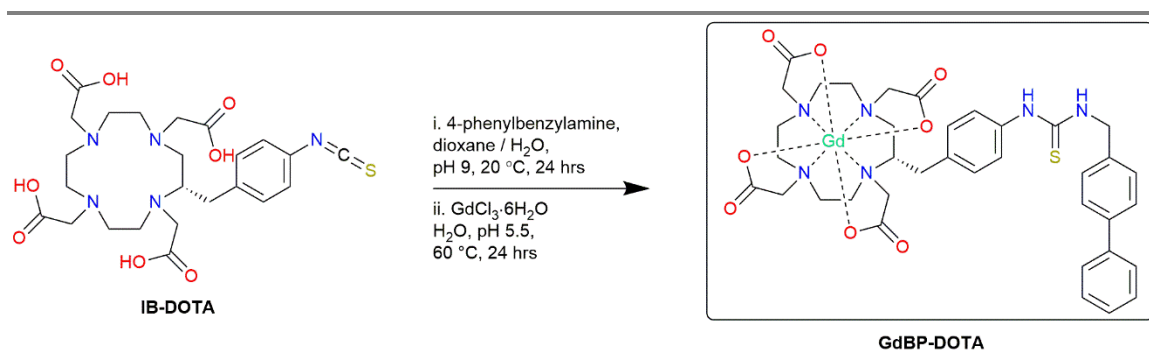


Figure 2.9. DFT modeling calculations of the distortion of the macrocyclic cage in GdNB-DOTA Corner (Blue), and Side (Pink).

2.7. Conjugation with a Biphenyl Moiety – Implications as a Bioconjugate

Although we were able to demonstrate that the Corner and Side isomer have different water exchange kinetics, the impact of this on relaxivity has not been thoroughly explored. Because the Side isomer self-associates in solution if that action is lifted it will still maintain a high relaxivity. By adding a biphenyl moiety *via* a thiourea off the macrocycle, the chelate will participate in hydrophobic interactions which in turn will induce it to tumble more slowly; the barrier of τ_R can be lifted and the effects of water exchange on relaxivity becomes evident.

The commercially available IB-DOTA (purchased from Macrocyclics®) was reacted in a biphasic solution of 4-phenylbenzylamine in water and dioxane (~20 °C, pH 9) to yield the target ligand, BP-DOTA. This was then subsequently chelated with $\text{GdCl}_3 \cdot 6\text{H}_2\text{O}$ in water at (pH 5.5 60 °C), then the Corner and Side regioisomers were separated *via* RP-HPLC to yield the two pure target chelates, Scheme 2.3.



Scheme 2.3. Synthesis of target chelate, GdBP-DOTA from IB-DOTA.

An addition of a biphenyl moiety has been shown to induce a chelate to form micelles in solution above a certain concentration, known as the critical micelle concentration (CMC).⁷¹ Through dynamic light scattering (DLS) it was determined that the Side forms a much larger micelle in comparison to the Corner; 18 nm compared with 10 nm, Figure 2.10. A micelle that is nearly twice the size of its regioisomer indicates the Side is self-associating prior to micellular formation.

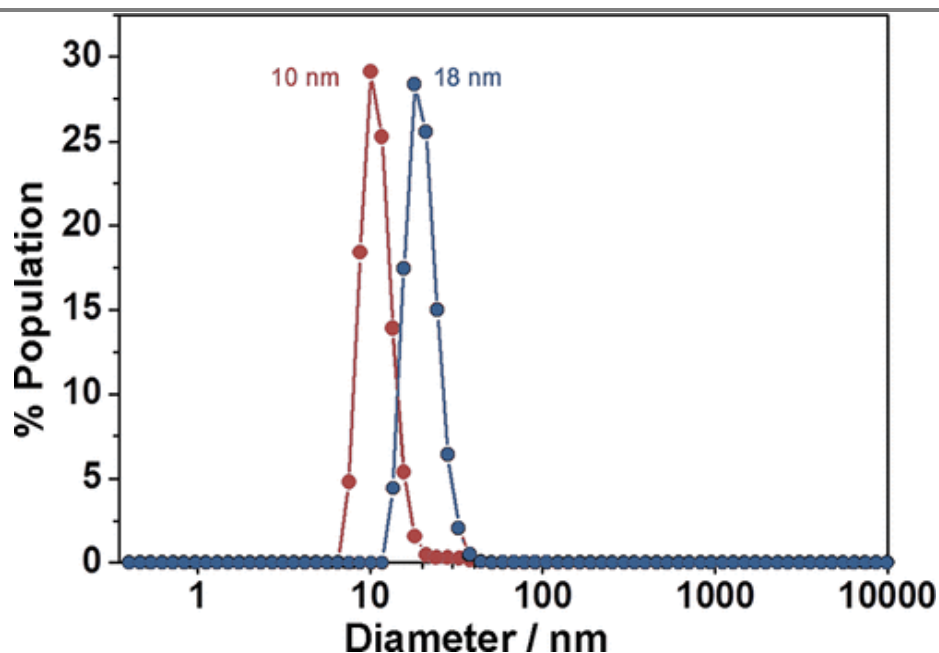


Figure 2.10. Dynamic light scattering (DLS) distribution of the micelles formed by the Corner (●) and Side (●) isomers of GdBP-DOTA.

NMRD profiles were generated for both Corner and Side isomers of GdBP-DOTA, Figure 2.11. The fitted NMRD profiles generated relaxometric values, Table 2.7. Reviewing the data generated for both chelates below their respective CMCs, illustrated as circles in Figure 2.11, the introduction of a bulky biphenyl moiety slowed down τ_R in comparison with the NB derivatives, and resulted in an expected increase in relaxivity. In

consistence with the relaxometric data from the NB-DOTA chelates, the Side tumbles much slower in solution in comparison with the Corner, 190 ps compared to 120 ps, respectively.

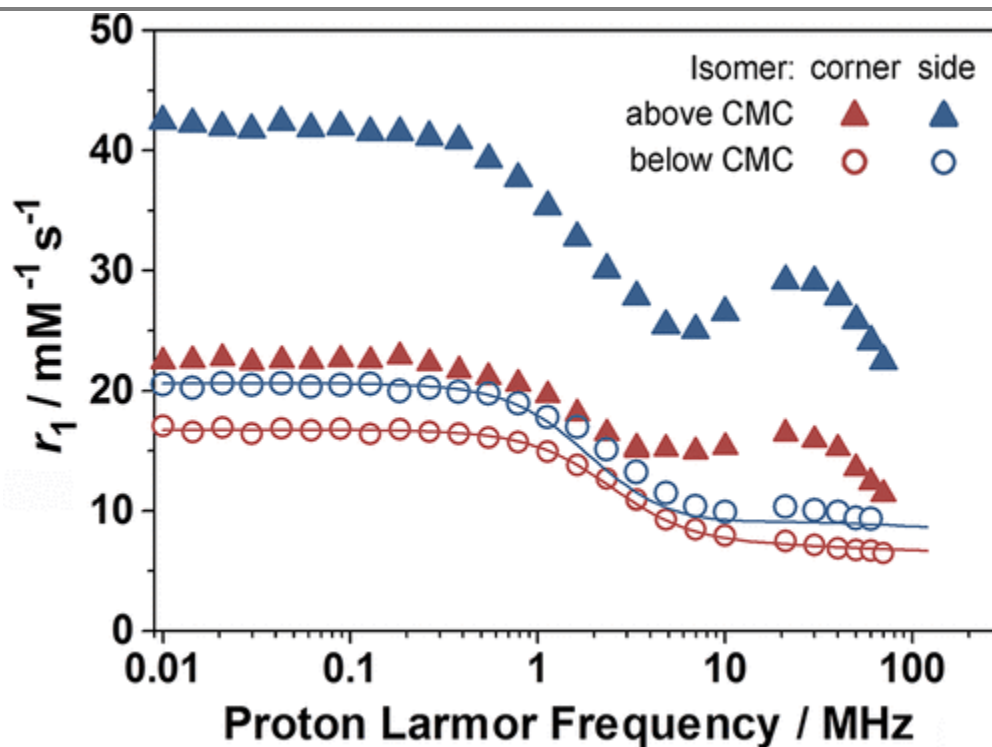


Figure 2.11. NMRD Profiles at 298 K of GdBP-DOTA Corner below the CMC (○), and above the CMC (▲); Side below the CMC (○), and above the CMC (▲). $[\text{Corner}]_{\text{below}} = 0.15 \text{ mM}$, $[\text{Corner}]_{\text{above}} = 1.51 \text{ mM}$; $[\text{Side}]_{\text{below}} = 0.2 \text{ mM}$, and $[\text{Side}]_{\text{above}} = 1.48 \text{ mM}$.

Although these data support the premise that the Side tumbles slower than the Corner due to self-association, this system cannot be fully appreciated while these chelates are behaving as discrete molecules in solution. Thus, increasing the concentration to the point of micellular formation, the effects of self-association observed in the Side can be highlighted.

Table 2.7. Relaxometric values from the fitted NMRD profiles of the Corner and Side isomers of GdBP-DOTA at 298 K below the CMC.

Chelate	Corner	Side
r_1 (mM ⁻¹ s ⁻¹)	8.3	11.6
r_{GdH} (Å)	3.005	3.055
Δ^2 ($\cdot 10^{19}$ s ⁻²)	1.10	1.08
τ_{M} (ns)	188	12.4
τ_{V} (ps)	19	17
τ_{R} (ps)	130	190

Fixed Values: $q = 1$, r_{GdH} , τ_{M}^{298} , $a = 4.0$ Å, and $D_{\text{GdH}}^{298} = 2.24 \times 10^{-5}$ cm²s⁻¹.

The linear dependence of T_1 on concentration of gadolinium can allow for the determination of the concentration in which a molecule forms a micelle. The CMC was determined by collecting T_1 at 298 K and 20 MHz as a function of chelate concentration, and the concentration in which the relaxation rate deviates from the linear dependence is the CMC. The resulting fitted data from the NMRD profiles as well as CMC determination are shown in Table 2.8, with the NMRD profiles above their respective CMC values are illustrated as the triangles in Figure 2.11.

Table 2.8. Critical micelle concentrations, micelle diameters, and relaxivities from the NMRD profiles of GdBP-DOTA Corner and Side above the CMC at 298 K and 20 MHz.

Chelate	Corner	Side
CMC (mM)	0.90	1.10
Micelle Diameter (nm)	10	18
r_1 (mM⁻¹s⁻¹)	16.4	29.2

As shown in the data in Table 2.8, the GdBP-DOTA Side has a higher CMC when compared with the Corner. These findings are surprising because the chelates are regioisomers of each other and thus have identical molecular weights and should have identical hydrodynamic volumes. The Side forming micelles at a higher concentration than the Corner further supports these chelates behaving differently in solution.

Analysis of the fitted relaxometric data from the NMRD profiles of GdBP-DOTA Corner and Side above their CMCs provides insight into the impact of two relaxometric properties on relaxivity. Incorporation of these hydrophobic chelates into micelles fully lifts the impact τ_R has on relaxivity. Thus, the true impact q/r^6 can be probed. As seen by the NMRD profiles of GdBP-DOTA Corner and Side above the CMC, they have very different relaxivities, Table 2.8. At 298 K and 20 MHz, the Side was found to have a relaxivity nearly double that of the Corner. Yet, while reviewing their τ_M values, the Side is exchanging water so rapidly, it is considered higher than optimal; the compensatory factor of its slow molecular tumbling, from its self-association, allows for the Side to have a much higher relaxivity value.

Thus, slow rotation has a greater impact on relaxivity than hydration state, especially at high fields. This is highlighted by the “hump” seen in the NMRD profile ~20 MHz. When the rotation of a chelate is substantially slowed, relaxivity is optimized, due to τ_R modulating close to the Larmor frequency of the protons on water. The incorporation of a large bulky group and subsequent micelle formation allows for this slowed rotation and therefore optimal relaxometric kinetics. Although the “hump” is observed in the Corner isomer, it is less pronounced due to its shorter τ_R .

The relaxometric results of the Side isomer are promising in terms of designing a bifunctional chelator with optimal relaxivity. However, it is important to recognize that the Side isomer constitutes only 25% of the overall sample of chelate and is incredibly expensive and difficult to synthesize. Furthermore, if we remove the impact of self-association of the Side, which most likely would not occur when a macrocycle substituted bifunctional chelator is incorporated into a bioconjugate, the detrimental impact of having a reduced hydration state would result in limited relaxivity.

2.8. Conclusions

Our independent experimental determination of τ_R for both regioisomers of GdNB-DOTA and TbNB-DOTMA *via* Curie relaxation studies allowed us to glean insight into the impact rotation has on relaxivity. These experimental data revealed that the Corner and Side tumble at different rates. We were able to demonstrate that the Side isomer self-associates in solution while the Corner does not, thus causing a longer τ_R and higher relaxivity. Yet the rotation was still too rapid to determine the impact on relaxometry.

Through the addition of a biphenyl moiety on the macrocycle, we lifted to barrier of rapid rotation of a small molecular weight chelate, to determine which has a greater influence on relaxivity: rotation or dissociative water exchange. We demonstrated that due to the extremely rapid dissociative exchange mechanism of the Side isomer, the amount of time water spends unbound is non-negligible. As a result, the rapid dissociative exchange mechanism of the Side isomer results in a reduced hydration state.

Although the Side has slower rotation than the Corner due to self-association in solution, this impact on optimal relaxivity is limited. When designing a scaffold for a bifunctional chelator, the final incorporation into the bioconjugate must be considered. The self-association seen in the Side isomer of both the nitrobenzyl and biphenyl derivative would likely not occur in a macromolecular bifunctional chelator. As a result, the faster than optimal dissociative water exchange kinetics of the Side would have a detrimental effect on relaxivity, due its reduced hydration state. The Corner isomer does not exhibit ideal rotational correlation or dissociative water exchange kinetics to be considered as a scaffold for a bifunctional chelator.

CHAPTER 3

COMPARISON OF THREE FUNCTIONALIZATION STRATEGIES

3.1. Building a Better Bifunctional Chelator

The growing prevalence of bifunctional chelators (BFCs) in laboratory settings has generated a myriad of data regarding ideal structure and function. Furthermore, the commercial availability for many macrocyclic and linear precursors allow researchers to easily alter the active moiety for a variety of functionalization applications. However, there are some considerations when designing this scaffold. Their ubiquity in the laboratory setting is not matched in clinical practice, and as a result, their long-term stability *in vivo* has not been addressed. Additionally, there has not been a thorough study into the impact on relaxometric properties based on the point and method of functionalization. Three commonly implemented strategies for attachment of the targeting vector are: off the macrocycle, through a monoamide pendant arm, or on the α -carbon of one of the pendant arms, as illustrated in Figure 3.1.

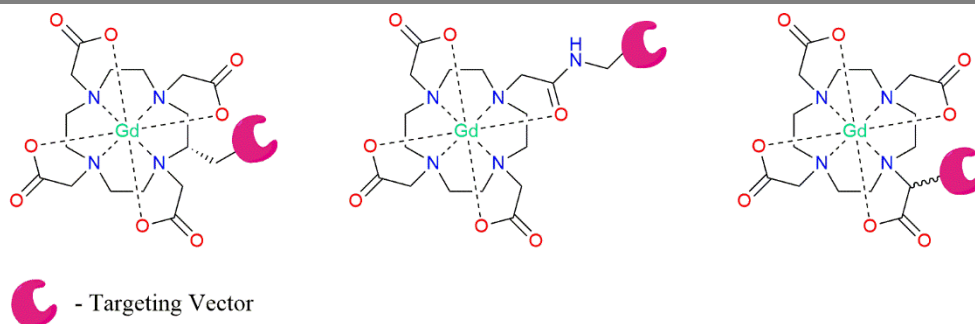


Figure 3.1. Point of attachment of a targeting vector on a DOTA-based BFC; off the macrocycle (Left), through a monoamide pendant arm (Center), or on the α -carbon of a pendant arm (Right).

In Chapter 2, the effects of substituting a nitrobenzyl moiety on the macrocycle ring of a DOTA chelate were explored. NB-DOTA is a well-established macrocyclic BFC precursor, and as a result, we sought to design ligand systems that can be compared directly to this structure in terms of efficacy and synthetic ease. This will allow for the direct comparison of the results in Chapter 2 with two new structures that were designed to be of a similar size.

The first structure we designed to directly compare to NB-DOTA is DO3A-NBAM. This monoamide substituted ligand has an identical molecular weight to NB-DOTA, which allows for direct comparison. The advantage of the NBAM pendant arm is two-fold; no stereocenters are generated on the chelate, and the synthesis is shorter and cheaper. A major advantage of this synthetic strategy is that the relatively mild conditions and inexpensive starting materials means it could be easily translated into a large-scale industrial setting. In contrast, the starting material for NB-DOTA, NB-cyclen, is synthetically difficult and low-

yielding, thus very expensive, secondly, once chelated, NB-DOTA adopts two distinct regioisomers that require costly separation *via* RP-HPLC.

However, one drawback of the NBAM system is in the effect of replacing a negatively charged acetate with a neutral amide has been shown to cause much slower water exchange.⁷² This is due to a reduction of electron density around the metal center, causing it to hold onto the water molecule for a longer time, even if it has been sufficiently relaxed. Therefore, the overall impact on relaxometry needs to be explored.

The second attachment strategy we explored for comparison to NB-DOTA is attaching a moiety on an α -carbon of one pendant arm. DOTA-NF differs from NB-DOTA and DO3A-NBAM by one methylene group due to the mechanism of synthesis; if the moiety were a benzyl rather than a phenyl substituent, the elimination product rather than the S_N2 would predominate. However, this slight difference is the closest possible synthetic structure that will allow for comparison. A benefit of this strategy is that it allows for the complex to maintain the electron dense tetra-acetate pendant arms unlike GdDO3A-NBAM, while also not chelating into distinct regioisomers like GdNB-DOTA. DOTA-NF chelates have been studied previously as a potential scaffold for a BFC, but thorough analysis of this structure as a bioconjugate have yet to be established.⁷³

These three structures have similar molecular weights and hydrodynamic volumes. This allows for the comparison of these three strategies in terms of their synthesis and properties. This direct comparison will allow for the determination of how attachment strategy influences relaxometry, as shown in Figure 3.2.

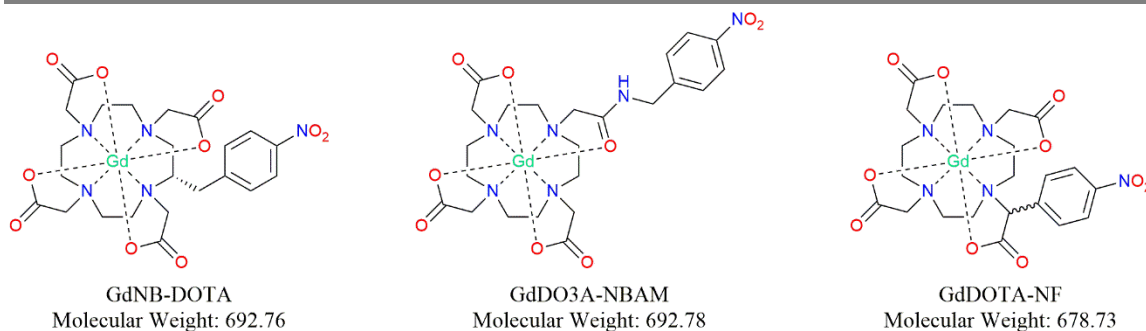


Figure 3.2. The three nitro-substituted macrocyclic chelates analyzed in Section 3.4.1.

Further exploration of these three chelates was taken by the addition of a biphenyl moiety. This group is added to the macrocyclic structure by first converting the nitro group to an isothiocyanate, thus transforming the ligand into a BFC. The addition of the bulky hydrophobic biphenyl group *via* a thiourea linkage allows for the differences of the location of the moiety to be probed while examining their behaviors as pseudo-BFCs. The three biphenyl-containing chelates are shown in Figure 3.3.

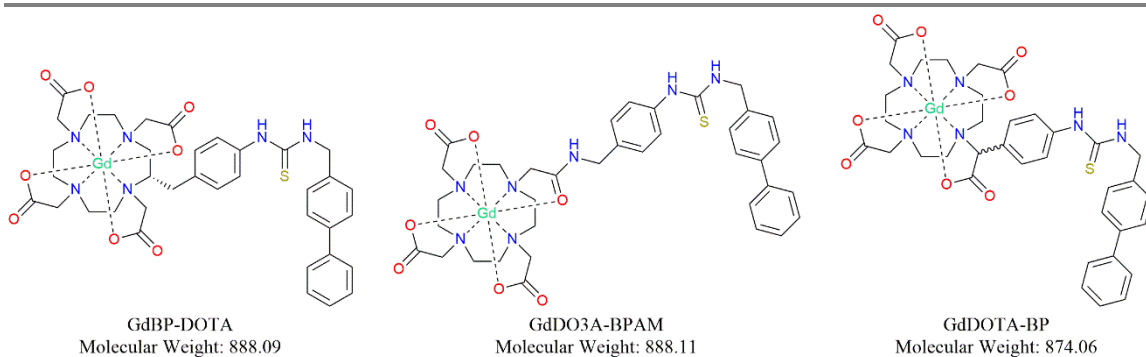
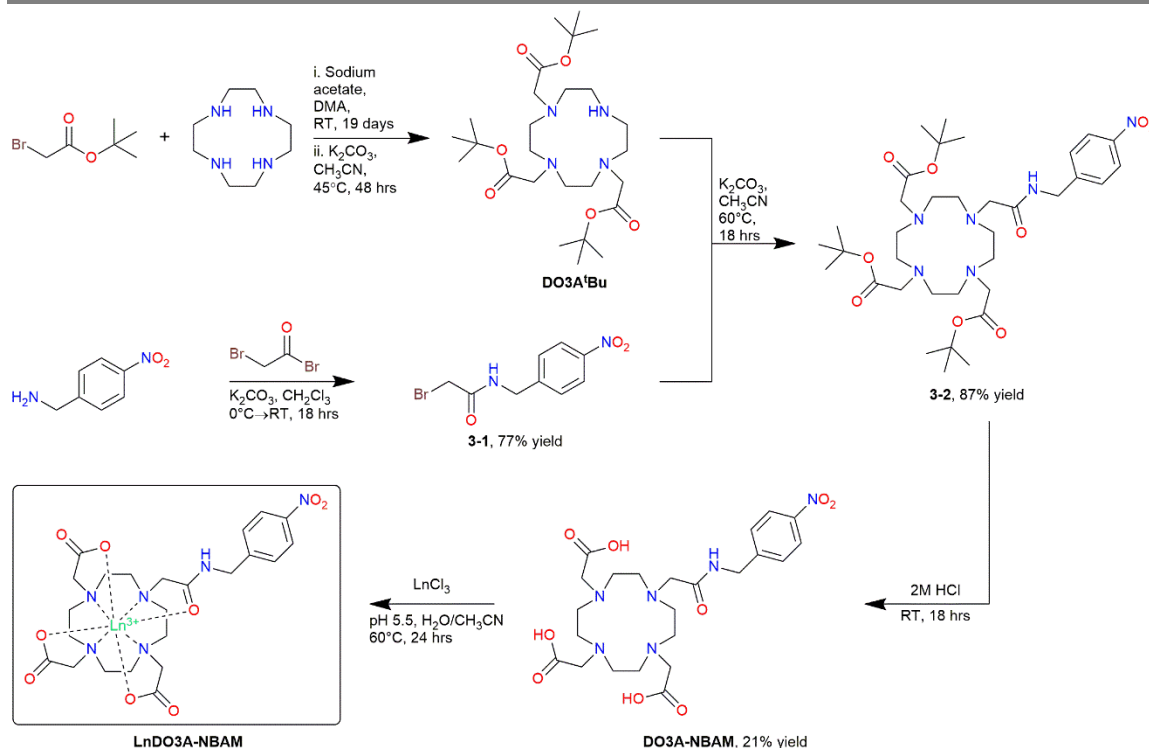


Figure 3.3. The three biphenyl-substituted macrocyclic chelates analyzed in Section 3.4.2.

3.2. Synthesis of Monoamide Attachment Strategy Chelates

3.2.1. Synthesis of Nitro-Substituted Monoamide Chelates (*LnDO3A-NBAM*)

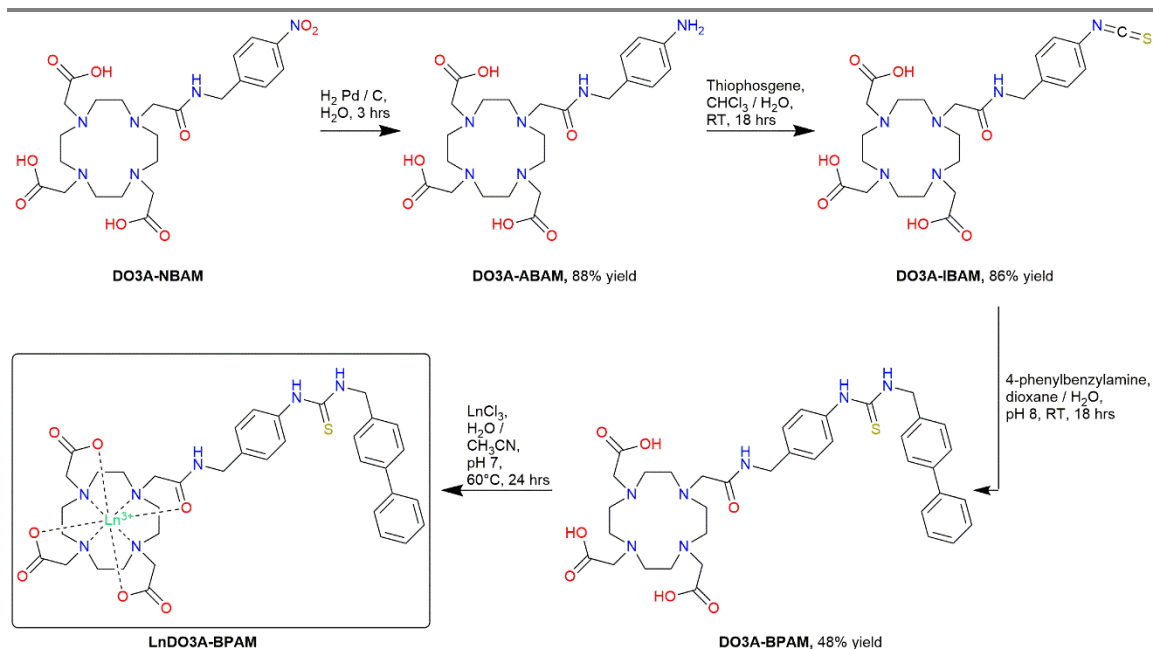
The total synthesis of *LnDO3A-NBAM* chelates is shown in Scheme 3.1. The *DO3A-tert-butyl* ester was prepared using the methods of Raghunand *et. al.*⁷⁴ A facile nucleophilic acyl substitution with 4-nitrobenzylamine generated the 2-bromo-*N*-(4-nitrobenzyl) acetamide (**3-1**, 77% yield).^{62,75} *DO3A-tert-butyl* ester was alkylated with potassium carbonate and acetonitrile at 60 °C using **3-1** to generate the protected ligand (**3-2**, 87% yield). The esters were cleaved using 4M HCl in water to generate the ligand (**DO3A-NBAM**, 21% yield). The ligand was chelated lanthanide chlorides (EuCl_3 , GdCl_3 , YbCl_3) in water and acetonitrile at pH 5.5 to yield the complex, then each was purified *via* RP-HPLC (***LnDO3A-NBAM***).



Scheme 3.1. Total synthesis of LnDO3A-NBAM Chelates. (Ln = Eu, Gd, Yb).

3.2.2. Synthesis of Biphenyl-Substituted Monoamide Chelates (LnDO3A-BPAM)

The introduction of the biphenyl moiety is shown in Scheme 3.2. This was achieved by first reducing the nitro group by hydrogenation with Pd/C as a catalyst in water to result in the amine derivative (**DO3A-ABAM**, 88% yield). The resulting amine ligand was converted to an isothiocyanate group with thiophosgene in a biphasic reaction with water and chloroform (**DO3A-IBAM**, 86% yield). A biphenyl group was introduced by coupling the isothiocyanate to the primary amine on 4-phenylbenzylamine in dioxane (**DO3A-BPAM**, 48% yield).



Scheme 3.2. Synthesis of LnDO3A-BPAM Chelates. (Ln = Eu, Gd, Yb).

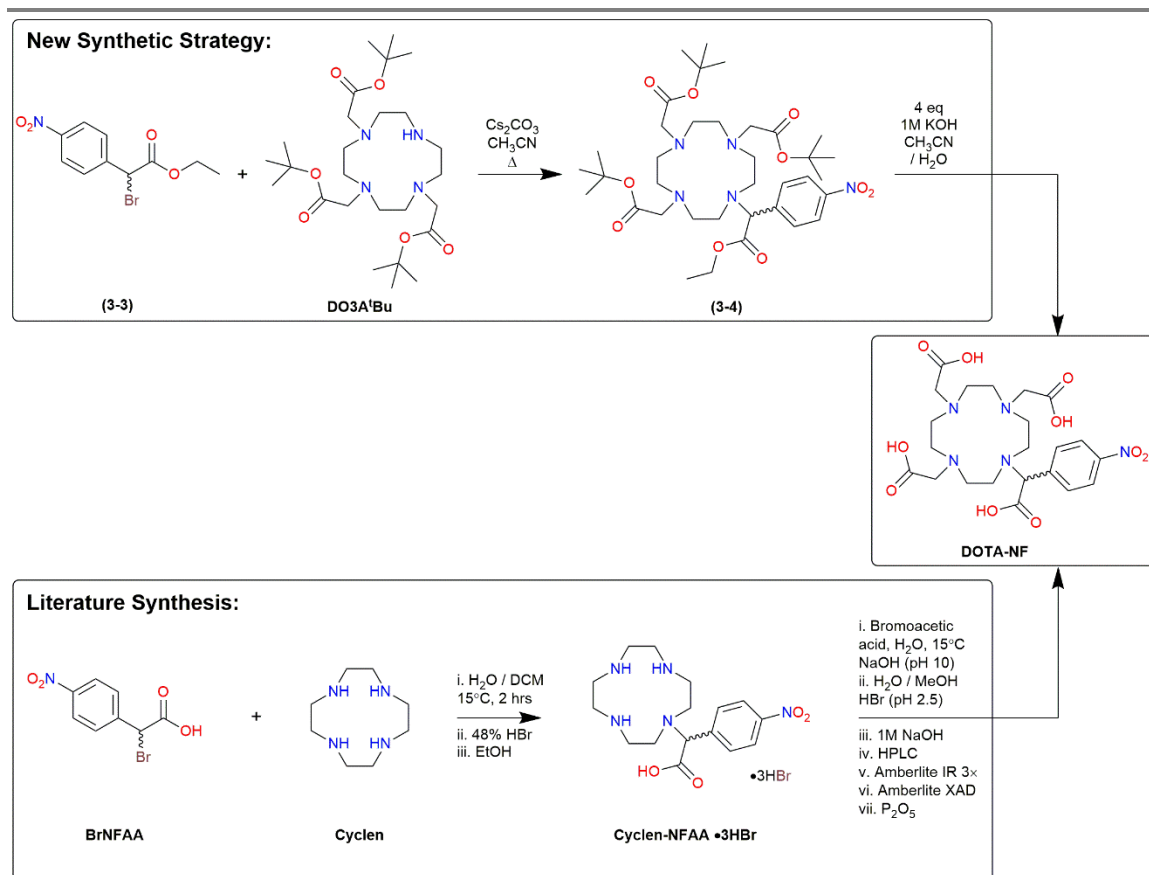
Although chelation of DOTA-type ligands is usually facile, the chelation of DO3A-BPAM was not. The typical chelation reaction occurs by mixing the deprotected ligand with excess metal chlorides in a solution of water at pH 5.5; to ensure solubility of both ligand and metal, and this solution is then gently heated at 60°C for 18 – 24 hours. Chelation is confirmed when the pH of the solution drops due to release of protons on the ligand. However, chelation of DO3A-BPAM did not occur under these conditions. The initial attempts of chelating DO3A-BPAM under standard conditions resulted in the expected drop in pH, and these solutions were purified *via* RP-HPLC. The chromatogram resulted in a single peak, which was confirmed to be pure ligand by $^1\text{H-NMR}$. We hypothesize the hydrophobic biphenyl moiety prevented the ligand from effectively going into solution to properly coordinate the free metal. One issue with the initial chelation reaction was solubility; the hydrophobicity of DO3A-BPAM prevented it from being

soluble in water, so the reaction mixture was stirred vigorously to ensure interaction of the metal and ligand. Hence, various solvents were attempted to get both the metal and ligand in solution, including: acetonitrile, dimethylformamide, dioxane, ethanol, and methanol. It was found that a mixture of a 1:1:1 acetonitrile, dioxane, and water at pH 8 afforded a chelate. The isolation of pure chelate *via* RP-HPLC was also slightly more difficult; free ligand, clean LnDO3A-BPAM chelate, as well as DOTA and LnDOTA due to hydrolysis of the amide, were found present in the individual fractions. The new chelation conditions were altered further to a solution of DO3A-BPAM and relevant metal chlorides (EuCl₃, GdCl₃, YbCl₃) in a mixture of acetonitrile and water at pH 7, high enough to be above the pK_a of the carboxylates but low enough to not hydrolyze the amide, and this allowed for a cleaner RP-HPLC chromatogram and pure product (**LnDO3A-BPAM**).

3.3. Synthesis of α -Carbon Pendant Arm Attachment Strategy Chelates

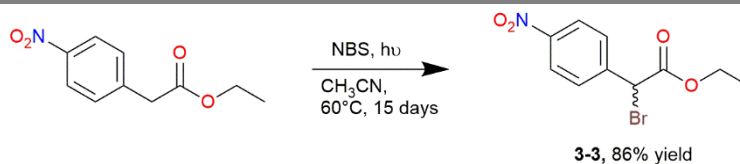
3.3.1. Synthesis of Nitro-Substituted α -Carbon Pendant Arm Chelates (LnDOTA-NF)

Although some relaxometric data was collected for GdDOTA-NF, not enough complex was generated to collect all necessary data, thus more chelate was needed to complete the analysis. A synthetic route to GdDOTA-NF has been developed by Aime *et. al.*⁷³ However, with a large quantity of DO3A-*tert*-butyl esters and it seemed that DOTA-NF could be synthesized following a similar route as DO3A-NBAM chelates. The comparison of these two synthetic strategies are shown in Scheme 3.3.



Scheme 3.3. Proposed synthetic strategy compared to the literature synthesis of DOTA-NF

Synthesis of a suitable alkylating agent was achieved by an adapted procedure from Lim *et. al.*, in which a bromide leaving group was installed on ethyl 2-(4-nitrophenyl)acetate *via* an allylic bromination using *N*-bromosuccinimide and irradiation.⁷⁶ This reaction results in a racemic ethyl 2-bromo-2-(4-nitrophenyl)acetate product as shown in Scheme 3.4 (**3-3**, 86% yield). The preparation of **3-3** used much milder conditions than a traditional bromination like that proposed by Harpp *et. al.*; *N*-bromosuccinimide with light in acetonitrile, resulting in a longer reaction time (15 days).⁷⁷



Scheme 3.4. Synthesis of ethyl 2-bromo-2-(4-nitrophenyl)acetate (3-3)

Although the new proposed preparation of the DOTA-NF ligand appears facile, the synthesis of the protected ligand proved to be unexpectedly challenging. Alkylation of DO3A-*tert*-butyl esters with **3-3** was a slow and low-yielding reaction. It was difficult to isolate appreciable quantities of the protected ligand **3-4**. Therefore, the reaction conditions were examined. Ligand alkylation optimization was pursued with a multivariable approach, with the rationale describe below.

In alkylation reactions, the base serves as a “proton sponge”; it coordinates free protons after the nucleophilic amine on the macrocycle attacks the electrophilic carbon on the arm. Cesium carbonate is typically used as the base in alkylations due to its high polarizability and when coupled with a polar aprotic solvent such as acetonitrile, its increased basicity facilitates C – N bond formation, thus it is common practice to use Cs₂CO₃ as the base for these reactions.⁷⁸ However, due to its large ionic radius, cesium has the lowest solvation in organic solvents. After multiple attempts in generating sufficient quantities of **3-4** using Cs₂CO₃ as the base, other bases were considered in order to improve their utility. Potassium carbonate is another common base that is used in alkylation reactions, and with its smaller ionic radius, has slightly higher solubility in organic solvents. Triethylamine is an organic base that effectively abstracts free protons and is

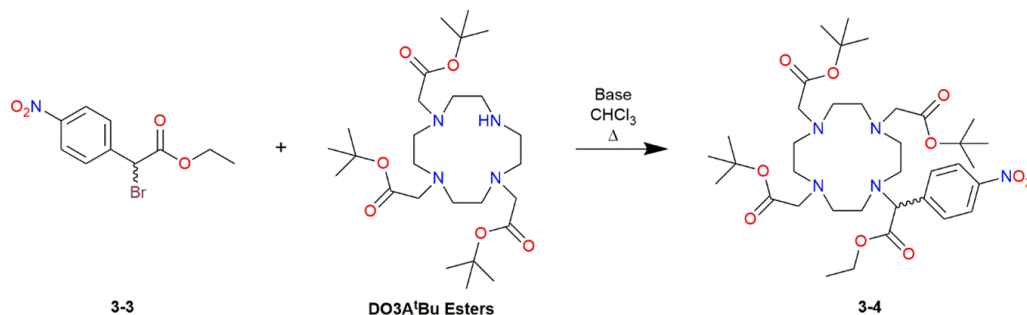
completely soluble in organic solvents. In the multivariable approach described in Table 3.1, both potassium carbonate and triethylamine were explored as bases.

Acetonitrile is a common S_N2 solvent for alkylations. However, many alkylations involving α -substituted alkylating agents report using chloroform as the solvent system. After multiple iterations utilizing acetonitrile as the solvent in the alkylation of DO3A-*tert*-butyl esters with **3-3**, changing the solvent to chloroform was done in the multivariable approach described in Table 3.1.

With preliminary alkylation attempts following the traditional reaction conditions of Cs_2CO_3 and acetonitrile, product formation was monitored by ESI-MS. We originally hypothesized this reaction was slower than previous alkylations; the sterics of a phenyl on an α -carbon are increased in comparison to the benzyl group observed with DO3A-NBAM synthesis. Thus, the reaction was tested at intervals of 24 hours by ESI-MS. However, we observed product degradation after reactions left for longer than 48 hours. As a result, for the multivariable approach, we stopped reactions at the 48-hour mark.

The variable reaction conditions are described in Table 3.1. Product formation was monitored by ESI-MS where the percent formation is compared to the percent of starting ligand DO3A-*tert*-butyl esters.

Table 3.1. Multi-variable approach to synthesis of the protected ligand (3-4) percent product formation after 24- and 48-hour reaction times.

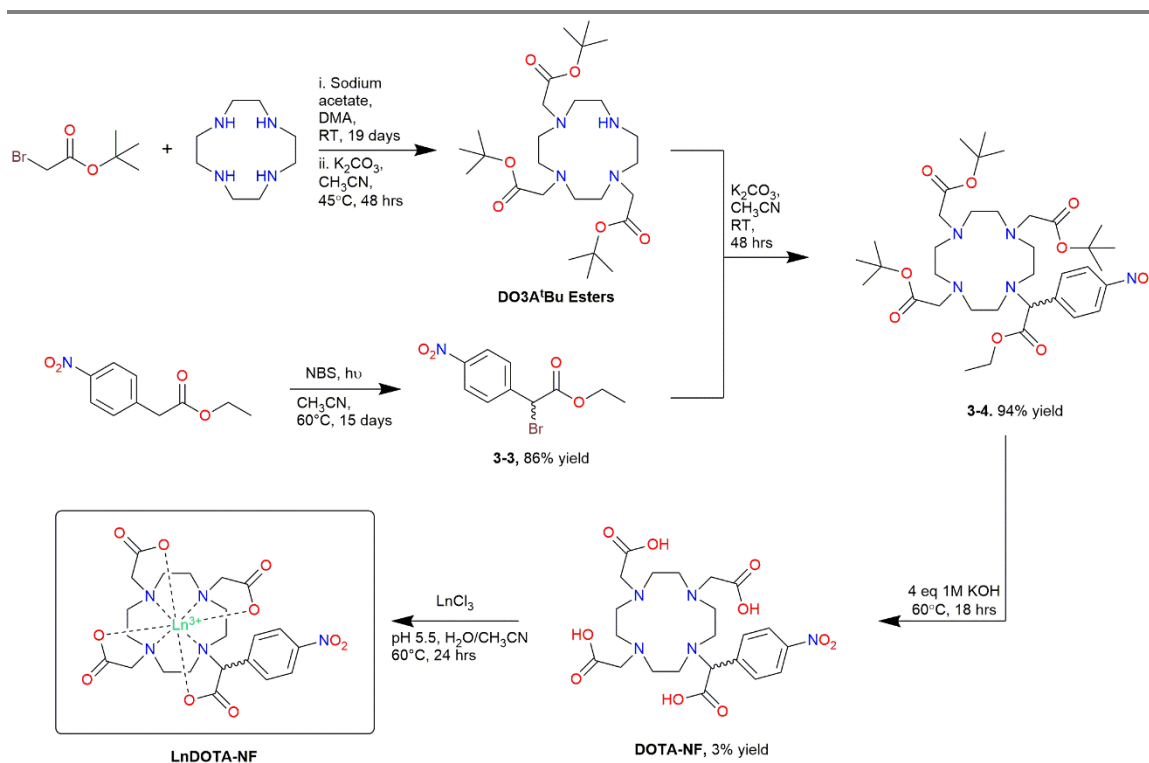


Base	Potassium Carbonate		Triethylamine		None	
RXN Time	60 °C	*20 °C	60 °C	*20 °C	60 °C	*20 °C
24 Hours	25%	57%	21%	22%	1%	1%
48 Hours	46%	66%	14%	38%	1%	1%

*Approximate reaction temperature

The results of this multivariable experiment were unexpected. The presence and type of base made a large impact; with the reactions containing no base having 1% product formation at both time points. Although triethylamine is more soluble in chloroform than potassium carbonate, the inorganic base had a higher product formation at both time points. The most surprising result is the reaction temperature. Under typical alkylation conditions, the reactions are heated between 40 °C and 70 °C, common practice is a reaction temperature of 60 °C. However, both base-containing reactions had higher product formation at both time points at the ambient reaction temperature (~20 °C). We are unsure as to why the lower temperature yielded more product, yet this experiment demonstrates that temperature had the greatest impact on product formation.

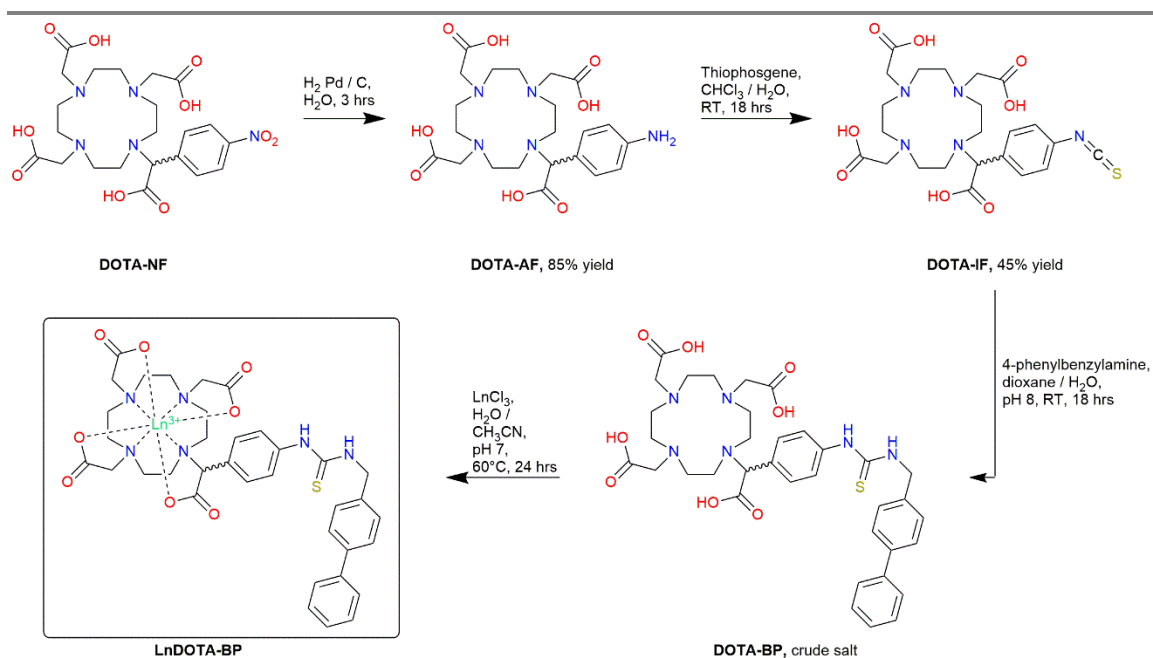
As a result of this multivariable approach, for optimal yield the final reaction conditions for alkylation of DO3A-*tert*-butyl esters with **3-3** utilized chloroform as the solvent, potassium carbonate as the base, at room temperature. After alkylation, to yield the protected ligand **3-4**, the *tert*-butyl esters and ethyl ester were hydrolyzed with potassium hydroxide, and the ligand was purified *via* RP-HPLC to generate the ligand **DOTA-NF**. The purified ligand was then chelated with lanthanide chlorides (Eu and Gd) with acetonitrile and water at 60 °C and pH 5.5, then purified *via* RP-HPLC to yield a clean chelate (**LnDOTA-NF**). The new total synthesis of LnDOTA-NF chelates is shown in Scheme 3.5.



Scheme 3.5. Total synthesis of LnDOTA-NF chelates. (Ln = Eu, Gd).

3.3.2. Synthesis of Biphenyl-Substituted α -Carbon Pendant Arm Chelates (LnDOTA-BP)

The biphenyl ligand, **DOTA-BP**, was synthesized using the same sequence of reactions as DO3A-BPAM, Scheme 3.6. DOTA-BP was chelated under the traditional conditions of chelation; a mixture of acetonitrile and water heated at 60 °C and pH 5.5, the crude chelation mixture was then purified *via* RP-HPLC to yield a pure product, LnDOTA-BP.



Scheme 3.6. Synthesis of LnDOTA-BP chelates. (Ln = Eu, Gd).

3.4. Analysis of the Three Nitro-Substituted Chelates

Analysis of the ^1H -NMR spectra of the europium complexes of each nitro-substituted chelate *via* line fitting in NUTS of the axial protons of the macrocycle affords the determination of the coordination geometry ratios. The percent square antiprism (SAP)

coordination geometry is shown in Table 3.2. As described previously, the SAP coordination geometry results in a shorter bond distance between the metal and the water molecule, and thus slower water exchange (k_{ex}).⁷⁹ Based on this, we would expect GdNB-DOTA Side with 45% SAP to have the fastest exchange, and the Corner isomer to have the slowest water exchange of the four isomers. However, another influencing factor is the coordinating ligands. GdDO3A-NBAM containing one neutral amide ligand will donate less electron density than its acetate counterparts, and as described earlier, will result in slower exchange. This coupled with its high SAP ratio would most likely result in the slowest water exchange of the four chelates.

Table 3.2. Structures of the parent complex EuDOTA and the three substitution strategies: Macrocycle (EuNB-DOTA), Monoamide Pendant Arm (EuDO3A-NBAM), and α -Carbon Pendant Arm (EuDOTA-NF), with their percent of SAP coordination geometry.

Chelate	EuDOTA	EuNB-DOTA		EuDO3A-NBAM	EuDOTA-NF
		Corner	Side		
MW	552.35	687.47		687.50	673.45
% SAP	85	95	45	91	65

After synthesis of the gadolinium complex of DO3A-NBAM, it was sent to our collaborator Professor Mauro Botta at the University of Eastern Piedmont Amedeo Avogadro in Torino, Italy where ¹⁷O-NMR and NMRD profiles were generated. The fitted Nuclear Magnetic Relaxation Dispersion (NMRD) profile and variable temperature ¹⁷O-

NMR transverse relaxation rate (R_{2p}) profile for this complex are shown in Figure 3.4. The NMRD profiles and ^{17}O -NMR R_{2p} profiles for GdNB-DOTA Corner and Side are shown in Chapter 2. The fitted data were then entered into SBM theory to generate relaxometric data, shown in Table 3.3. The fitted relaxometric data for GdDOTA, GdNB-DOTA Corner and Side, and GdDOTA-NF are included in Table 3.3 to allow for comparison.

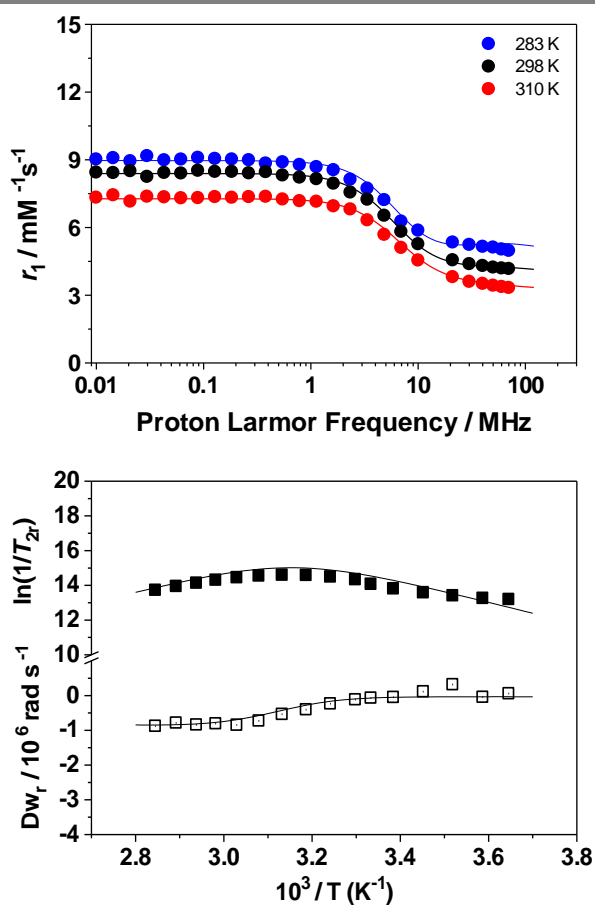


Figure 3.4. relaxivity as a function of magnetic field strength (NMRD profile) of GdDO3A-NBAM (Left), and the temperature dependence of the reduced ^{17}O NMR transverse relaxation rate (■), and chemical shift (□) measured at 67.8 MHz (Right).

Table 3.3. Calculated relaxometric values from the fitted ^{17}O -NMR R_{2p} and NMRD profiles of GdDOTA, GdNB-DOTA, GdDO3A-NBAM, and GdDOTA-NF, at 298 K and 20 MHz.

[†]Values from Aime *et. al.*⁵¹

Chelate	[†] GdDOTA	GdNB-DOTA		GdDO3A-NBAM	GdDOTA-NF
		Corner	Side		
τ_M (ns)	261	188*	12.4*	463* \pm 52	140*
ΔH_M (kJ·mol ⁻¹)	58.1	45.7	37.2*	51.3 \pm 3.0	50.0
τ_R (ps)	66	90	120	67	90
ΔH_R (kJ·mol ⁻¹)	16.1 \pm 7.4	17	16	17	16.9
τ_V (ps)	7.7	19.7	18	13.2	8.3
Δ^2 ($\cdot 10^{19} \text{ s}^{-2}$)	1.6	0.86	1.2	5.6	3.5
A_Q/\hbar ($\cdot 10^6 \text{ rad}\cdot\text{s}^{-1}$)	-3.7	-3.4	-3.5	-3.4 \pm 0.2	-3.0
$\diamond r_{\text{GdH}}$ (Å)	3.02	3.005	3.055	3.0	3.0
r_1 (mM ⁻¹ s ⁻¹)	4.6	5.8	6.1	4.4	5.4

*Weighted average of SAP and TSAP, [†]SAP,

\diamond Fixed in fitting procedure.

Fixed values: $q = 1$, $D_{\text{GdH}}^{298} = 22.4 \cdot 10^{-10} \text{ m}^2\text{s}^{-1}$, $\Delta H_V = 1.0 \text{ kJ}\cdot\text{mol}^{-1}$.

At high fields, the major influence on relaxivity is the rotational correlation time, τ_R . If chelates tumble too quickly in solution they are unable to effectively interact with and relax water molecules. All five of the chelates presented in Table 3.3 are considered low-molecular weight chelates, and as a result, their relaxivities will be limited by their rapid tumbling. The parent structure, GdDOTA has the lowest relaxivity of all five chelates. This is due primarily to size; the nitrobenzyl substituted chelates have higher

molecular weights and hydrodynamic volumes, and will tumble slower in solution than GdDOTA, resulting in their higher relaxivities. However, if we review the four nitrobenzyl-substituted chelates, they have vastly different tumbling rates, and thus relaxivities as illustrated in Figure 3.5. Yet, these chelates were designed to be as identical as possible; their structures differ by a methylene, and their molecular weights are within 14 units of each other. Thus, we would expect them to behave similarly in solution, and tumble at close to the same rate. Yet, even the Corner and Side isomers tumble differently, with the Side tumbling much slower than the Corner.

As described in detail in Chapter 2, it is evident the Side isomer self-associates in solution, resulting in a slower tumbling rate in comparison with the Corner. The τ_R value of GdDOTA-NF is the same as that of the Corner isomer of GdNB-DOTA. This leads us to hypothesize that it does not self-associate in solution and is in line with other small molecular weight chelates. GdDO3A-NBAM has shown no evidence of self-association and as a result, its τ_R is much shorter in comparison with NB-DOTA chelates. The differences in tumbling rates must arise from the location of the substituent on the DOTA scaffold. This in turn could cause the chelates to differ in terms of hydrodynamic the extent of self-association.

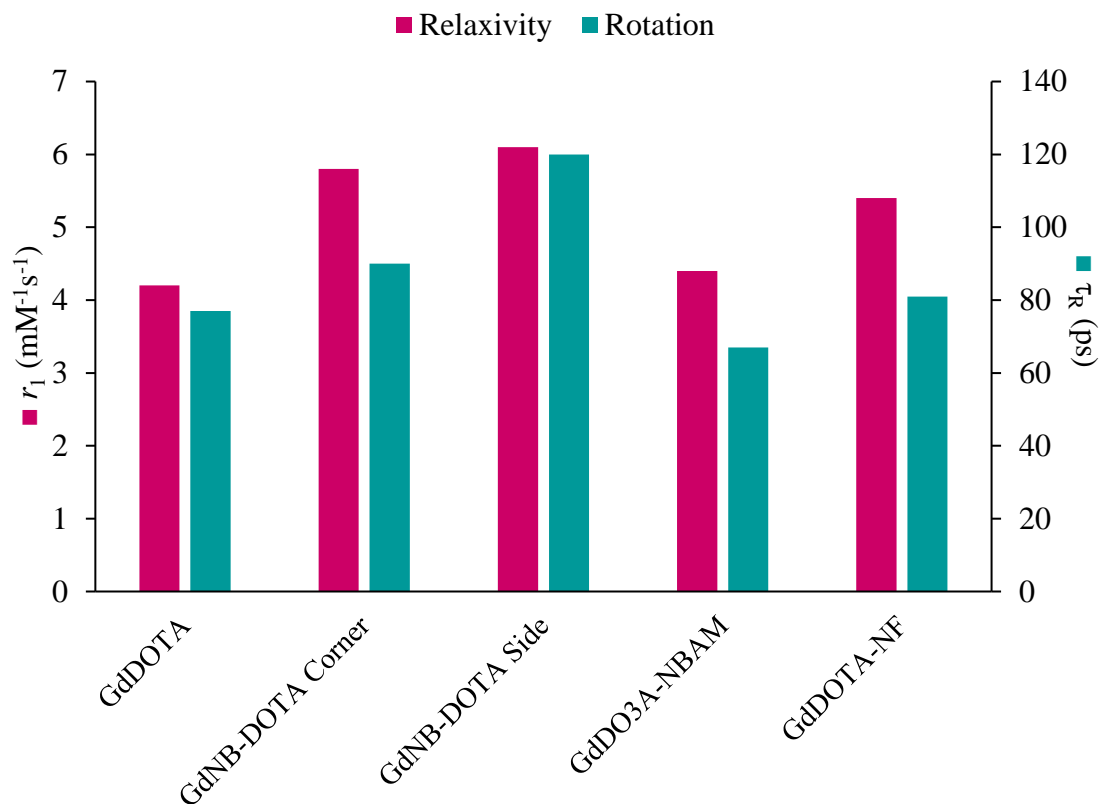


Figure 3.5. Relaxivities (\blacksquare r_1) and rotational correlation times (\blacksquare τ_R) of the four chelates examined herein, compared to the parent structure, GdDOTA, at 20 MHz and 298 K.

A secondary influence on relaxivity is the preferred coordination geometry of the chelate. With no moiety, GdDOTA has a preferred coordination of approximately 85% SAP.⁸⁰ The introduction of a nitrobenzyl group on the macrocycle, which generates two new regioisomers in which the substituent is on the Corner or Side carbon of the cycle, causes the coordination geometry to diverge. The Corner isomer increases to adopt a 95% preferred SAP geometry whereas the Side decreases to a 45% SAP conformation.⁸¹ This division of coordination geometry arises from a steric effect when substituting on the macrocycle; the equatorial position on the Side carbon is more sterically hindered, and

requires the chelate to adopt the taller cage of the TSAP geometry.⁵⁰ As stated previously, GdDO3A-NBAM has a high SAP conformation, this coincides with what is observed for amide-containing DOTA-based ligands, with chelates of DOTAM employing exclusively SAP conformation.⁸² GdDOTA-NF has been shown to have a slightly lower SAP conformation than its parent GdDOTA; although the major species, it exists only approximately 65% in the SAP geometry. This is in line with other α -substituted chelates; GdDOTMA adopts a 25% SAP coordination geometry.⁵¹ The increased sterics imparted by substituting on the α -carbon of each pendant arm results in the unusually high TSAP conformation of rigid tetra-methylated chelates. This effect is lessened in GdDOTA-NF due to only one arm being substituted. However, the bulkiness of a nitrophenyl group still imparts sterics on the ligand structure, thus increasing the preference to the TSAP geometry.⁷³

Because coordination geometry directly impacts the access of water molecules to the lanthanide center, it is no surprise that these chelates have drastically different τ_M values. The TSAP coordination geometry causes the water to be pushed away from the lanthanide center, resulting in faster exchange. The higher TSAP geometry of the Side awards it the shortest τ_M which results in a reduced hydration state (q/r^6) and directly impacts relaxometry (see Chapter 2). The Corner has a slower τ_M , considered slightly longer than optimal, and as a result has a relaxivity slightly lower than the Side.

As predicted, GdDO3A-NBAM has the longest water exchange lifetime (τ_M) of the five chelates, and therefore slowest water exchange rate (k_{ex}). The rate limiting step of a

dissociative exchange mechanism is breaking of the metal-ligand bond, with the reduced electron density of a monoamide coupled with high its high SAP ratio, results in a longer than optimal τ_M value, which therefore results in an expected low relaxivity. Yet, the relaxivity measured for GdDO3A-NBAM is comparable to GdDOTA; this is expected for chelates in the fast water exchange regime that are limited by τ_R .²⁹

Conversely, GdDOTA-NF has the second shortest τ_M of the chelates surveyed. Its faster water exchange is not so fast that it would suffer from a reduction in hydration state (q/r^6) like observed in GdNB-DOTA Side. From the perspective of water exchange, GdDOTA-NF has the highest potential of optimal relaxometry. However, the true impact of water exchange kinetics is not fully appreciated while these chelates are dominated by the effects of rotation (τ_R).

It is impossible to truly probe the impact water exchange kinetics has on efficacy whilst these chelates are small, due to the overwhelming influence of τ_R . At higher magnetic field strengths, theory dictates optimal rotational correlation time to be in the nanosecond range, while all four of these chelates have τ_R values in the picosecond range.³⁴ Therefore, to fully appreciate the impact of τ_M on relaxivity, the rate of tumbling must be reduced by ligand modification. The addition of a bulky biphenyl group to the ligand structure allows us to lift the barrier of τ_R , and fully probe how the point of moiety attachment impacts τ_M and ultimately relaxivity.

3.5. Analysis of the Three Biphenyl-Substituted Chelates

To allow for molecular tumbling to be slowed, a bulky biphenyl moiety was attached to each of the three studied structures. This allowed for a thorough analysis on how attachment strategy influences relaxometry.

3.5.1. Critical Micelle Concentration Studies

After synthesis of the gadolinium complexes of DO3A-NBAM and BP-DOTA Corner and Side, they were sent to our collaborator Professor Mauro Botta at the University of Eastern Piedmont Amedeo Avogadro in Torino, Italy where ^{17}O -NMR and NMRD profiles were generated. The fitted Nuclear Magnetic Relaxation Dispersion (NMRD) profiles for GdDO3A-NBAM below the critical micelle concentration (CMC) and above the CMC are shown in Figure 3.6. The fitted NMRD profiles for GdBP-DOTA Corner and Side are shown in Chapter 2. The gadolinium complex of DOTA-BP has been sent to Professor Mauro Botta, however due to the COVID-19 outbreak, ^{17}O -NMR and NMRD profiles are still in the process of collection.

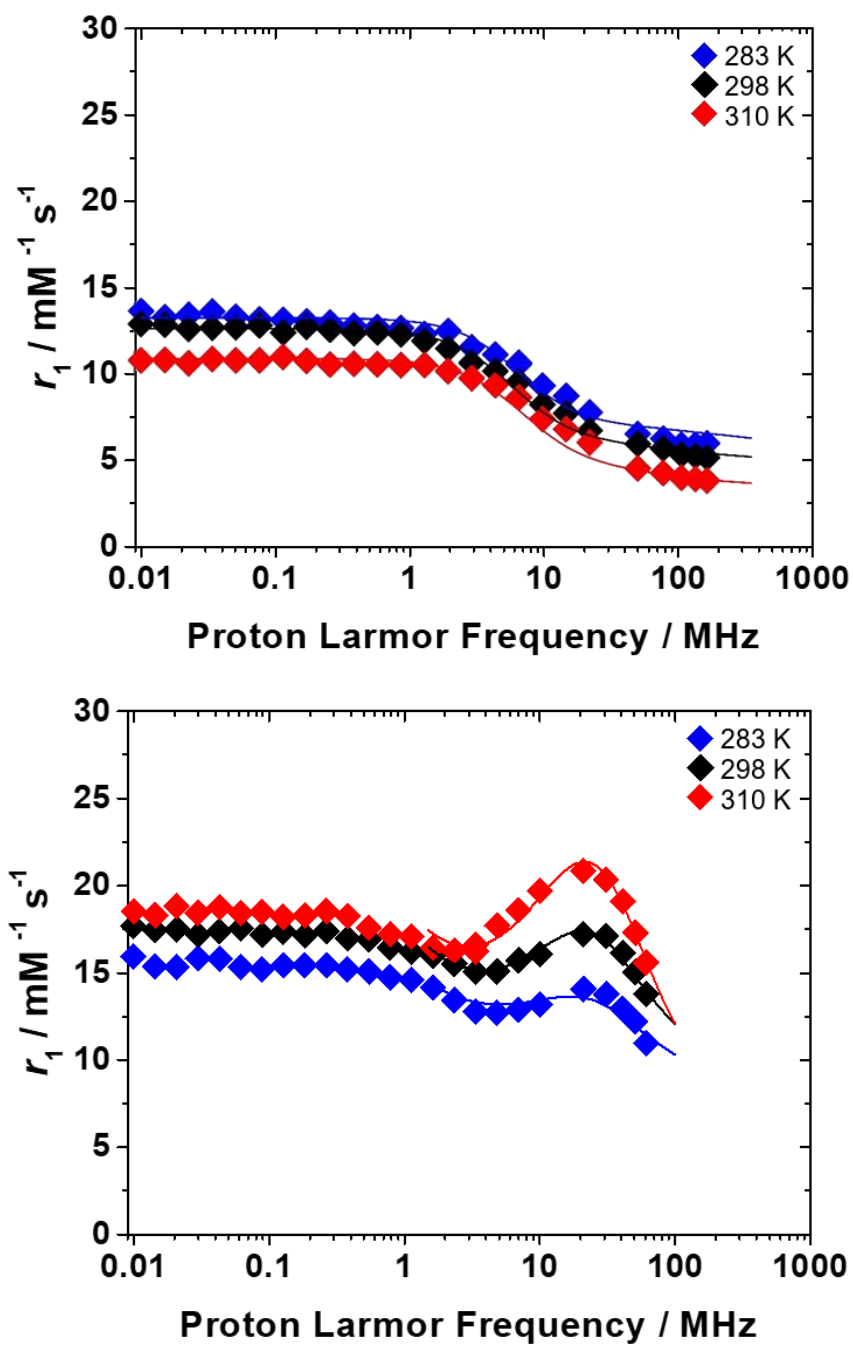


Figure 3.6. NMRD Profiles of GdDO3A-BPAM below its CMC (Top), and above its CMC (Bottom).

The CMC is the concentration at which a chelate forms a micelle in solution. Amphiphilic chelates will spontaneously form micelles in solution at a specific concentration, where their hydrophobic moieties will pre-assemble due to repulsive interactions with their hydrophilic counterparts.⁸³

The CMC is determined by measuring the relaxation rate (R_1) of the solution while titrating in the chelate, the inflection point is the CMC. The measured R_1 for each chelate, GdBP-DOTA Corner, Side, and GdDO3A-BPAM were fitted to Equation 3.1 after collection, shown in Figure 3.7 and Table 3.4. Forming a micelle in solution slows down molecular tumbling and allows for the barrier of τ_R to be lifted, and the true impact of τ_M on relaxivity can be explored.

As shown in Table 3.4, GdDO3A-BPAM forms micelles at a lower concentration than the Corner or Side isomer of GdBP-DOTA. A difference in CMC typically arises due to size of the discrete chelate; CMC decreases with increasing size.⁸⁴ Yet, these three chelates have nearly identical molecular weights and hydrodynamic volumes. These data suggest that the orientation of the monoamide pendant arm is such that the structure of GdDO3A-BPAM is larger than both isomers of GdBP-DOTA, resulting in a lower CMC. Secondly, GdDO3A-BPAM forms smaller micelles compared to both isomers of GdBP-DOTA. This coupled with an already known longer than optimal τ_M , would result in GdDO3A-BPAM to have lower than optimal relaxivity.

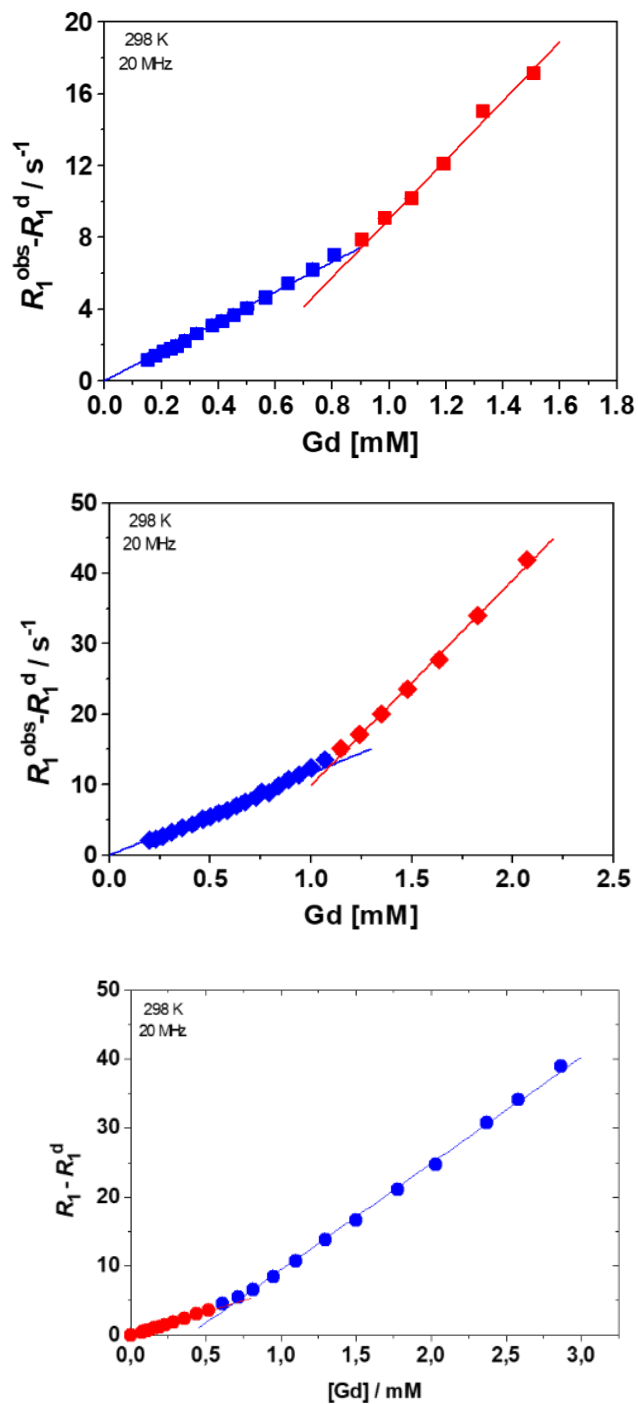


Figure 3.7. Determination of the critical micelle concentration (CMC) of GdBP-DOTA Corner (■ Top), Side (◆ Center), and GdDO3A-BPAM (● Bottom).

$$R_1^{\text{obs}} - R_1^{\text{d}} = R_{1\text{p}} = (r_1^{\text{n.a.}} - r_1^{\text{a}}) \times \text{CMC} + r_1^{\text{a}} \times C$$

Equation 3.1. Equation to determine critical micelle concentration, R_1^{obs} = measured longitudinal relaxation rate constant in the presence of the chelate, R_1^{d} = measured relaxation rate constant in the absence of the of chelate, $r_1^{\text{n.a.}}$ = relaxivity of the non-aggregated chelate, r_1^{a} = relaxivity of the aggregated chelate, C = concentration of the chelate.

Table 3.4. Critical micelle concentrations (CMC), micelle diameters, and relaxivities above their respective CMCs for GdBP-DOTA Corner and Side isomers, and GdDO3A-BPAM, at 298 K and 20 MHz.

Chelate	GdBP-DOTA		GdDO3A-BPAM
	Corner	Side	
CMC (mM)	0.90	1.10	0.68
Micelle Diameter (nm)	10	18	4
r_1 Above CMC ($\text{mM}^{-1}\text{s}^{-1}$)	16.4	29.2	15.4

The fitted relaxometric data for GdDO3A-BPAM were entered into SBM theory to generate relaxometric data, shown in Table 3.4. To determine relaxivity above the CMC, the traditional SBM theory is not sufficient due to the impact of local and global rotation. The Lipari–Szabo approach is used to determine the influence of each of these rotational motions on relaxivity, shown in Table 3.4. A combined NMRD profile for all three chelates above their respective CMC values is shown in Figure 3.8. The fitted relaxometric data generated for GdBP-DOTA Corner and Side, and GdDO3A-BPAM below their respective CMCs is shown in Table 3.5.

Table 3.5. Calculated relaxometric values from the fitted ^{17}O -NMR R_{2p} and NMRD profiles of GdBP-DOTA Corner and Side isomers, and GdDO3A-BPAM, below their respective CMCs, at 298 K and 20 MHz.

Chelate	GdBP-DOTA		GdDO3A-BPAM
	Corner	Side	
τ_M (ns)	188*	12.4*	463*
τ_R Global (ps)	130	190	131
τ_V (ps)	19	17	25
Δ^2 ($\cdot 10^{19} \text{s}^{-2}$)	1.10	1.08	1.4
$\diamond r_{\text{GdH}}$ (Å)	3.005	3.055	3.0
r_1 ($\text{mM}^{-1}\text{s}^{-1}$)	8.3	11.6	6.7

*Weighted average of SAP and TSAP.

\diamond Fixed in fitting procedure.

Fixed values: $q = 1$, $D_{\text{GdH}}^{298} = 22.4 \cdot 10^{-10} \text{ m}^2\text{s}^{-1}$, $\Delta H_V = 1.0 \text{ kJ}\cdot\text{mol}^{-1}$.

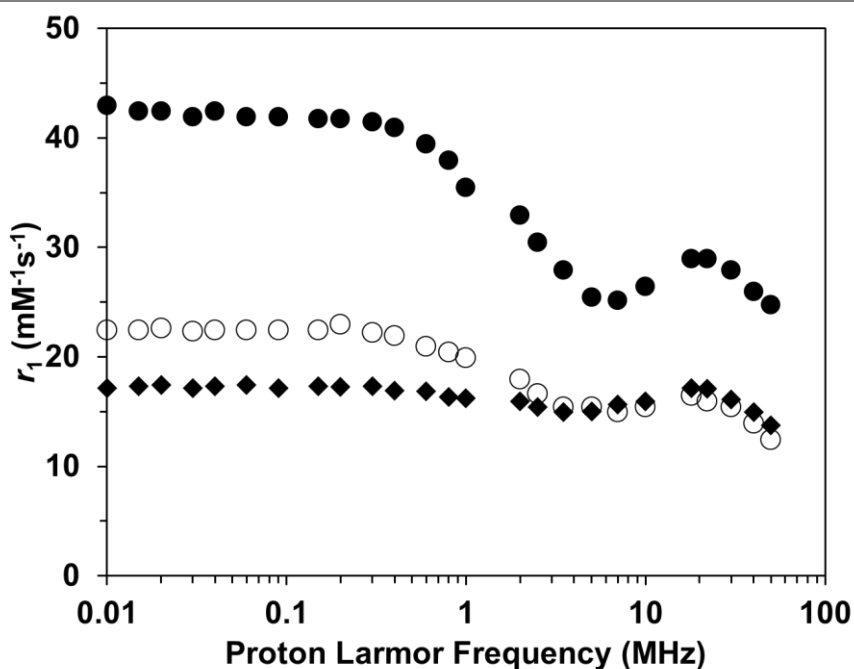


Figure 3.8. NMRD profiles of GdBP-DOTA Corner (○), GdBP-DOTA Side (●), and GdDO3A-BPAM (◆) above their respective CMC values, at 298 K.

Above the CMC, the water molecules organize into a hydration shell, therefore the water exchange that is measured is not the typical mechanism observed for a small molecular weight chelate. Instead, the water molecule bound to the chelate exchanges with one in the pre-organized layer, rather than the bulk water outside the micelle. Thus, we see a much longer τ_M above the CMC for all three of these chelates. The impact of micellar formation is seen most strikingly on rotation. Above the CMC, rotation slows to the nanosecond range; according to SBM theory, this drastically slowed tumbling rate will give rise to higher relaxivity values. Additionally, by lifting the barrier of τ_R , we see the impact water exchange has on relaxivity. The fitted relaxometric values of GdDO3A-BPAM above its CMC are shown in Table 3.6.

Table 3.6. Relaxometric data from the fitted ^{17}O -NMR and NMRD profiles of GdDO3A-BPAM above its CMC value, at 298 K and 20 MHz.

GdDO3A-BPAM Above the CMC	
τ_M (ns)	721 \pm 130
ΔH_M (kJ \cdot mol $^{-1}$)	53.1
τ_R Global (ps)	5400 \pm 200
ΔH_R (kJ \cdot mol $^{-1}$)	17
τ_V (ps)	20
Δ^2 ($\cdot 10^{19}$ s $^{-2}$)	0.41
A_0/\hbar ($\cdot 10^6$ rad \cdot s $^{-1}$)	-2.9
$\blacklozenge r_{\text{GdH}}$ (Å)	3.0
r_1 (mM $^{-1}$ s $^{-1}$)	15.4

*Weighted average of SAP and TSAP.

\blacklozenge Fixed in fitting procedure.

Fixed values: $q = 1$, $D_{\text{GdH}}^{298} = 22.4 \cdot 10^{-10}$ m 2 s $^{-1}$, $\Delta H_V = 1.0$ kJ \cdot mol $^{-1}$.

Both below and above the CMC GdDO3A-BPAM has a much longer τ_M when compared to the Corner and Side isomers of GdBP-DOTA. This results in the chelate falling out of the fast water exchange regime. Although its relaxivity value above the CMC is similar to the Corner isomer of GdBP-DOTA, they cannot be compared directly due to the different sizes of their micelles. Though GdDO3A-BPAM forms the smallest micelles, its global rotation (τ_R) decreased significantly. This slowed tumbling results in the increased relaxivity of GdDO3A-BPAM, however the benefits of slowed tumbling resulting in higher relaxivities cannot be fully achieved while this chelate exchanges water so slowly.

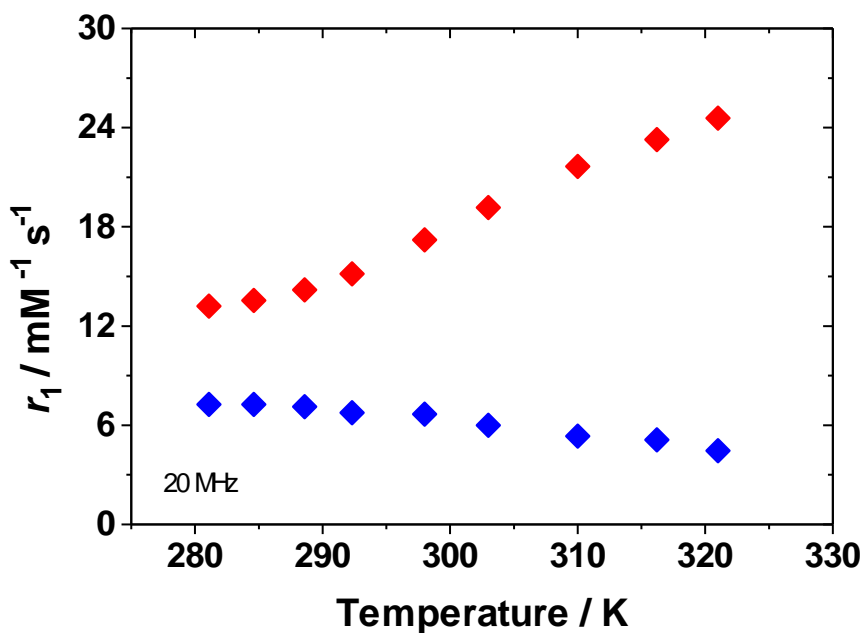


Figure 3.9. Temperature dependence of relaxivity for GdDO3A-BPAM below the CMC (Blue) and above the CMC (Red).

This is highlighted when observing the relaxivity as a function of temperature, Figure 3.9. As temperature increases, GdDO3A-BPAM has a reduction in relaxivity below

the CMC, however, above the CMC relaxivity increases. This opposition of observed relaxivity arises from differing water exchange regimes for this chelate. When chelates increase in size, their molecular tumbling slows. The reduction in τ_R causes the chelate to fall out of the fast water exchange regime, as observed above the CMC. τ_R gets shorter with increasing temperature resulting in a decrease in relaxivity if the chelate is in the slow exchange regime. However, if the relaxivity increases with increasing temperature, exchange is fast enough that an increase in τ_R can maintain the chelate in the fast exchange regime. Referring to the SBM Mountain Plot described in Chapter 1, τ_M and τ_R can be a wide range of values without influencing a major change in relaxivity. However, as relaxivity is increased, the values of τ_M and τ_R have a much narrower range for optimal relaxivity. Thus, when water exchange is slowed like in GdDO3A-BPAM, it falls out of the range to have the highest relaxivity. This limits the functionality of GdDO3A-BPAM as an effective contrast agent.

Comparing these three chelates above their CMC values demonstrates the influence τ_M has on relaxivity. GdDO3A-BPAM has much too slow water exchange to be considered optimal. In contrast, the Side isomer of GdBP-DOTA has much too fast water exchange, resulting in a reduced hydration state of the chelate, which in turn limits its efficacy. GdBP-DOTA Corner has a water exchange rate that is slightly slower than optimal, and we hypothesize the GdDOTA-BP will have a k_{ex} slightly closer to optimal. We can mimic the effects of k_{ex} on bioconjugate efficacy by incorporating these chelates into a large macromolecule, poly- β -cyclodextrin. Then, we can truly compare the impact of too slow water exchange (GdDO3A-BPAM), versus a reduced hydration state (GdBP-DOTA Side).

3.5.2. Incorporation into Poly- β -Cyclodextrin

Dilute solutions of GdDO3A-BPAM, GdBP-DOTA Corner, and GdBP-DOTA Side were prepared and poly- β -cyclodextrin, a macrocyclic oligosaccharide, was titrated in. The longitudinal relaxation rate was collected at 20 MHz and 298 K, Figure 3.10. The biphenyl moieties on these chelates has been shown to bind with the polysaccharide and can provide information on the binding affinity. Next, NMRD profiles for these three chelates incorporated into poly- β -cyclodextrin were collected, Figure 3.11. The fitted profiles were used to generate relaxometric data, Table 3.7.

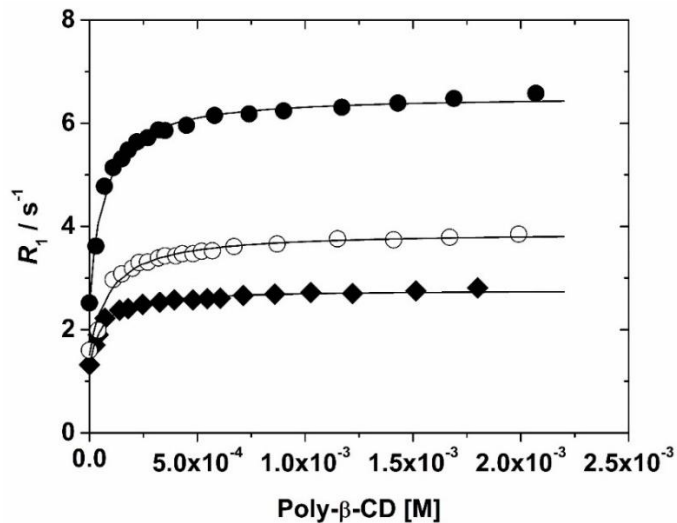


Figure 3.10. Longitudinal relaxation rates for the three chelates GdBP-DOTA Corner (O), GdBP-DOTA Side (\bullet), and GdDO3A-BPAM (\blacklozenge), as a function of concentration of poly- β -cyclodextrin, at 298 K and 20 MHz.

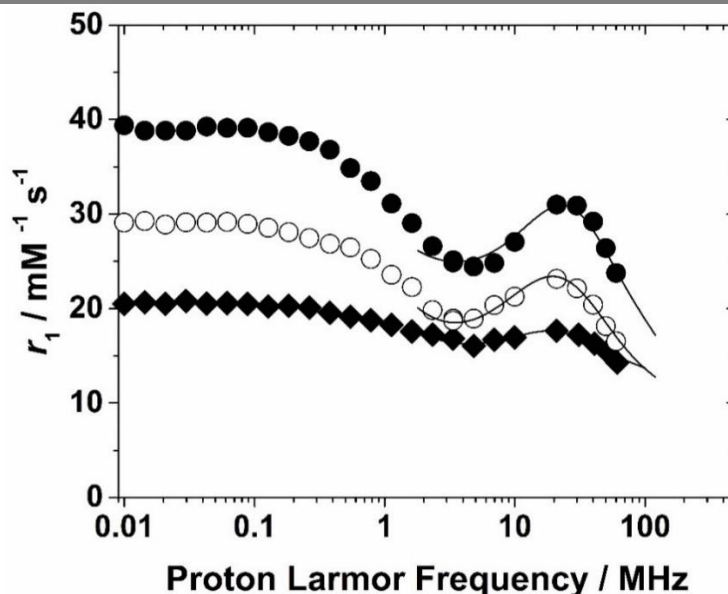


Figure 3.11. Fitted NMRD profiles of GdBP-DOTA Corner (O), GdBP-DOTA Side (●), and GdDO3A-BPAM (◆) conjugated with poly- β -cyclodextrin, at 298 K.

Table 3.7. Calculated relaxometric values from the fitted ^{17}O -NMR R_{2p} and NMRD profiles of GdBP-DOTA Corner, GdBP-DOTA Side, and GdDO3A-BPAM incorporated with poly- β -cyclodextrin at 298 K and 20 MHz.

Chelate	GdBP-DOTA with poly- β -CD		GdDO3A-BPAM with poly- β -CD
	Corner	Side	
K_a (mM^{-1})	1.075 ± 0.105	1.580 ± 0.092	1.740 ± 0.130
◆ τ_M (ns)	188*	12.4*	463*
τ_R Global (ps)	4100 ± 200	4100 ± 200	4100 ± 200
τ_R Local (ps)	330 ± 20	640 ± 20	410 ± 30
τ_V (ps)	23 ± 1	13 ± 2	15 ± 2
Δ^2 ($\cdot 10^{19} \text{s}^{-2}$)	0.36	0.37	0.3
◆ r_{GdH} (\AA)	3.005	3.055	3.0
r_1 Bound ($\text{mM}^{-1}\text{s}^{-1}$)	23.4 ± 0.3	30.8 ± 0.2	17.1 ± 0.1

*Weighted average of SAP and TSAP.

◆ Fixed in fitting procedure.

Fixed values: $q = 1$, $D_{\text{GdH}}^{298} = 22.4 \cdot 10^{-10} \text{ m}^2\text{s}^{-1}$, $\Delta H_V = 1.0 \text{ kJ}\cdot\text{mol}^{-1}$.

The NMRD data were fitted using the SBM equations as well as the Lipari–Szabo approach to generate their relaxivities as bound bioconjugates at 20 MHz and 298 K, Table 3.7. The binding affinities of the chelates to poly- β -cyclodextrin were determined using a 1:1 binding model. These data show that the binding affinity to poly- β -cyclodextrin is much higher for GdDO3A-BPAM in comparison with the Corner and Side isomers. Because all three of these chelates have the same biphenyl hydrophobic moiety that will interact with poly- β -cyclodextrin, the differentiation between binding constants must arise from another characteristic of the chelate.

As described in Chapter 2, the Side isomer of GdBP-DOTA has a preferred TSAP coordination geometry, this would most likely cause it to interact with poly- β -cyclodextrin in a different fashion than its Corner counterpart.⁷⁵ It has been observed that the neutral carbonyl of a monoamide has shown to bring the poly- β -cyclodextrin moiety closer to the lanthanide, resulting in a higher binding affinity.⁸⁵ This could account for the higher binding affinity seen in GdDO3A-BPAM. Tightness of binding correlates to longer τ_R values due to the contributions of both local rotation of the chelate within the bioconjugate and global rotation of the entire system.

Although GdDO3A-BPAM has lower relaxivity in comparison to both isomers of GdBP-DOTA, this value does not take into consideration the impact a higher binding affinity has on the change in the observed relaxation rate constant (R_1). To probe how this would impact the contrast seen on an image clinically, we can calculate the change in ΔR_1 using Equation 3.2. If the total concentration of gadolinium is fixed to a typical clinical

dose (0.1 mM), and it is assumed that any unbound bioconjugate is cleared and does not contribute to relaxation, it is evident that GdDO3A-BPAM with its lower relaxivity imparts a large change on the observed R_1 , as shown in Table 3.8. Although the greatest change is observed in the Side isomer of GdBP-DOTA, this only constitutes 25% of the total mixture, and the lower contribution of the Corner would play into the overall observed change. Thus, the higher binding affinity of GdDO3A-BPAM would increase the signal intensity and thus overall generated image contrast.

$$\Delta R_1 = r_1 \times [\text{Gd}]$$

Equation 3.2. The measured difference in relaxation rate to determine contrast in an image, where r_1 is the relaxivity of the contrast agent in $\text{mM}^{-1}\text{s}^{-1}$ and $[\text{Gd}]$ is the concentration of gadolinium in mM.

Table 3.8. Mathematical determination of the binding affinity on the change in relaxation rate constant (ΔR_1), where K_a is the binding affinity, GdT is the concentration of the target dose of GBCA.

	GdBP-DOTA		GdDO3A-BPAM
	Corner	Side	
K_a (mM^{-1})	1.075	1.580	1.740
GdT (mM)	8.92×10^{-3}	1.22×10^{-2}	1.31×10^{-2}
r_1 ($\text{mM}^{-1}\text{s}^{-1}$)	23.4	30.8	17.1
ΔR_1 (ms)	208.7	375.3	224.5

3.6. Conclusions and Future Directions

When designing a bifunctional chelator, it is important to recognize the impact the mechanism of substitution as well as position of the targeting vector has on relaxivity. The three main functionalization strategies, off a macrocycle, through a monoamide pendant

arm, and on an α -carbon on a pendant arm, represented by GdNB-DOTA, GdDO3A-NBAM, and GdDOTA-NF, respectively, highlight the relaxometric influence of substitution on the DOTA scaffold. We have demonstrated that substitution alters coordination geometry, and as a result, water exchange kinetics. For optimal relaxivity, the ideal water exchange rate is a finite range. These values can be tuned by altering the chemical structure of the ligand, and therefore care must be taken when selecting a substitution position on the macrocycle.

Our results comparing these three strategies highlight the impact the point of attachment dramatically influences relaxometric properties. The two monoamide derived chelates both exhibited slow water exchange due to the nature of a coordinating amide pendant arm. This slowed exchange will be a limiting factor on relaxivity once the barrier of τ_R is lifted and the chelate is incorporated into a bioconjugate. Both the Corner and Side isomers of the macrocycle substituted chelates had some advantageous properties; the slowed molecular tumbling of the Side isomer results in an increased relaxivity, but this is limited by the fact it also suffers from a reduced q/r^6 , and comprises only 25% of the solution mixture. We therefore conclude that neither the macrocycle substitution strategy nor the monoamide substitution strategy will result in the ideal scaffold for a BFC. The α -carbon pendant arm strategy resulted in a high relaxivity, slowed molecular tumbling, as well as a water exchange rate that is fast but does not cause a reduction in q/r^6 . More information will be available for a full comparison, but we hypothesize the data generated for the biphenyl derivative of this strategy will result in the highest relaxivity.

CHAPTER 4

TETRA α -CARBON SUBSTITUTION:

SYNTHESIS & RELAXOMETRY

4.1. Substitution on the α -Carbon Pendant Arm of DOTA

With the increasing utility of DOTA chelates, researchers began altering the structure by substitution of moieties and examining their effects. DOTMA, in which a methyl group is installed on each α -carbon of the pendant arm, was first described by Brittain and Desreux in 1984.⁸⁶ Further substitution patterns were synthesized, with the most common α -substituted chelates being the various mono, tri and tetra-substituted ligands shown in Figure 4.1.^{73,87-89}

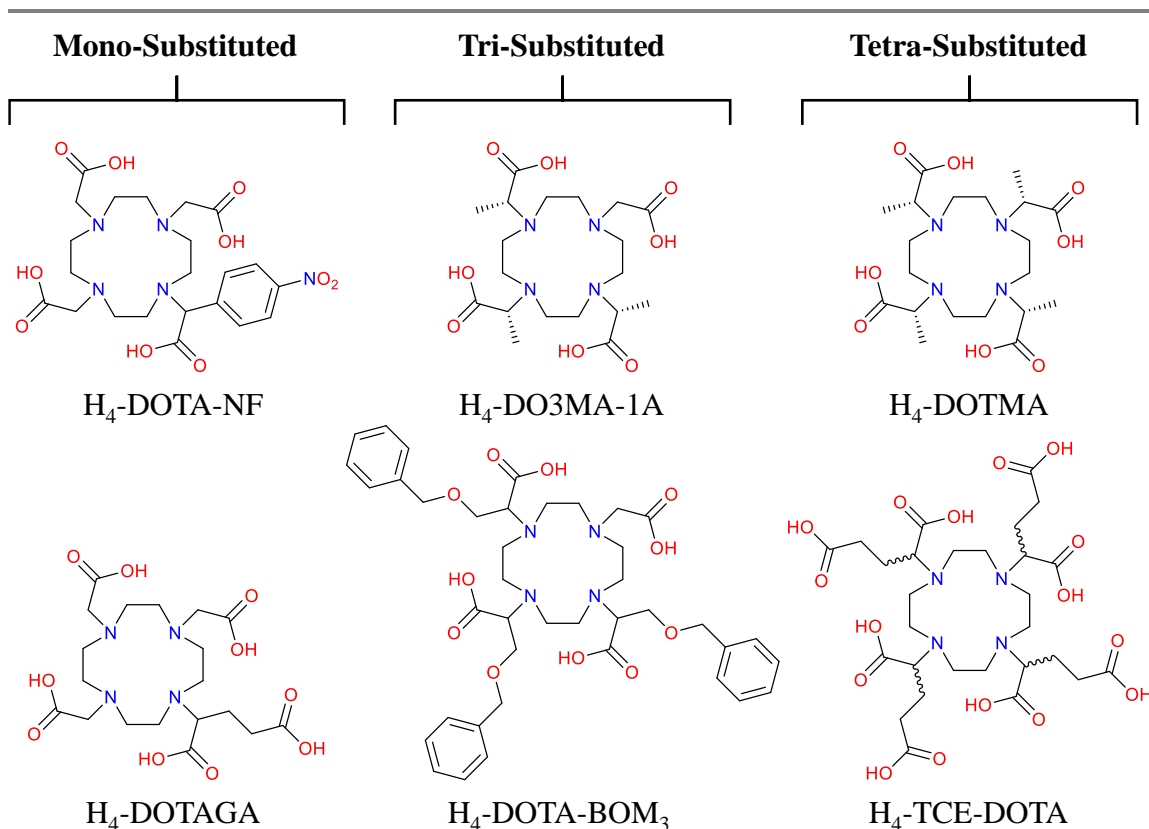


Figure 4.1. Common pendant arm α -substituted ligands. The introduction of a substituent on the α -carbon of a pendant arm imparts a stereogenic center, some of which are selected for in stereospecific reactions, others result in a mixture of diastereoisomers or racemates.

4.2. Properties of α -Carbon Pendant Arm Substituted Chelates

The addition of a substituent on one or multiple α -carbon pendant arm has an impact on multiple functions of the chelate. The original investigations into DOTMA proved an opportunity to explore the impact the introduction of four chiral centers have on photophysical properties.⁸⁶ Whereas many researchers found the introduction of moieties on the α -carbon to impart a handle for functionalization or further optimization of relaxometric properties.⁸⁷ Although α -carbon substitution was not expected to change the

binding of a lanthanide to the ligand system, it was anticipated it would alter certain relaxometric properties. The effect tetra-substitution has on these properties is explored in the context of DOTMA chelates.

4.2.1. Stereochemistry of α -Carbon Pendant Arm Substituted DOTA Derivatives

Tetra-substitution of the pendant arms of DOTA introduces four new stereocenters. The lowest energy conformation for pendant arm α -carbon substitution is when all four arms maintain the same stereochemistry.⁹⁰ The notations for the helicity of the system are denoted as Λ or Δ for the pendant arms, and $\lambda\lambda\lambda\lambda$ or $\delta\delta\delta\delta$ for the conformation of the macrocycle. The helicity determines the coordination geometry of the ligand, with $\Lambda(\delta\delta\delta\delta)$ or $\Delta(\lambda\lambda\lambda\lambda)$ producing the SAP isomer, and $\Lambda(\lambda\lambda\lambda\lambda)$ or $\Delta(\delta\delta\delta\delta)$ producing the TSAP geometry. The introduction of a methyl group to each α -carbon pendant arm increases the preferential coordination geometry of DOTMA chelates to be predominately TSAP.

The DOTMA structure first introduced by Brittain and Desreux produced the most studied ligand today, the *RRRR*-enantiomer (Λ). The most facile synthesis involves an enantiospecific reaction of the amino acid alanine to synthesize the *S*-propionate arms, and subsequent S_N2 to alkylate onto 1,4,7,10-tetraazacyclododecane (cyclen), resulting in the arms retaining the same *RRRR* stereochemistry. Although four enantiomers of DOTMA are possible, two are inaccessible through arm rotation seen with DOTA; substitution on each pendant arm locks out the interconversion, Figure 4.2. This is due to the torsional strain introduced with α -carbon substitution. As a result, the ligand will preferentially substitute the methyl group *anti* to the lanthanide.

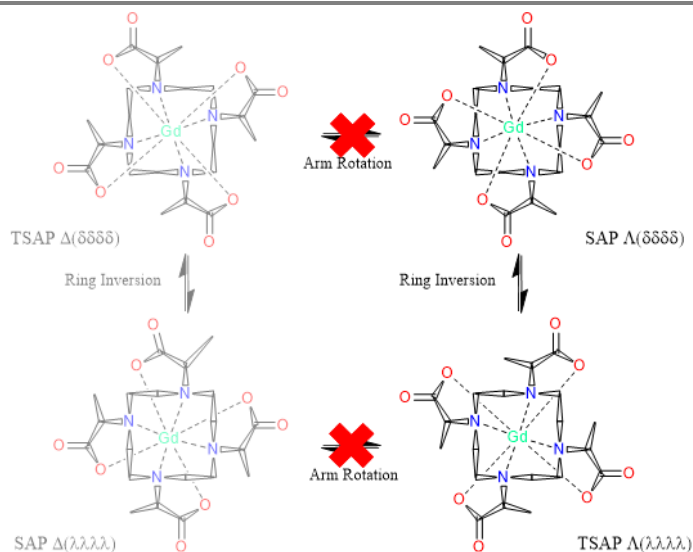


Figure 4.2. The four possible stereoisomers of GdDOTMA. The two structures with Δ arm helicity (left) are inaccessible from the Λ conformation (right) due to the α -substituted methyl groups freezing out arm rotation.

The Δ arm conformation is possible if starting from *R*-propionate arm starting materials, however, is much less common due to the expense associated with *R*-amino

acids. Beginning with racemic starting materials for the arms does not afford an enantiopure product. A study in which each pendant arm was equipped with a carboxyethyl arm showed the varying properties the four stereoisomeric products.⁸⁹ Interestingly, some of these structures were able to interconvert *via* arm rotation.

Although chelates of TCE-DOTA allowed researchers to glean insight into the various properties of diastereoisomers of a tetra α -carbon substituted structure, it is not the ideal model for a GBCA. These various structures will have differing chemical properties including kinetic inertness and relaxivity. Therefore, it is important to use a synthetic strategy that is stereospecific to result exclusively in the homochiral conformation. This affords the most kinetically robust structure.

4.2.2. *Water Exchange Kinetics*

As described by Webber and Woods, the impact of the exchange event on the structure of the ligand had not been fully appreciated.⁶⁴ The ligand undergoes a structural change when the water is bound versus unbound. When a water molecule is coordinated to the chelate, the ligand cage is open to accommodate the water. When the water leaves, the lanthanide sinks down in the cage simultaneously to its ionic radius decreasing. The cage collapses slightly around the metal center, causing a slightly closed conformation. This process repeats when a new water molecule coordinates to the metal. This dynamic process influences the mechanism of exchange observed for macrocyclic chelates and needs to be explored further.

As described with NB-DOTA chelates in Chapters 2 and 3, a higher ratio of TSAP in solution results in a very short water exchange lifetime, τ_M .⁶³ GdNB-DOTA Side exists 55% in the TSAP coordination geometry, and exchanges water very quickly, with a τ_M of 12.4 ns. GdDOTMA in contrast, exists 81% in the TSAP geometry and yet has τ_M of 85 ns.⁹¹

4.2.3. Relaxivity of α -Substituted Chelates

The introduction of a substituent on each α -carbon pendant arm has shown to have a drastic impact on coordination geometry as well as water exchange kinetics. However, the change in relaxivity is minimal. This is due to the overwhelming influence of chelate rotation, τ_R . As seen with previously explored small molecular weight chelates, the impact of ligand modification is only observed when the barrier of τ_R is lifted.

4.3. Synthetic Strategy of Tetra α -Carbon Substituted Chelates

We wanted to expand the library of α -carbon substitution to determine if relaxometric properties could be tuned based on functional group. With the promising preliminary results of a more kinetically robust chelate with α -carbon pendant arm tetra-substitution, we wanted to explore the impact of changing this moiety. Furthermore, we wanted to create a structure that would eventually allow a handle for functionalization for use as a BFC. Once the target compound is identified, the R-group can be modified to include a reactive moiety such as an azide (like seen in DOTAZA), a monoamide (as explored in Chapter 3), or a carboxylate (TCE-DOTA).

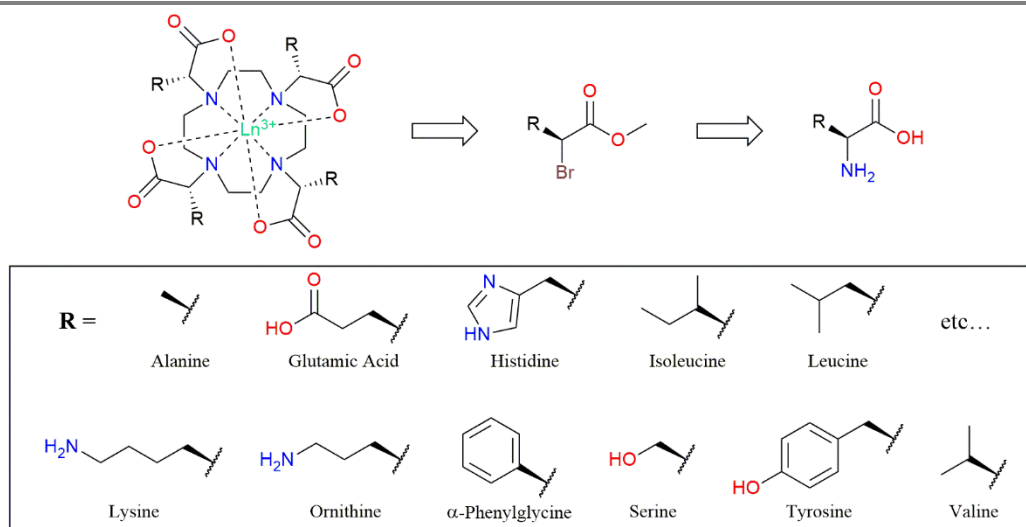


Figure 4.3. Retrosynthetic pathway to various α -carbon substituted pendant arm chelates with potential chiral amino acid starting materials.

With the ubiquity of chiral amino acids, we saw the potential for the synthesis of a variety of pendant arms that could be synthesized in the same fashion to alkylate onto cyclen, Figure 4.3. These stereospecific reactions result in the homochiral ligand, allowing for the most kinetically robust chelate. The three structures proposed herein have increasing sterics, with all four α -carbon pendant arms containing either isopropyl (DOTⁱPrA), isobutyl (DOTⁱBuA), or phenyl (DOTFA) moieties, Figure 4.4.

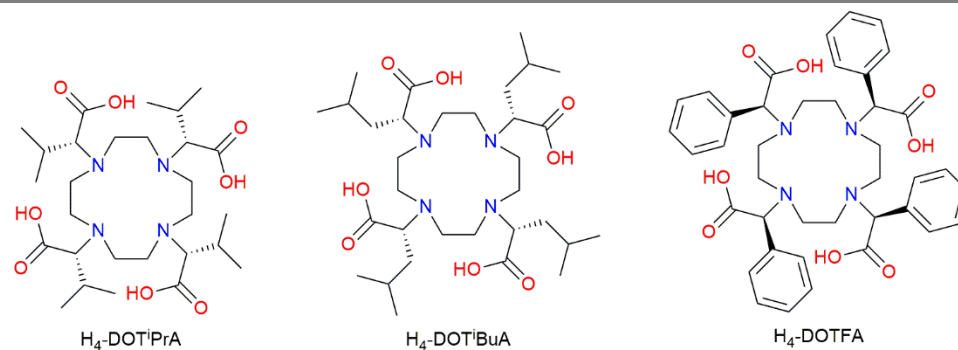
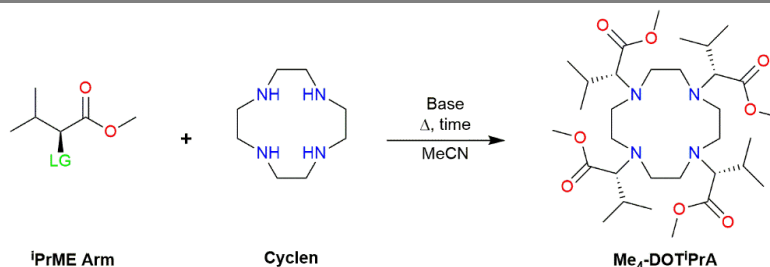


Figure 4.4. The three tetra-substituted ligand systems studied, tetra-isopropyl (**H₄-DOTⁱPrA**, Left), tetra-isobutyl (**H₄-DOTⁱBuA**, Center), and tetra-phenyl (**H₄-DOTFA**, Right)

4.3.1. Attempted Synthesis of DOTⁱPrA

The synthetic strategy for the protected tetra-isopropyl ligand, Me₄-DOTⁱPrA was proposed by installing a leaving group (LG) on the methyl ester of the amino acid L-valine, then alkylating this arm onto cyclen. This stereospecific reaction where all four arms alkylate sequentially results in a homochiral protected ligand with all isopropyl groups maintaining *R* configuration, Scheme 4.1. Monitoring of alkylation progress was performed *via* ESI-MS where the percent of each alkylation species was determined by comparing their relative intensities in the mass spectrum.



Scheme 4.1. Proposed synthetic strategy for the tetra-isopropyl protected ligand, Me₄-DOTⁱPrA, where LG denotes the leaving group.

The first leaving group investigated was a bromide. A double S_N2 diazotization reaction of the amino acid L-valine results in an enantiospecific retention of stereochemistry to convert the amine to a bromide.⁹² A methyl ester protection group was installed on (*S*)-2-bromo-3-methylbutanoic acid *via* a Fisher esterification to produce methyl (*S*)-2-bromo-3-methylbutanoate (**ⁱPr-1**), Scheme 4.2 Top. However, when **ⁱPr-1** was used to alkylate cyclen, the predominate species was di- and tri-alkylated. The reaction conditions were tuned to optimize tetra-alkylation, such as: base (K_2CO_3 , and Cs_2CO_3), temperature (60°C, 70°C, and 80°C), and reaction time (24 hrs, 48 hrs, up to four weeks). None of these conditions yielded tetra-alkylated in appreciable quantities, therefore we sought to find a better leaving group that would pull electron density away from the α -carbon.

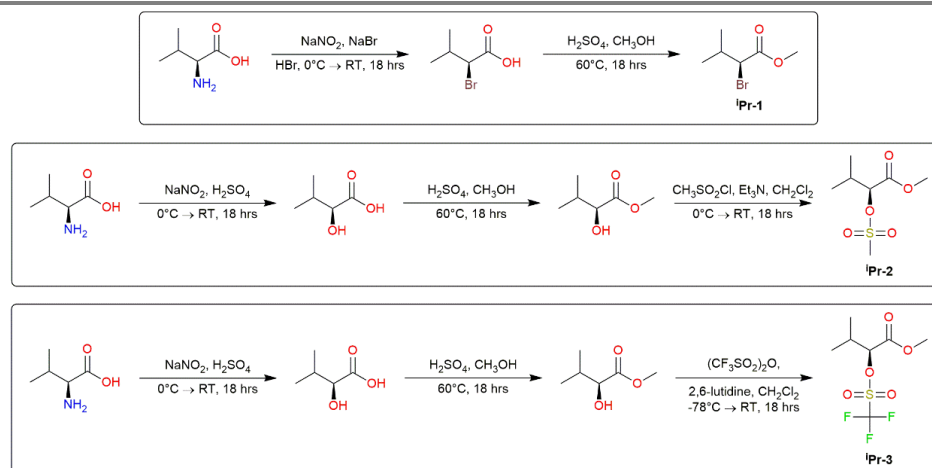
The second leaving group attempted was a mesylate. This leaving group can be installed under similar mild conditions like the bromide. A similar double S_N2 reaction was performed on L-valine, in this instance the amine was converted to a hydroxyl group. Methyl ester protection groups were installed on (*S*)-2-hydroxy-3-methylbutanoic acid *via* a Fisher esterification to produce methyl (*S*)-2-hydroxy-3-methylbutanoate. The hydroxyl group was converted to a mesylate *via* a substitution reaction to yield methyl (*S*)-3-methyl-2-((methylsulfonyl)oxy) butanoate (**ⁱPr-2**), Scheme 4.2 Middle. Cyclen was alkylated with **ⁱPr-2** with cesium carbonate in dry dichloromethane under air free conditions. Although this reaction progressed faster than the corresponding bromide, the predominate reaction products remained di- and tri-alkylated cyclens.

The final attempt to tetra-alkylate cyclen was to use install a triflate at the α -carbon. Triflates are excellent leaving groups due to the stability of their conjugate base and pull

the greatest electron density away from the α -carbon due to the trifluoro group. A triflate of methyl L-alaninate can be used to synthesize Me₄-DOTMA, so we sought to utilize this established procedure.⁹¹ However, they are extremely reactive when exposed to water, and thus must be installed under air- and water-free conditions. The hydroxyl group was converted to a triflate *via* a substitution reaction in dry dichloromethane with lutidine under air- and water-free conditions to yield methyl (*S*)-3-methyl-2-(((trifluoromethyl)sulfonyl)oxy) butanoate (**¹Pr-3**), Scheme 4.2 Bottom. The reaction of **¹Pr-3** with cyclen was performed under air- and water-free conditions. This reaction yielded the highest ratio of tetra-alkylated ligand, however di- and tri-alkylated was still present in appreciable quantities. Secondly, the installation of a triflate is notoriously low yielding due to its susceptibility to hydrolyze when exposed to moisture, thus we sought to seek a different route for synthesizing a tetra-substituted bulky ligand. The results of all three of these synthetic attempts are shown in Table 4.1.

Table 4.1. Comparison of the three leaving group strategies for alkylating cyclen with an ¹Pr methyl ester after four days of reacting.

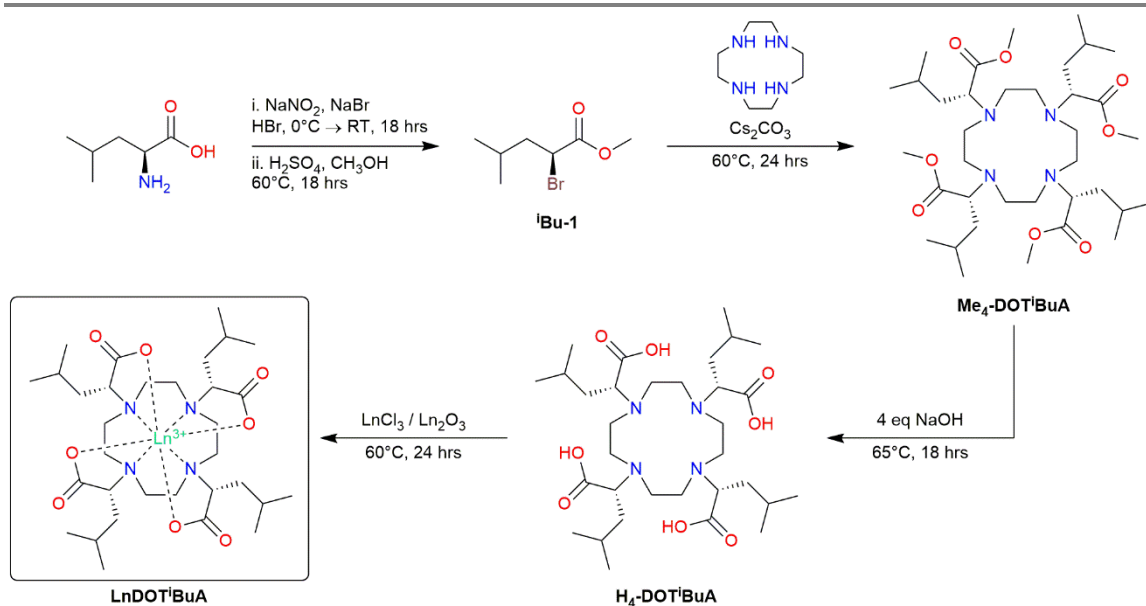
LG Strategy	Me-DO(¹Pr)A	Me ₂ -DO(²Pr)A	Me ₃ -DO(³Pr)A	Me ₄ -DOT ¹Pr A
Bromide (¹Pr-1)	64%	27%	9%	–
Mesylate (¹Pr-2)	37%	49%	12%	2%
Triflate (¹Pr-3)	4%	34%	31%	31%



Scheme 4.2. Synthesis of i Pr Methyl Ester Arms. The brominated arm i Pr-1 (Top), the mesylate arm i Pr-2 (Middle), and the triflate arm i Pr-3 (Bottom)

4.3.2. Attempted Synthesis of DOT i BuA Chelates

The lack of successful tetra-alkylation with the isopropyl-substituted prompted us to seek a different substituent on the α -carbon. We hypothesized that replacing the isopropyl moiety with an isobutyl would reduce the steric hindrance on the α -carbon and allow for it to be more susceptible to nucleophilic attack. This reaction sequence followed the same proposed for Me₄-DOT i PrA where a double S_N2 diazotization reaction of the amino acid L-leucine results in an enantiospecific retention of stereochemistry to convert the amine to a bromide.⁹² A methyl ester protection group was installed on (S)-2-bromo-4-methylpentanoic acid *via* a Fisher esterification to produce methyl (S)-2-bromo-4-methylpentanoate (i Bu-1). Subsequent alkylation onto cyclen results in the protected ligand, Me₄-DOT i BuA, Scheme 4.3.



Scheme 4.3. Proposed synthetic pathway for LnDOTⁱBuA chelates.

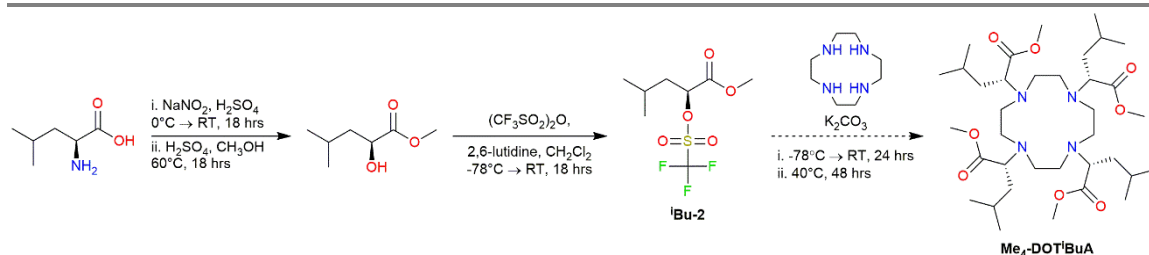
Surprisingly, the alkylation of cyclen with **ⁱBu-1** proceeded quicker than the isopropyl derivative. However, di- and tri-alkylated species were still present in the reaction mixture in appreciable quantities. This reaction appeared to go towards di-alkylated quickly, with no mono-alkylated species present after three days. After additional equivalents of **ⁱBu-1** were added to the reaction mixture, and a continued reaction time of ~18 weeks, the reaction mixture consisted of exclusively tri- and tetra-alkylated, Table 4.2. The reaction mixture was then column purified to isolate the tetra-alkylated Me₄-DOTⁱBuA at 36% yield. The isolated protected ligand underwent ester hydrolysis and chelation with europium chloride. Unfortunately, the remaining ligand was in such low quantities that chelation with gadolinium was not productive.

Table 4.2. ESI-MS reaction monitoring of tetra Me₄-DOTⁱBuA formation compared with di- and tri-alkylated species (Me₂-DO(2ⁱBuA) and Me₃-DO(3ⁱBuA), respectively).

BrBuME Arm

Reaction Time (days)	Me ₂ -(DO(2 ⁱ Bu)A)	Me ₃ -DO(3 ⁱ Bu)A	Me ₄ -DOT ⁱ BuA
3	37%	60%	3%
20	30%	61%	9%
68	31%	58%	11%
97	28%	40%	32%
130	—	25%	75%

A triflate leaving group was attempted for the tetra-isobutyl ligand, as shown in Scheme 4.4. The reaction was very low yielding, and workable quantities of protected ligand was not synthesized. Due to the difficulty of producing enough tetra-alkylated ligand, this project was discontinued. The comparison of the two attempted leaving group strategies is illustrated in Table 4.3.



Scheme 4.4. Synthesis of $\text{Me}_4\text{-DOT}^i\text{BuA}$ *via* alkylation of cyclen with the triflate derivative of the isobutyl arm ($^i\text{Bu-2}$).

Table 4.3. Comparison of the two leaving group strategies for alkylating cyclen with an ^iBu methyl ester after four days of reacting.

LG Strategy	$\text{Me}_2\text{-DO}(2^i\text{Bu})\text{A}$	$\text{Me}_3\text{-DO}(3^i\text{Bu})\text{A}$	$\text{Me}_4\text{-DOT}^i\text{BuA}$
Bromide ($^i\text{Bu-1}$)	37%	60%	3%
Triflate ($^i\text{Bu-2}$)	14%	63%	23%

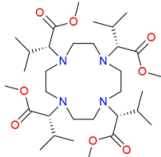
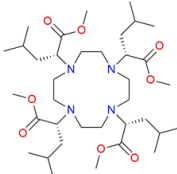
4.3.3. Comparing the Isopropyl and Isobutyl Substitution Strategies

Both an isopropyl and an isobutyl derivative were synthesized to produce a tetra-alkylated cyclen. Various leaving groups were surveyed for their ability to rapidly result in exclusively tetra-alkylated product. It is evident upon the comparison of these two substituents that the reduced sterics on the α -carbon associated with an isobutyl group results in a higher ratio of tetra-alkylated cyclen in solution when compared with its isopropyl counterpart, Table 4.4. However, both $^i\text{Pr-1}$ and $^i\text{Bu-1}$ demonstrate that a

bromide leaving group yields predominately di- and tri-alkylated cyclens, and appreciable ratios of tetra-alkylated only occur after reacting for 130 days.

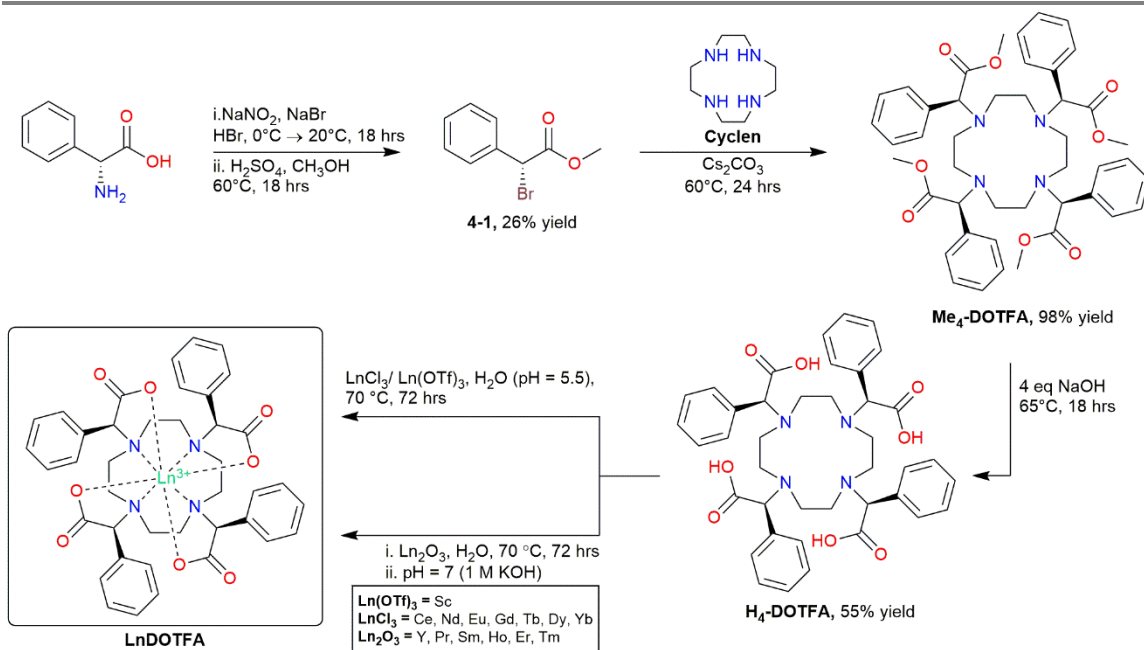
To reduce the reaction time by increasing the electrophilicity of the α -carbon, we sought to replicate the previously published synthesis for DOTMA *via* installation of a triflate leaving group for both the isopropyl and isobutyl strategies.⁹¹ However, like the bromide reactions the alkylation reactions of cyclen were unable to generate a high ratio of tetra-substituted cyclens in solution, Table 4.4. Both the ⁱPr and ⁱBu substitution strategies proved to be unsuccessful in generating exclusively tetra-substituted protected ligands, regardless of leaving group type. We hypothesize the electrophilicity at the α -carbons of the methyl ester of L-valine and L-leucine were not sufficient to be prone to nucleophilic attack from the amine on cyclen. Secondly, the increased sterics imparted on both compounds by the introduction of larger aliphatic groups prevented an effective opening for nucleophilic attack of the macrocyclic cyclen. More optimization experiments in which different reaction conditions are surveyed might increase the proportion of tetra-alkylated in solution, however the amount of effort required to isolate appreciable quantities of ligand does not yield either strategy as advantageous.

Table 4.4. Comparing two leaving group strategies for the alkylation of cyclen with an ^iPr or ^iBu methyl ester with their highest percentage of tetra-alkylated after the reaction was stopped.

LG Strategy	Reaction Time (days)	 $\text{Me}_4\text{-DOT}^i\text{PrA}$	 $\text{Me}_4\text{-DOT}^i\text{BuA}$
Bromide	130	36%	75%
Triflate	4	31%	23%

4.3.4. Synthesis of DOTFA Chelates

The double $\text{S}_{\text{N}}2$ diazotization of D- α -phenylglycine results in an enantiospecific retention of stereochemistry resulting in (*R*)-2-bromo-2-phenylacetic acid. A methyl ester protection group was installed *via* a Fischer esterification to produce methyl (*R*)-2-bromo-2-phenylacetate (**4-1**). Cyclen is alkylated with **4-1** *via* an $\text{S}_{\text{N}}2$ which results in an inversion of stereochemistry, resulting in the protected ligand $\text{Me}_4\text{-DOTFA}$. Unlike the attempted tetra-isopropyl and tetra-isobutyl derivatives explored previously, $\text{Me}_4\text{-DOTFA}$ alkylated within 24 hours. Given the increased steric demand of this alkylating agent, this is a surprising result. The increased electrophilicity of the α -carbon imparted by the corresponding phenyl group presumably made this alkylation facile. The esters were then hydrolyzed with 4 eq of 1M KOH to produce the ligand $\text{H}_4\text{-DOTFA}$. $\text{H}_4\text{-DOTFA}$ was chelated with appropriate lanthanide (III) chlorides or oxides, then purified *via* RP-HPLC to yield colorless solids. The reaction sequence is illustrated in Scheme 4.5.



Scheme 4.5. Total synthesis of LnDOTFA chelates.

4.4. Analysis of LnDOTFA Chelates

4.4.1. Structural Analysis of DOTFA Chelates

After gadolinium in the lanthanide series, chelates of DOTA have shown to exist primarily in the SAP coordination geometry. However, when a methyl group is substituted on the α -carbon of all four pendant arms, this preference shifts to TSAP. Previous studies have shown that the ratio of coordination geometry in DOTA chelates is lanthanide ion dependent. The early lanthanides preferentially adopt the more-open TSAP geometry to accommodate their larger ionic radii, whereas the later lanthanides, with their smaller ionic radii, maintain a higher proportion of SAP.⁸⁰ While this trend is observed slightly for DOTMA chelates, they maintain a predominance of TSAP across the entire lanthanide

series, with a maximum ratio of SAP being approximately 30% for dysprosium, as shown in Figure 4.5.⁹¹

Analysis of the $^1\text{H-NMR}$ spectra of LnDOTFA allowed for determination of their coordination geometry ratios. Due to the C_4 symmetry of these chelates, the spectra produced by all the LnDOTFA chelates exhibit one peak representing the TSAP coordination geometry and one representing the SAP coordination geometry. As shown in Figure 4.6, chelates of DOTA preferentially maintain the SAP coordination geometry with the exception for the early lanthanides, whereas tetra α -carbon substituted chelates have a preferred TSAP coordination geometry universally across the series.⁹¹ Lanthanide contraction is observed across the lanthanide series, in which the ionic radius decreases as atomic number increases.

As a result, SAP predominates in the later lanthanides for chelates of DOTA. In contrast, the addition of a moiety on the α -carbon pendant arm alters the ligand structure so the SAP coordination geometry is less accessible. Although DOTMA and DOTFA chelates exhibit similar preferential TSAP coordination geometry, their ratios are different. DOTMA reaches its maximum SAP ratio at terbium with a mole fraction of 0.3, whereas DOTFA reaches its maximum SAP at erbium with a mole fraction of 0.43. These values give insight into the water exchange mechanism occurring in α -carbon substituted chelates.

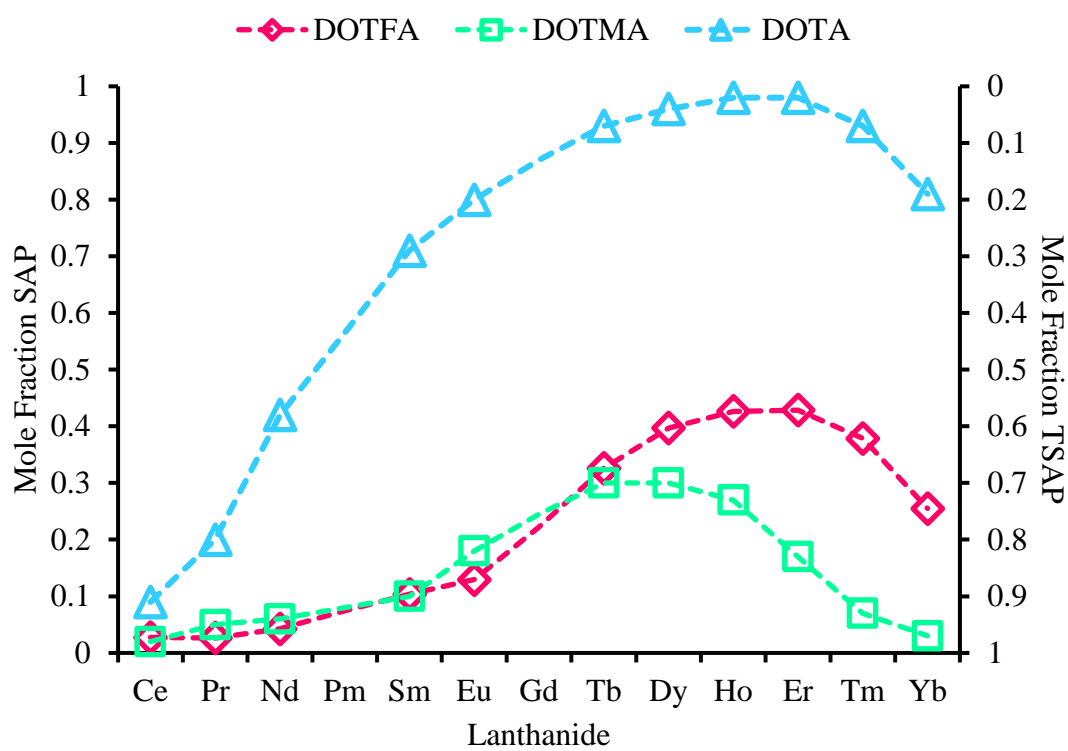


Figure 4.5. Coordination geometry mole fractions for LnDOTA (Δ), LnDOTMA (\square), and LnDOTFA (\diamond).

4.4.2. Relaxometric Analysis of GdDOTFA

4.4.2.1. Results and Discussion on the Discrete Chelate

The purified GdDOTFA chelate was sent to our collaborator, Professor Mauro Botta at the University of Eastern Piedmont Amedeo Avogadro in Torino, Italy for ^{17}O -NMR and NMRD experiments. The simultaneously fitted NMRD profiles and VT ^{17}O -NMR data for GdDOTFA are shown in Figure 4.6, and fitting parameters are in Table 4.5. The fitted relaxometric data for GdDOTA and GdDOTMA are included in for comparison.

Table 4.5. Calculated relaxometric values from the fitted ^{17}O -NMR R_{2p} and NMRD profiles of GdDOTA, GdDOTMA, and GdDOTFA, at 298 K and 20 MHz. ‡ Values from Aime *et. al.*⁹¹

	‡ GdDOTA		GdDOTMA		GdDOTFA	
	SAP	TSAP	SAP	TSAP	SAP	TSAP
MW ($\text{g}\cdot\text{mol}^{-1}$)	557.64		613.75		862.03	
Eu Mole Fraction	0.83	0.17	0.19	0.81	0.22	0.78
τ_{M} (ns)	360	53	370	50	303 ± 18	16.5 ± 0.5
ΔH_{M} ($\text{kJ}\cdot\text{mol}^{-1}$)	58.1 ± 2.5	41.9 ± 3.1	53.4 ± 2.9	40.3 ± 2.2	58.5 ± 4.1	27.7 ± 1.4
τ_{R} (ps)	66 ± 3		81 ± 2		161 ± 6	
τ_{V} (ps)	7.7 ± 0.3		7.9 ± 0.4		25 ± 2	
Δ^2 ($\cdot 10^{19} \text{ s}^{-2}$)	1.6 ± 0.1		1.7 ± 0.1		0.68 ± 0.02	
A_o/\hbar ($\cdot 10^6 \text{ rad}\cdot\text{s}^{-1}$)	-3.7 ± 0.1		-3.7 ± 0.2		-3.6 ± 0.1	
r_{GdH} (\AA)	3.02		3.10		3.0	
r_1 ($\text{mM}^{-1}\text{s}^{-1}$)	4.6		4.9		7.7	

These values fixed in fitting: $\Delta H_{\text{V}} = 1.0 \text{ kJ}\cdot\text{mol}^{-1}$, $D_{\text{GdH}}^{298} = 22.4 \cdot 10^{-10} \text{ m}^2\text{s}^{-1}$, $q = 1$.

*Fixed during fitting

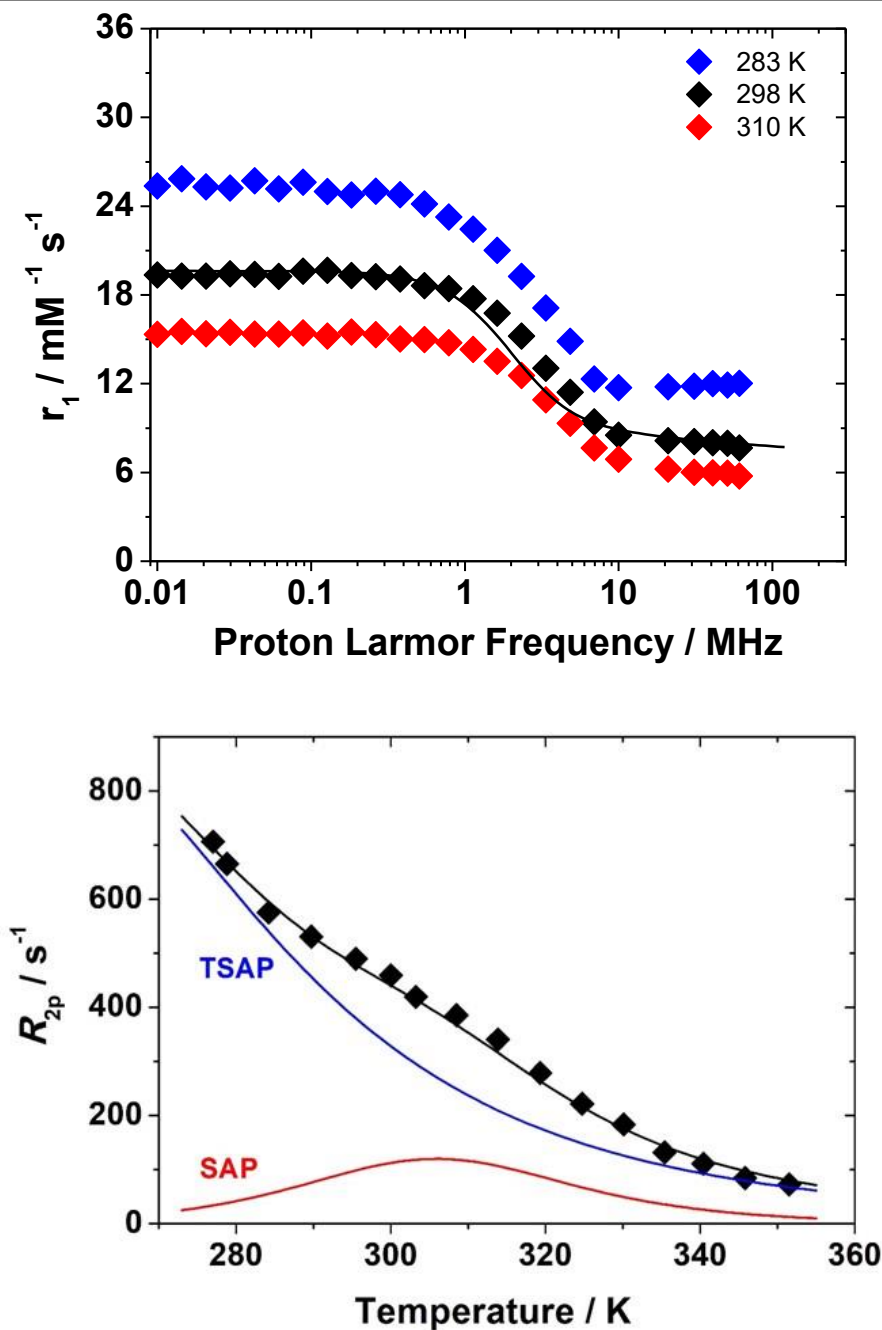


Figure 4.6. ^1H -NMRD profiles of GdDOTFA at 283 K, 298 K, and 310 K and pH 6.6 (Top); temperature dependence of the transverse ^{17}O water relaxation rate (R_{2p}) at 67.8 MHz and pH 6.6 (Bottom).

The relaxometric data shown in Table 4.5 show some striking differences between GdDOTFA and the two established chelates GdDOTA and GdDOTMA. GdDOTFA has a much longer rotational correlation time (τ_R) than either GdDOTA or GdDOTMA. This is not surprising due to the bulky phenyl rings contributing to the slowed tumbling. The τ_R of GdDOTFA is more comparable to that of the Side isomer of GdNB-DOTA ($\tau_R = 120$ ps).⁶³ As described in Chapter 2, the Side isomer self-associates in solution, giving rise to its slow molecular tumbling. Although these two chelates tumble at a similar rate, their relaxivities are quite different. GdDOTFA has a much higher r_1 ($7.7 \text{ mM}^{-1}\text{s}^{-1}$) than the Side ($6.1 \text{ mM}^{-1}\text{s}^{-1}$).⁶³ The discrepancy in relaxivity arises from their differences in water exchange. As explored in Chapter 2, GdNB-DOTA Side undergoes an extremely rapid dissociative water exchange process results in a reduction in q/r^6 , which in turn results in a reduction in relaxivity.⁶³ Although the Side isomer is able to compensate for its extremely rapid water exchange by slowed molecular tumbling, its sub-optimal water exchange kinetics cannot outmatch those of GdDOTFA.

A similar comparison in molecular tumbling can be made with GdDOTMA. The lower molecular weight of GdDOTMA results in its shorter τ_R in relation to GdDOTFA. As the dominating influence of relaxivity in smaller molecular weight chelates, this in turn gives GdDOTMA a much lower r_1 than GdDOTFA. As a result of its higher percentage of SAP in solution, τ_M for GdDOTMA is much longer than that of GdDOTFA. As low-molecular weight chelates that tumble quickly in solution, τ_M does not have as great of an influence over relaxivity for either of these chelates. Yet, we can glean insight into water exchange by reviewing their R_2 plots and τ_M values. The ^{17}O plot for each coordination

isomer of GdDOTFA shows the transverse relaxation rate as a function of temperature, Figure 4.6 Bottom. The curve generated for the SAP isomer shows the expected bell curve with its maximum at approximately 305 K. This indicates that the chelate exchanges water in the fast exchange regime. In contrast, curve of the TSAP isomer does not reach its maximum in the experimental range. As seen with the Side isomer of GdNB-DOTA, the maximum of this curve is reached at a much lower temperature. This is indicative of the extremely rapid water exchange regime, resulting in a reduction of q/r^6 . Although the TSAP coordination isomer of GdDOTFA does peak at a low temperature, there is no evidence of a reduction in hydration state; its relaxivity is the highest of the chelates surveyed.

Electronic spin relaxation (T_{1e}) is defined by τ_V and Δ^2 and influence the dipole-dipole interaction of the paramagnetic lanthanide and the ligating water. The influence of electronic relaxation predominates at low fields and optimization is through structural manipulation of the ligand. The larger the molecule, the greater the influence of electron spin relaxation, so due to the larger molecular weight of GdDOTFA, we would expect τ_V to have a large influence on relaxivity.⁴⁴ Secondly, because τ_V is a measure of electron spin relaxation as a result of intra- and inter-molecular collisions between different electronic dipoles, there is a potential that the large phenyl groups reduce these types of interactions by shielding the lanthanide center, resulting in a much longer τ_V than the other two chelates.

4.4.3. *Lifting the Barrier of τ_R*

4.4.3.1. *β -Cyclodextrin Binding Studies*

With the promising preliminary data of GdDOTFA we probed its relaxometric potential more thoroughly through macromolecular binding studies. β -cyclodextrin was titrated into of a solution of GdDOTFA at 0.18mM, and the longitudinal relaxation rate was collected at 20 MHz and 298 K. This experiment was then repeated with poly- β -cyclodextrin, a large macromolecular version of β -cyclodextrin. These collected binding curves are shown in Figure 4.7. and their fitted data in Table 4.6. The slowed molecular tumbling with the chelate incorporated into the macromolecular sugar results in the expected increased relaxivity. This is comparable to the Side isomer of GdBP-DOTA incorporated with poly- β -cyclodextrin. However, GdDOTFA has a much lower binding affinity for cyclodextrin in comparison with either regioisomer of GdBP-DOTA; both of which have K_a values three orders of magnitude higher than that of GdDOTFA. This is most likely the result of the structure of the chelate; its slightly smaller molecular weight indicates a lower hydrodynamic volume, which would prevent it from effectively interacting within the binding pocket of β -cyclodextrin.

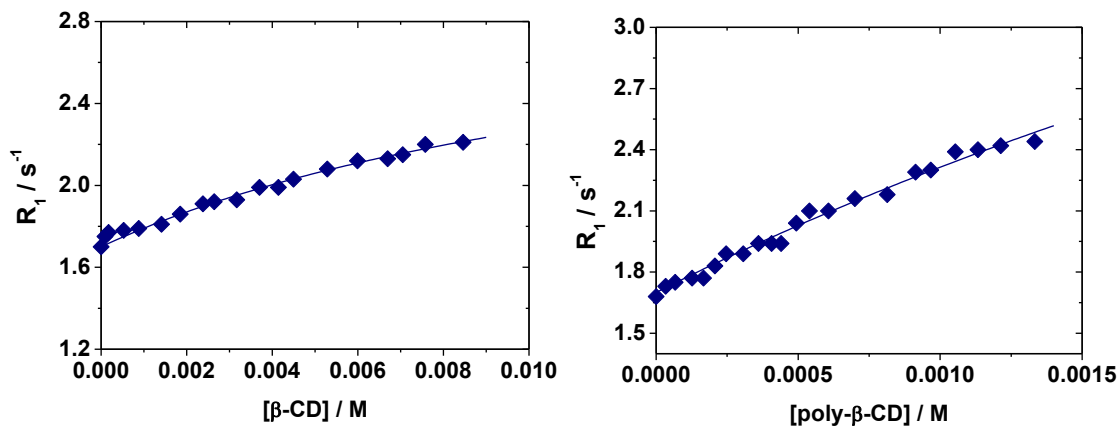


Figure 4.7. The observed longitudinal relaxation rate of water (R_1) as a function of concentration of β -cyclodextrin (Left) or poly- β -cyclodextrin (Right) in a solution of GdDOTFA [0.18 mM] at 20 MHz and 298 K.

Table 4.6. Selected data for GdDOTFA bound with β -cyclodextrin and poly- β -cyclodextrin at 20 MHz, and 298 K. [GdDOTFA] = 0.18 mM.

	β -Cyclodextrin	Poly- β -Cyclodextrin
MW (g·mol ⁻¹)	1,300	15,000
K_a (M ⁻¹)	147.6	155.1
r_1 Bound (mM ⁻¹ s ⁻¹)	14.3	32.1

4.4.3.2. Human Serum Albumin Studies

Another macromolecule of interest is human serum albumin (HSA). Using HSA as a biologically relevant bioconjugate has allowed researchers to deem feasibility for chelate behavior *in vivo*. For the purposes of GdDOTFA, it provides information on efficacy by slowing down the barrier of molecular tumbling, to probe if water exchange kinetics are optimal. The relaxivities for both β -cyclodextrin bioconjugates were promising and

prompted investigation on how GdDOTFA would behave if it were incorporated into a larger protein as a pseudo-BFC.

Because GdDOTFA does not contain a targeting vector, the binding to HSA will be through non-specific hydrophobic interactions potentially with one of its drug binding sites. One method to probe the interaction of a molecule with blood-based proteins is differential scanning calorimetry (DSC), which generates a curve of molar heat capacity as a function of temperature. This allows for the thermodynamics of conformational changes in proteins during different binding events. Through this, we can determine how GdDOTFA binds to HSA and other proteins in blood, as well as its binding capacity. These experiments were carried out by our collaborators Matthew Eskew and Dr. A. Benight. DSC melting experiments involved temperature scans at 1 °C/minute and were carried out on HSA (2 mg/mL) alone, and GdDOTFA (200 μ M) in HSA (2 mg/mL). The thermogram generated shows the partial molar heat capacity (C_p) of the plasma as a function of temperature and shows the interaction of the binding event of the chelate to the four major proteins in blood, Figure 4.8. If a ligand binds to the native state of a plasma protein, it will stabilize it, thus increasing its melting temperature, which would correlate to a peak shift to a higher temperature on the thermogram. If GdDOTFA binds preferentially to the native state of HSA, the temperature at which the bound protein-ligand complex denatures will be higher than the temperature at which free HSA unfolds.

The thermograph generated shows the four major proteins present in serum and their corresponding unfolding events, with the small peak at ~ 50 °C corresponding to fibrinogen, the large peak at ~ 65 °C corresponding to HSA, the shoulder peak at ~ 75 °C

corresponding to immunoglobulins A and G (IgA, IgG), and the small peak at ~ 85 °C corresponding to transferrin. The upshift in temperature of the HSA peak when GdDOTFA is present indicates a weak binding event occurring, and as a result, overlaps with the IgG/IgA peak. These preliminary data suggest that although GdDOTFA interacts with the components of plasma, these interactions are weak, therefore despite the inclusion of four hydrophobic groups, the pharmacokinetics are unlikely to be substantially impacted. This means that GdDOTFA has potential for use *in vivo* because it would not bind too strongly with plasma preventing it from being effectively cleared. The interactions between those chelates and HSA did not seem as strong as GdDOTFA. Secondary studies into binding sites remain unfinished due to the outbreak of COVID-19.

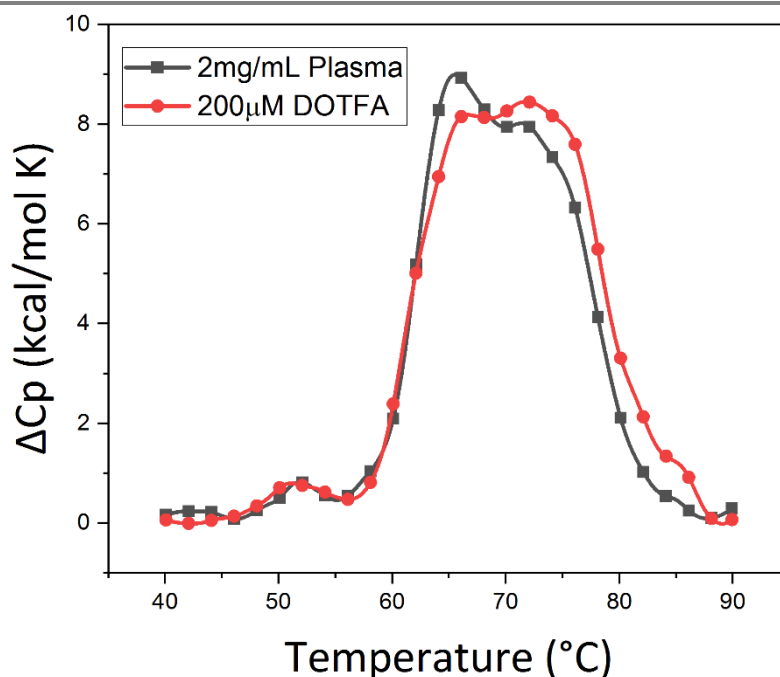


Figure 4.8. The change in partial heat capacity (ΔC_p) as a function of temperature for the binding of GdDOTFA with plasma (\bullet), and the change in partial heat capacity as a function of temperature of pure plasma (\blacksquare)

According to the SBM theory, if τ_R and τ_M are optimized, the maximum relaxivity that is achievable for a GBCA is $100 \text{ mM}^{-1}\text{s}^{-1}$ at 20 MHz. This is illustrated in the mountain plot in Figure 4.9. Although there have been many attempts to use SBM theory to design a chelate with optimal τ_R and τ_M values, it is difficult to predict the behavior of the chelate in solution. As described in Chapter 1, the higher the relaxivity, the tighter the bounds τ_R and τ_M can be, thus it becomes increasingly difficult to achieve extremely high r_1 values.

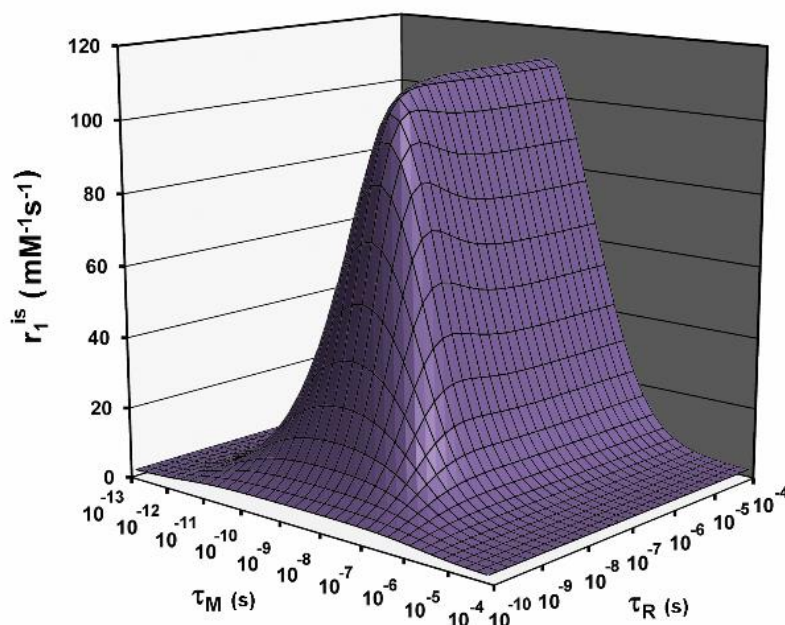


Figure 4.9. When other SBM parameters are optimized, the influence of the water exchange lifetime (τ_M) and rotational correlation time (τ_R) on relaxivity (r_1) are realized. ($B_0 = 0.5 \text{ T}$)

The proton relaxation rate (R_1) of water was measured as a function of concentration of HSA, with GdDOTFA at 0.09 mM, Figure 4.10. and Table 4.5. This allowed for the determination of the binding capacity of GdDOTFA to HSA as well as a relaxivity. The experimentally determined binding capacity of GdDOTFA and HSA is

much higher than previously studied chelates. We hypothesize that its four hydrophobic phenyl groups fit well into one or multiple the drug binding sites, restricting molecular motion even more than a single interaction (τ_R local), but this needs to be explored with further experiments.⁹³ Furthermore, the multiple drug binding sites of HSA bind allosterically; binding of one molecule alters the behavior of subsequent binding.

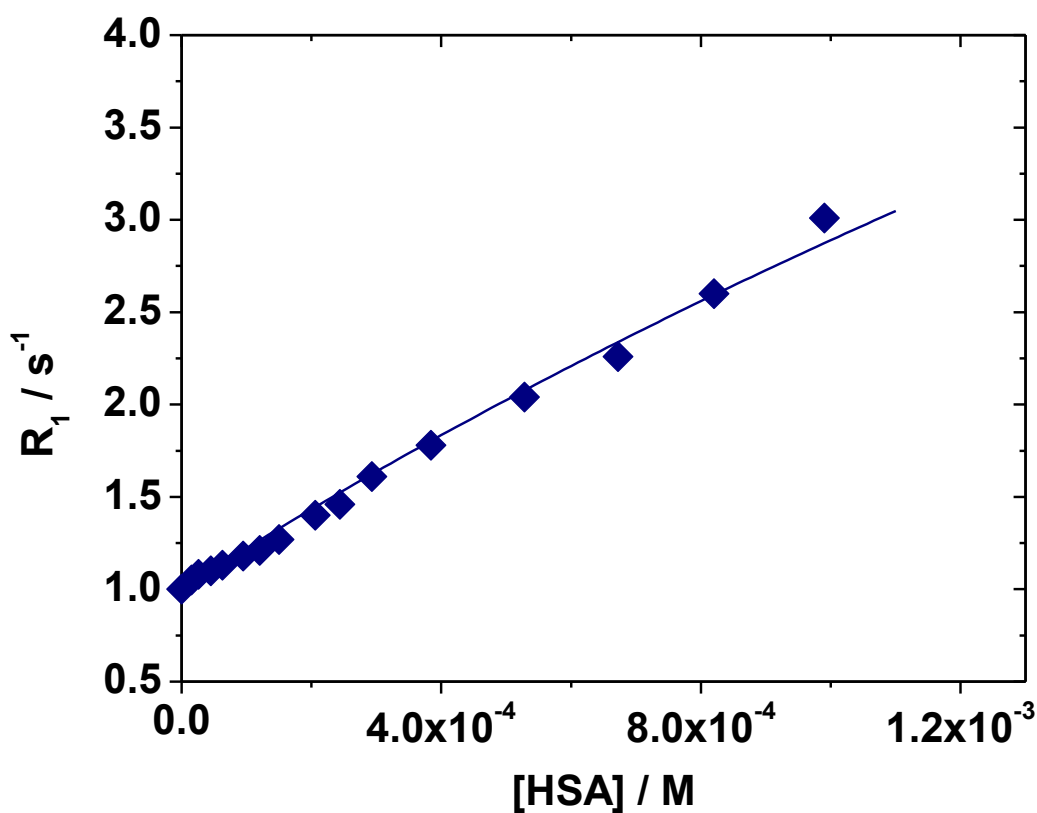


Figure 4.10. The observed longitudinal relaxation rate of water (R_1) as a function of concentration of human serum albumin in a solution of GdDOTFA [0.09 mM] at 20 MHz and 298 K.

Table 4.7. The binding affinity (K_A) of GdDOTFA to human serum albumin (HSA) and the relaxivity of the bound chelate to HSA at 20 MHz and 298 K.

	HSA
K_a (M^{-1})	220.1
r_1 Bound ($mM^{-1}s^{-1}$)	110.3

The relaxivity for GdDOTFA bound to HSA was found to be $110.3 \text{ mM}^{-1}\text{s}^{-1}$; the highest possible relaxivity according to the SBM model! Although these results are in the context of incorporation into a large protein ($MW_{\text{HSA}} = 66.5 \text{ KD}$) it must also be considered that the binding constant is weak, therefore at any time only a small fraction of GdDOTFA is in the bound form. GdDOTFA has better τ_M and τ_R than previously discussed chelates, but both values are not considered optimal according to SBM. Because HSA has multiple drug binding sites, it can bind more than one GdDOTFA chelate, causing a high relaxivity. However, when other phenyl-containing macrocyclic chelates were tested with HSA, their relaxivities were half of GdDOTFA.⁷⁵ The extremely high relaxivity observed when GdDOTFA is bound to HSA could be in part its high binding affinity. When a chelate is bound to a macromolecule, there is local rotation of the chelate within the bioconjugate, as well as rotation of the global structure. Because GdDOTFA binds so effectively to HSA, it is possible its local rotation is limited, and global rotation is the major or sole contributor to τ_R . At this magnetic field strength, relaxivity is defined by τ_R and a large slowly tumbling structure would facilitate high relaxivity. The slow rotation and high binding affinity of GdDOTFA coupled with a τ_M value that is considered fast, but not so fast that the chelate

experiences a reduced hydration state, would result in the extremely high relaxivity observed in this experiment.

The only explanation for this extremely high relaxivity must lie within τ_M . Theory dictates the only way to reach the top of the SBM mountain is either a large influence of second sphere water, which is not observed in the crystallographic data presented in Chapter 5, or more likely, a change in water exchange mechanism. The barrier of τ_R is lifted when GdDOTFA is conjugated into HSA, therefore the predominating influence of relaxivity is water exchange. The only means in which GdDOTFA can maintain such a high relaxivity without contradicting SBM theory is if the mechanism of exchange is not dissociative. Thus, an investigation into the water exchange mechanism needs to be addressed.

According to variable pressure NMR experiments conducted by Merbach *et. al.*, nearly all small molecular weight chelates of gadolinium exchange water in a pure dissociative fashion.⁴¹ If we view water exchange as a continuum, with associative on one end of the spectrum and dissociative on the other, interchange will lie in the center. The water exchange mechanism of a chelate is determined *via* its calculated activation volume (ΔV^\ddagger); a negative ΔV^\ddagger correlates to associative, positive ΔV^\ddagger with dissociative. Where the magnitude of ΔV^\ddagger describes the location of the exchange mechanism on the continuum. The most definitive determination of water exchange mechanism is *via* variable pressure $^1\text{H-NMR}$. Unfortunately, the only researcher performing these experiments in our field has retired and his instrument is currently non-functioning. Therefore, we were unable to collect these data to conclusively prove a change in water exchange mechanism in the

solution state. Further studies into the mechanistic impact of water exchange were conducted in the solid state and are provided in Chapter 5.

4.5. Conclusions and Future Directions

The initial goal of the structures studied herein was to determine how the nature of an α -carbon substituent affected the structural and relaxometric behavior of the chelate. Although tetra-isopropyl or tetra-isobutyl chelates were not successfully isolated, the exercise into determining various synthetic strategies gleaned insight into mechanism of tetra substitution, as well as provide evidence into which moieties are unsuccessful.

The surprising synthetic ease of a tetra-phenyl substituted chelate, LnDOTFA, provided potential for an ideal scaffold for use as an MRI contrast agent. The relaxometric results of GdDOTFA were surprising; it has one of the highest relaxivity as a discrete chelate of all the small molecular weight chelates studied in our group thus far. GdDOTFA has a water exchange rate that is considered very fast, yet this does not have a negative influence on hydration state nor relaxivity. This is the result of the means in which it exchanges water. Preliminary evidence suggest that GdDOTFA does not undergo a pure dissociative water exchange mechanism. This is quite unique; nearly all octadentate macrocyclic chelates exchange water in an exclusive dissociative fashion. Although further studies are required in order to confirm a change in water exchange mechanism, this preliminary evidence require a change in thinking of the way GBCAs behave relaxometrically.

The most promising results of the relaxometric experiments of GdDOTFA have been its incorporation into macromolecules. Binding to the polysaccharides β -cyclodextrin and poly- β -cyclodextrin resulted in the expected increase in relaxivity due to slowed molecular tumbling. However, the high relaxivities were not drastically higher than observed in other chelates. It was not until GdDOTFA was introduced into a solution of HSA that its relaxometric potential was fully observed. Although GdDOTFA had a low binding affinity for HSA, the relaxivity recorded of this experiment is higher than what had been established as possible by SBM theory. This was very surprising and unexpected. Larger biphenyl-containing chelates have shown a drastic increase in relaxivity when bound to HSA, however they were not of this magnitude, and not from weak hydrophobic interactions.⁷⁵ We hypothesize that the binding of GdDOTFA to the various drug binding sites of HSA is different than observed with other macrocyclic chelates, and this interaction will need to be probed further.

The high relaxivity observed when GdDOTFA is bound to HSA changes the way we view SBM theory as determination of optimal relaxometry. As illustrated by the SBM mountain plot in Figure 4.7, at increasingly longer values of τ_R , the value of τ_M to achieve high relaxivity narrows to a very tight range. The τ_M value for GdDOTFA as a discrete chelate does not fit into this range, and according to SBM, should result in a much lower relaxivity. Therefore, we propose a different mechanism of water exchange exhibited by GdDOTFA; one that is not considered purely dissociative but closer to interchange on the water exchange continuum. Further studies will need to be conducted to fully explore the

mechanism by which GdDOTFA exchanges water; but at present we may hypothesize that some interchange character could account for its extremely high relaxivity.

Although GdDOTFA is not considered a BFC due to the lack of handle for bioconjugation, its high relaxometric potential makes it an incredibly useful chelate. Incorporating α -substituted phenyl groups onto a macrocyclic BFC scaffold could provide higher relaxivity than a non-substituted chelate, as has been demonstrated with DOTMA derived BFCs.³⁶ Furthermore, with evidence that a rigid tetra-substituted chelate imparts higher kinetic inertness, a DOTFA-derived BFC might prevent dechelation *in vivo*. Further kinetic and thermodynamic studies will need to be completed to confirm this. Nonetheless, the DOTFA scaffold is synthetic versatile and advantageous, its gadolinium complex ideal relaxometrically, and has a high potential for being modified as a BFC system.

CHAPTER 5

TETRA α -CARBON SUBSTITUTION:

CRYSTAL STRUCTURES OF DOTFA CHELATES

5.1. Introduction

After analyzing GdDOTFA relaxometrically, detailed in Chapter 4, we wanted to explore the crystallographic nature of various DOTFA chelates. Previously published X-ray crystal data from chelates of DOTMA was the first incidence of gleaning solution state behavior from the solid state.⁷⁰ By crystallizing DOTFA across the lanthanide (Ln^{3+}) series, we can utilize this established precedence to greater understand how DOTFA behaves when it exchanges water, providing supporting evidence into its behavior relaxometrically. Crystal structure analysis allows for the determination of the number of water molecules bound to the lanthanide center, denoted as hydration number, q . Water molecule distances greater than a certain value, typically $>3 \text{ \AA}$, are considered uncoordinated, whereas $<3 \text{ \AA}$ are considered coordinated. In DOTA-based chelates, q is defined by the coordination number (CN) of the lanthanide of interest; chelates with a water molecule bound have a CN = 9 and chelates without a water molecule bound have a CN = 8. Thus, it is typically described that a chelate that is hydrated is $q = 1$, and dehydrated is $q = 0$.

Defining hydration by only analyzing q is an incomplete description of hydration and does not account for important structural changes that occur within the system. For chelates of DOTMA, their high TSAP ratios result in a longer metal-water distance. This coupled with the lanthanide contraction across the series can cause the measured bond

distance to be longer than what is typically considered hydrated. An analysis must also account for the change in ionic radius that occurs as the coordination number changes. This impacts how we view hydration; for example, GdDOTMA has an $r_{\text{LnH}} = 2.5 \text{ \AA}$ and is considered hydrated. In contrast, HoDOTMA has an $r_{\text{LnH}} = 2.66 \text{ \AA}$ and is considered dehydrated. Thus, it must be addressed how we should describe the hydrated ion of these intermediate cases.⁷⁰ Secondly, the conformational changes that occur to both the ligand structure as well as the ionic radius when the water exchange process occurs are not accounted for in these measurements. Thus, it is imperative to include other analyses to fully describe hydration, as well as define this concept. There is an important distinction between hydration and q ; they are not interchangeable concepts or values. q is a quantified description of the number of water molecules bound, whereas hydration incorporates this number, but also includes the position of the bound water molecule. Thus, we can view hydration as a non-binary construct. Combining these concepts accounts for other factors that influence what defines a hydrated chelate.

Our group has demonstrated that chelates of DOTMA show a continuum of hydration, in which hydration is not a binary value of one (hydrated) or zero (dehydrated), rather it exists as a spectrum in which some chelates of DOTMA exist as partially hydrated.⁷⁰ This evidence is quite groundbreaking; up until this seminal publication, some researchers would interpret that fractional hydration numbers to mean that some chelates crystallizing with one water molecule coordinated at $<3 \text{ \AA}$, and some crystallizing with one water molecule $>3 \text{ \AA}$, resulting in a net q value of <1 .²⁹ This justification for observed partial hydration states in various octadentate lanthanide chelates implies that individual

complexes crystallize differently, but this is not observed in crystal structure analysis. Thus, the best explanation is that chelates of DOTMA with q values that are less than one but greater than zero are partially hydrated; meaning that they cannot be described as CN = 9 or CN = 8 and their water-lanthanide distances are between values that is what is typically considered hydrated or dehydrated. The results of this publication indicated that further study into the crystal structures tetra-substituted chelates was warranted, thus we grew crystals of DOTFA chelates.

One method to determine whether a chelate is hydrated is analysis of its d/c ratio.⁹⁴ This measurement is a ratio of the distance from the nitrogen plane to the lanthanide center (d) over the distance from the nitrogen plane to the oxygen plane (c), as shown in Figure 5.1. The d/c ratio decreases linearly with decreasing ionic radius. This allows for a more direct determination of hydration, due to the increased accuracy in measuring the location of the lanthanide within the cage.⁹⁵ As the lanthanide contraction occurs across the series, the metal drops within the cage, resulting in a decrease of the d/c ratio. This corresponds with a loss of a coordinated water molecule, rendering the complex $q = 0$, and describing hydration without the requirement of determination of water molecule location.

There are other structural parameters that can be measured to glean insight into chelate hydration. Three angles, the O-Ln-O angle, the antiprism torsion angle α , and the NCCN angle, along with the area of the oxygen plane, all influence chelate hydration, as shown in Figure 5.1. The O-Ln-O angle and the oxygen plane area, O_4 , both correlate to a linear decrease with decreasing ionic radius. Lukeš *et. al.* have proposed that an O-Ln-O angle of less than 136° results in an O_4 area that is too small to coordinate water, thus this

measurement can distinguish between hydration states.⁹⁶ α shows the torsion angle between the nitrogen and oxygen planes, and a smaller angle indicates a longer distance between these two planes.⁹¹ An interesting conformational change occurs to the N-C-C-N angle during the dissociative water exchange process. When the water molecule leaves, the lanthanide drops into the macrocycle cage, because of its decreasing ionic radius. This in turn causes the N-C-C-N torsion angle to decrease, resulting in increasing distortion.⁷⁰ This piece of evidence demonstrates the impact dissociative water exchange has on both the metal and the ligand structure.

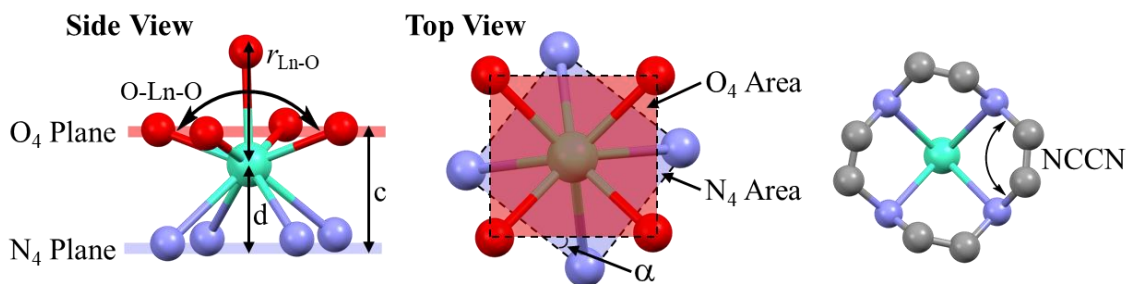


Figure 5.1. Left: Side view depiction of the d/c ratio and the O-Ln-O torsion angle. Center: Top view depiction of the O₄ and N₄ areas, and the torsion angle of the antiprism, α . Right: The NCCN angle, carboxylates and substituents removed for clarity.

5.2. Crystallization and Structural Analysis of LnDOTFA Chelates

5.2.1. Crystallization

Synthesis of the ligand DOTFA, its chelation with appropriate lanthanide triflates, chlorides, and oxides, and their RP-HPLC purification is described in Chapter 4. X-ray quality crystals were grown by dissolving the lyophilized and filtered chelates in a minimal volume of water. The solution was gently heated until complete dissolution was achieved.

The heat was then turned off and they were partially covered to facilitate crystal growth. The X-ray quality crystals were solved by our collaborator, Dr. Ed Valente at the University of Portland.

5.2.2. Crystal Structure Hydration

The chelates of DOTFA all formed similar crystal structures upon analysis. Four selected crystal structures of the later lanthanides are shown in Figure 5.2. The crystallographic data are shown in Table 5.1.

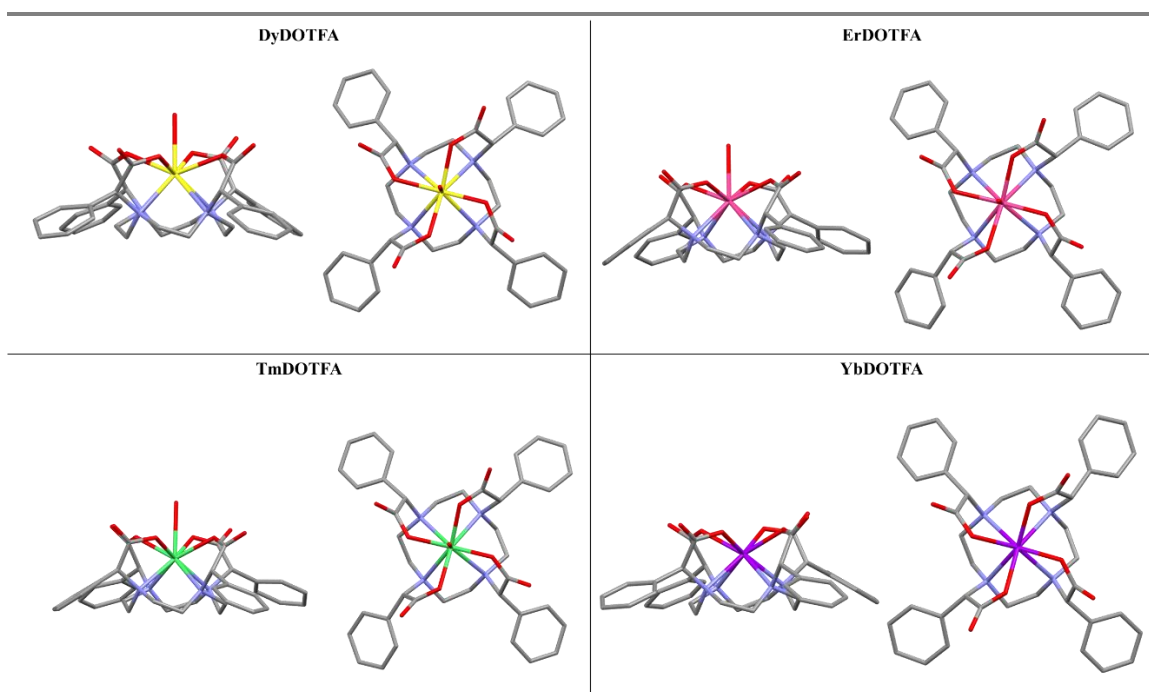


Figure 5.2. Later lanthanide crystal structures of DOTFA chelates: DyDOTFA (●), ErDOTFA (●), TmDOTFA (●), YbDOTFA (●). YbDOTFA is the only structure that crystallized without an apical water coordinated.

Analysis of all chelates of DOTFA demonstrated a preferential coordination geometry of TSAP, like that observed with chelates of DOTMA.⁷⁰ Upon observation of

the crystal structures of the later lanthanides, it is evident that YbDOTFA (●) did not crystallize with a water molecule bound and is considered completely dehydrated. In the crystal structure of TmDOTFA (●) the Mercury software shows a water molecule “bound”. However, the Ln-OH₂ distance is 2.661 Å, too long to be considered a formal bond. In Figure 5.3, the Ln-OH₂ distance is plotted against the ionic radius. The ionic radius is calculated using the same Pauling hard-sphere approach used in the analysis of DOTMA chelates.⁷⁰ The linear dependence of the coordination number on ionic radius is important due to the difficulty in accurately determining coordination number independently. Instead, the ionic radius is calculated and then mathematically applied to coordination number values determined by Shannon.⁹⁷ The ionic radius is calculated by averaging both the four Ln-O distances and four Ln-N distances and subtracting the corresponding ionic radii of oxygen and nitrogen, respectively, as shown in Equation 5.1.

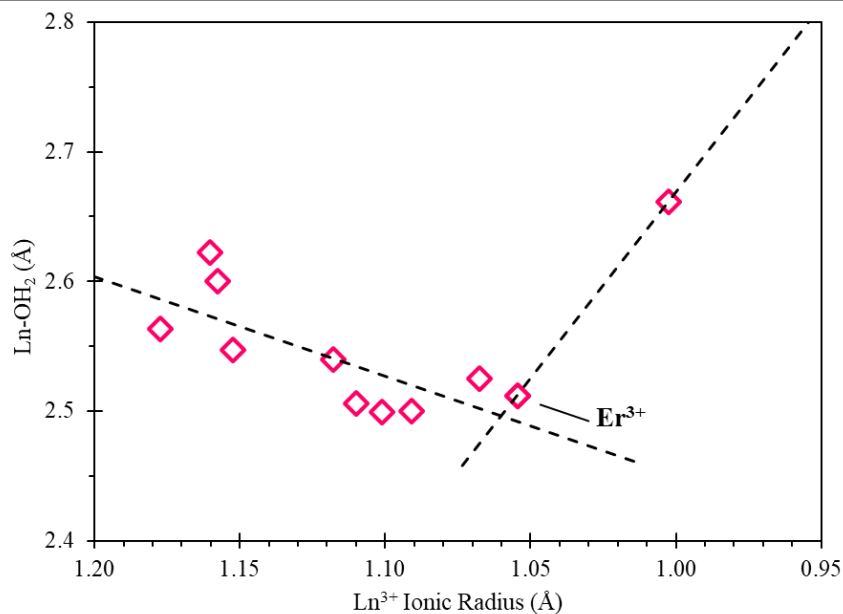


Figure 5.3. Metal-water distances versus lanthanide ionic radius for DOTFA chelates.

$$\text{I. R.}^{\text{Ln}} = \frac{[(\text{Ln} - \text{N}) - \text{I. R.}^{\text{N}}] + [(\text{Ln} - \text{O}) - \text{I. R.}^{\text{O}}]}{2}$$

Equation 5.1. Calculation to determine the ionic radius (I.R.) for a lanthanide is dependent on the average ionic radii of the four coordinating oxygens (O) and four coordinating nitrogens (N).

The data presented in Figure 5.3 show the Ln-OH₂ distance decreasing linearly with decreasing ionic radius until Er³⁺. Thus, a clear break in this trend is observed at Er³⁺. An “erbium break” would be a new concept in lanthanide chemistry, however, would be analogous to the commonly referenced gadolinium break. The behavior observed in DOTFA chelates is quite different from DOTMA, which exhibits a linear decrease in the Ln-OH₂ distance across the lanthanide series.⁷⁰ The gadolinium break, which is well documented in many chelates derived from DOTA, is the point in which chelates shift in their properties after gadolinium.⁹⁸ This erbium break is surprising as chelates of DOTMA follow the typical trend of the gadolinium break; where hydration properties shift.

Table 5.1. Calculated values from crystallographic data for chelates of DOTFA.

Ln^{3+}	Calculated Ionic Radius (Å)	Calculated Coordination Number	Space Group	Chelates in Unit Cell	d/c Ratio	q	Ln-OH_2 Distance (Å)
Ce	1.177	8.65	PBCN	1	0.70	1	2.563
Pr	1	1.160	P1	1	0.69	1	2.622
	2	1.158		2			2.600
Nd	1.152	8.80	PBCN	1	0.68	1	2.547
Sm	1.118	8.74	PBCN	1	0.68	1	2.540
Eu	1.110	8.82	PBCN	1	0.67	1	2.509
Gd	1.101	8.89	PBCN	1	0.66	1	2.499
Tb	1.091	8.93	PBCN	1	0.67	1	2.500
Dy	1.065	8.72	PBCN	1	0.66	1	2.525
Er	1.055	8.87	PBCN	1	0.66	1	2.512
Tm	1.003	8.15	PBCN	1	0.60	1	2.661
Yb	0.984	7.98	PBCN	1	0.58	0	–

The ionic radii of each Ln^{3+} ion in DOTFA were plotted across the lanthanide series, then the ionic radius dependence on coordination number is plotted as dashed lined boundaries for both $\text{CN} = 8$ and $\text{CN} = 9$ adopted from Shannon, Figure 5.4.⁹⁷ These CN bounds highlight that chelates of DOTFA maintain a CN close to 9 through ErDOTFA, and then TmDOTFA and YbDOTFA both reduce to a $\text{CN} = 8$. This is in stark contrast to DOTMA, which exhibits a gradual change from 9 to 8 over the later lanthanide series. However, as stated previously, hydration should not be considered a discrete differentiation between $q = 1$ and $q = 0$, but a continuum from hydrated through partially hydrated, to dehydrated. This is well described by the gradual change observed in DOTMA chelates,

where the change in CN begins to occur at Gd and the IR begins to decrease steadily. In contrast, DOTFA chelates show an abrupt change from $q = 1$ to $1 = 0$ at a later point in the series. This approach to chelate hydration is highlighted in Figure 5.5. As the only “dehydrated” chelate in the curve in Figure 5.5, TmDOTFA remains the outlier with its small ionic radius and reduced coordination number.

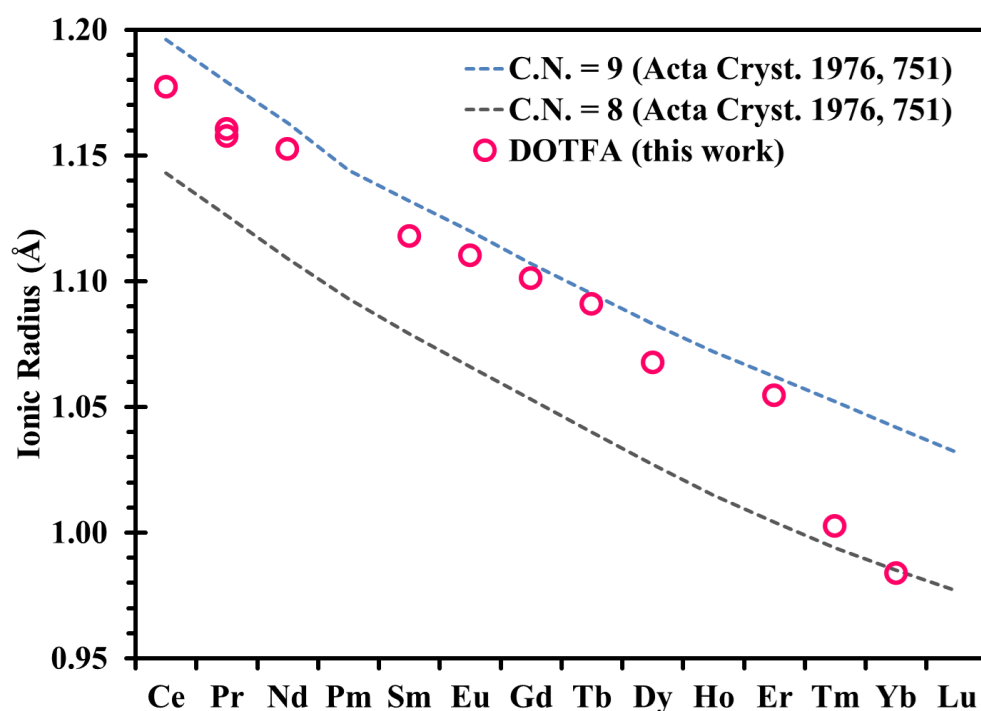


Figure 5.4. Ionic radii calculated for each chelate of DOTFA. The gray and blue lines are calculated CNs of the lanthanide, taken from Shannon.⁹⁷

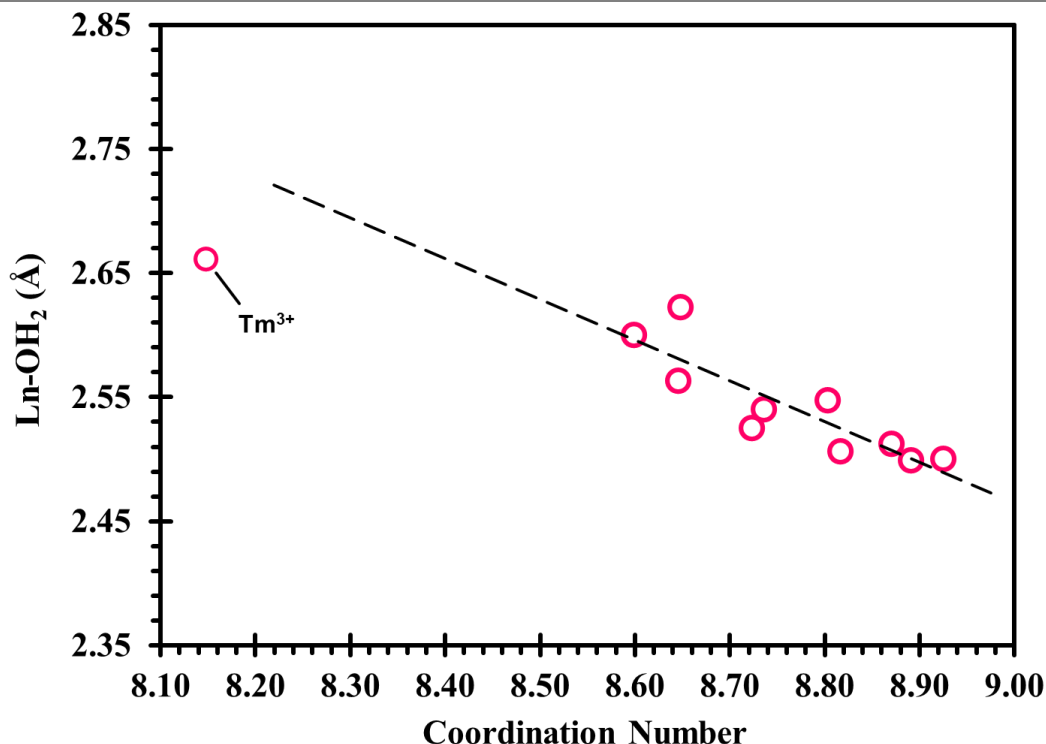


Figure 5.5. Calculated coordination numbers for each chelate of DOTFA based on water-lanthanide distance.

The longer metal-water distances observed in the later lanthanides are indicative of partial hydration. This is reflected in their reduced calculated coordination numbers. This had been established by our group previously; DOTMA chelates exhibiting fractional hydration occurs across the lanthanide series.⁷⁰ Although the chelates of DOTFA follow a similar trend as chelates of DOTMA, there are some noticeable differences that potentially provide insights into water exchange. We originally hypothesized that the bulkier phenyl pendant arms would weigh down the pendant arms, causing water exchange to slow. However, the relaxometric results in Chapter 4 demonstrate that exchange is faster in GdDOTFA than in GdDOTMA. Upon crystal structure analysis, it appears the phenyl

groups pull the acetate arms down in such a manner to allow better access for water to bind in comparison with chelates of DOTMA. This is supported by examining the O-Ln-O angle, Figure 5.6. In chelates of DOTMA, the O-Ln-O angle was shown to contract linearly across the series. This linear contraction is observed from Ce^{3+} to Er^{3+} in DOTFA chelates, but this contraction is more gradual. This supports the hypothesis that the phenyl groups hold the chelate in a more “open” conformation. After Er^{3+} , the O-Ln-O angle begins to decrease sharply, resulting in an O-Ln-O angle of YbDOTFA is comparable to that of YbDOTMA .

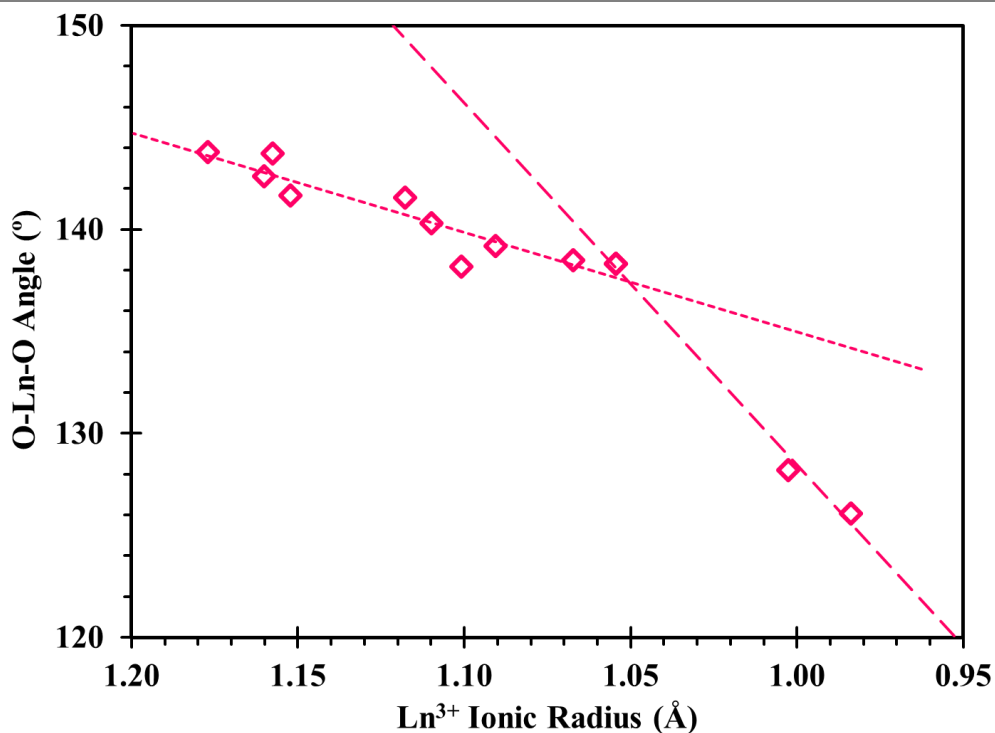


Figure 5.6. Lanthanide ionic radius as a function of O-Ln-O angle for LnDOTFA.

This difference can be seen in their corresponding d/c ratios, Figure 5.7, which effectively affords the position of the metal within the ligand cage. The d/c ratios across

LnDOTFA follow a similar trend to the O-Ln-O angle and again are quite different from the linear behavior observed for LnDOTMA. In the middle of the lanthanide series, the d/c ratio is larger for DOTFA than observed for DOTMA. This indicates that until Er^{3+} , the metal ion lies closer to the O_4 plane in DOTFA than it does in DOTMA. corresponding to an increased hydration in comparison. This renders the metal ion more accessible to water and correspondingly increase hydration in comparison.

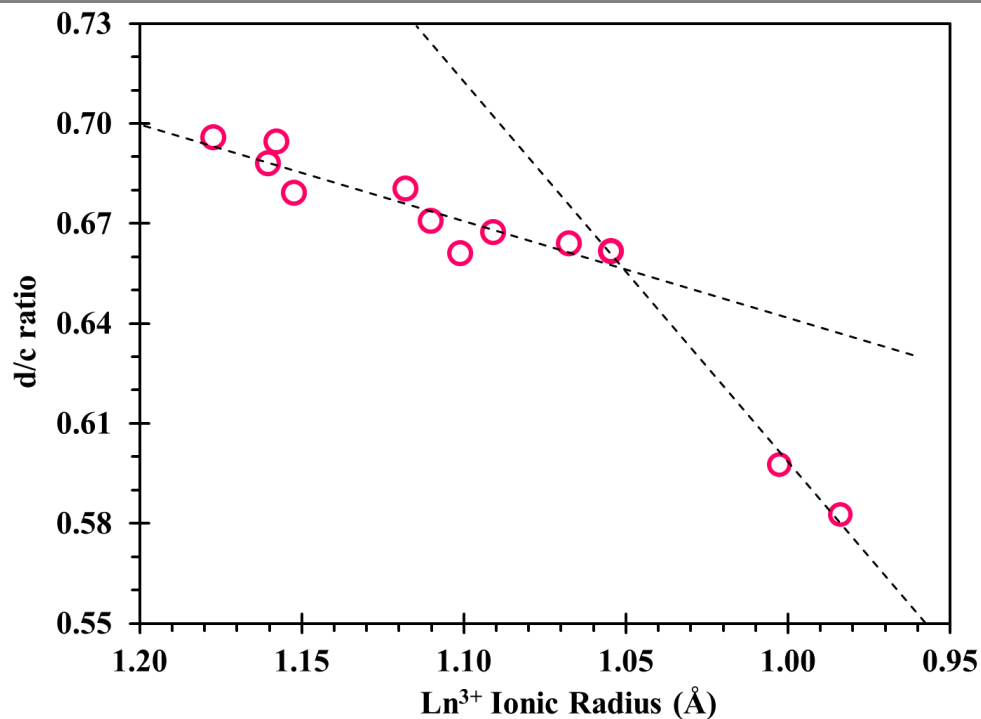


Figure 5.7. Ionic radius as a function of d/c ratio for LnDOTFA.

5.2.3. Water Exchange Mechanism via Crystal Structure Analysis

It has been demonstrated that there is a linear correlation between the coordination number calculated from ionic radius and the metal-water distance.⁷⁰ This correlation allows for the change in metal-water distance to be indicative of fractional coordination, which in

turn elucidates hydration. If we consider the series to all be GdDOTFA, the first chelate (CeDOTFA) would represent GdDOTFA as a CN = 10. Whereas the last chelate in the series (YbDOTFA) would embody GdDOTFA as CN = 7. This approach places the center of the series, actual GdDOTFA, as CN = 8.5. We can then contemplate what this means for the water exchange mechanism. A CN of 8.5 implies that gadolinium is partially hydrated; but this does not reflect its performance relaxometrically. Thus, the more likely explanation is that the partial CN = 8.5 does not reflect a semi-hydrated chelate, instead it is a chelate with a long Ln-OH₂ distance that exchanges water via a different mechanism. This is further supported via analysis of the ionic radius of GdDOTFA. As described previously, when the water uncoordinates, the ionic radius of the lanthanide decreases, thus if GdDOTFA is exchanging water dissociatively, we would observe a small ionic radius in the transition state.

The crystallographic data show that DOTFA does not lose a coordinated molecule until the ionic radius of the lanthanide is less than 1.003 Å, which occurs at Tm³⁺. In contrast, DOTMA begins to lose coordinated water molecules at 1.032 Å, which occurs at Dy³⁺. This may be significant in terms of understanding the mechanism of exchange occurring in GdDOTFA. Convention states that GdDOTMA undergoes dissociative water exchange, thus in the transition state Gd³⁺ is CN = 8. The ionic radius of an eight coordinate Gd³⁺ is 1.053 Å. This value is larger than the 1.033 Å at which DyDOTMA has a stable $q = 0$ complex in the crystal structure. However, this difference does not render these complexes dissimilar. In a high energy transition state, it is likely that GdDOTMA could lose a coordinated water molecule to become CN = 8. In contrast, the crystallographic data

suggest that this is not the case for GdDOTFA; the chelate does not lose a coordinated water molecule because its open conformation promotes hydration. As described in Chapter 1, water exchange is considered a continuum of associative-interchange-dissociative mechanisms. The more open structure of DOTFA most likely allows greater access to the incoming water molecule while the existing water molecule remains bound or close. This in turn leads to more interchange character in the mechanism. The high relaxivity experienced by GdDOTFA while maintaining a short τ_M also suggest such a change in mechanism, as explored in Chapter 4. Although future experiments are required to confirm, this is the first time that crystallographic data imply a change in water exchange mechanism.

5.3. Racemization in DOTFA Chelates

Upon receiving solved crystal structures of DOTFA chelates it was immediately clear that all 15 chelates existed as a racemic mixture of *RRRR* and *SSSS* according to their space groups. Yet, the synthesis of DOTFA chelates is stereospecific; each reaction step apart from chelation is an S_N2 reaction from an enantiopure amino acid starting material and should result in an exclusive *SSSS* conformation at each α -carbon pendant arm. The space group revealing a racemic mixture of the two homochiral species, mean that a mechanism is occurring facilitating this conversion.

However, with four chiral centers, the number of possible isomers is much higher than the found homochiral racemate. If racemization were occurring at each chiral center separately, we would observe two enantiomeric pairs of four diastereoisomers, and the ^1H -

NMR spectra of LnDOTFA chelates would reflect a mixture of diastereoisomers, like that in the simulated spectrum in Figure 5.8.

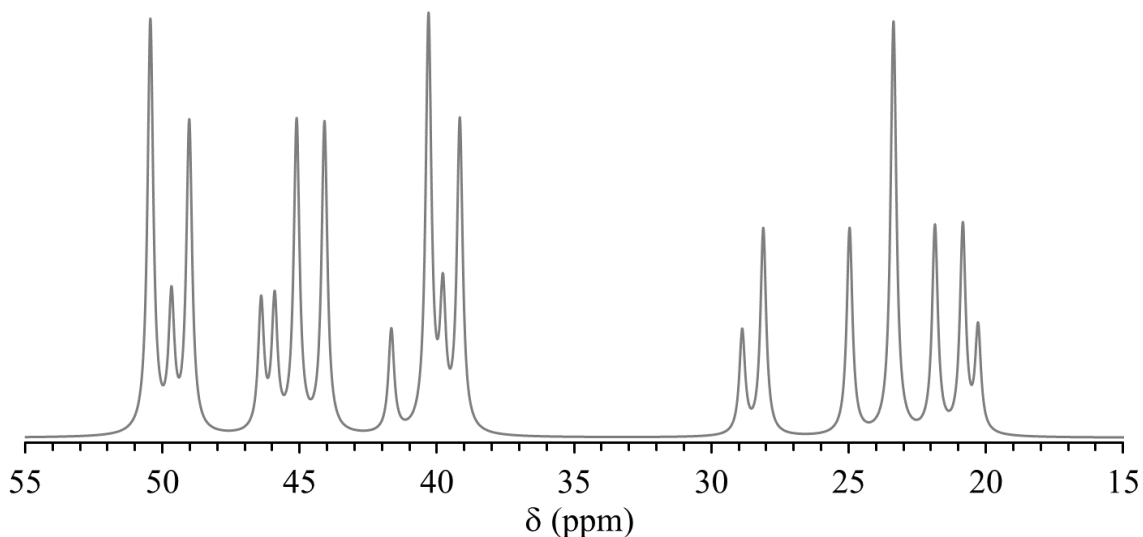


Figure 5.8. Simulated $^1\text{H-NMR}$ spectrum of racemic EuTCE-DOTA.

Because we only observe the two coordination geometries of SAP and TSAP in the $^1\text{H-NMR}$ spectra of all DOTFA chelates, the other possible diastereoisomers must be inaccessible. Substitution on the α -carbon prevents arm rotation, and it has been shown that arms bind and rotate cooperatively.⁹⁹ The enantiopure D- α -phenylglycine should facilitate the homochiral SSSS ligand upon alkylation, thus it is unlikely that the other possible diastereoisomers would arise due to the higher energy conformation required with racemization.¹⁰⁰ Because we were unsure if DOTFA chelates were existing as a mixture of diastereoisomers at some point in the enantiospecific synthesis and then resolving to the homochiral racemate, or if they were simply racemizing during chelation, two experiments were conducted to determine the point of racemization.

5.3.1. Chiral Shift Reagent Study on the Bromoacetate Alkylating Agent

We first decided to check the enantiopurity of the bromo-alkylating agent, **4-1**. A small amount (5 mg) of the chiral shift reagent, europium tris[3-(trifluoromethylhydroxymethylene)-(+)-camphorate] was added to **4-1** and an $^1\text{H-NMR}$ spectrum was collected. If both enantiomers were present, the shift reagent would in effect act as a chiral derivatizing agent wherein the topicity of the chiral protons (*S*) and (*R*) would no longer be isochronis and would be distinguishable by NMR. The $^1\text{H-NMR}$ spectra before and after the addition of the chiral shift reagent are shown in Figure 5.9. As shown by the spectrum in Figure 5.9 Bottom, the chiral proton at ~ 5.4 ppm did not split into two peaks, therefore the alkylating agent **4-1** is enantiopure.

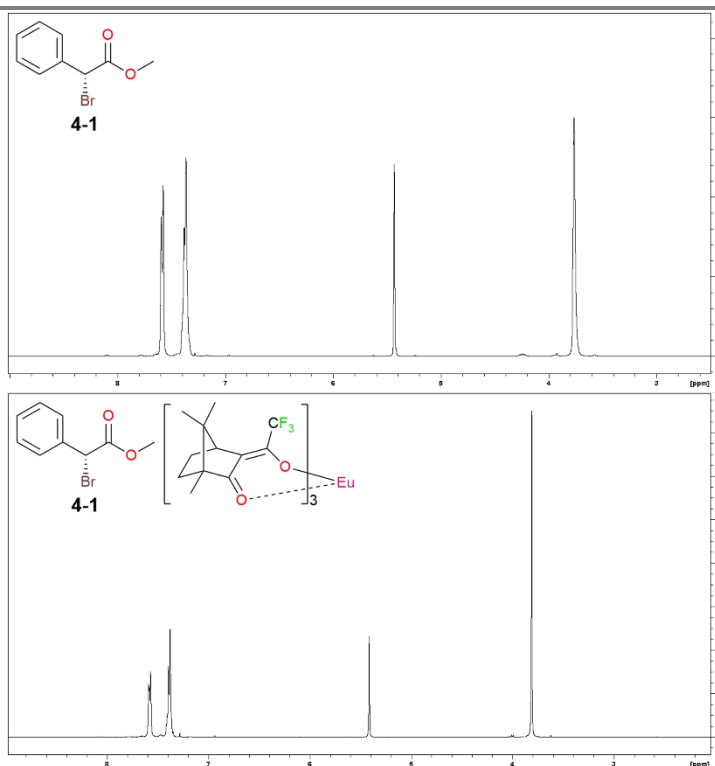


Figure 5.9. $^1\text{H-NMR}$ spectra of **4-1** (Top) and **4-1** with the chiral shift reagent (Bottom).

5.3.2. α_D Measurements in DOTFA

Next, α_D measurements were collected *via* polarimetry on Me₄-DOTFA, H₄-DOTFA, and two enantiopure chelates of DOTFA. These data are presented in Table 5.2. In no cases were rotation of plane polarized light observed.

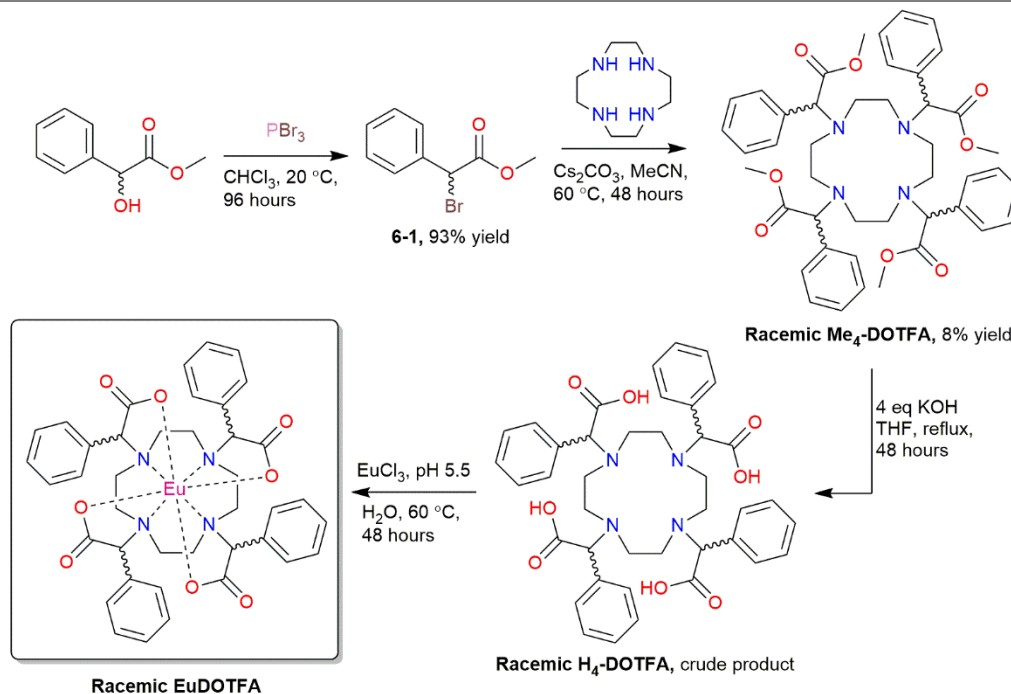
Table 5.2. α_D values for products in each synthetic step of synthesizing DOTFA chelates.

Sample	Temperature (°C)	α_D
Me ₄ -DOTFA	20.6	0.00
DOTFA-2K	22.5	0.00
DOTFA Crystals	21.7	0.00
SmDOTFA	20.6	+0.01
GdDOTFA	23.2	+0.01

5.3.3. Synthesis and Analysis of Racemic EuDOTFA

The inconclusive data generated from the α_D experiment led us to explore the impact of racemization by synthesizing EuDOTFA from a racemic starting material. There are three potential results of this experiment depending on how this reaction sequence racemizes. First, the racemic starting material could give rise to six potential diastereoisomers in solution: *RRRR* (*SSSS*), *RSSS* (*SRRR*), *RSRS*, and *RRSS*.⁹⁹ A second option is that if racemization occurs in order to achieve the lowest energy conformation the

product would be a mixture of 50% *RRRR* and 50% *SSSS*. Finally, it is possible that only the D-isomer of the starting amino acid racemizes, which would result in a product mixture of 25% *SSSS* and 75% *RRRR*. DL-methyl mandelate was reacted with phosphorus tribromide in chloroform at ~ 20 °C for 96 hours to yield the bromide starting material (**5-1**) and the crude product was used without further isolation, shown in Scheme 5.2. A mixture of **5-1** and cyclen was heated in acetonitrile for 48 hours to yield a crude protected ligand (**Racemic Me₄-DOTFA**). Upon analysis *via* ESI-MS, it was shown that the reaction solution was a mixture of di-, tri-, and tetra-alkylated ligand, and was subsequently purified *via* column chromatography to isolate the tetra-alkylated Me₄-DOTFA product. The methyl esters were hydrolyzed with 1M KOH in THF at reflux to yield a crude ligand (**Racemic H₄-DOTFA**). The ligand was chelated with europium chloride in water at pH 5.5 to yield a crude complex (**Racemic EuDOTFA**).



Scheme 5.1. Synthesis of racemic EuDOTFA.

Analysis of the $^1\text{H-NMR}$ spectrum of the racemic $\text{H}_4\text{-DOTFA}$ ligand shows a mixture of diastereoisomers, with no diastereoisomers predominant (data not shown). Upon chelation, the $^1\text{H-NMR}$ spectrum of the racemic EuDOTFA also revealed a mixture of diastereoisomers, however, the homochiral $RRRR$ and $SSSS$ conformations were the majority species. These data suggest that the chelation of $\text{H}_4\text{-DOTFA}$ promotes the homochiral configuration as the lowest energy conformation, and this most likely occurs during chelation, Figure 5.10. Further studies are needed in order to confirm that racemization occurs during chelation, and the mechanism of action, but these preliminary data suggest that reaction conditions facilitate the homochiral as the predominate species, as well as reduce the presence of other diastereoisomers.

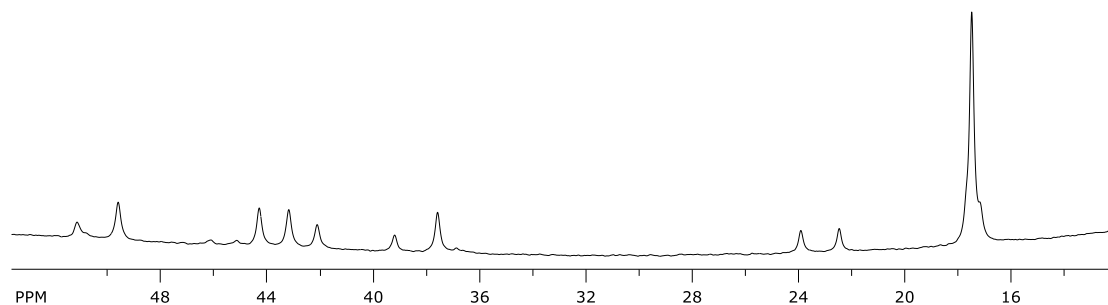


Figure 5.10. Zoomed in section of the ^1H -NMR spectrum of Racemic EuDOTFA. The axial protons in this region show the predominance of the homochiral (*RRRR/SSSS*) conformation in the large TSAP peak at ~ 18 ppm, and the smaller SAP peak at ~ 50 ppm.

5.4. Conclusions

With the relaxometric success of GdDOTFA, it was important to glean more information on how chelates of this ligand behave in the solid state. Analysis of the crystal structures of DOTFA chelates revealed some surprising information. The calculated values from the crystal structures are strongly indicative that there is a change in water exchange mechanism for GdDOTFA. Because DOTFA does not become dehydrated until the ionic radius of the lanthanide is below 1.003 \AA and the ionic radius of GdDOTFA with a CN = 8 is greater than that, these data suggest that GdDOTFA does not exchange water under a pure dissociative mechanism; rather has some influence of interchange. These data are supported by the relaxometric data found in Chapter 4, GdDOTFA having an extremely high relaxivity, while maintaining a short τ_M , mean that it must exchange water differently.

These data give rise to the implication of DOTFA-derived chelates as BFCs. Although DOTFA does not contain a handle to attach a targeting vector, these preliminary studies were essential to probe the utility of functionalizing off the α -carbon pendant arm.

Due to the extremely high relaxivity of the parent GdDOTFA, modification studies are currently being undertaken in our group to alter DOTFA into a BFC. Modification of this structure provides the ideal scaffold for a high relaxivity agent, and although further study is required to explore stability, precedence indicates that modified DOTFA chelates will maintain a superior safety profile than their traditional DOTA counterparts.⁹¹

A secondary surprising result of the crystallographic study of DOTFA chelates was the discovery that DOTFA forms a racemate upon chelation. Although the reaction sequence of DOTFA chelates is enantiospecific, we hypothesize the π system of the aromatic ring on the α -carbon pendant arm stabilizes the system upon chelation, causing enolization. Although this was unexpected and unintended, these results are not negative. Because this reaction preferentially racemizes DOTFA chelates to the lowest energy conformation, this implies that a non-enantiopure starting material can force the reaction towards the homochiral *RRRR/SSSS*. Further optimization studies would be required to facilitate this reaction, but the implication is that costly enantiopure synthetic strategies would not be required when synthesizing DOTFA derived BFCs.

CHAPTER 6

OTHER CHELATES OF INTEREST: DO3A-MONOAMIDES

6.1. Monoamides in Medicine and Research

6.1.1. Background

Monoamides have been a facile route of conjugation in the biomedical industry for some time.^{101,102} The ability to couple a variety of active amines, such as lysine residues in proteins, to *N*-hydroxysuccinimide esters (NHS) has allowed for a variety of biomolecules to be synthesized quickly and effectively, Figure 6.1.¹⁰³ These amine coupling reactions can take place at physiological pH as well as under relatively mild conditions, which make them an advantageous approach for synthesis of biologically robust linkages. The most common use of the NHS coupling reaction is tagging relevant biomolecules such as proteins and antibodies with fluorescent probes in order to glean important biological information.¹⁰⁴

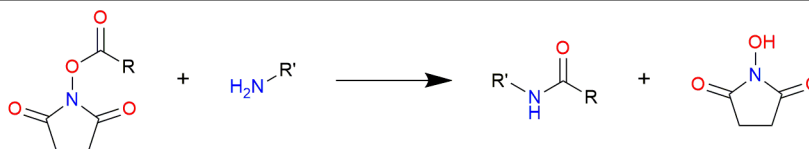


Figure 6.1. Active coupling of *N*-hydroxysuccinimide ester with a terminal amine to form an amide and *N*-hydroxysuccinimide.

Monoamide containing gadolinium-based MRI contrast agents (GBCAs) are relatively commonplace in clinically settings. Two clinically available linear agents, Omniscan™ and OptiMARK® both contain two amides in which the carbonyl coordinates

the metal, Figure 6.2. The resulting chelates have a neutral charge, resulting in a reduced osmolality.³²

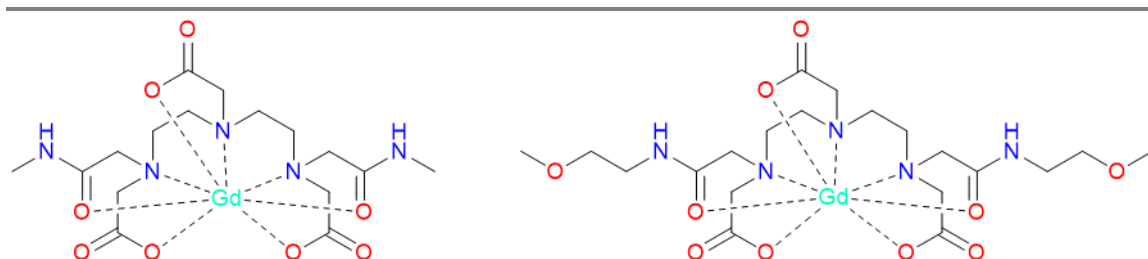


Figure 6.2. The structures of two clinically available MRI contrast agents containing amides. **Omniscan™** (gadodiamide) (left), and **OptiMARK®** (gadoversetamide) (right).

6.1.2. Properties of Amides as GBCAs

The implication of replacing two coordinating ligands with a neutral amide is a resulting net charge of 0. This change of coordinating ligand directly impacts the relaxometric properties of the chelate. This phenomenon is highlighted in Table 6.1. GdDTPA²⁻, the scaffold by which many linear chelates are derived from, has a water exchange lifetime, τ_M , of 303 ns. However, when two acetate coordinating pendant arms are replaced with acetamide arms (GdDTPA-BMA) or methoxyethyl acetamide arms (GdDTPA-BMEA), τ_M increases by an order of magnitude. Macrocyclic agents, derived from the ligand DOTA, also show the impact of replacing carboxylates with amides. GdDOTAM³⁺ and GdDTMA³⁺ both contain tetraamide coordinating pendant arm, changing the charge of both complexes to 3+. The impact on water exchange is dramatic; τ_M is on the order of thousands of nanoseconds versus hundreds for GdDOTA⁻. This drastic change in water exchange impacts the efficacy of a chelate as an MRI contrast agent. In order to have maximum efficacy as a contrast agent, defined as relaxivity (r_1), requires the

water exchange rate to be rapid. Due to the nature of amide containing chelates, relaxivity is not optimized; r_1 for GdDOTAM³⁺ is half of its tetracarboxylate counterpart, GdDOTA⁻ (2.5 mM⁻¹s⁻¹ and 4.5 mM⁻¹s⁻¹, respectively).

One interesting finding in comparing the chelates in Table 6.1, is their difference in activation volumes, ΔV^\ddagger . This value defines the mechanism of water exchange. Ligand exchange mechanisms for chelates can either be associative, interchange, and dissociative.⁴⁰ As described in detail in Chapter 1, these mechanisms are not discrete, but in fact lie on a continuum from associative at one end to dissociative at the other, with interchange in the middle. Although all GBCAs exchange water through a dissociative mechanism, they can lie on different parts of the continuum. By replacing carboxylate pendant arms with neutral amides, the dissociative character is decreased; GdDOTA⁻ has an activation volume of 10.5 cm³mol⁻¹ and EuDOTAM³⁺ has a ΔV^\ddagger of 4.9 cm³mol⁻¹.¹⁰⁵

Table 6.1. Selected relaxometric properties of linear and macrocyclic chelates, comparison of amide containing and non-amide containing complexes.^{29,32,106}

	Chelate	τ_M (ns)	r_1^* (mM ⁻¹ s ⁻¹)	ΔV^\ddagger (cm ³ mol ⁻¹)
Linear	GdDTPA ²⁻ (Magnevist®)	303	4.3	12.5
	GdDTPA-BMA (Omniscan™)	2×10 ³	4.58	7.3
	GdDTPA-BMEA (OptiMARK™)	2.6×10 ³	4.7	7.4
Macrocyclic	GdDOTA ⁻ (Dotarem®)	244	4.8	10.5
	GdDOTAM ³⁺	1.9×10 ⁴	2.5	4.9**
	GdDTMA ³⁺	1.7×10 ⁴	2.5	6.9**

*298 K, 20 MHz, **Eu(III) chelates.

6.1.3. Chemical Exchange Saturation Transfer

Although amide containing ligand systems do not have optimal relaxometric properties to be optimal GBCAs, their slow water exchange kinetics allow them to have utility in a different modality of medical imaging. Chemical exchange saturation transfer (CEST) is a methodology that provides information about biological processes *via* ligand exchange systems, as described in detail in Chapter 1. First described by Balaban *et al.*, CEST can illuminate metabolic processes, temperature, pH and other physiological information.¹⁰⁷ Through low power saturation pulses, CEST differentiates between two pools of exchangeable protons.

For biological processes such as metabolism, many exchangeable labile protons on metabolic molecules of interest are in such low concentrations in comparison to the bulk water of the system, their peaks are completely buried under the water signal. Thus, in order to probe these systems, their labile protons of interest, need to be separated from the bulk water system. Using a para-CEST agent, allows for the protons to be shifted away from the bulk water signal. Paramagnetic anisotropic lanthanide (III) chelates have shown to be effective shift reagents, shifting the exchangeable water molecule protons to hundreds of PPM away from the bulk water solvent signal. Commonly lanthanide (III) ions used for para-CEST agents are europium, dysprosium, holmium, erbium, thulium, and ytterbium.

For a para-CEST agent to be effective when coupled with the low power saturation CEST pulse sequence, the exchange rate between the two pools of water needs to be slow. Thus, the slow water exchange kinetics of an amide-containing ligand system is ideal for maximum CEST effect. Altering the structure of H₄-DOTA by integrating amide

coordinating pendant arms, allows for the amide proton to exhibit simple exchange with the bulk water.¹⁰⁸ The CEST shift reagent can shift this exchangeable proton away from the bulk water peak, and altering the type of coordinating amide can impact the rate of this exchange process. This slow exchange process probed by a para-CEST system allows researchers to glean information about metabolic rates due to water playing an integral role in the metabolism of various biologically relevant molecules.

6.1.4. Bimodal Agents and Bifunctional Chelators

With the growing prevalence of bifunctional chelators (BFCs) in laboratory settings, the ideal structure to attach a targeting vector to a macrocyclic scaffold has yet to be established. As described in Chapter 3, functionalizing through a monoamide pendant arm provides a facile handle for subsequent bioconjugation. As shown with GdDO3A-NBAM in Chapter 3, the substitution of one carboxylate pendant arm with a monoamide slows water exchange substantially. Although not ideal for a GBCA, this slowed water exchange could be implemented into a BFC for use as a para-CEST agent. This would allow for a bimodal agent in which metabolic processes of interest could be monitored *via* selective conjugation with a biologically relevant molecule.

Furthermore, by exploring different amide pendant arms the ligand structure can be tuned in order to find a GBCA with optimized water exchange kinetics. Ratnakar *et al.* has described the impact on water exchange based on the type of functional group in the para-position of a phenyl-derived monoamide.¹⁰⁹ The electronic impact of the type of group highlights the impact a withdrawing or donating group has on k_{ex} , with donating groups increasing the exchange rate substantially. The increased electron density being donating

towards the lanthanide center will reduce the electronic deficiency, thus increasing the rate of water exchange. If these effects could be increased, a monoamide pendant arm containing a functionalizable moiety might provide to be a facile approach to a BFC structure.

6.2. Synthesis of Monoamide Chelates

Three monoamide pendant arm containing chelates were synthesized with assistance from Alexis Newberry. They were chosen due to their differing sterics as well as electronic properties. Two primary amines and one secondary amine were selected for conversion to a monoamide, aniline, benzylamine and dibenzylamine, as shown in Figure 6.3. The synthesis of the three monoamides was completed *via* a facile nucleophilic acyl substitution, adapted from Woods *et al.*⁸ Syntheses for the DO3A-phenylamide and DO3A-Benzylamide ligands have been reported previously with slightly different conditions and lower yields.¹¹⁰ The synthesis proposed herein utilized mild conditions and robust yields, and did not require silica-column purification of the ligands like in the literature.

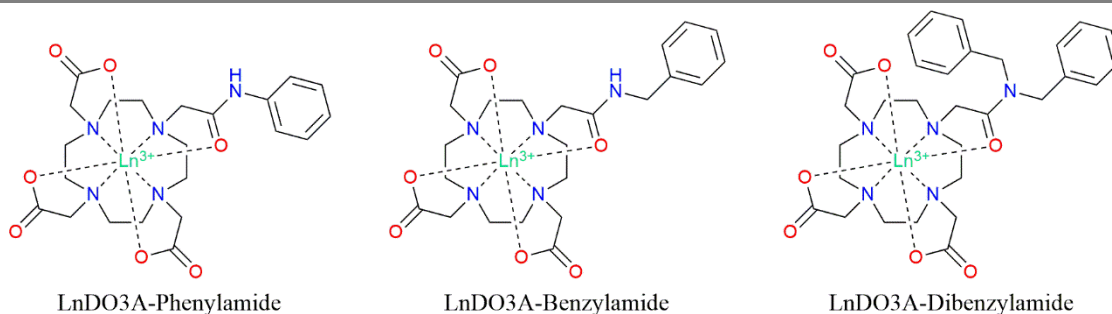
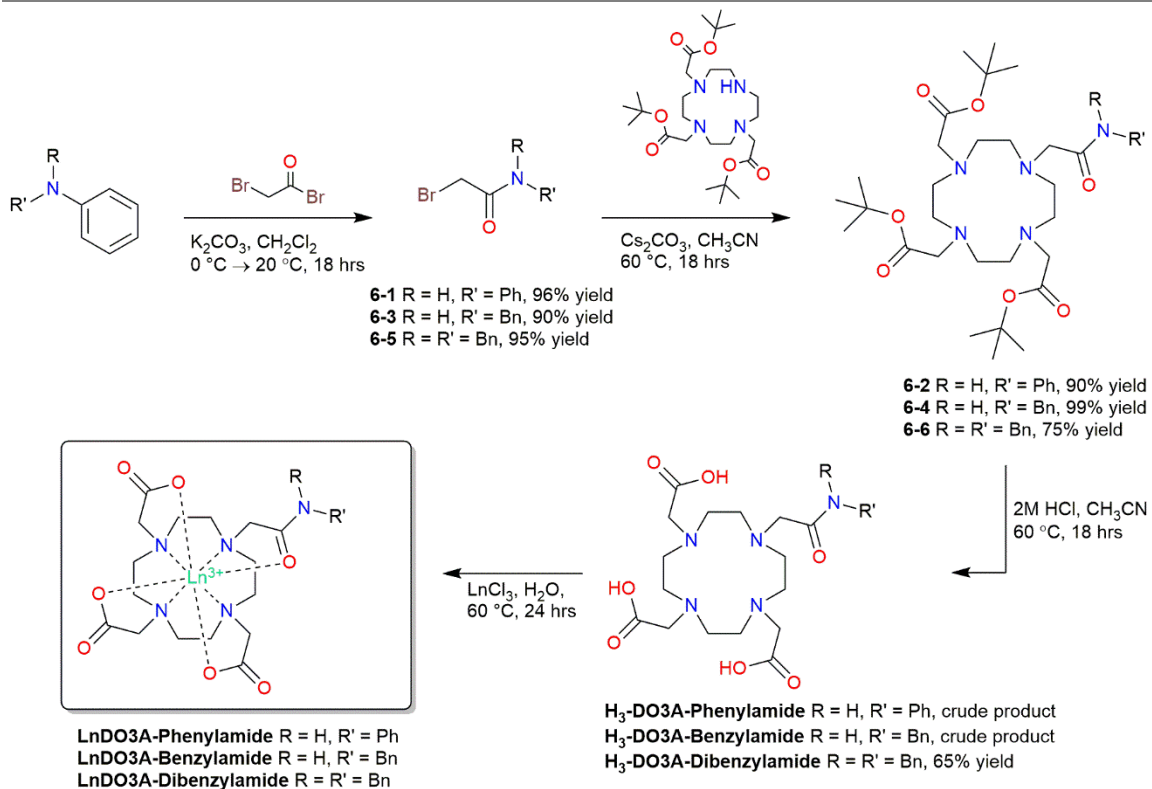


Figure 6.3. The three monoamide containing chelates explored herein. (Ln = Eu, Gd, Yb).

All three monoamide chelates were synthesized using the same procedure, Scheme 6.1. The DO3A-*tert*-butyl ester was prepared using the methods of Raghunand *et. al.*⁷⁴ A facile nucleophilic acyl substitution with aniline and potassium carbonate in dichloromethane at 60 °C generated the bromo-amide alkylating agent (**6-1**, 96% yield; **6-3**, 90% yield; **6-5**, 95% yield). DO3A-*tert*-butyl ester was alkylated with potassium carbonate and acetonitrile at 60 °C using the bromo-amide alkylating agent to generate the protected ligand (**6-2**, 90% yield; **6-4**, 99% yield; **6-6**, 75% yield). The esters were cleaved using 4M HCl in water to generate the ligand (**DO3A-Phenylamide**, crude; **DO3A-Benzylamide**, crude; **DO3A-Dibenzylamide**, 65% yield). The dibenzylamide protected ligand (**6-6**) was subject to column purification to yield a pure product. The ligand was chelated lanthanide chlorides (EuCl₃, GdCl₃, YbCl₃) in water and acetonitrile at pH 5.5 to yield the complex, each was then purified *via* RP-HPLC (**LnDO3A-Phenylamide**, **LnDO3A-Benzylamide**, and **LnDO3A-Dibenzylamide**).



Scheme 6.1. Total synthesis of LnDO3A-Monoamide chelates (Ln = Eu, Gd, Yb).

6.3. Analysis of the Monoamide Chelates

After RP-HPLC purification, $^1\text{H-NMR}$ spectra were collected for both the europium and ytterbium complexes of the three ligands produced. Analysis of the $^1\text{H-NMR}$ spectra of the ytterbium complexes of each chelate *via* line fitting in NUTS of the axial protons of the macrocycle affords the determination of the coordination geometry ratios, Figure 6.4. The percent square antiprism (SAP) coordination geometry is shown in Table 6.2. These data show the expected high ratio of SAP for all three monoamides synthesized. The ratio of SAP was higher in all three YbDO3A-monoamide chelates than the tetraamide YbDOTAM. However, this is not entirely surprising, it has previously been

demonstrated that increasing the number of coordinating amide pendant arms from one to two, results in an increase in the percentage of TSAP in solution.^{111,112} The high ratio of SAP for all three chelates would increase the shift difference of the protons on an $^1\text{H-NMR}$ spectrum. As a result, both YbDO3A-Phenylamide and YbDO3A-Benzylamide would make good candidates for CEST analysis. Because YbDO3A-Dibenzylamide does not contain an exchangeable proton, it would not be able to undergo CEST. CEST experiments were started on both chelates, however due to the outbreak of COVID-19 were not completed.

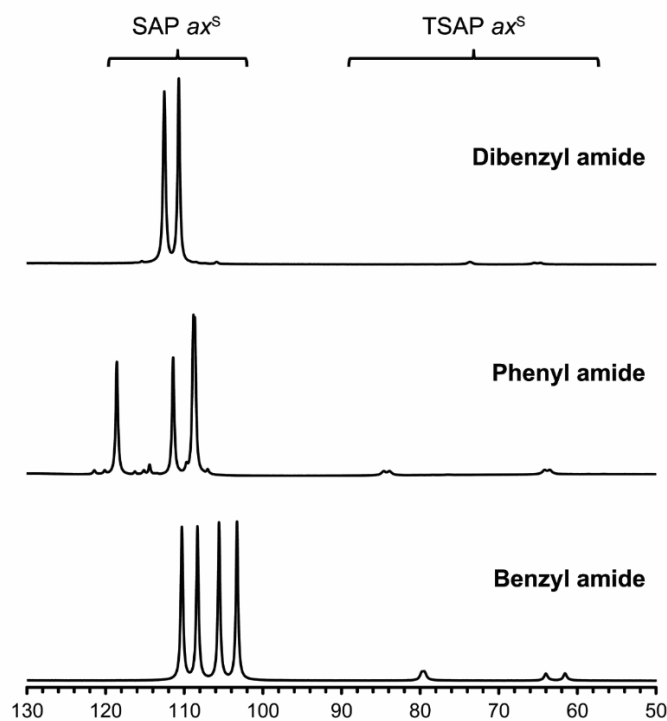


Figure 6.4. Axial proton regions of the macrocycle in the $^1\text{H-NMR}$ spectra of Yb complexes of DO3A-Dibenzylamide (Top), DO3A-Phenylamide (Center), and DO3A-Benzylamide (Bottom).

Table 6.2. Coordination geometry ratios for amide-containing chelates.*Values from Aime *et. al.*⁵¹ †Values from Aime *et. al.*¹⁰⁶

Chelate	% SAP
*YbDOTA	81
†YbDOTAM	84
YbDO3A-Phenylamide	90
YbDO3A-Benzylamide	95
YbDO3A-Dibenzylamide	91

One unexpected piece of data arose upon analysis of the ¹H-NMR spectra of the Yb complexes. Analyzing the shifts of the axial protons on the macrocycle and the aromatic protons on the monoamide pendant arm revealed strong evidence that these complexes maintain different orientations. This is evident when the shifts of these protons of the three chelates are compared. The differences in axial proton shifts observed in the ¹H-NMR spectra of the three YbDO3A-Mononamides are subtle, however, are in slightly different locations, with YbDO3A-Phenylamide having the furthest downfield shifted peak, Figure 6.4. Analyzing the aromatic region of the ¹H-NMR spectra for the three chelates, it is more apparent that their aromatic protons have very different shifts, Figure 6.5.

The aromatic protons of YbDO3A-Phenylamide are shifted slightly downfield, whereas YbDO3A-Benzylamide and YbDO3A-Dibenzylamide both have upfield shifted aromatic protons. This difference can be attributed to the position of the aromatic group within the magnetic field induced by the *f*-electrons of the Yb³⁺ ion. The protons on aromatic substituted chelates typically shift in the region that is seen in their ligand structures, in the range of ~7 – 10 ppm. However, if the orientation of the aromatic group

is positioned in a way that it is influenced by the paramagnetic lanthanide, an upfield shift can occur. What is interesting about these three monoamides is that the addition of a methylene group results in a shift of the aromatic protons. Furthermore, the induced shift experienced by YbDO3A-Benzylamide and YbDO3A-Dibenzylamide are different; the aromatic protons of YbDO3A-Benzylamide are shifted upfield, while YbDO3A-Dibenzylamide has aromatic protons in the same upfield region as YbDO3A-Benzylamide but also some that are slightly downfield of those.

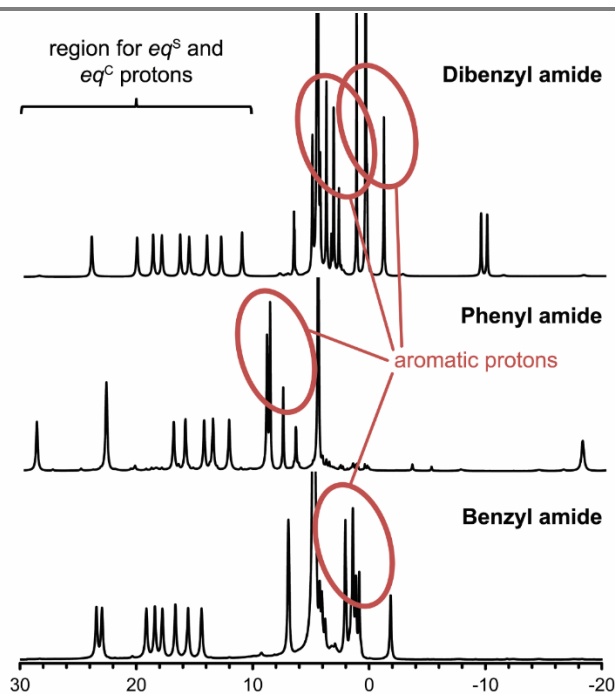


Figure 6.5. Aromatic proton regions in the ^1H -NMR spectra of Yb complexes of DO3A-Dibenzylamide (Top), DO3A-Phenylamide (Center), and DO3A-Benzylamide (Bottom).

Although these differences in observed proton shifts in these chelates appear to be structural in origin, crystal structures of analogs of tetra-phenylamide and tetra-benzylamide chelates have been published and may provide greater insight into these

structural changes. The crystal structure of the Tm^{3+} complex of the tetra-*para*-methoxyphenylamide from Milne *et. al.* shows the phenyl groups of the amide pendant arms to be oriented up towards the oxygen plane, as shown in Figure 6.6 Left.¹¹³ The addition of a methylene group as seen in the Gd^{3+} complex of the tetra-*para*-methyl-benzylamide derivative from Basal *et. al.* orients the benzylic groups of the amide pendant arms down towards the nitrogen plane, as shown in Figure 6.6 Right.¹¹⁴

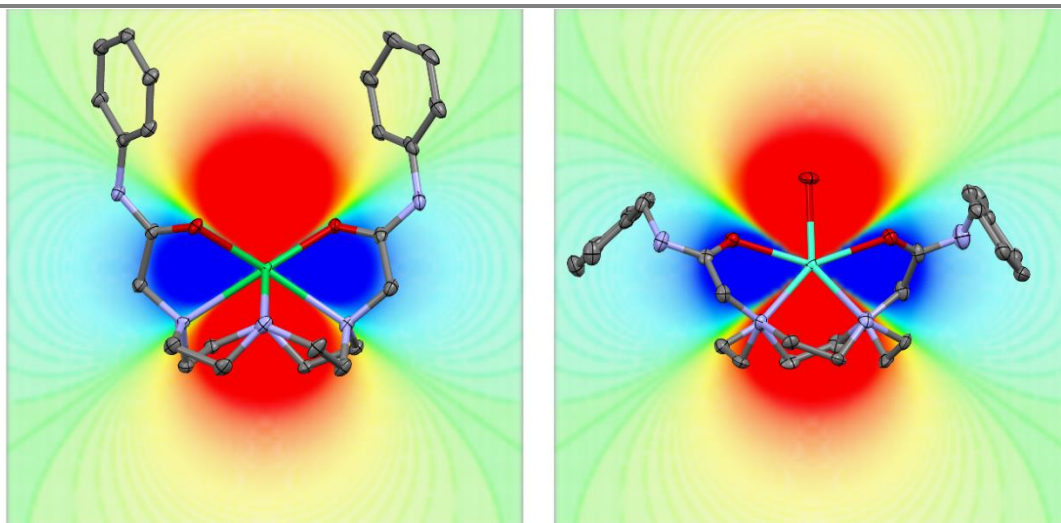


Figure 6.6. The superposition of the crystal structures of the *p*-OMe derivative of Tm Tetra-phenylamide (Left) and the *p*-Me derivative of Gd Tetra-benzylamide (Right) on a heat map of the magnetic field induced by the paramagnetic Ln^{3+} ion. In each case two pendant arms of the chelate and any aromatic substituents are not shown for clarity. The magnetic field is assumed to be perfectly axial with the principal magnetic axis aligned along the Ln-OH_2 bond (if present). Red regions correspond to a downfield shift for Ln^{3+} and blue regions correspond to upfield shifts in the $^1\text{H-NMR}$. Crystal structures obtained from Milne *et. al.* and Basal *et. al.*^{113,114}

When these crystal structures are superimposed onto a “heat map”, where the blue region indicates upfield shifts and red indicates downfield shifts, it is evident why the

change in shift is observed for the DO3A-Monoamides. The phenyl groups of the tetraphenylamide chelate (Figure 6.7 Left) are in the orange-yellow region of the superimposed heat map; this corresponds to downfield shifts in the observed $^1\text{H-NMR}$ spectrum. In contrast, the benzyl substituents on the tetrabenzylamide chelate (Figure 6.7 Right) are completely in the blue region of the heat map which reflects upfield shifts in the $^1\text{H-NMR}$ spectrum.

These data suggest that the type of amide substituent influences structure and would therefore impact how the three DO3A-Monoamide chelates behave in solution. We would expect that DO3A-Phenylamides would have slower water exchange due to the greater influence of the paramagnetic lanthanide; this would likely correspond to a shorter metal-water bond distance. Both DO3A-Benzylamide and DO3A-Dibenzylamide chelates would likely have faster water exchange than the phenylamide derivative. Their structures are less influenced by the paramagnetic lanthanide as demonstrated by their upfield shifts, which would result in a longer metal-water distance and thus faster exchange.

6.4. Conclusions and Future Directions

We presented a facile and inexpensive synthesis for three different DO3A-monoamides. This synthetic strategy facilitates alteration of the monoamide pendant arm by using different primary or secondary starting amines. The three ligands synthesized, DO3A-Phenylamide, DO3A-Benzylamide, and DO3A-Dibenzylamide represent attractive scaffolds to study slower exchanging systems. YbDO3A-Phenylamide and YbDO3A-Benzylamide provide two novel structures to study the CEST effect in a monoamide-substituted chelate. Unfortunately, CEST collection was interrupted due to the COVID-19

pandemic and data is still being processed. We hypothesize that both YbDO3A-Phenylamide and YbDO3A-Benzylamide will have long τ_M values due to their near 100% SAP coordination geometry ratios, resulting in a high CEST effect. This should also reduce relaxivity as gadolinium chelates, as seen with GdDO3A-NBAM in Chapter 3.

The shift differences in the aromatic protons on the phenyl and benzyl substituents on the Yb complexes of these three chelates elucidated interesting information about structure. These unexpected shift differences can be explained when reviewing crystal structures of tetraamide analogs. The orientation of the aromatic ring on these chelates is up in the phenylamide derivative, and down in the benzylamide derivative. Thus, the addition of a methylene group alters the structure drastically enough to result in differences in $^1\text{H-NMR}$ spectra. These preliminary data suggest that these differences could influence the rate in which these monoamide chelates exchange water, with DO3A-Phenylamide most likely having a slower water exchange rate than DO3A-Benzylamide and DO3A-Dibenzylamide due to its closer proximity to the lanthanide center.

The increased hydrophobicity of LnDO3A-Dibenzylamide chelates should allow it to have a slower rotational correlation time in solution. This makes this scaffold an intriguing option necessitating further exploration into a dibenzyl-substituted chelate and comparing them to non-aromatic substituted monoamide chelates. The data presented in Chapter 3 explores the impact of a monoamide substituted chelate as a potential BFC scaffold. Although the chelates presented herein do not contain an active moiety for functionalization, their structures represent the impact slightly tuning the monoamide-substituted scaffold has on water exchange and relaxivity. The higher ratio of TSAP for

chelates of DO3A-Dibenzylamide might provide a slightly shorter τ_M than other monoamide substituted chelates, rendering it a better tuned structure as a GBCA. Relaxometric data is currently being collected on the gadolinium chelates of all three structures, and these data will give further insight into the effect structure has on function. These data could help facilitate tuning the scaffold of DO3A-NBAM explored in Chapter 3, to develop a more robust and effective BFC.

CHAPTER 7

EXPERIMENTAL

7.1. General Procedural Remarks

All reagents and solvents were obtained from commercial sources and used as received. 18.2 M Ω -cm water was used in all reactions, workups, purification, and analysis. All dry solvents were obtained from a solvent still with adsorption columns for oxygen and water.

HPLC purified compounds utilized a Waters 2545 Quaternary Gradient Module affixed with a Phenomenex Luna C18(2) 50 \times 250 mm column. All methods applied a 50 mL/min flow rate, continuous He sparge, a polar phase of aqueous 0.037% HCl (w/w), and an organic phase of 100% acetonitrile. The gradient used in each purification is described below. Absorption was monitored using a Waters 2489 UV-Vis detector at wavelengths described below.

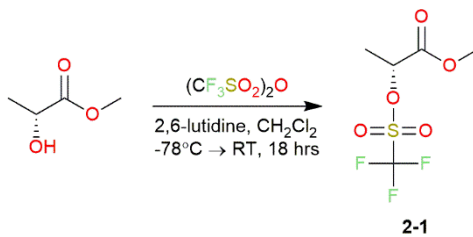
All NMR analyses were conducted on a Bruker Avance II+ spectrometer operating at 400.13 MHz with a 5 mm BBFO probe, or a Bruker Avance III+ spectrometer operating at 600.14 MHz with a 5 mm TXI probe, when denoted. Temperature controlled experiments utilized the installed variable temperature controller model 2416 with a BCU-05 chiller. All NMR spectra were obtained by preparing synthesized compounds in 99.9% enriched D₂O, CD₃CN, or CDCl₃.

Mass spectra were acquired on a ThermoElectron LTQ-Orbitrap Discovery high resolution mass spectrometer.

7.2. Synthesis, purification, and characterization of Chapter 2 Complexes

7.2.1. Synthesis of TbNB-DOTMA S-SSSS Corner and Side Isomers

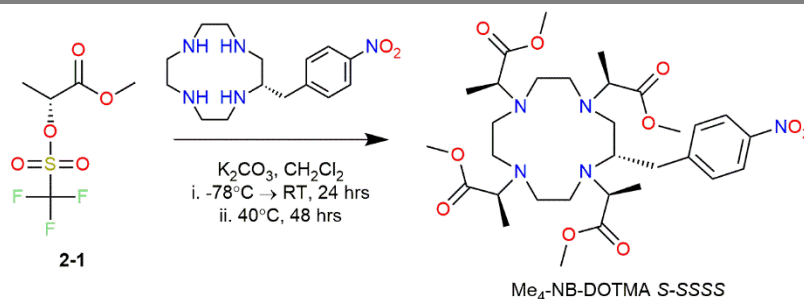
7.2.1.1. Methyl (R)-2-(((trifluoromethyl)sulfonyl)oxy)propanoate (**2-1**)



Scheme 7.1. Synthesis of methyl (R)-2-(((trifluoromethyl)sulfonyl)oxy)propanoate (2-1**).**

On a Schlenk line under inert conditions (N_2 gas), methyl-D-lactate (0.91 mL, 9.6 mmol) was dissolved in dry dichloromethane, and the reaction mixture was cooled to -78 °C. 2,6-Lutidine (1.34 mL, 11.5 mmol) was added to the cooled reaction mixture. A solution of trifluoromethanesulfonic anhydride (1.93 mL, 11.5 mmol) dissolved in dry dichloromethane (50 mL) was added to the reaction mixture *via* cannula dropwise. Then the reaction mixture was stirred at -78 °C for 4 hours. The reaction solvents were then removed *in vacuo*. Under a stream of flowing N_2 , hexanes were added to the pale pink residue and stirred vigorously. The biphasic mixture was separated *via* decanting, and the hexane layer was retained. Hexanes were removed *in vacuo* to afford a colorless oil product, Scheme 7.1 (**2-1**, 1.13 g, 50% yield). The product was used as obtained without characterization.

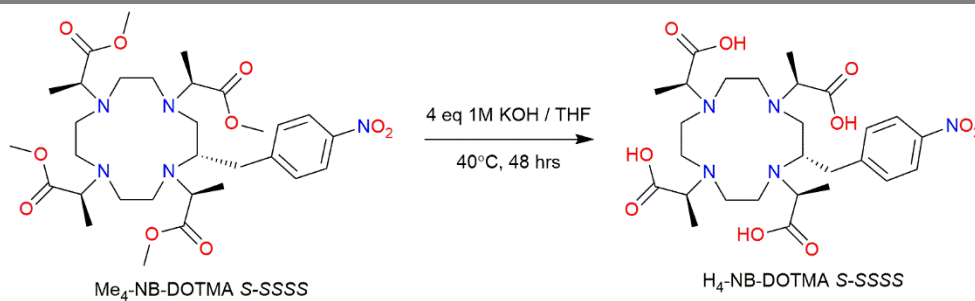
7.2.1.2. Tetramethyl 2,2',2'',2'''-((S)-2-(4-nitrobenzyl)-1,4,7,10-tetraazacyclododecane-1,4,7,10-tetrayl)(2S,2'S,2''S,2'''S)-tetrapropionate (**S-SSSS Me₄-NB-DOTMA**)



Scheme 7.2. Synthesis of protected methyl ester ligand (**Me₄-NB-DOTMA S-SSSS, 2-2**) via alkylation of **2-1** onto NB-cyclen.

On a Schlenk line under inert conditions (N_2) dry dichloromethane (100 mL) was added to a mixture of (*S*)-2-(4-nitrobenzyl)-1,4,7,10-tetraazacyclododecane (0.1 g, 0.325 mmol) and potassium carbonate (0.2841 g, 1.63 mmol), and the reaction mixture was cooled to -78°C . A mixture of **2-1** (1.13 g, 4.8 mmol) in dry dichloromethane (50 mL) was added dropwise *via* cannula to the reaction mixture. The reaction was stirred from -78°C – RT under flowing N_2 for 18 hours. The reaction was then heated at 40°C under flowing N_2 for 48 hours. The reaction mixture was washed three times with a potassium carbonate solution (pH 10), and the organic layer was dried *in vacuo* to afford a dark yellow oil crude product, confirmed by MS (**ESMS ESI(+)** m/z : 652.36 ($[\text{M}]^+$, 100%)), Scheme 7.2 (**Me₄-NB-DOTMA S-SSSS**). The product was used without further purification.

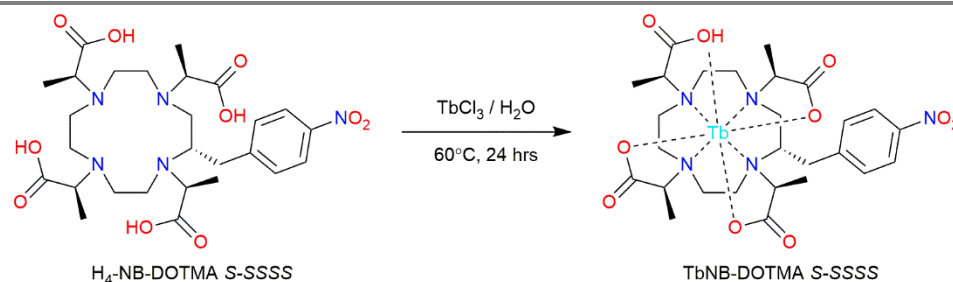
7.2.1.3. (2*S*,2'*S*,2''*S*,2'''*S*)-2,2',2'',2'''-((*S*)-2-(4-nitrobenzyl)-1,4,7,10-tetraazacyclododecane-1,4,7,10-tetrayl)tetrapropionic acid (**S-SSSS H₄-NB-DOTMA**)



Scheme 7.3. Synthesis of ligand *S*-SSSS H₄-NB-DOTMA via methyl ester hydrolysis of *S*-SSSS Me₄-NB-DOTMA.

The crude reaction mixture of Me₄-NB-DOTMA *S*-SSSS was dissolved in THF (10 mL) and 8 equivalents of 1M KOH (5.2 mL) was added. The reaction was heated at 60 °C for 48 hours, until the biphasic solution became monophasic. The solvents were removed *via* lyophilization to yield a crude brown solid. The product was not isolated and used without further purification, Scheme 7.3 (**H₄-NB-DOTMA *S*-SSSS**).

7.2.1.4. *Terbium tetramethyl 2,2',2'',2'''-((S)-2-(4-nitrobenzyl)-1,4,7,10-tetraazacyclododecane-1,4,7,10-tetrayl)(2S,2'S,2''S,2'''S)-tetraacetate (S-SSSS TbNB-DOTMA Corner and Side isomers)*



Scheme 7.4. Synthesis of target chelate, *S-SSSS TbNB-DOTMA* via chelation of *S-SSSS H₄-NB-DOTMA* with TbCl_3 .

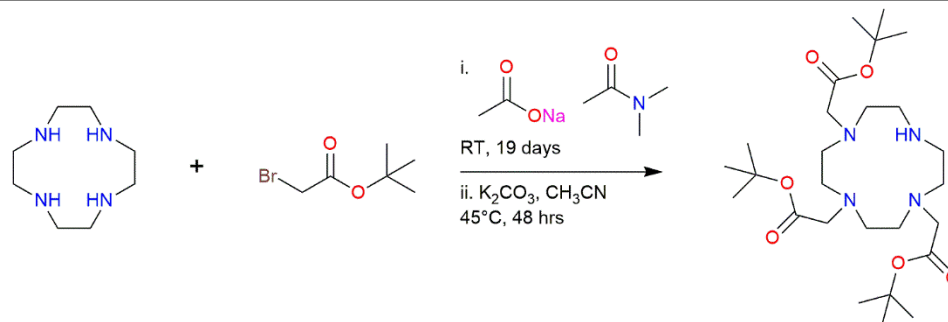
Terbium (III) chloride (2 equivalents) and the crude reaction mixture of *H₄-NB-DOTMA S-SSSS* and dissolved in water. The solution pH was adjusted to 5.5 with dilute KOH and heated the reaction was at 60 °C for 48 hours, Scheme 7.4. The solvents were removed *via* lyophilization to yield a crude waxy solid. The crude residue was subjected to separation and purification *via* RP-HPLC utilizing the solvent system in Table 7.1.

Table 7.1. RP-HPLC purification method for LnNB-DOTMA chelates.

Time (minutes)	% A (0.037% HCl)	%B (100% MeCN)
0 – 3	78	22
18	65	35
20	65	35
20.1	78	22
26 – 26.1	78	22

The HPLC fractions were dried *via* lyophilization to yield two colorless solids, the Corner ($R_T = 16.8$ minutes, 10 mg, 4% yield) and Side ($R_T = 19.8$ minutes, 8.7 mg, 4% yield) (**S-SSSS TbNB-DOTMA Corner and Side**). Both chelates were verified by ^1H -NMR and the data consistent with previously published spectra.¹¹⁵ **TbNB-DOTMA Corner 400 MHz D₂O; ^1H (ppm):** δ : -378.52 (1H), -350.98 (1H), -335.08 (1H), -321.02 (1H), -150.30 (1H), -103.06 (1H), -94.93 (1H), -91.47 (1H), -61.95 (1H), -56.60 (1H), -51.81 (1H), -49.36 (1H), -32.09 (1H), 1.3732 (1H), 1.60 (1H), 1.98 (1H), 3.61 (1H), 6.93 (1H), 7.75 (1H), 9.65 (1H), 11.08 (1H), 16.56 (1H), 17.08 (1H), 36.20 (1H), 51.99 (1H), 56.58 (1H), 60.78 (1H), 63.89 (1H), 68.36 (1H), 73.64 (1H), 85.57 (1H), 89.61 (1H), 93.84 (1H), 116.16 (1H), 121.89 (1H), 146.93 (1H), 197.62 (1H), 463.73 (1H). **TbNB-DOTMA Side 400 MHz D₂O; ^1H (ppm):** δ : -470.91 (1H), -386.78 (1H), -347.39 (1H), -345.56 (1H), -112.14 (1H), -100.91 (1H), -95.26 (1H), -75.13 (1H), -72.66 (1H), -60.64 (1H), -59.85 (1H), -57.06 (1H), -54.52 (1H), -23.10 (1H), -15.77 (1H), -1.76 (1H), -1.39 (1H), 0.14 (1H), 0.91 (1H), 1.36 (1H), 1.59 (1H), 1.97 (1H), 2.75 (1H), 3.51 (1H), 7.50 (1H), 8.22 (1H), 53.31 (1H), 61.84 (1H), 64.72 (1H), 71.33 (1H), 98.24 (1H), 118.97 (1H), 169.96 (1H), 172.09 (1H), 243.33 (1H), 298.47 (1H), 319.85 (1H), 324.95 (1H).

7.3. Synthesis, purification, and characterization of Chapter 3 Complexes

7.3.1. DO3A *tert*-Butyl Esters Synthesis (Used in Chapter 3 and Chapter 5 Complexes)**Scheme 7.5.** Synthesis of DO3A-*tert*-butyl esters.

i. **Alkylation.** On a Schlenk line under inert conditions (N_2 gas), 1, 4, 7, 10-tetraazacyclododecane (cyclen, 25 g, 0.145 mol) was dissolved in dimethylacetamide (428 mL, 4.6 mol). Sodium acetate (37.8 g, 0.41 mol) was added to the stirring solution. *tert*-Butyl bromoacetate (63.9 mL, 0.41 mol) in dimethylacetamide (70 mL) was added dropwise using a pressure equalized drop funnel, and the reaction mixture was stirred for 18 hours under nitrogen purge. After the addition of the *tert*-butyl bromoacetate solution, the reaction flask was stoppered and left to stir at room temperature for 19 days.

The reaction mixture was then filtered through a sintered glass filter. The liquid filtrate was reduced *in vacuo* to yield more solid, this solid was combined with the original filter cake. The filter cake was dried under vacuum for 18 hours. The filter cake was then washed with chloroform through the sintered glass filter into a separatory funnel. The chloroform solution was washed with water (3×200 mL), and the organic solvents were

dried (Na_2SO_4) and removed *in vacuo*. The residual solids were further dried on the diaphragm pump for 18 hours.

ii. **Neutralization of the HBr Salt.** The dried solid was weighed to determine the amount of potassium carbonate to add to neutralize the HBr salt product. The mass of potassium carbonate needed was determined *via* Equation 6.1.

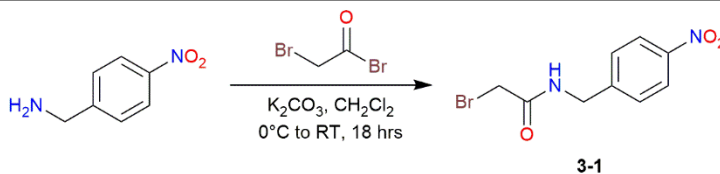
$$\text{g K}_2\text{CO}_3 = \left[\frac{(\text{g crude HBr Salt Solid} \times 276.42 \text{ g/mol})}{676.52 \text{ g/mol}} \right]$$

Equation 7.1. Determination of mass of potassium carbonate to add to the DO3A^tBu ester HBr salt to effectively neutralize.

The dried solid was dissolved in 100 mL acetonitrile, and potassium carbonate (30.46 g, 0.11 mol) was added to the solution. The reaction mixture was stirred and heated at 45°C for 48 hours. After the reaction time, the solution was filtered through a filtered glass funnel, and organic solvents were removed *in vacuo* to yield a dark yellow residue. The residue was extracted 3 × 200 mL diethyl ether to yield a bright orange oil (**DO3A-*tert*-butyl esters**, 39.9 g, 53% yield). The orange oil was recrystallized out of hexanes and dichloromethane *via* a slow evaporation of solvents to yield a colorless fluffy powder. ¹H-NMR and ¹³C-NMR spectra were consistent with previously published data (**ESMS ESI(+)** *m/z*: 515.38 ([M + 1]⁺, 100%)).⁷⁴

7.3.2. Synthesis of DO3A-NBAM derivatives

7.3.2.1. 2-Bromo-N-(4-nitrobenzyl) acetamide (3-1).

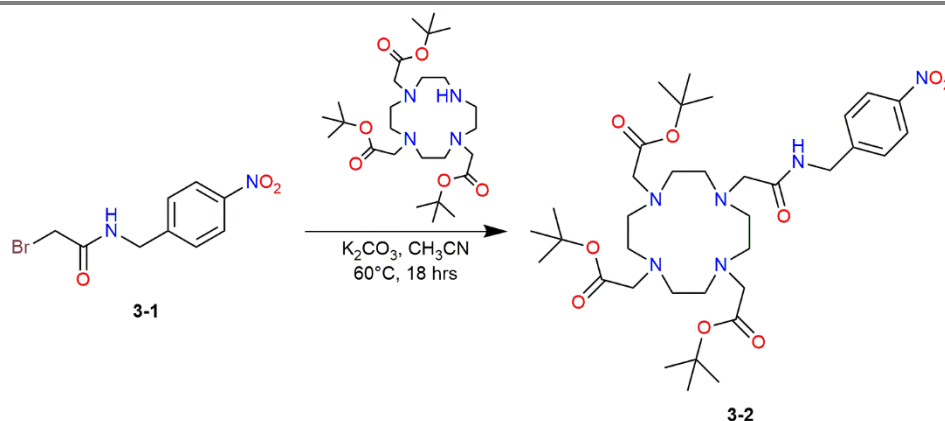


Scheme 7.6. Synthesis of 2-bromo-N-(4-nitrobenzyl) acetamide (3-1).

4-nitrobenzylamine (0.5 g, 2.7 mmol) was dissolved in 2M potassium carbonate solution (20 mL) and cooled to 0°C. Bromo acetyl bromide (0.46 mL, 5.3 mmol) was dissolved in dichloromethane (20 mL) and added dropwise to the 4-nitrobenzylamine solution over the span of one hour. The reaction mixture stirred until it reached room temperature for 18 hours, Scheme 7.6. The opaque solution was extracted with dichloromethane (3 × 50 mL), and the organic layer was dried (Na₂SO₄) and solvents removed *in vacuo* to afford a colorless solid product. The colorless solid was diluted with methanol (15 mL) and heated at 70°C until dissolved. The solution was heated until the volume was reduced to <5 mL and then allowed to slowly cool to room temperature. After cooling, colorless cubic-like crystals formed. The isolated and dried crystals were characterized (**3-1**, 0.67 g, 77% yield). **600MHz CDCl₃; ¹H (ppm):** δ: 3.89 (s, 2H), 4.52 (d, *J* = 6.14 Hz, 2H), 6.92 (s, 1H), 7.38 (d, *J* = 8.42 Hz, 2H), 8.13 (d, *J* = 8.23 Hz, 2H); **¹³C (ppm):** δ: 28.88, 43.41, 124.01, 128.31, 144.91, 147.51, 165.89. **ESMS ESI(-) *m/z*:** 271.08334 ([M]⁻, 100%), 273.08334 ([M+2]⁻, 98%). **FT-IR ν_{max} = 4000 cm⁻¹ (cm⁻¹):**

695.91 (C–Br), 1108.55 (ar N–O), 1317.98 (amide C–N), 1344.57 (ar N=O), 1513.74 (ar sp^2 C=C), 1630.07 (amide C=O), 3010.76 (ar sp^2 C–H), 3261.45 (amide N–H).

7.3.2.2. *Tris-tert-butyl 2, 2', 2''-(10-2((4-nitrobenzyl)amino)-2-oxoethyl)-1, 4, 7, 10-tetraazacyclododecane-1, 4, 7 triyl)triacetate. (3-2)*

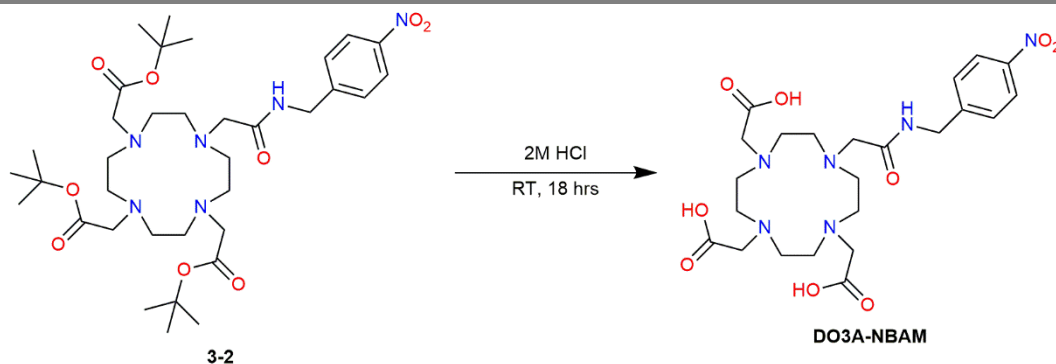


Scheme 7.7. Synthesis of the protected ligand (3-2) via alkylation of 3-1 onto DO3A-*tert*-butyl esters.

DO3A-*tert*-butyl ester (0.5 g, 0.97 mmol) was dissolved in acetonitrile (40 mL). Potassium carbonate (0.67 g, 4.8 mmol) and **3-1** (0.32 g, 1.2 mmol) were added, and the reaction mixture stirred at 40°C for 18 hours, Scheme 7.7. After cooling to room temperature, the solvents were removed *in vacuo*. The opaque brown residue was extracted with dichloromethane (3 × 50 mL), and the organic layer was dried (Na₂SO₄) and solvents removed *in vacuo* to afford a translucent yellow oil product, the protected ligand (**3-2**, 0.61 g, 87% yield). **400 MHz CD₃CN; ¹H (ppm):** δ: 1.45 (27H, s, ^tBu), 2.01 – 2.88 (18H, m, -CH₂), 3.05 – 4.74 (8H, m, -CH₂), 4.48 (2H, s, benzylic -CH₂), 7.56 (2H, d, *J* = 9 Hz, ar -CH), 8.16 (2H, d, *J* = 9 Hz, ar -CH). **¹³C (ppm):** δ: 27.8 (9C, ^tBu), 41.6 (1C, -CH₂), 49.4 –

56.8 (8C, broad, $\text{NCH}_2\text{CH}_2\text{N}$), 57.9 (3C $-\text{CH}_2$), 62.5 (1C, $-\text{CH}_2$), 81.9 (2C, $\text{C}(\text{CH}_3)_3$), 82.1(1C, $\text{C}(\text{CH}_3)_3$), 124.0 (1C, ar $\text{C}(\text{CH})_2$), 128.6 (2C, ar $\text{C}-\text{H}$), 128.8 (2C, ar $\text{C}-\text{H}$), 147.4 (1C, ar CNO_2), 173.0 (2C, $\text{C}=\text{O}$), 173.1 (1C, $\text{C}=\text{O}$), 173.4 (1C, $\text{C}=\text{O}$). **ESMS ESI(+)** m/z : 729.41348 ($[\text{M} + \text{Na}]^+$, 100%). **FT-IR** $\nu_{\text{max}} = 4000 \text{ cm}^{-1} (\text{cm}^{-1})$: 1106.33 (ester $\text{C}-\text{O}$), 1155.36 (ar $\text{N}=\text{O}$), 1225.24 (amide $\text{C}-\text{N}$), 1342.91 (ar $\text{N}-\text{O}$), 1605.56 (ar $\text{sp}^2 \text{C}=\text{C}$), 1667.13 (amide $\text{C}=\text{O}$), 1724.92 (ester $\text{C}=\text{O}$), 2824.42 (ar $\text{sp}^2 \text{C}-\text{H}$), 2975.38 (amide $\text{C}-\text{H}$). $R_f = (\text{Si}_2\text{O}_2, (\text{CH}_2\text{CH}_3)_2\text{O}) 0.125$.

7.3.2.3. Synthesis of 2, 2', 2''-(10-2((4-nitrobenzyl)amino)-2-oxoethyl)-1, 4, 7, 10-tetraazacyclododecane-1, 4, 7 triyl)triacetic acid. (DO3A-NBAM)

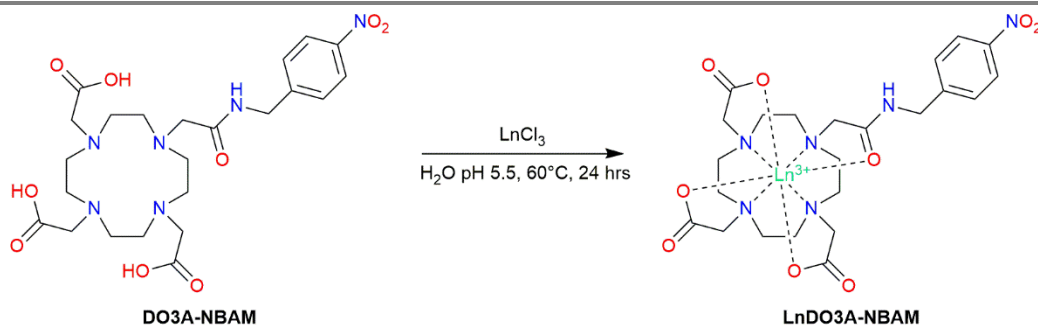


Scheme 7.8. Synthesis of the ligand DO3A-NBAM via tert-butyl ester hydrolysis of the protected ligand (3-2) in acid.

3-2 (0.84 g, 1.19 mmol) was dissolved in 4M HCl (20 mL) and stirred for 18 hours, Scheme 7.8. The acidic solution was neutralized with KOH to pH 6.5 and solvents were removed by lyophilization to yield a solid product (**DO3A-NBAM**, 0.16 g, 24% yield). **400 MHz D₂O; ¹H (ppm):** δ : 2.69 – 3.58 (16H, m, $\text{NCH}_2\text{CH}_2\text{N}$), 3.69 – 4.30 (8H, m, $-\text{CH}_2$), 4.43 (2H, s, $-\text{CH}_2$), 7.41 (2H, d, $J = 9 \text{ Hz}$, ar $-\text{CH}$), 8.07 (2H, d, $J = 9 \text{ Hz}$, ar $-\text{CH}$), **¹³C**

(ppm): δ : 43.0 (1C, $-\underline{\text{C}}\text{H}_2$) 47.5 – 54.7 (8C, broad, $\text{N}\underline{\text{C}}\text{H}_2\underline{\text{C}}\text{H}_2\text{N}$), 60.9 (4C, $-\underline{\text{C}}\text{H}_2$), 123.7 (2C, ar $-\underline{\text{C}}\text{H}$), 128.0 (2C, ar $-\underline{\text{C}}\text{H}$), 145.7 (1C, ar $-\underline{\text{C}}(\text{CH})_2$), 146.8 (1C, ar $-\underline{\text{C}}\text{NO}_2$), 173.9 (4C, $\underline{\text{C}}=\text{O}$). ESMS-ESI(-) m/z : 537.2316 ($[\text{M} - 1]^-$, 100%). FT-IR ν_{max} = 4000 cm^{-1} (cm^{-1}): aromatic N–O 1162.28 cm^{-1} , amide C–N 1213.76 cm^{-1} , aromatic N=O 1344.57 cm^{-1} , carboxylic acid C–O 1387.93 cm^{-1} , aromatic sp^2 C=C 1606.37 cm^{-1} , amide C=O 1676.20 cm^{-1} , carboxylic acid C=O 1724.58 cm^{-1} , aromatic sp^2 C–H 2967.79 cm^{-1} , carboxylic acid O–H 3084.30 cm^{-1} , amide N–H 3356.83 cm^{-1} . R_f = (Si_2O_2 , $(\text{CH}_2\text{CH}_3)_2\text{O}$) 0.075.

7.3.2.4. *Ln(III)-(2, 2', 2''-(10-2((4-nitrobenzyl)amino)-2-oxoethyl)-1, 4, 7, 10-tetraazacyclododecane-1, 4, 7 triyl)triacetate*. (**LnDO3A-NBAM**)



Scheme 7.9. Chelation of the ligand DO3A-NBAM with lanthanide chlorides (EuCl_3 , GdCl_3 , YbCl_3) to produce target complexes.

DO3A-NBAM (0.049 g, 0.09 mmol) and $\text{GdCl}_3 \cdot 6\text{H}_2\text{O}$ (0.072 g, 0.19 mmol) were dissolved in H_2O (10 mL) and acetonitrile (2 mL). The pH was adjusted to 5.5 with KOH and the reaction was stirred and heated at 60°C for 48 hours, Scheme 7.9. The solution was purified by RP-HPLC, with absorbance monitoring at $\lambda = 270$ nm and 205 nm. The solvent system utilized is described in Table 7.2. The RP-HPLC purification yielded a colorless solid product (**GdDO3A-NBAM**, $R_T = 6.9$ minutes, 8.5 mg, 14% yield). ESMS-ESI(-)

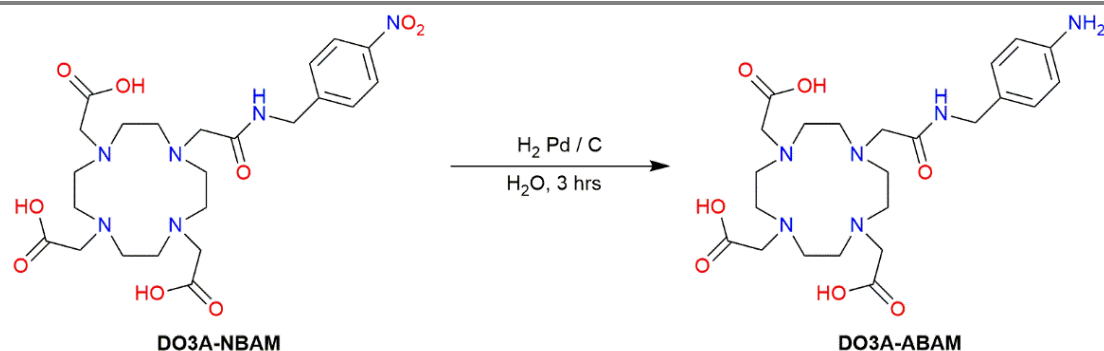
m/z: 692.13 ([M]⁻ with appropriate isotope distribution). **EuDO3A-NBAM** ¹H-NMR **400 MHz D₂O (ppm)**: δ: -18.14 (1H), -18.02 (1H), -17.08 (1H), -16.59 (1H), -16.25 (1H), -15.96 (1H), -13.88 (1H), -13.79 (1H), -12.32 (1H), -11.50 (1H), -8.93 (1H), -8.05 (1H), -7.64 (1H), -7.18 (1H), -5.67 (1H), -5.02 (1H), -3.49 (1H), -2.78 (1H), -1.91 (1H), -1.03 (1H), -0.39 (1H), -0.19 (1H), 2.88 (1H), 3.17 (1H), 4.40 (1H), 6.05 (1H), 6.33 (1H), 32.76 (1H), 33.48 (1H), 34.20 (1H).

Table 7.2. RP-HPLC purification method for LnDO3A-NBAM chelates.

Time (minutes)	% A (0.037% HCl)	%B (100% MeCN)
0 – 5	78	22
12	77	23
13 – 15	20	80
16	78	22
18 – 18.1	78	22

7.3.3. DO3A-BPAM Derivatives

7.3.3.1. 2, 2', 2''-(10-2((4-aminobenzyl)amino)-2-oxoethyl)-1, 4, 7, 10-tetraazacyclododecane-1, 4, 7 triyl)triacetic acid. (**DO3A-ABAM**)

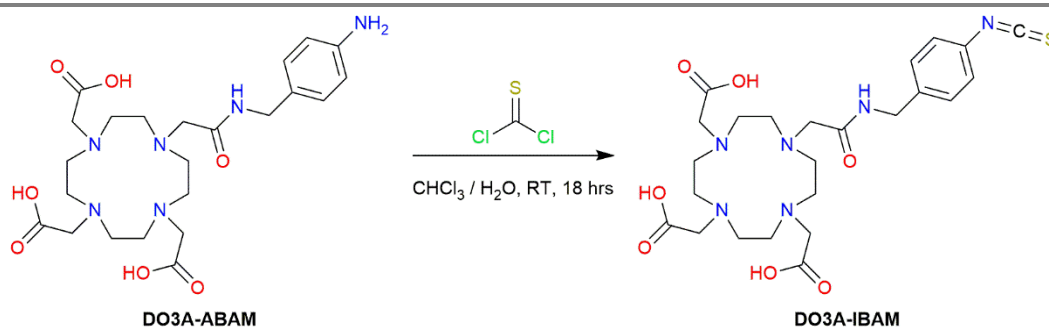


Scheme 7.10. Synthesis of **DO3A-ABAM** *via* hydrogenation of **DO3A-NBAM** with Pd/C.

DO3A-NBAM (0.8604 g, 1.6 mmol) dissolved in H₂O (20 mL) in a 500 mL hydrogenator vessel. A catalytic amount of 10% Pd/C was added, and the reaction mixture was shaken on a Parr Hydrogenator under H₂ at 10 PSI for three hours, Scheme 7.10. The solution was subsequently filtered, and solvents were removed by lyophilization, to yield an orange solid (**DO3A-ABAM**, 0.735 g, 87% yield). **400 MHz D₂O; ¹H (ppm):** δ: 2.92 – 3.95 (16H, m, NCH₂CH₂N), 3.51 – 3.95 (8H, m, -CH₂), 4.34 (2H, s, -CH₂), 7.32 (2H, d, *J* = 8 Hz, ar -CH), 7.40 (2H, d, *J* = 8 Hz, 2H, d, ar -CH). **¹³C (ppm):** δ: 42.5 (1C, -CH₂), 47.5 – 51.0 (8C, broad, NCH₂CH₂N), 55.1 (4C, -CH₂), 122.9 (2C, ar -CH), 128.6 (2C, ar -CH), 138.9 (1C, ar -CNH₂), 141.4 (1C, ar -C(CH₂)₂), 171.6 (4C, C=O). (**ESMS-ESI(+)** *m/z*: 509.4167 ([*M* + 1]⁺, 100%). **FT-IR** ν_{max} = **4000 cm⁻¹ (cm⁻¹):** 1214.07 (carboxylic acid C–O), 1350.83 (amide C–N), 1550.43 (ar sp² C=C), 1675.78 (amide C=O), 1718.80

(carboxylic acid C=O), 2591.12 (ar sp^2 C–H), 2853.73 (carboxylic acid O–H), 3361.90 (ar amine). R_f = (Si₂O₂, CH₃OH) 0.25.

7.3.3.2. 2, 2', 2''-(10-2((4-isothiocyanatobenzyl)amino)-2-oxoethyl)-1, 4, 7, 10-tetraazacyclododecane-1, 4, 7 triyl)triacetic acid. (**DO3A-IBAM**)

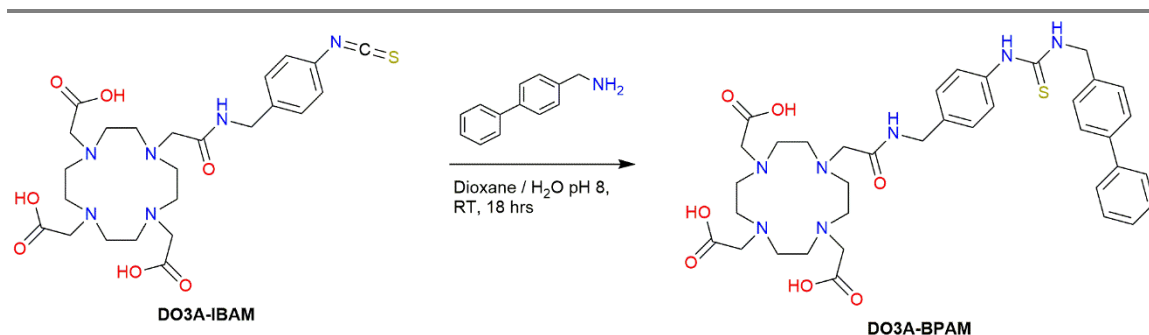


Scheme 7.11. Synthesis of **DO3A-IBAM** from **DO3A-ABAM**.

DO3A-ABAM (0.1093 g, 0.21 mmol) was dissolved in H₂O (10 mL, pH = 2). Thiophosgene (0.05 mL) was dissolved in chloroform (10 mL). The organic solution was added to the aqueous mixture and stirred vigorously at room temperature for 18 hours, Scheme 7.11. The mixture was then washed with chloroform (30 mL). The aqueous phase was dried *via* lyophilization to afford a light orange solid product (**DO3A-IBAM**, 0.102 g, 86% yield). **400 MHz D₂O; ¹H (ppm):** δ : 2.82 – 3.43 (16H, m, NCH₂CH₂N), 3.52 – 3.92 (8H, m, -CH₂), 4.32 (2H, s, -CH₂), 7.23 (J = 8 Hz, 2H, d, ar -CH), 7.71 (J = 8 Hz, 2H, d, ar -CH). **¹³C (ppm):** δ : 41.8 (1C, -CH₂), 46.1 – 51.1 (8C, broad, NCH₂CH₂N), 52.4 (4C, -CH₂), 125.0 (2C, ar -CH), 127.7 (2C, ar -CH), 128.7 (1C, ar -C(CH₂)₂), 133.0 (1C, ar -C(CH₂)₂), 136.4 (1C, NCS), 172.8 (4C, C=O). **ESMS-ESI(+)** m/z : 551.23 ([M + 1]⁺, 100%). **FT-IR ν_{max} = 4000 cm⁻¹ (cm⁻¹):** 1161.44 (carboxylic acid C–O), 1214.71 (amide

C–N), 1537.53 (ar sp^2 C=C), 1673.14 (amide C=O), 1723.59 (carboxylic acid C=O), 2099.67 (ar N=C=S), 2971.58 (ar sp^2 C–H), 3084.69 (carboxylic acid O–H).

7.3.3.3. 2, 2', 2''-(10-(2-((4-(3-([1, 1'-biphenyl]-4-ylmethyl)thioureido)benzyl)amino)-2-oxoethyl)-1, 4, 7, 10-tetraazacyclododecane-1, 4, 7-triyl)triacetic acid (**DO3A-BPAM**)

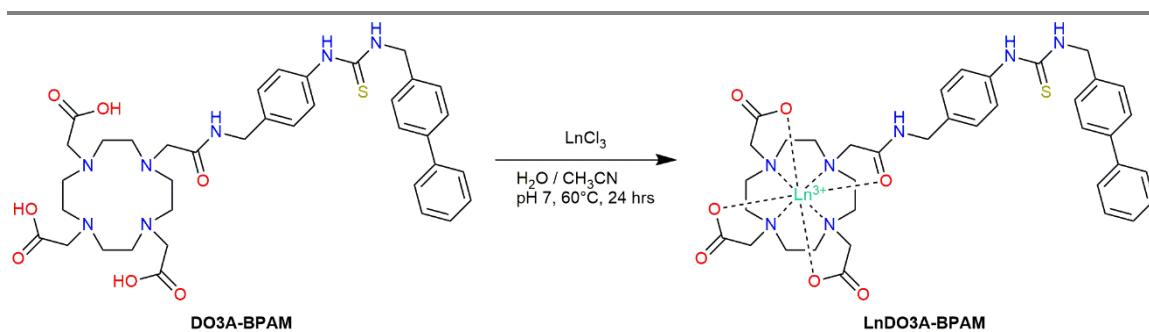


Scheme 7.12. Synthesis of the target ligand, **DO3A-BPAM** from **DO3A-IBAM**.

DO3A-IBAM (0.1022 g, 0.19 mmol) was dissolved in H₂O (5 mL). The pH was adjusted to 8 with KOH. 4-phenylbenzylamine (0.0671 g, 0.4 mmol) dissolved in dioxane (7 mL) was added to the aqueous reaction mixture and it was stirred at room temperature for 18 hours, Scheme 7.12. The flocculent solution was adjusted to pH 7 with HCl and solvents were removed *via* lyophilization to afford a crude fluffy colorless solid (**DO3A-BPAM**, 0.051g, 48% yield). **400 MHz CD₃CN; ¹H (ppm):** δ : 1.19 (2H, s, -CH₂), 1.49 (2H, s, -CH₂), 1.74 (2H, s, -CH₂), 1.76 (2H, s, -CH₂), 1.91 – 2.03 (16H, NCH₂CH₂N), 4.07 (2H, s, CH₂), 4.73 (2H, s, -CH₂), 7.31 (2H, $J = 8$ Hz, d, ar -CH), 7.39 (4H, $J = 8$ Hz, d, ar -CH), 7.49 ($J = 8$ Hz, 3H, t, ar -CH), 7.58 (2H, $J = 8$ Hz, d, ar -CH), 7.62 (2H, $J = 8$ Hz, d, ar -CH), **¹³C (ppm):** δ : 36.4 (4C, broad, -CH₂), 41.6 (2C, -CH₂), 51.6 – 62.3 (8C, broad, NCH₂CH₂N), 111.4 – 125.0 (18C, broad, ar -C(CH)₂), 166.2 (4C, C=O), 190.8 (1C, C=S)

ESMS-ESI(+) m/z : 734.33 ($[M + 1]^+$, 100%), 772.28 ($[M + K]^+$, 50%). **FT-IR** ν_{\max} = **4000** cm^{-1} (cm^{-1}): 733.60 (thiourea C=S), 1087.07 (carboxylic acid C–O), 1220.66 (amide C–N), 1485.16 (thiourea C–N), 1599.83 (ar sp^2 C=C), 1675.77 (amide C=O), 1718.81 (carboxylic acid C=O), 2963.55 (ar sp^2 C–H), 3214.77 (amide N–H), 3372.74 (carboxylic acid O–H). R_f = (Si_2O_2 , CH_3OH) 0.125.

7.3.3.4. *Ln(III)-(2, 2', 2''-(10-(2-((4-(3-([1, 1'-biphenyl]-4-ylmethyl) thioureido) benzyl) amino)-2-oxoethyl)-1, 4, 7, 10-tetraazacyclododecane-1, 4, 7-triyl) triacetate) (LnDO3A-BPAM)*



Scheme 7.13. Chelation of the ligand DO3A-BPAM with lanthanide chlorides (EuCl_3 , GdCl_3) to produce target complexes.

DO3A-BPAM (0.0592 g, 0.081 mmol), and $\text{EuCl}_3 \cdot \text{H}_2\text{O}$ (0.033 g, 0.091 mmol) were dissolved in H_2O (10 mL), the pH of the solution was adjusted to 7 with 1M KOH. The reaction was heated and stirred at 70°C for 24 hours, Scheme 7.13. The solution was purified by RP-HPLC, with absorbance monitoring at $\lambda = 254$ nm and 205 nm. The solvent system utilized is outlined in Table 7.3. The fractions were lyophilized to yield a colorless solid (**EuDO3A-BPAM**, $R_T = 22.3$ minutes, 19.1 mg, 27% yield). **400 MHz D_2O ; ^1H EuDO3A-BPAM:** δ : -16.438 (1H), -14.845 (1H), -12.683 (1H), -8.305 (1H), -6.796

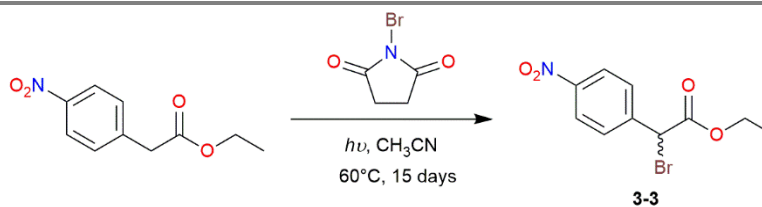
(1H), -6.293 (1H), -4.476 (1H), -1.067 (1H), 1.819 (4H), 2.758 (1H), 3.041 (1H), 3.593 (1H), 3.707 (1H), 4.165 (8H), 7.497 (5H), 7.692 (8H), 32.183 (1H), 32.641 (1H), 33.338 (1H), 34.313 (1H). **GdDO3A-BPAM ESMS-ESI(-) m/z :** 887.2176 ($[M - 1]^-$, with appropriate Gd isotope distribution).

Table 7.3. RP-HPLC purification method for LnDO3A-BPAM chelates.

Time (minutes)	% A (0.037% HCl)	%B (100% MeCN)
0 – 5	100	0
10	100	0
20	20	80
25	20	80
30 – 30.1	100	0

7.3.4. Synthesis of DOTA-NF Derivatives

7.3.4.1. Ethyl 2-bromo-2-(4-nitrophenyl) acetate (3-3)

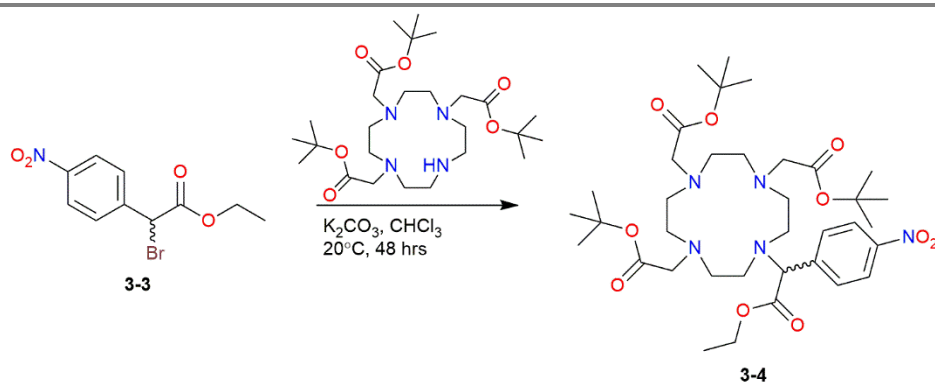


Scheme 7.14. Synthesis of ethyl 2-bromo-2-(4-nitrophenyl) acetate (3-3).

Ethyl 4-nitrophenylacetate (10.05 g, 48 mmol) and *N*-bromo succinimide (12.84 g, 72 mmol) were dissolved in acetonitrile (50 mL). The reaction mixture was equipped with a condenser and was irradiated with a 72-watt UV (365 – 395 nm) light, and heated at 60°C for 15 days, Scheme 7.14. After the reaction time, the dark red liquid was filtered through a sintered glass funnel with diethyl ether. The filtered solution was extracted $3 \times$

100 mL with diethyl ether, and the organic layer was dried *in vacuo* to afford a dark orange oil product (**3-3**, 15.2 g, 86% yield). The spectra for **3-3** were consistent with previously published literature (ESMS-ESI(-) *m/z*: 287.9700 ($[M - 1]^-$, 100%), 285.9722 ($[M - 2]^-$, 98%)).^{116,117} The resulting crude product was used without further purification.

7.3.4.2. *tri-tert-butyl 2,2',2''-(10-(2-ethoxy-1-(4-nitrophenyl)-2-oxoethyl)-1,4,7,10-tetraazacyclododecane-1,4,7-triyl) triacetate (3-4)*

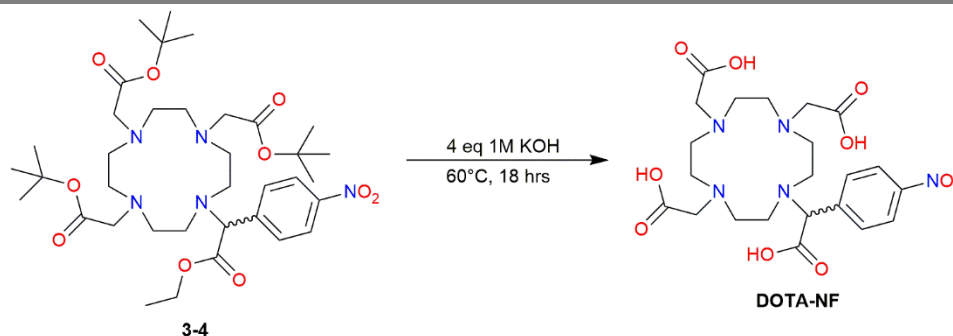


Scheme 7.15. Synthesis of the protected ligand (**3-4**) *via* alkylation of **3-3** onto DO3A-*tert*-butyl esters.

Multiple reaction conditions were attempted to effectively alkylate DO3A-*tert*-butyl esters with **3-3**. The various reaction attempts are discussed in Chapter 3. The reaction that yielded the highest amount of the protected ligand, **3-4**, is shown in Scheme 7.15. DO3A-*tert*-butyl esters (0.104 g, 0.2 mmol), **3-3** (87 mg, 0.3 mmol), and potassium carbonate (55 mg, 0.4 mmol) were dissolved in chloroform (10 mL). The reaction mixture was stirred at ambient temperature ($\sim 20^\circ C$) for 48 hours. The resulting reaction mixture was extracted with water, to yield a dark red residue (**3-4**, 0.14 g, 94% yield). **600 MHz CD_3CN ; 1H (ppm):** δ : 1.48 (27H, s, $^tBu-CH_3$), 2.10 – 3.08 (16H, m, NCH_2CH_2N), 3.38

(2H, s, $-\underline{\text{CH}}_2$), 3.74 (2H, q, $-\underline{\text{CH}}_2\text{CH}_3$), 4.0 (1H, s, $-\underline{\text{CH}}$), 4.19 (3H, t, $-\text{CH}_2\underline{\text{CH}}_3$), 5.32 (4H, s, $-\underline{\text{CH}}_2$), 8.20 (2H, $J = 9$ Hz, d, ar $-\underline{\text{CH}}$), 8.28 (2H, $J = 9$ Hz, d, ar $-\underline{\text{CH}}$). ^{13}C (ppm): δ : 14.0 (1C, $-\underline{\text{CH}}_2\text{CH}_3$), 28.7 (9C, $^t\text{Bu}-\underline{\text{C}}\text{H}_3$), 48.1 – 55.7 (8C, broad, $\text{N}\underline{\text{C}}\text{H}_2\underline{\text{C}}\text{H}_2\text{N}$), 62.7 (3C, $-\underline{\text{C}}\text{H}_2$), 71.1 (1C, $-\text{CH}_2\underline{\text{C}}\text{H}_3$), 82.4 (1C, $-\underline{\text{C}}\text{H}$), 95.5 (3C, $\underline{\text{C}}(\text{CH}_3)_3$), 123.6 (4C, ar $-\underline{\text{C}}\text{H}$), 131.1 (2C, ar $-\underline{\text{C}}(\text{CH})_2$), 173.1 (4C, $\underline{\text{C}}=\text{O}$). **ESMS-ESI(+)** m/z : 744.42 ($[\text{M} + \text{Na}]^+$, 100%), 722.43 ($[\text{M} + 1]^+$, 12%). **FT-IR** $\nu_{\text{max}} = 4000 \text{ cm}^{-1}$ (cm^{-1}): 1159.38 (nitro $\text{N}=\text{O}$), 1258.33 (ester $\text{C}-\text{O}$), 1347.10 (nitro $\text{N}-\text{O}$), 1597.90 (ar $\text{sp}^2 \text{C}=\text{C}$), 1726.49 (ester $\text{C}=\text{O}$), 2979.61 (ar $\text{sp}^2 \text{C}-\text{H}$). **R_f** = (Si_2O_2 , 50% $(\text{CH}_2\text{CH}_3)_2\text{O}$ / 50% hexanes) 0.53.

7.3.4.3. 2,2',2''-(10-(carboxy(4-nitrophenyl)methyl)-1,4,7,10-tetraazacyclododecane-1,4,7-triyl)triacetic acid (**DOTA-NF**)



Scheme 7.16. Synthesis of the ligand **DOTA-NF** *via* ester hydrolysis of the protected ligand (**3-4**) in base.

A crude sample of **3-4** (4.9 g, 6.8 mmol) was added to a solution of 1M KOH (44 mL) and acetonitrile (50 mL). The reaction mixture was heated at 60 °C for 48 hours, Scheme 7.16. The crude reaction mixture was purified *via* RP-HPLC using the solvent system described in Table 7.4, with absorbance monitoring at $\lambda = 270$ nm and 254 nm. The

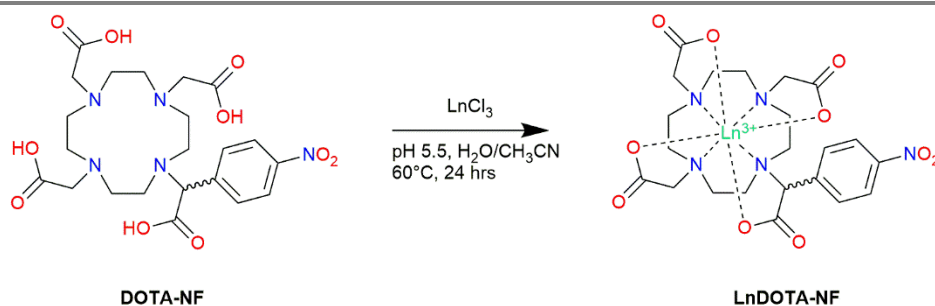
fractions were freeze dried to yield a colorless solid ($R_T = 15.4$ minutes, 0.111 g, 3% yield).

The NMR and MS spectra were consistent with previously published data (**DOTA-NF**, ESMS-ESI(+) m/z : 526.21 ($[M + 1]^+$, 100%)).⁷³

Table 7.4. RP-HPLC method used for nitrophenyl containing ligands.

Time (minutes)	% A (0.037% HCl)	%B (100% MeCN)
0 – 5	100	0
10	60	40
25	20	80
26	100	0
31 – 31.1	100	0

7.3.4.4. *Ln(III)-(2,2',2''-(10-(carboxy(4-nitrophenyl)methyl)-1,4,7,10-tetraazacyclododecane-1,4,7-triyl)triacetate) (LnDOTA-NF)*



Scheme 7.17. Chelation of DOTA-NF with lanthanide chlorides (EuCl₃, GdCl₃).

DOTA-NF (0.102 g, 0.194 mmol) and GdCl₃·6H₂O (0.148 g, 0.4 mmol) were dissolved in water (10 mL) and acetonitrile (10 mL), the pH was adjusted to 5.5 with 1M KOH. The reaction was heated at 60 °C for 48 hours, Scheme 7.17. The chelation mixture was purified *via* RP-HPLC according to the method in Table 7.5. The fractions were lyophilized to yield a colorless solid (**GdDOTA-NF**, $R_T = 15.7$ minutes, 11 mg, 8% yield).

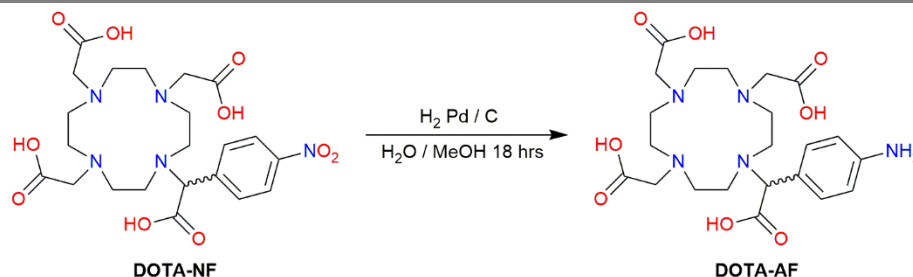
The $^1\text{H-NMR}$ spectrum of the europium complex is consistent with previously published data (**EuDOTA-NF 400 MHz, D₂O, ^1H (ppm) δ** : -18.05 (1H), -17.57 (1H), -16.85 (1H), -16.05 (1H), -15.16 (1H), -14.81 (1H), -11.24 (1H), -10.64 (1H), -10.10 (1H), -8.98 (1H), -8.52 (1H), -7.90 (1H), -7.41 (1H), -6.45 (1H), -6.21 (1H), -5.89 (1H), -5.49 (1H), -5.21 (1H), -4.69 (1H), -4.25 (1H), -3.89 (1H), -3.54 (1H), -2.58 (1H), -2.36 (1H), -1.54 (1H), -0.94 (1H), -0.30 (1H), 0.46 (1H), 1.21 (1H), 1.40 (1H), 1.61 (1H), 1.92 (1H), 1.97 (1H), 2.17 (1H), 2.71 (1H), 3.22 (1H), 3.41 (1H), 3.60 (1H), 3.68 (1H), 5.92 (1H), 6.96 (1H), 7.56 (1H), 7.71 (1H), 7.84 (1H), 8.06 (1H), 8.79 (1H), 12.73 (1H), 13.71 (1H), 14.57 (1H), 16.32 (1H), 33.87 (1H), 35.11 (1H), 36.43 (1H), 37.30 (1H)).⁷³

Table 7.5. RP-HPLC method for nitrophenyl containing chelates.

Time (minutes)	% A (0.037% HCl)	%B (100% MeCN)
0 – 5	100	0
15	20	80
18	20	80
22	20	80
24	100	0
25	100	0
28 – 28.1	100	0

7.3.5. Synthesis of DOTA-BP Derivatives

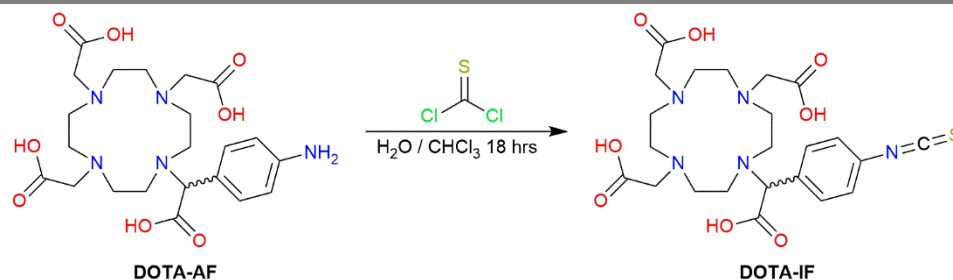
7.3.5.1. 2,2',2''-(10-((4-aminophenyl)(carboxy)methyl)-1,4,7,10-tetraazacyclododecane-1,4,7-triyl)triacetic acid (DOTA-AF)



Scheme 7.18. Reduction of DOTA-NF to DOTA-AF utilizing Pd/C.

DOTA-NF (0.3 g, 0.57 mmol) dissolved in H₂O (10 mL) and methanol (10 mL) in a 500 mL hydrogenator vessel. A catalytic amount of 10% Pd/C was added, and the reaction mixture was shaken on a Parr Hydrogenator under H₂ at 20 PSI for three hours, Scheme 7.18. The solution was subsequently filtered, and solvents were removed by lyophilization, to yield an orange solid (DOTA-AF, 0.24 g, 85% yield). **400 MHz D₂O; ¹H (ppm):** δ : 2.93 – 3.67 (16H, m, NCH₂CH₂N), 3.94 (6H, s, -CH₂), 5.25 (1H, s, -CH), 7.24 (2H, $J = 8$ Hz, d, ar -CH), 7.35 (2H, $J = 8$ Hz, ar -CH). **ESMS-ESI(+)** m/z : 519.1383 ([M + Na]⁺, 100%). **FT-IR** $\nu_{\text{max}} = 4000 \text{ cm}^{-1} (\text{cm}^{-1})$: 1109.55 (carboxylic acid C–O), 1346.62 (amine C–N), 1599.75 (ar sp² C=C), 1629.04 (carboxylic acid C=O), 2854.63 (ar sp² C–H), 3107.25 (carboxylic acid O–H), 3360.63 (amine N–H). **R_f** = (Si₂O₂, CH₃OH) 0.125.

7.3.5.2. 2,2',2''-(10-(carboxy(4-isothiocyanatophenyl)methyl)-1,4,7,10-tetraazacyclododecane-1,4,7-triyl)triacetic acid (**DOTA-IF**)

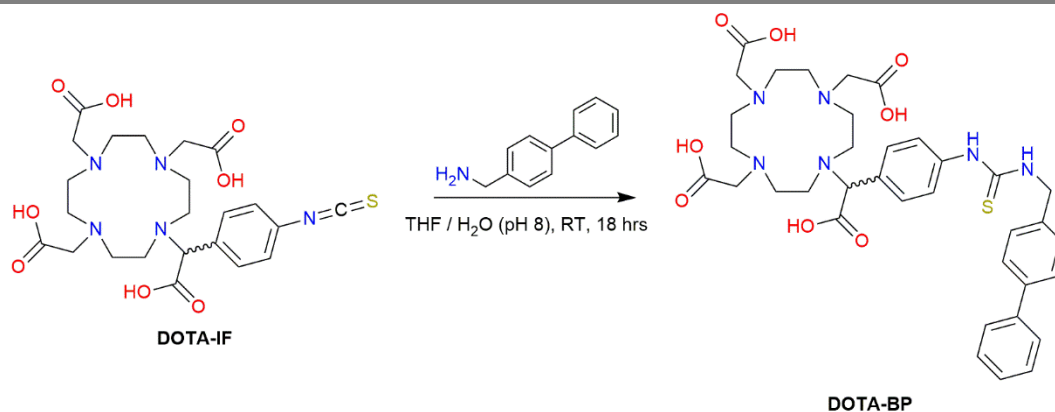


Scheme 7.19. Synthesis of **DOTA-IF** from **DOTA-AF**.

DOTA-AF (0.2404 g, 0.49 mmol) was dissolved in H₂O (15 mL). Thiophosgene (0.13 mL) was dissolved in chloroform (10 mL). The organic solution was added to the aqueous mixture and stirred vigorously at room temperature for 18 hours, Scheme 7.19. The reaction mixture was washed with chloroform (50 mL). The aqueous phase was dried *via* lyophilization to afford a light orange solid product (**DOTA-IF**, 0.12 g, 45% yield).

400 MHz D₂O; ¹H (ppm): δ: 2.61 (1H, s, -CH), 2.92 – 3.71 (16H, m, NCH₂CH₂N), 3.92 (2H, s, -CH₂), 4.13 (4H, s, -CH₂), 7.64 (2H, *J* = 10 Hz, d, ar -CH), 8.22 (2H, *J* = 10 Hz, d, ar -CH). **ESMS-ESI(-) *m/z*:** 536.18 ([*M* – 1]⁻, 100%). **FT-IR ν_{max} = 4000 cm⁻¹ (cm⁻¹):** 1192.33 (carboxylic acid C–O), 1655.23 (ar sp² C=C), 1720.58 (carboxylic acid C=O), 2097.64 (ar N=C=S), 3050.17 (ar sp² C–H), 3194.97 (carboxylic acid O–H).

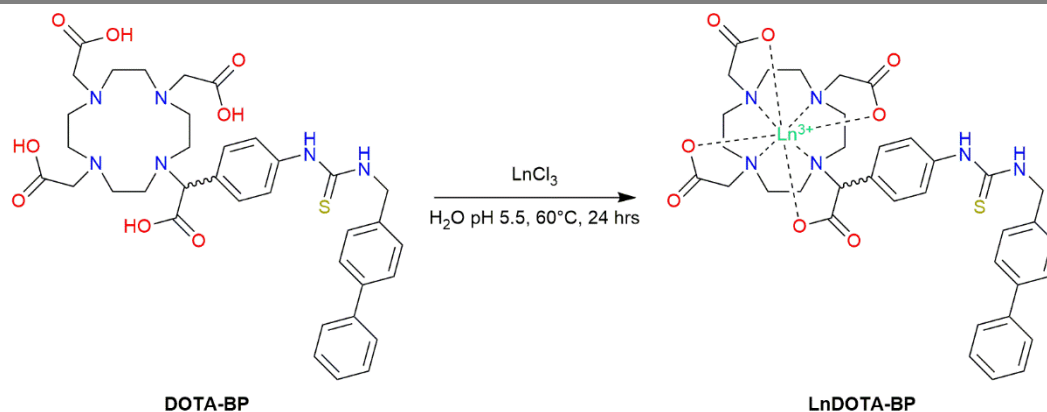
7.3.5.3. 2,2',2''-(10-((4-(3-([1,1'-biphenyl]-4-ylmethyl) thioureido) phenyl) (carboxy) methyl) -1,4,7,10-tetraazacyclododecane-1,4,7-triyl) triacetic acid (**DOTA-BP**)



Scheme 7.20. Synthesis of the target ligand, **DOTA-BP**, from **DOTA-IF**.

DOTA-IF (0.1175 g, 0.22 mmol) was dissolved in H₂O (10 mL) and the pH was adjusted to 8 with 1M KOH, then tetrahydrofuran was added (10 mL). 4-phenylbenzylamine (0.0867 g, 0.47 mmol) was added, and the reaction mixture was stirred at ambient temperature (~20 °C) for 18 hours, Scheme 7.20. The reaction mixture was dried via lyophilization to yield a light yellow solid (**DOTA-BP potassium salt**, 0.19 g). **400 MHz D₂O; ¹H (ppm):** δ: 2.48 (2H, s, -CH₂), 2.98 – 3.60 (16H, m, NCH₂CH₂N), 3.89 (1H, s, -CH), 4.18 (6H, s, -CH₂), 7.41 (1H, *J* = 8 Hz, t, ar -CH), 7.51 (4H, *J* = 8 Hz, t, ar -CH), 7.68 (4H, *J* = 8 Hz, dd, ar -CH). **ESMS-ESI(+)** *m/z*: 798.9275 ([M + 2K]⁺, 10%), 562.8433 ([M – BP]⁺, 100%). **FT-IR** ν_{max} = **4000 cm⁻¹ (cm⁻¹):** 1155.92 (thiourea C=S), 1220.89 (thiourea C–N), 1388.29 (carboxylic C–O), 1596.00 (ar sp² C=C), 1643.82 (carboxylic acid C=O), 2915.24 (ar sp² C–H), 3361.02 (carboxylic acid O–H).

7.3.5.4. *Ln(III)-(2,2',2''-(10-((4-(3-([1,1'-biphenyl]-4-ylmethyl) thioureido) phenyl) (carboxy) methyl)-1,4,7,10-tetraazacyclododecane-1,4,7-triyl) triacetate) (LnDOTA-BP)*



Scheme 7.21. Chelation of DOTA-BP with lanthanide chlorides (EuCl₃, GdCl₃).

DOTA-BP (0.0543 g, 0.075 mmol) and EuCl₃·6H₂O (0.058 g, 0.16 mmol) were dissolved in water (10 mL), and acetonitrile (5 mL). The pH was adjusted to 5.5 with 1M KOH and the reaction mixture was stirred at 60 °C for 24 hours, Scheme 7.21. The reaction mixture was purified *via* RP-HPLC utilizing the method in Table 7.6. The fractions were lyophilized to yield a colorless solid (**EuDOTA-BP** R_T = 21.0 minutes, 0.015 g, 23% yield)

600 MHz D₂O; ¹H EuDO3A-BPAM (ppm): δ: -18.26 (1H), -17.74 (1H), -17.06 (1H), -16.13 (1H), -15.13 (1H), -14.83 (1H), -11.26 (1H), -10.78 (1H), -10.13 (1H), -9.05 (1H), -8.53 (1H), -7.88 (1H), -7.47 (1H), -6.54 (1H), -6.26 (1H), -5.58 (1H), -5.24 (1H), -4.81 (1H), -4.19 (1H), -4.02 (1H), -3.72 (1H), -2.71 (1H), -2.43 (1H), -1.55 (1H), -1.0 (1H), -0.44 (1H), 0.01 (1H), 0.30 (1H), 0.81 (1H), 1.17 (1H), 1.34 (1H), 1.50 (1H), 1.98 (1H), 2.13 (1H), 2.58 (1H), 2.82 (1H), 3.04 (1H), 3.22 (1H), 3.37 (1H), 3.61 (1H), 4.15 (1H),

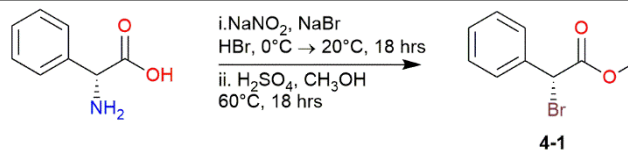
5.79 (1H), 7.47 (1H), 7.67 (1H), 12.51 (1H), 13.49 (1H), 14.43 (1H), 16.11 (1H), 33.71 (1H), 34.92 (1H), 36.21 (1H), 37.19.

Table 7.6. RP-HPLC method to purify biphenyl containing chelates.

Time (minutes)	% A (0.037% HCl)	%B (100% MeCN)
0 – 5	100	0
10	100	0
20	20	80
25	20	80
28 – 28.1	100	0

7.4. Synthesis, purification, and characterization of Chapter 4 Complexes

7.4.1. Methyl (R)-2-bromo-2-phenylacetate (4-1)

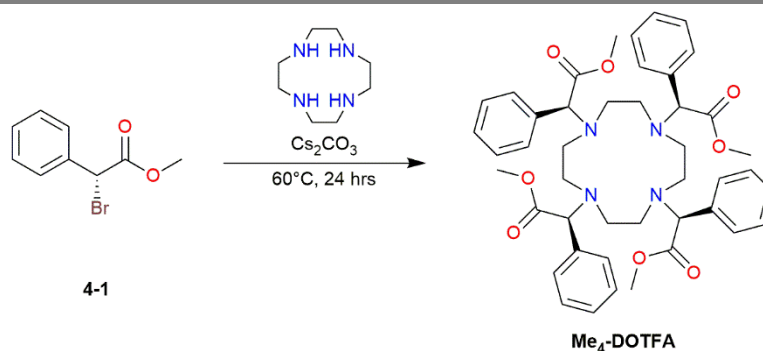


Scheme 7.22. Two-step synthesis of methyl (R)-2-bromo-2-phenylacetate (4-1).

i. D- α -phenylglycine (10 g, 0.066 mols) and sodium bromide (54 g, 0.53 mols) were dissolved in 2M HBr (120 mL) and cooled to 0°C. Sodium nitrite (5 g, 0.073 mol) was added to the reaction mixture over the course of several hours, allowing for brown gas to dissipate after each addition. Once the addition of the sodium nitrite was complete, the diazotization reaction was stirred for 18 hours allowing the reaction mixture to come to room temperature. The reaction mixture was extracted diethyl ether (3 \times 60 mL) and water, and the organic phase was dried *in vacuo* to yield a colorless oil, Scheme 7.22.

ii. The crude reaction mixture from the diazotization reaction was dissolved in methanol (50 mL) and sulfuric acid (1 mL) and heated at 60°C for 18 hours. Once completed, the solvents were removed *in vacuo* and the crude oil was extracted with diethyl ether (3 × 60 mL) and potassium carbonate mixture in water (pH 10). The organic layer was dried *in vacuo* to yield a crude, colorless oil. The crude product was purified *via* gradient column chromatography (10% diethyl ether in hexanes – 100% diethyl ether, with a MeOH wash), organic solvent removed *in vacuo* to yield a pure colorless oil (**4-1**, 7.87 g, 26% yield). NMR spectra were consistent with previously published data (**400 MHz CDCl₃**; **¹H (ppm):** δ: 3.76 (3H, s, -CH₃), 5.43 (1H, s, -CH), 7.36 (3H, *J* = 7 Hz, t, ar -CH), 7.58 (2H, *J* = 7 Hz, d, 2H)).⁹²

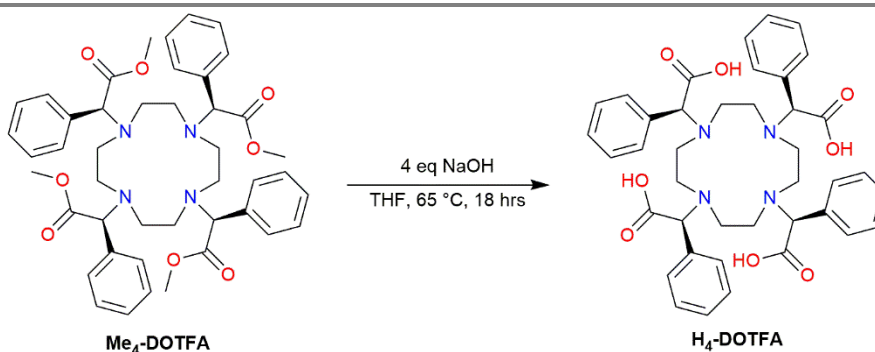
7.4.2. Tetramethyl 2, 2', 2'', 2'''-(1, 4, 7, 10-tetraazacyclododecane-1, 4, 7, 10-tetrayl) (2*S*, 2'*S*, 2''*S*, 2'''*S*)-tetrakis (2-phenylacetate) (Me₄-DOTFA)



Scheme 7.23. Synthesis of Me₄-DOTFA *via* alkylation of 4-1 onto cyclen.

4-1 (5 g, 0.022 mols), 1, 4, 7, 10-tetraazacyclododecane (cyclen, 0.75 g, 0.0044 mols), and cesium carbonate (7.11 g, 0.022 mols) was dissolved in acetonitrile (50 mL) and stirred at 60°C for 24 hours, Scheme 7.23. After alkylation, the organic solvents were removed *in vacuo* and was extracted with dichloromethane (3 × 60 mL) and water. The organic solvents were removed *in vacuo* to yield a dark yellow oil (**Me₄-DOTFA**, 3.30 g, 98% yield). **400 MHz CD₃CN; ¹H (ppm):** δ: 2.6 – 3.0 (16H, m, NCH₂CH₂N); 3.63 (12H, s, -CH₃); 4.42 (4H, s, -CH); 7.27 (4H, *J* = 10 Hz, m); 7.32 (8H, *J* = 10 Hz, t); 7.34 (8H, *J* = 10 Hz, d). **¹³C (ppm):** δ: 51.5 (8C, NCH₂CH₂N), 68.5 (4C, -CH₃), 128.3 (4C, ar -CH), 128.7 (8C, ar -CH), 129.6 (8C, ar -CH), 129.7 (4C, ar -C(CH₂)₂), 137.6 (4C, -CH), 173.1 (4C, C=O). **ESMS-ESI(+)** *m/z*: 765.3854 ([M+1]⁺, 39%), 787.3673 ([M+Na]⁺, 100%). **FT-IR** ν_{\max} = 4000 cm⁻¹ (cm⁻¹): 1152.46 (C–O, ester), 1599.43 (ar sp² C=C), 1731.49 (C=O, ester), 2950.14 (ar sp² C–H). **MP:** 74.5 – 76.4 °C.

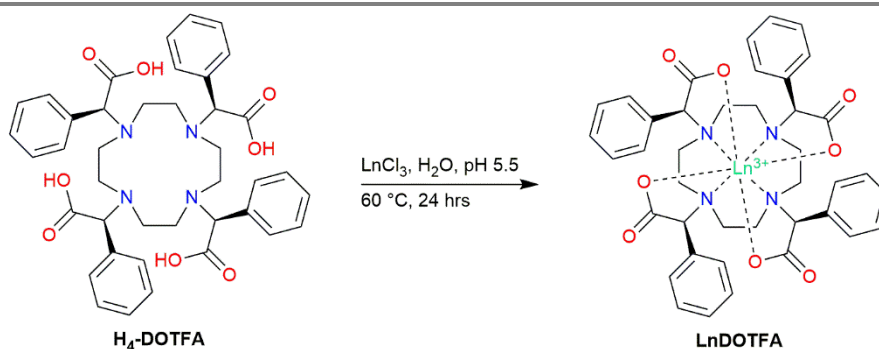
7.4.3. (2*S*, 2'*S*, 2''*S*, 2'''*S*)-2, 2', 2'', 2'''-(1, 4, 7, 10-tetraazacyclododecane-1, 4, 7, 10-tetrayl) tetrakis (2-phenylacetic acid) (H₄-DOTFA)



Scheme 7.24. Synthesis of ligand H₄-DOTFA from protected ligand Me₄-DOTFA.

Me₄-DOTFA (0.5 g, 0.654 mmol) and sodium hydroxide (0.25 g, 0.621 mmols) was dissolved in tetrahydrofuran (10 mL) and water (10 mL). The reaction mixture was heated at 65°C for 18 hours, Scheme 7.24. The pH of the solution was lowered to 3 with hydrochloric acid and the aqueous solvent were removed *via* lyophilization to yield a colorless solid (**H₄-DOTFA**, 0.24 g, 55% yield). **400 MHz D₂O; ¹H (ppm):** δ: 2.33 – 2.59 (16H, m, NCH₂CH₂N), 4.22 (4H, s, -CH); 7.23 (8H, *J* = 13 Hz, m, ar -CH); 7.35 (8H, *J* = 13 Hz, m, ar -CH); 7.43 (4H, *J* = 13 Hz, d, ar -CH). **¹³C (ppm):** δ: 58.5 (8C, NCH₂CH₂N), 95.2 (4C, -CH), 125.3 – 129.5 (24C, broad, ar C(CH)₅), 176.4 (4C, C=O). **FTMS ESI(-) *m/z*:** 707.3095 ([M-1]⁻, 100%), 729.2909 ([M+Na]⁻, 80%). **FT-IR ν_{max} = 4000 cm⁻¹ (cm⁻¹):** 1101.77 (carboxylic acid C–O), 1575.51 (ar sp² C=C), 1589.47 (carboxylic acid C=O), 2976.45 (ar sp² C–H), 3345.90 (carboxylic acid O–H).

7.4.4. Ln(III)-(2*S*, 2'*S*, 2''*S*, 2'''*S*)-2, 2', 2'', 2'''-(1, 4, 7, 10-tetraazacyclododecane-1, 4, 7, 10-tetrayl) tetrakis (2-phenylacetate) from lanthanide chloride salts (LnDOTFA)



Scheme 7.25. Synthesis of target chelate LnDOTFA (Ln = Eu, Gd).

DOTFA (0.03 g, 0.034 mmol) and lanthanide chloride (EuCl₃, or GdCl₃) (0.1 mmol) were dissolved in water (10 mL). The pH of the solution was adjusted to 5.5 with

potassium hydroxide and heated at 70°C for 48 hours, Scheme 7.25. The chelates were purified by RP-HPLC, with absorbance monitoring at $\lambda = 205$ nm and 254 nm. The solvent system utilized is described in Table 7.7. The fractions were freeze dried to yield a colorless solid ($R_T = 22.3$ minutes, 0.019 g, 27% yield). **EuDOTFA 400 MHz D₂O; ¹H (ppm):** δ : -23.451 (1H); -10.439 (1H); -9.409 (2H); -5.584 (1H); -5.120 (1H); -4.808 (2H); -1.769 (1H); 1.503 (2H); 2.069 (1H); 5.768 (4H); 6.401 (2H); 6.724 – 6.982 (20H); 17.4519 (1H), 43.0135 (1H). **GdDOTFA FTMS ESI(-) *m/z*:** 862.2112 ($[M]^-$, 100%).

Table 7.7. RP-HPLC purification method for LnDOTFA chelates.

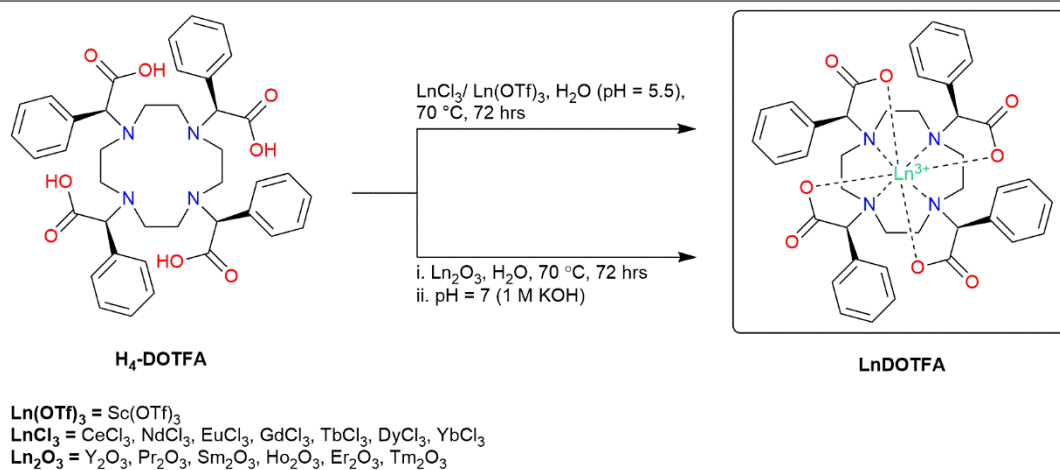
Time (minutes)	% A (0.037% HCl)	%B (100% MeCN)
0 – 5	100	0
15 – 22	20	80
24 – 28.1	100	0

7.5. Synthesis, purification, and characterization of Chapter 5 Complexes

7.5.1. General Remarks

The synthesis of the target ligand, H₄-DOTFA is described in Section 7.4.

7.5.2. *Ln(III)-(2S, 2'S, 2''S, 2'''S)-2, 2', 2'', 2'''-(1, 4, 7, 10-tetraazacyclododecane-1, 4, 7, 10-tetrayl) tetrakis(2-phenylacetate) (LnDOTFA)*



Scheme 7.26. Synthesis of LnDOTFA from corresponding lanthanide triflates, chlorides, and oxides. (Ln = Y, Sc, Ce, Pr, Nd, Sm, Eu, Gd, Tb, Dy, Ho, Er, Tm, Yb)

7.5.2.1. *Ln(III)-(2S, 2'S, 2''S, 2'''S)-2, 2', 2'', 2'''-(1, 4, 7, 10-tetraazacyclododecane-1, 4, 7, 10-tetrayl) tetrakis(2-phenylacetate) from lanthanide triflates (LnDOTFA, Ln = Sc)*

DOTFA (0.03 g, 0.034 mmol) and scandium triflate (0.1 mmol) were dissolved in water (10 mL). The pH of the solution was adjusted to 5.5 with potassium hydroxide and heated at 70 °C for 48 hours. The chelates were purified by RP-HPLC, with absorbance monitoring at $\lambda = 205$ nm and 254 nm. The solvent system utilized is described in Table 7.7. The fractions were freeze dried to yield a colorless solid ($R_T = 20.1$ minutes).

The purified ScDOTFA chelate was recrystallized by adding the filtered lyophilized solids in minimal volumes of water. These solutions were gently heated at 60 °C until complete dissolution, then the heat was turned off and they were partially covered to facilitate crystal growth.

7.5.2.2. *Ln(III)-(2 S, 2'S, 2''S, 2'''S)-2, 2', 2'', 2'''-(1, 4, 7, 10-tetraazacyclododecane-1, 4, 7, 10-tetrayl) tetrakis(2-phenylacetate) from lanthanide chlorides (LnDOTFA, Ln = Ce, Nd, Eu, Gd, Tb, Dy, Yb)*

DOTFA (0.03 g, 0.034 mmol) and lanthanide chloride (Ln = Ce, Nd, Eu, Gd, Tb, Dy, Yb, 0.1 mmol) were dissolved in water (10 mL). The pH of the solution was adjusted to 5.5 with potassium hydroxide and heated at 70 °C for 48 hours. The chelates were purified by RP-HPLC, with absorbance monitoring at $\lambda = 205$ nm and 254 nm. The solvent system utilized is described in Table 7.7. The fractions were freeze dried to yield a colorless solid (R_T CeDOTFA = 21.2 minutes, 60% yield; R_T NdDOTFA = 20.8 minutes, 41% yield; R_T EuDOTFA = 21.8 minutes, 54% yield; R_T GdDOTFA = 21.3 minutes, 34% yield; R_T TbDOTFA = 21.8 minutes, 20% yield; R_T DyDOTFA = 21.8 minutes, 30% yield; R_T YbDOTFA = 22.0 minutes, 22% yield).

The purified chelates were recrystallized by adding the filtered lyophilized solids in minimal volumes of water. These solutions were gently heated at 60 °C until complete dissolution, then the heat was turned off and they were partially covered to facilitate crystal growth.

7.5.2.3. *Ln(III)-(2 S, 2'S, 2''S, 2'''S)-2, 2', 2'', 2'''-(1, 4, 7, 10-tetraazacyclododecane-1, 4, 7, 10-tetrayl) tetrakis(2-phenylacetate) from lanthanide oxides (LnDOTFA, Ln = Y, Pr, Sm, Ho, Er, Tm)*

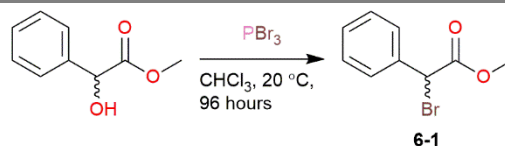
DOTFA (0.03 g, 0.034 mmol) and lanthanide oxide (Ln = Y, Pr, Sm, Ho, Er, Tm, 0.1 mmol) were dissolved in water (10 mL) and heated at 70 °C for 72 hours. The reaction

mixture was pH adjusted to 7 with 1M KOH. The chelates were purified by RP-HPLC, with absorbance monitoring at $\lambda = 205$ nm and 254 nm. The solvent system utilized is described in Table 7.7. The fractions were freeze dried to yield a colorless solid (R_T YDOTFA = 20.8 minutes; R_T PrDOTFA = 21.1 minutes, 66% yield; R_T SmDOTFA = 21.2 minutes, 49% yield; R_T HoDOTFA = 21.7 minutes, 43% yield; R_T ErDOTFA = 21.6 minutes, 46% yield; R_T TmDOTFA = 21.9 minutes, 28% yield).

The purified chelates were recrystallized by adding the filtered lyophilized solids in minimal volumes of water. These solutions were gently heated at 60 °C until complete dissolution, then the heat was turned off and they were partially covered to facilitate crystal growth.

7.5.3. Synthesis of Racemic EuDOTFA

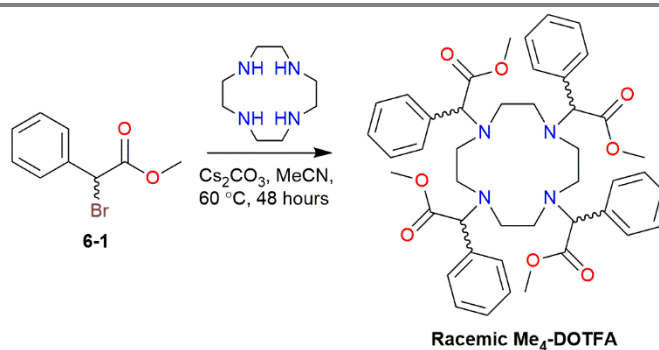
7.5.3.1. DL-methyl 2-bromo-2-phenylacetate (6-1)



Scheme 7.27. Synthesis of DL-methyl 2-bromo-2-phenylacetate (6-1).

Methyl DL-mandelate (5 g, 30 mmol) was added to chloroform (20 mL). Phosphorus tribromide (5.7 mL, 60 mmol) was added to the reaction mixture. The reaction was stirred at 20 °C for 96 hours, Scheme 7.27. The reaction mixture was extracted with water (3 × 20 mL) to yield a colorless oil (**6-1**, 6.48 g, 93% yield).

7.5.3.2. *DL-tetramethyl* 2,2',2'',2'''-(1,4,7,10-tetraazacyclododecane-1,4,7,10-tetrayl)tetrakis(2-phenylacetate) (**Racemic Me₄-DOTFA**)

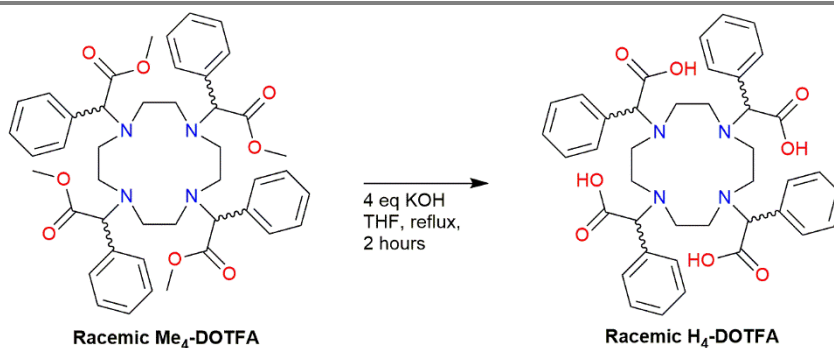


Scheme 7.28. Synthesis of the protected ligand **Racemic Me₄-DOTFA** *via* alkylation of **6-1** onto cyclen.

6-1 (3.3 g, 15 mmols), 1, 4, 7, 10-tetraazacyclododecane (cyclen, 0.5 g, 5.8 mmols), and cesium carbonate (4.7 g, 15 mmols) was dissolved in acetonitrile (50 mL) and stirred at 60 °C for 24 hours, Scheme 7.28. After alkylation, the organic solvents were removed *in vacuo* and the remaining residue was extracted with dichloromethane (3 × 60 mL) and water. The organic layer was dried (Na₂SO₄). The solvents were removed *in vacuo* to yield a dark yellow crude oil. The crude product was purified *via* gradient column chromatography (50% diethyl ether in hexanes, 100% MeOH, with a 10% NH₄OH in

MeOH wash), organic solvent removed *in vacuo* to yield a pure colorless oil (**Racemic Me₄-DOTFA**, 0.18 g, 8% yield). FTMS ESI(+) *m/z*: 765.39 ([M+1]⁺, 100%).

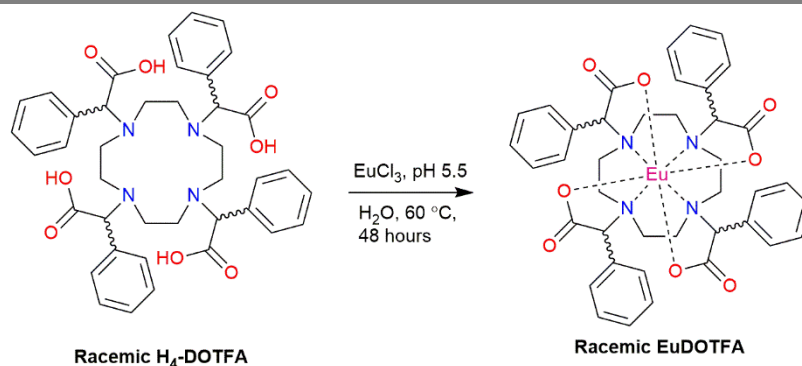
7.5.3.3. *DL*-2,2',2'',2'''-(1,4,7,10-tetraazacyclododecane-1,4,7,10-tetrayl)tetrakis(2-phenylacetic acid) (**Racemic H₄-DOTFA**)



Scheme 7.29. Synthesis of target ligand **Racemic H₄-DOTFA** *via* methyl ester hydrolysis of the protected ligand **Racemic Me₄-DOTFA** in base.

Racemic Me₄-DOTFA (0.18 g, 0.24 mmol) was added to tetrahydrofuran (5 mL). 1M KOH was added (4 equivalents, 0.94 mmol) and the reaction mixture was stirred at 60 °C for 48 hours, Scheme 7.29. The aqueous layer was dried by lyophilization to yield a crude colorless salt that was used without further purification (**Racemic DOTFA**). FTMS ESI(-) *m/z*: 707.31 ([M-1]⁻, 100%).

7.5.3.4. *DL-Eu(III)-2,2',2'',2'''-(1,4,7,10-tetraazacyclododecane-1,4,7,10-tetrayl)tetrakis(2-phenylacetate)* (**Racemic EuDOTFA**)



Scheme 7.30. Synthesis of target chelate Racemic EuDOTFA.

Racemic DOTFA (0.17 g, 0.24 mmol) and europium chloride (0.18 g, 0.47 mmol) was added to water and the pH was adjusted to 5.5 with 1M HCl. The reaction mixture was stirred at 60 °C for 48 hours, Scheme 7.30. The reaction mixture solvents were removed by lyophilization to yield a crude chelate (**Racemic EuDOTFA**). **400 MHz D₂O; ¹H (ppm):** δ: -25.46 (1H), -23.57 (1H), -23.41 (1H), -22.64 (1H), -22.01 (1H), -17.16 (1H), -15.86 (1H), -14.79 (1H), -14.01 (1H), -13.40 (1H), -13.12 (1H), -11.79 (1H), -11.54 (1H), -11.30 (1H), -10.82 (1H), -10.12 (1H), -9.37 (1H), -9.0 (1H), -8.75 (1H), -7.98 (1H), -7.37 (1H), -7.14 (1H), -6.89 (1H), -6.35 (1H), -5.96 (1H), -5.62 (1H), -4.99 (1H), -4.71 (1H), -4.31 (1H), -3.81 (1H), -2.63 (1H), -1.72 (1H), -1.24 (1H), -0.78 (1H), -0.36 (1H), 1.08 (1H), 1.93 (1H), 2.65 (1H), 3.00 (1H), 3.27 (1H), 3.60 (1H), 5.69 (1H), 5.85 (1H), 6.21 (1H), 6.43 (1H), 6.76 (1H), 7.06 (1H), 7.25 (1H), 7.35 (1H), 17.46 (1H), 22.46 (1H), 23.94 (1H), 37.64 (1H), 39.30 (1H), 42.08 (1H), 43.25 (1H), 44.36 (1H), 49.67 (1H), 51.21 (1H).

7.6. Synthesis, purification, and characterization of Chapter 6 Complexes

7.6.1. General Remarks

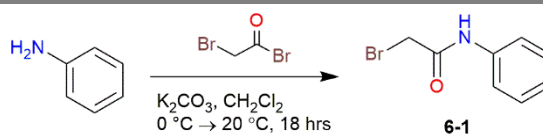
The synthesis of the starting ligand, DO3A^tBu esters, is described in Section 6.3.1 and Scheme 6.5. The RP-HPLC purification method for all chelates described is shown in Table 7.8.

Table 7.8. RP-HPLC purification method of LnDO3A-Monoamide Chelates.

Time (minutes)	% A (0.037% HCl)	%B (100% MeCN)
0 – 5	78	22
12	77	23
13 – 15	20	80
16 – 18.1	78	22

7.6.2. Synthesis of Aniline Derived Monoamides

7.6.2.1. 2-bromo-N-phenylacetamide (6-1)

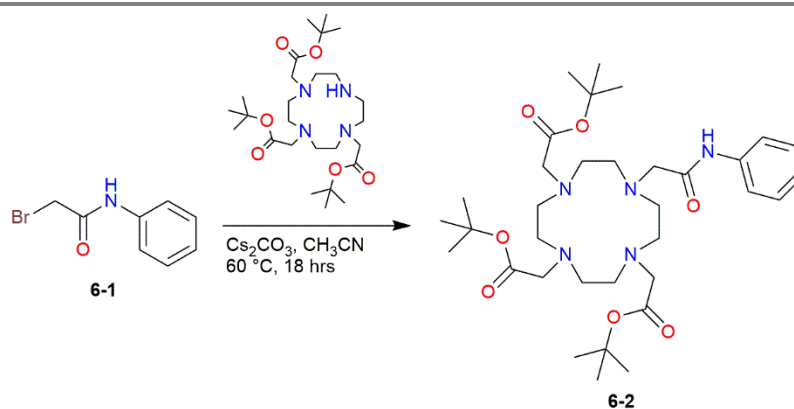


Scheme 7.31. Synthesis of 2-bromo-N-phenylacetamide (6-1).

Aniline (2 g, 21.5 mmol) was dissolved in 2M potassium carbonate solution (20 mL) and cooled to 0°C. Bromo acetyl bromide (5.2 mL, 43 mmol) was dissolved in dichloromethane (20 mL), and added dropwise to the aniline solution over the span of one hour. The reaction mixture was allowed to stir to room temperature for 18 hours, Scheme 7.31. The reaction mixture was extracted with dichloromethane (3 × 50 mL), and the organic layer was dried (Na₂SO₄). Solvents were removed *in vacuo* to afford a colorless

fluffy solid (**6-1**, 4.4 g, 96% yield). Spectra were consistent with previously published data (400 MHz CDCl₃; ¹H (ppm): δ: 1.63 (2H, s, -CH₂), 7.20 (1H, *J* = 8 Hz, t, ar -CH), 7.39 (2H, *J* = 8 Hz, t, -CH), 7.56 (2H, *J* = 8 Hz, d, ar -CH)).¹¹⁸

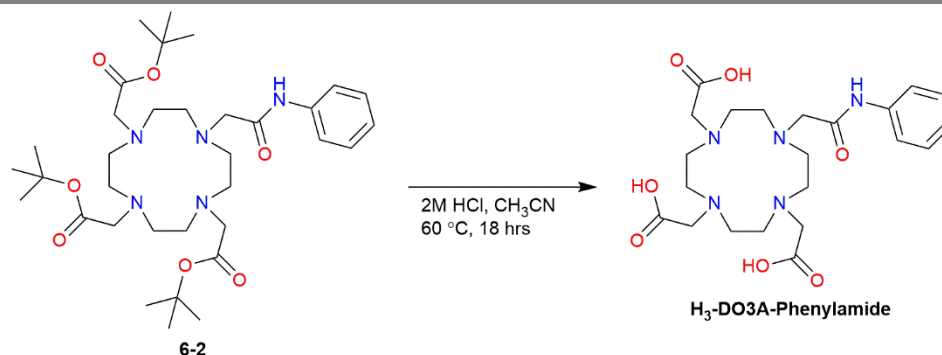
7.6.2.2. *Tris-tert-butyl 2,2',2''-(10-(2-oxo-2-(phenylamino) ethyl)-1,4,7,10-tetraazacyclododecane-1,4,7-triyl) triacetate (6-2)*



Scheme 7.32. Synthesis of the protected ligand (**6-2**) via alkylation of **6-1** onto DO3A-*tert*-butyl esters.

A mixture of DO3A-*tert*-butyl esters (0.3 g, 0.583 mmol) and cesium carbonate (0.38 g, 1.17 mmol) was added to acetonitrile (15 mL). **6-1** (0.187 g, 0.87 mmol) was added, and the reaction mixture was stirred at 60°C for 18 hours, Scheme 7.32. The reaction mixture was extracted with dichloromethane (3 × 15 mL), and the organic layer was dried (Na₂SO₄). Solvents were removed *in vacuo* to afford a waxy yellow solid (**6-2**, 0.38 g, 90% yield). FTMS ESI(+) *m/z*: 648.4322 ([M+1]⁺, 10%), 670.4138 ([M+Na]⁺, 100%).

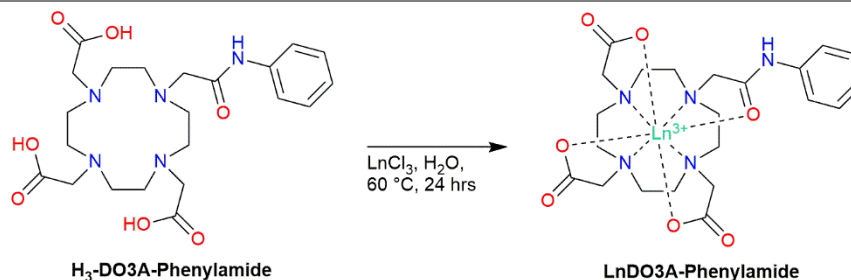
7.6.2.3. 2,2',2''-(10-(2-oxo-2-(phenylamino) ethyl)-1,4,7,10-tetraazacyclododecane-1,4,7-triyl) triacetic acid (**DO3A-Phenylamide**)



Scheme 7.33. Synthesis of the ligand **DO3A-Phenylamide** via *tert*-butyl ester hydrolysis of the protected ligand (**6-2**) in acid.

6-2 (0.3755 g, 0.58 mmol) was dissolved in 1M HCl (3.5 eq) and acetonitrile (10 mL). The reaction mixture was stirred and heated at 60°C for 18 hours, Scheme 7.33. Once reaction was complete, solvents were removed by lyophilization affording a crude salt product. The product was confirmed by ESI-MS and consistent with previously published data (**DO3A-Phenylamide**). (FTMS ESI(+)) m/z : 480.2448 ($[M+1]^+$, 100%), 502.2265 ($[M+Na]^+$, 30%).¹¹⁰

7.6.2.4. Ln (III)-2,2',2''-(10-(2-oxo-2-(phenylamino) ethyl)-1,4,7,10-tetraazacyclododecane-1,4,7-triyl) triacetate Chelates (**Ln-DO3A Phenylamide**)



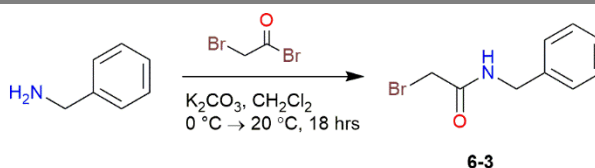
Scheme 7.34. Synthesis of target chelates **LnDO3A-Phenylamide** (Ln = Eu, Gd, Yb).

DO3A-Phenylamide (0.1778 g, 0.371 mmol) and lanthanide chlorides (0.737 mmol) were dissolved in H₂O (10 mL) and acetonitrile (2 mL). The pH was adjusted to 5.5 with 1M KOH and the reaction was stirred and heated at 60°C for 24 hours, Scheme 7.34. The solution was purified by RP-HPLC, with absorbance monitoring at $\lambda = 254$ nm and 205 nm. The solvent system utilized is shown in Table 7.8. RP-HPLC purification yielded a colorless solid product (**EuDO3A-Phenylamide** $R_T = 4.8$ minutes, 79% yield; **GdDO3A-Phenylamide** $R_T = 4.9$ minutes, 78% yield; **YbDO3A-Phenylamide** $R_T = 5.7$ minutes, 31% yield). ¹H-NMR spectra of the Yb and Eu products were consistent with previously published data (**YbDO3A-Phenylamide 400 MHz D₂O**; ¹H (ppm): δ : -51.67 (1H), -50.60 (1H), -50.15 (1H), -49.52 (1H), -47.18 (1H), -44.86 (1H), -40.06 (1H), -39.47 (1H), -38.49 (1H), -37.41 (1H), -36.24 (1H), -35.79 (1H), -34.83 (1H), -31.41 (1H), -30.57 (1H), -29.80 (1H), -26.54 (1H), -26.09 (1H), -24.38 (1H), -22.51 (1H), -21.20 (1H), -17.78 (1H), -16.19 (1H), -13.96 (1H), -7.33 (1H), -4.76 (1H), -3.14 (1H), -1.83 (1H), 0.61 (1H), 0.73 (1H), 0.96 (1H), 1.55 (1H), 1.69 (1H), 1.94 (1H), 2.41 (1H), 2.83 (1H), 3.02 (1H),

4.01 (1H), 4.22 (1H), 6.86 (1H), 7.94 (1H), 9.09 (1H), 9.35 (1H), 12.64 (1H), 14.75 (1H), 16.33 (1H), 17.35 (1H), 18.79 (1H), 20.71 (1H), 23.16 (1H), 28.95 (1H), 62.32 (1H), 82.55 (1H), 107.31 (1H), 109.89 (1H), 112.80 (1H), 117.10 (1H)).¹¹⁰

7.6.3. Synthesis of Benzylamine Derived Monoamides

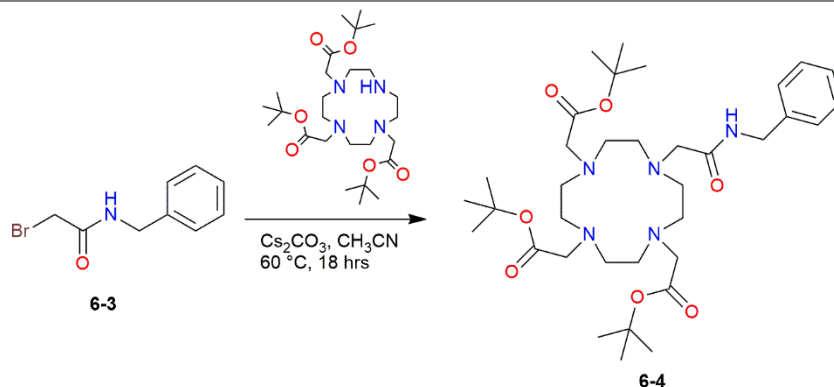
7.6.3.1. N-benzyl-2-bromoacetamide (6-3)



Scheme 7.35. Synthesis of N-benzyl-2-bromoacetamide (6-3).

Benzylamine (2 g, 18.7 mmol) was dissolved in 2M potassium carbonate solution (20 mL) and cooled to 0 °C. Bromo acetyl bromide (4.5 mL, 37 mmol) was dissolved in dichloromethane (20 mL), and added dropwise to the benzylamine solution over the span of one hour. The reaction mixture was allowed to stir to room temperature for 18 hours, Scheme 7.35. The reaction mixture was extracted with diethyl ether (3 × 50 mL), and the organic layer was dried (Na₂SO₄). The solvents were removed *in vacuo* to afford a colorless solid product (**6-3**, 3.9 g, 91% yield). NMR spectra were consistent with previously published data (**400 MHz CDCl₃**; **¹H (ppm)**: δ: 3.97 (2H, s, -CH₂), 4.51 (2H, d, -CH₂), 7.31 (1H, *J* = 8 Hz, t, ar -CH), 7.35 (2H, *J* = 8 Hz, t, -CH), 7.39 (2H, *J* = 8 Hz, d, ar -CH)).¹¹⁹

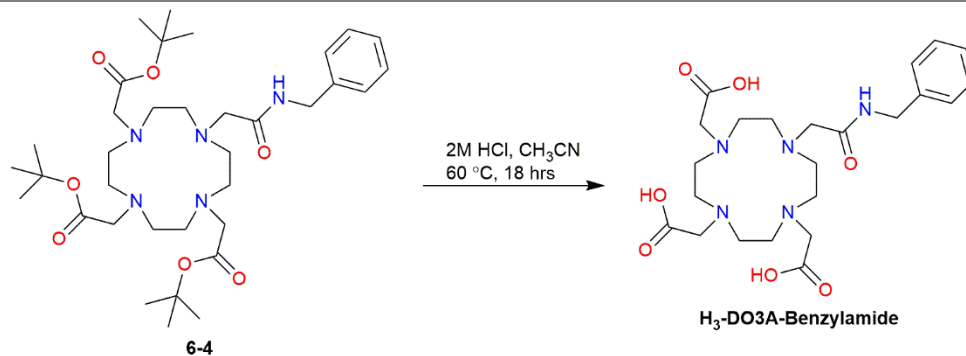
7.6.3.2. *Tris-tert-butyl 2,2',2''-(10-(2-(benzylamino)-2-oxoethyl)-1,4,7,10-tetraazacyclododecane-1,4,7-triyl) triacetate (6-4)*



Scheme 7.36. Synthesis of the protected ligand (**6-4**) via alkylation of **6-3** onto DO3A-*tert*-butyl esters.

A mixture of DO3A-*tert*-butyl ester (0.3 g, 0.583 mmol) and cesium carbonate (0.38 g, 1.17 mmol) was added to acetonitrile (15 mL). **6-3** (0.199 g, 0.87 mmol) was added, and the reaction mixture was stirred at 60 °C for 18 hours, Scheme 7.36. The reaction mixture was extracted with dichloromethane (3 × 15 mL), and the organic layer was dried (Na₂SO₄). The solvents were removed *in vacuo* to afford a dark orange oil (**6-4**, 0.39 g, 99% yield). FTMS ESI(+) *m/z*: 662.4480 ([M+1]⁺, 100%), 684.6296 ([M+Na]⁺, 15%).

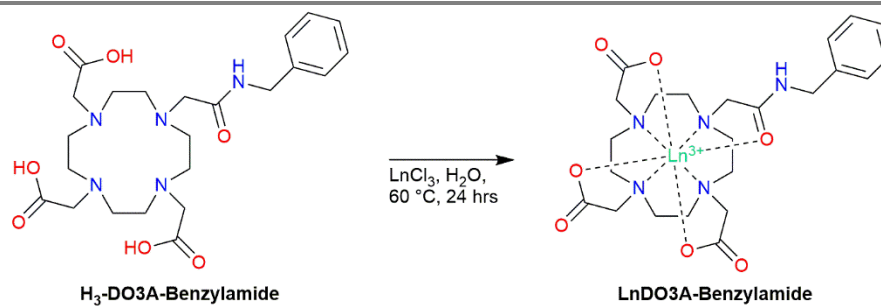
7.6.3.3. 2,2',2''-(10-(2-(benzylamino)-2-oxoethyl)-1,4,7,10-tetraazacyclododecane-1,4,7-triyl)triacetic acid (**DO3A-Benzylamide**)



Scheme 7.37. Synthesis of the ligand **DO3A-Benzylamide** via *tert*-butyl ester hydrolysis of the protected ligand (**6-4**) in acid.

6-4 (0.3894 g, 0.59 mmol) was dissolved in 1M HCl (3.5 eq) and acetonitrile (10 mL). The reaction mixture was stirred and heated at 60 °C for 18 hours, Scheme 7.37. Once reaction was complete, solvents were removed by lyophilization to yield a crude salt product (**DO3A-Benzylamide**). FTMS ESI(+) *m/z*: 494.2606 ([M+1]⁺, 100%).

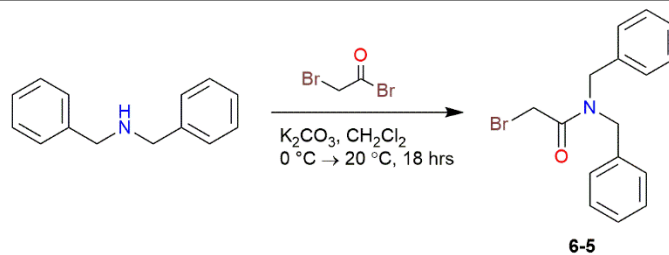
7.6.3.4. Ln (III) -2,2',2''-(10-(2-(benzylamino)-2-oxoethyl)-1,4,7,10-tetraazacyclododecane-1,4,7-triyl) triacetate Chelates (**LnDO3A-Benzylamide Chelates**)



Scheme 7.38. Synthesis of target chelates **LnDO3A-Benzylamide** (Ln = Eu, Gd, Yb).

DO3A-Benzylamide (0.1788 g, 0.362 mmol) and lanthanide chloride (0.727 mmol) were dissolved in H₂O (10 mL) and acetonitrile (2 mL). The pH was adjusted to 5.5 with 1M KOH and the reaction was stirred and heated at 60°C for 48 hours, Scheme 7.38. The solution was purified by RP-HPLC, with absorbance monitoring at $\lambda = 254$ nm and 205 nm. The solvent system utilized is described in Table 7.8. RP-HPLC purification yielded a colorless solid product (**EuDO3A-Benzylamide** $R_T = 6.1$ minutes, 39% yield; **GdDO3A-Benzylamide** $R_T = 6.4$ minutes, 40% yield; **YbDO3A-Benzylamide** $R_T = 5.7$ minutes, 20% yield). ¹H-NMR spectra of the europium and ytterbium product complexes was consistent with previously published data (**YbDO3A-Benzylamide 400 MHz D₂O; ¹H (ppm):** δ : -69.03 (1H), -68.64 (1H), -68.21 (1H), -67.05 (1H), -63.77 (1H), -51.13 (1H), -47.54 (1H), -45.03 (1H), -39.15 (1H), -37.80 (1H), -36.87 (1H), -35.40 (1H), -31.31 (1H), -28.99 (1H), -26.86 (1H), -25.47 (1H), -21.40 (1H), -19.32 (1H), -18.32 (1H), -17.62 (1H), -16.03 (1H), -14.59 (1H), -12.41 (1H), -11.89 (1H), -9.17 (1H), -7.75 (1H), -5.54 (1H), -5.05 (1H), -4.71 (1H), -3.47 (1H), -3.10 (1H), -1.88 (1H), 0.81 (1H), 1.12 (1H), 1.36 (1H), 2.01 (1H), 2.91 (1H), 3.19 (1H), 3.75 (1H), 4.04 (1H), 4.21 (1H), 6.94 (1H), 8.10 (1H), 9.22 (1H), 12.01 (1H), 14.35 (1H), 15.53 (1H), 16.62 (1H), 17.73 (1H), 18.40 (1H), 19.13 (1H), 20.32 (1H), 21.84 (1H), 22.94 (1H), 23.41 (1H), 26.99 (1H), 28.32 (1H), 65.09 (1H), 73.52 (1H), 110.63 (1H), 112.48 (1H)).¹²⁰

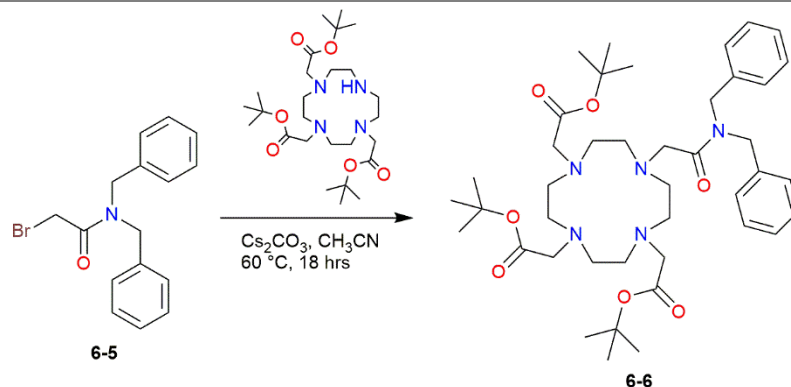
7.6.4. Synthesis of Dibenzylamine Derived Monoamides

7.6.4.1. *N,N*-dibenzyl-2-bromoacetamide (**6-5**)

Scheme 7.39. Synthesis of *N,N*-dibenzyl-2-bromoacetamide (6-5**).**

Dibenzylamine (5 g, 25.2 mmol) was dissolved in 2M potassium carbonate solution (40 mL) and cooled to 0 °C. Bromo acetyl bromide (4.6 mL, 38 mmol) was dissolved in dichloromethane (20 mL), and added dropwise to the dibenzylamine solution over the span of one hour. The reaction mixture was allowed to stir to room temperature for 18 hours, Scheme 7.39. The reaction mixture was extracted with dichloromethane (3 × 50 mL) and K₂CO₃ solution (pH 10). The organic layer was dried (Na₂SO₄). The solvents were removed *in vacuo* to afford a pale-yellow oil (**6-5**, 7.7 g, 95% yield). ¹H-NMR spectra were consistent with previously published data (400 MHz CDCl₃; ¹H (ppm): δ: 3.95 (2H, s, -CH₂), 4.56 (2H, s, -CH₂), 4.65 (2H, s, -CH₂), 7.23 (4H, *J* = 8 Hz, dd, ar -CH), 7.35 (4H, *J* = 8 Hz, m, -CH), 7.41 (2H, *J* = 8 Hz, t, ar -CH)).¹²¹

7.6.4.2. *Tris-tert-butyl 2,2',2''-(10-(2-(dibenzylamino)-2-oxoethyl)-1,4,7,10-tetraazacyclododecane-1,4,7-triyl) triacetate (6-6)*

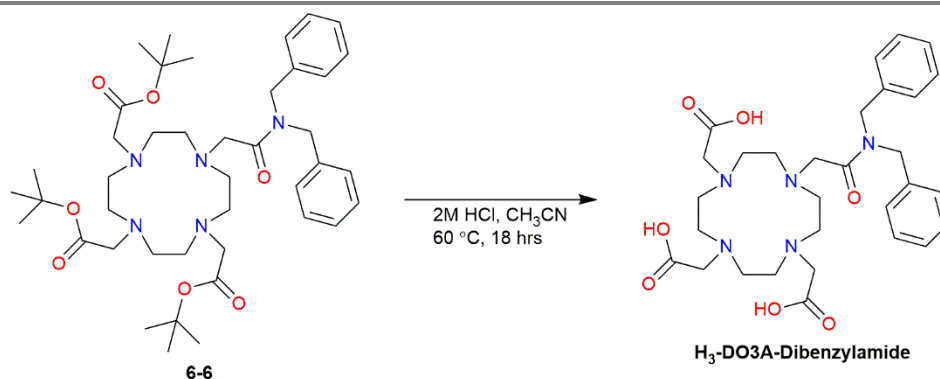


Scheme 7.40. Synthesis of the protected ligand (**6-6**) *via* alkylation of **6-5** onto DO3A-*tert*-butyl esters.

A mixture of DO3A-*tert*-butyl ester (0.1187 g, 0.231 mmol) and cesium carbonate (0.1282 g, 0.393 mmol) was added to acetonitrile (15 mL). **6-5** (0.1051 g, 0.330 mmol) was added, and the reaction mixture was stirred at 60 °C for 18 hours. The reaction mixture was extracted with dichloromethane (3 × 15 mL), and the organic layer was dried (Na₂SO₄). The solvents were removed *in vacuo* to afford a crude dark orange oil, Scheme 7.40. The crude product was purified *via* gradient column chromatography (10% methanol in dichloromethane), organic solvent removed *in vacuo* to yield a pure colorless oil (**6-6**, 0.12 g, 75% yield). **400 MHz CD₃CN**; **¹H**: δ: 1.45 (27H, m, tBu -CH₃), 2.05 – 2.98 (16H, m, NCH₂CH₂N), 3.29 (6H, s, -CH₂), 4.48 (4H, s, -CH₂), 5.48 (2H, s, -CH₂), 7.22 – 7.40 (10H, *J* = 8 Hz, m, ar -CH). **¹³C**: δ: 27.8 (9C, tBu -(CH₃)₃), 49.3 (1C, -CH₂), 49.5 (1C, -CH₂), 52.0 – 56.1 (8C, NCH₂CH₂N), 81.9 (1C, -CH₂), 82.1 (1C, -CH₂), 127.1 (2C, ar -CH), 127.8 (1C, ar -CH), 128.0 (1C, ar -CH), 128.8 (1C, ar -CH), 129.3 (2C, ar -CH), 137.0 (1C,

ar $\text{-}\underline{\text{C}}(\text{CH}_2)_2$, 138.0 (1C, ar $\text{-}\underline{\text{C}}(\text{CH}_2)_2$), 139.1 (2C, ar $\text{-}\underline{\text{C}}\text{H}$), 172.8 (1C, $\underline{\text{C}}=\text{O}$) 173.4 (1C, $\underline{\text{C}}=\text{O}$), 173.6 (2C, $\underline{\text{C}}=\text{O}$). **FTMS ESI(+)** m/z : 752.4942 ($[\text{M}+1]^+$, 49%), 774.4760 ($[\text{M}+\text{Na}]^+$, 100%). **FT-IR** ν_{max} = **4000 cm^{-1} (cm^{-1})**: 1160.57 (ester C–O), 1226.16 (amide C–N), 1495.27 (ar sp^2 C=C), 1645.94 (amide C=O), 1726.57 (ester C=O), 2975.45 (ar sp^2 C–H). **R_f** = (Si₂O₂, 90% CH₂Cl₂ / 10% CH₃OH) 0.7.

7.6.4.3. 2,2',2''-(10-(2-(dibenzylamino)-2-oxoethyl)-1,4,7,10-tetraazacyclododecane-1,4,7-triyl) triacetic acid (**DO3A-Dibenzylamide**)

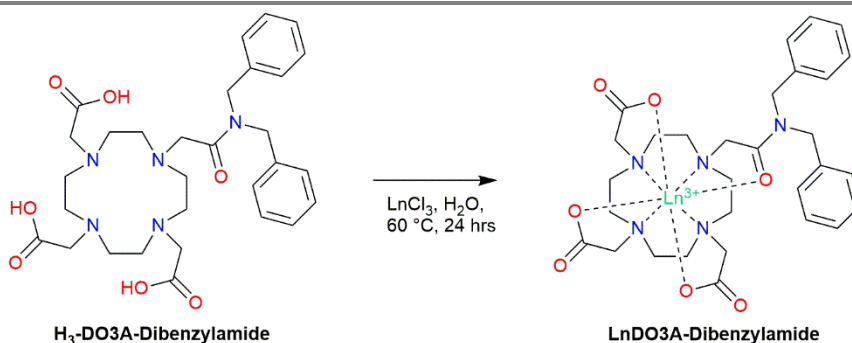


Scheme 7.41. Synthesis of the ligand **DO3A-Dibenzylamide** *via tert-butyl ester hydrolysis of the protected ligand (6-6) in acid.*

6-6 (0.39 g, 0.59 mmol) was dissolved in 1M HCl (3.5 eq) and acetonitrile (10 mL). The reaction mixture was stirred and heated at 60 °C for 18 hours, Scheme 7.41. Once reaction was complete, solvents were removed by lyophilization (**DO3A-Dibenzylamide**, 0.44 g, 40% yield). **400 MHz D₂O**; **¹H**: δ : 2.71 – 3.52 (16H, m, NCH₂CH₂N), 3.75 (4H, s, $\text{-}\underline{\text{C}}\text{H}_2$), 4.15 (4H, m, $\text{-}\underline{\text{C}}\text{H}_2$), 4.41 (2H, s, $\text{-}\underline{\text{C}}\text{H}_2$), 4.51 (2H, s, $\text{-}\underline{\text{C}}\text{H}_2$), 7.13 (4H, $J = 11$ Hz, m, ar $\text{-}\underline{\text{C}}\text{H}$), 7.25 (4H, $J = 11$ Hz, m, ar $\text{-}\underline{\text{C}}\text{H}$), 7.37 (2H, $J = 11$ Hz, m, ar $\text{-}\underline{\text{C}}\text{H}$). **¹³C**: δ : 42.3 (2C, $\text{-}\underline{\text{C}}\text{H}_2$), 47.6 – 49.8 (8C, broad, NCH₂CH₂N), 51.5 (1C, $\text{-}\underline{\text{C}}\text{H}_2$), 52.1(1C, $\text{-}\underline{\text{C}}\text{H}_2$),

53.0(1C, $-\underline{\text{C}}\text{H}_2$), 126.8 (2C, ar $-\underline{\text{C}}\text{H}$), 128.2 (4C, ar $-\underline{\text{C}}\text{H}$), 128.9 (4C, ar $-\underline{\text{C}}\text{H}$), 129.2 (2C, ar $-\underline{\text{C}}(\text{CH})_2$), 173.5 (1C, $\underline{\text{C}}=\text{O}$), 174.4 (43C, $\underline{\text{C}}=\text{O}$). **FTMS ESI(+)** m/z : 584.3076 ($[\text{M}+1]^+$, 100%). **FT-IR** $\nu_{\text{max}} = 4000 \text{ cm}^{-1}$ (cm^{-1}): 1112.35 (carboxylic acid C–O), 1223.09 (amide C–N), 1604.33 (ar sp^2 C=C), 1646.72 (amide C=O), 1733.68 (carboxylic acid C=O), 2973.47 (ar sp^2 C–H), 3366.45 (carboxylic acid O–H).

7.6.4.4. Ln (III) $-2,2',2''-(10-(2-(\text{dibenzylamino})-2\text{-oxoethyl})-1,4,7,10\text{-tetraazacyclododecane-1,4,7-triyl)triacetate}$ Chelates (**LnDO3A-Dibenzylamide**)



Scheme 7.42. Synthesis of target chelates **LnDO3A-Dibenzylamide** (Ln = Eu, Gd, Yb).

DO3A-Dibenzylamide (0.22 g, 0.377 mmol) and lanthanide chloride (0.75 mmol) were dissolved in H_2O (10 mL) and acetonitrile (5 mL). The pH was adjusted to 5.5 with 1M KOH and the reaction was stirred and heated at 60°C for 48 hours, Scheme 7.42. The solution was purified by RP-HPLC, with absorbance monitoring at $\lambda = 254 \text{ nm}$ and 205 nm. The solvent system utilized is described in Table 7.8. RP-HPLC purification yielded a colorless solid product (**EuDO3A-Dibenzylamide** $R_T = 6.8$ minutes, 0.024 g, 9% yield; **GdDO3A-Dibenzylamide** $R_T = 6.1$ minutes, 0.11 g, 39% yield; **YbDO3A-Dibenzylamide** $R_T = 10.3$ minutes, 0.080 g, 31% yield). **YbDO3A-Dibenzylamide 400**

MHz D₂O; ¹H (ppm): δ : -65.03 (1H), -64.44 (1H), -63.33 (1H), -61.72 (1H), -47.56 (1H), -45.92 (1H), -44.85 (1H), -43.30 (1H), -41.41 (1H), -33.93 (1H), -32.40 (1H), -31.55 (1H), -28.00 (1H), -27.34 (1H), -25.60 (1H), -18.07 (1H), -11.27 (1H), -9.86 (1H), -9.31 (1H), -0.98 (1H), 0.46 (1H), 0.58 (1H), 1.37 (1H), 2.68 (1H), 2.88 (1H), 3.34 (1H), 3.54 (1H), 3.96 (1H), 4.48 (1H), 5.16 (1H), 6.70 (1H), 6.75 (1H), 7.31 (1H), 7.98 (1H), 11.22 (1H), 13.02 (1H), 14.23 (1H), 15.80 (1H), 16.54 (1H), 18.14 (1H), 18.45 (1H), 20.30 (1H), 24.15 (1H), 28.67 (1H), 61.70 (1H), 64.09 (1H), 79.77 (1H), 103.20 (1H), 105.54 (1H), 108.33 (1H), 110.28 (1H).

1. Röntgen, W. C. On a New Kind of Rays. *Science* **3**, 227–231 (1896).
2. Oldendorf, W. H. Radiant energy apparatus for investigating selected areas of the interior of objects obscured by dense material. (1963).
3. Oldendorf, W. H. Isolated Flying Spot Detection of Radiodensity Dis-Continuities- Displaying the Internal Structural Pattern of a Complex Object. *IRE Transactions on Bio-Medical Electronics* **8**, 68–72 (1961).
4. Damadian, R. Tumor Detection by Nuclear Magnetic Resonance. *Science* **171**, 1151–1153 (1971).
5. Lauterbur, P. C. Image Formation by Induced Local Interactions: Examples Employing Nuclear Magnetic Resonance. *Nature* **242**, 190 (1973).
6. Mansfield, P., Pykett, I. L. & Morris, P. G. Human whole body line-scan imaging by NMR. *The British journal of radiology* **51**, 921 (1978).
7. Reivich, M. & Sokoloff, L. Application of the 2-deoxy-D-glucose method to the coupling of cerebral metabolism and blood flow. *Neurosciences Research Program bulletin* **14**, 474 (1976).
8. Barnett, S. B. *et al.* International recommendations and guidelines for the safe use of diagnostic ultrasound in medicine. *Ultrasound in Medicine & Biology* **26**, 355–366 (2000).
9. Ferrara, K., Pollard, R. & Borden, M. Ultrasound Microbubble Contrast Agents: Fundamentals and Application to Gene and Drug Delivery. *Annu. Rev. Biomed. Eng.* **9**, 415–447 (2007).

10. Kaiho, T. & Kaiho, T. *Iodine Chemistry and Applications*. (John Wiley & Sons, Incorporated, 2014).
11. Krause, W. & Schneider, P. W. Chemistry of X-Ray Contrast Agents. in *Contrast Agents II: Optical, Ultrasound, X-Ray and Radiopharmaceutical Imaging* (ed. Krause, W.) 107–150 (Springer, 2002). doi:10.1007/3-540-46009-8_4.
12. Cheng, Y. *et al.* Preliminary clinical results for PET/MR compared with PET/CT in patients with nasopharyngeal carcinoma. *Oncology Reports* **43**, 177–187 (2019).
13. Yang, C.-T. *et al.* PET-MR and SPECT-MR multimodality probes: Development and challenges. *Theranostics* **8**, 6210–6232 (2018).
14. Heiss, W.-D. Hybrid PET/MR Imaging in Neurology: Present Applications and Prospects for the Future. *J Nucl Med* **57**, 993–995 (2016).
15. Nitz, W. R. & Reimer, P. Contrast mechanisms in MR imaging. *European Radiology* **9**, 1032–1046 (1999).
16. Metastatic Disease - Breast Cancer - Case 4. <http://casemed.case.edu/clerkships/neurology/Web%20Neurorad/breast%20ca4.htm>.
17. Su, H.-Y., Wu, C.-Q., Li, D.-Y. & Ai, H. Self-assembled superparamagnetic nanoparticles as MRI contrast agents— A review. *Chinese Phys. B* **24**, 127506 (2015).
18. Laurent, S., Elst, L. V. & Muller, R. N. Superparamagnetic Iron Oxide Nanoparticles for MRI. in *The Chemistry of Contrast Agents in Medical Magnetic Resonance Imaging* 427–447 (John Wiley & Sons, Ltd, 2013). doi:10.1002/9781118503652.ch10.

19. Wang, Y.-X. J. Current status of superparamagnetic iron oxide contrast agents for liver magnetic resonance imaging. *World J Gastroenterol* **21**, 13400–13402 (2015).
20. Schwert, D., Davies, J. & Richardson, N. Non-gadolinium-based MRI contrast agents. *Contrast Agents I* **221**, 165–199 (2002).
21. Sherry, A. D., Caravan, P. & Lenkinski, R. E. Primer on gadolinium chemistry. *Journal of Magnetic Resonance Imaging* **30**, 1240–1248 (2009).
22. Gries, H. Extracellular MRI contrast agents based on gadolinium. *Contrast Agents I* **221**, 1–24 (2002).
23. Grobner, T. Gadolinium – a specific trigger for the development of nephrogenic fibrosing dermopathy and nephrogenic systemic fibrosis? *Nephrol Dial Transplant* **21**, 1104–1108 (2006).
24. Schlaudecker, J. D. & Bernheisel, C. R. Gadolinium-Associated Nephrogenic Systemic Fibrosis. *AFP* **80**, 711–714 (2009).
25. Lin, S.-P. & Brown, J. J. MR contrast agents: Physical and pharmacologic basics. *Journal of Magnetic Resonance Imaging* **25**, 884–899 (2007).
26. Desreux, J. F. Nuclear Magnetic Resonance Spectroscopy of Lanthanide Complexes With a Tetraacetic Tetraaza Macrocycle. Unusual Conformation Properties. *Chemischer Informationsdienst* **11**, no–no (1980).
27. Hermann, P., Kotek, J., Kubiček, V. & Lukeš, I. Gadolinium(iii) complexes as MRI contrast agents : ligand design and properties of the complexes. *Dalton Transactions* **0**, 3027–3047 (2008).

28. Jung, K.-H. *et al.* Gd Complexes of Macrocyclic Diethylenetriaminepentaacetic Acid (DTPA) Biphenyl-2,2'-bisamides as Strong Blood-Pool Magnetic Resonance Imaging Contrast Agents. *J. Med. Chem.* **54**, 5385–5394 (2011).
29. Caravan, P., Ellison, J. J., McMurry, T. J. & Lauffer, R. B. Gadolinium(III) Chelates as MRI Contrast Agents: Structure, Dynamics, and Applications. *Chem. Rev.* **99**, 2293–2352 (1999).
30. Brücher, E. Kinetic Stabilities of Gadolinium(III) Chelates Used as MRI Contrast Agents. in *Contrast Agents I* 103–122 (Springer, Berlin, Heidelberg, 2002). doi:10.1007/3-540-45733-X_4.
31. Cher, T. & Szklaruk, J. MR contrast agents: applications in hepatobiliary imaging. *Applied Radiology* **39**, (2010).
32. Tóth, É., Helm, L. & Merbach, A. E. Relaxivity of MRI Contrast Agents. in *Contrast Agents I* (ed. Krause, W.) vol. 221 61–101 (Springer Berlin Heidelberg, 2002).
33. Caravan, P., Farrar, C. T., Frullano, L. & Uppal, R. Influence of molecular parameters and increasing magnetic field strength on relaxivity of gadolinium- and manganese-based T1 contrast agents. *Contrast Media & Molecular Imaging* **4**, 89–100 (2009).
34. Jacques, V. *et al.* High relaxivity MRI contrast agents part 2: Optimization of inner- and second-sphere relaxivity. *Invest Radiol* **45**, 613–624 (2010).
35. Aime, S., Barbero, L., Botta, M. & Ermondi, G. Determination Of Metal-Proton Distances And Electronic Relaxation Times In Lanthanide Complexes By Nuclear Magnetic Resonance Spectroscopy. *Journal Of The Chemical Society-Dalton Transactions* 225–228 (1992).

36. Wiener, E. C. *et al.* Bifunctional Chelates Optimized for Molecular MRI. *Inorg. Chem.* **53**, 6554–6568 (2014).
37. Lipari, G. & Szabo, A. Model-free approach to the interpretation of nuclear magnetic resonance relaxation in macromolecules. 1. Theory and range of validity. *J. Am. Chem. Soc.* **104**, 4546–4559 (1982).
38. Powell, D. H. *et al.* Structural and Dynamic Parameters Obtained from ¹⁷O NMR, EPR, and NMRD Studies of Monomeric and Dimeric Gd³⁺ Complexes of Interest in Magnetic Resonance Imaging: An Integrated and Theoretically Self-Consistent Approach1. *J. Am. Chem. Soc.* **118**, 9333–9346 (1996).
39. D'Angelo, P. *et al.* Revised Ionic Radii of Lanthanoid(III) Ions in Aqueous Solution. *Inorg. Chem.* **50**, 4572–4579 (2011).
40. Caravan, P., Esteban-Gómez, D., Rodríguez-Rodríguez, A. & Platas-Iglesias, C. Water exchange in lanthanide complexes for MRI applications. Lessons learned over the last 25 years. *Dalton Trans.* **48**, 11161–11180 (2019).
41. Gonzalez, G., Powell, D. H., Tissieres, V. & Merbach, A. E. Water-exchange, electronic relaxation, and rotational dynamics of the MRI contrast agent [Gd(DTPA-BMA)(H₂O)] in aqueous solution: a variable pressure, temperature, and magnetic field oxygen-17 NMR study. *J. Phys. Chem.* **98**, 53–59 (1994).
42. Aime, S. *et al.* Conformational and Coordination Equilibria on DOTA Complexes of Lanthanide Metal Ions in Aqueous Solution Studied by ¹H-NMR Spectroscopy. *Inorg. Chem.* **36**, 2059–2068 (1997).

43. Burai, L. *et al.* Novel Macrocyclic EuII Complexes: Fast Water Exchange Related to an Extreme M-O Water Distance. *Chemistry – A European Journal* **9**, 1394–1404 (2003).
44. Kruk, D., Nilsson, T. & Kowalewski, J. Nuclear spin relaxation in paramagnetic systems with zero-field splitting and arbitrary electron spin. *Phys. Chem. Chem. Phys.* **3**, 4907–4917 (2001).
45. Borel, A., Tóth, E., Helm, L., Jánossy, A. & Merbach, A. E. EPR on aqueous Gd³⁺ complexes and a new analysis method considering both line widths and shifts. *Phys. Chem. Chem. Phys.* **2**, 1311–1317 (2000).
46. Bertini, I., Luchinat, C., Parigi, G. & Ravera, E. *Solution NMR of paramagnetic molecules : applications to metalloproteins and models.* (Elsevier Science Ltd., 2001).
47. Horrocks, W. DeW. & Sudnick, D. R. Lanthanide ion probes of structure in biology. Laser-induced luminescence decay constants provide a direct measure of the number of metal-coordinated water molecules. *J. Am. Chem. Soc.* **101**, 334–340 (1979).
48. Meyer, M., Dahaoui-Gindrey, V., Lecomte, C. & Guilard, R. Conformations and coordination schemes of carboxylate and carbamoyl derivatives of the tetraazamacrocycles cyclen and cyclam, and the relation to their protonation states. *Coordination Chemistry Reviews* **178**, 1313–1405 (1998).
49. Aime, S., Barge, A., Botta, M., Sousa, A. S. D. & Parker, D. Direct NMR Spectroscopic Observation of a Lanthanide-Coordinated Water Molecule whose

- Exchange Rate Is Dependent on the Conformation of the Complexes. *Angewandte Chemie International Edition* **37**, 2673–2675 (1998).
50. Payne, K. M. & Woods, M. Isomerism in Benzyl-DOTA Derived Bifunctional Chelators: Implications for Molecular Imaging. *Bioconjugate Chem.* **26**, 338–344 (2015).
51. Aime, S. *et al.* Properties, Solution State Behavior, and Crystal Structures of Chelates of DOTMA. *Inorg. Chem.* **50**, 7955–7965 (2011).
52. Pritchard, J. H., Ackerman, M., Tubis, M. & Bland, W. H. Indium-III-Labeled Antibody Heavy Metal Chelate Conjugates: A Potential Alternative to Radioiodination. *Proceedings of the Society for Experimental Biology and Medicine* **151**, 297–302 (1976).
53. Brechbiel, M. W. Bifunctional Chelates for Metal Nuclides. *Q J Nucl Med Mol Imaging* **52**, 166–173 (2008).
54. Woods, M., Kovacs, Z. & Sherry, A. D. Targeted Complexes of Lanthanide(III) Ions as Therapeutic and Diagnostic Pharmaceuticals. *Journal of Supramolecular Chemistry* **2**, 1–15 (2002).
55. Caravan, P. Strategies for increasing the sensitivity of gadolinium based MRI contrast agents. *Chem. Soc. Rev.* **35**, 512–523 (2006).
56. Avedano, S., Botta, M., Haigh, J. S., Longo, D. & Woods, M. Coupling Fast Water Exchange to Slow Molecular Tumbling in Gd³⁺ Chelates: Why Faster Is Not Always Better. *Inorg. Chem.* **52**, 8436–8450 (2013).

57. Beeby, A. *et al.* Non-radiative deactivation of the excited states of europium, terbium and ytterbium complexes by proximate energy-matched OH, NH and CH oscillators: an improved luminescence method for establishing solution hydration states. *J. Chem. Soc., Perkin Trans. 2* 493–504 (1999) doi:10.1039/a808692c.
58. Muller, R. N. *et al.* Physicochemical Characterization of MS-325, a New Gadolinium Complex, by Multinuclear Relaxometry. *Eur. J. Inorg. Chem.* **1999**, 1949–1955 (1999).
59. Tirco, G., Webber, B. C., Kucera, B. E., Young, V. G. & Woods, M. Analysis of the Conformational Behavior and Stability of the SAP and TSAP Isomers of Lanthanide(III) NB-DOTA-Type Chelates. *Inorg. Chem.* **50**, 7966–7979 (2011).
60. Woods, M., Botta, M., Avedano, S., Wang, J. & Sherry, A. D. Towards the rational design of MRI contrast agents: a practical approach to the synthesis of gadolinium complexes that exhibit optimal water exchange. *Dalton Trans.* 3829–3837 (2005) doi:10.1039/B510778D.
61. Webber, B. Investigation of the Structure and Dynamics of Regioisomeric Eu³⁺ and Gd³⁺ Chelates of NB-DOTMA: Implications for MRI Contrast Agent Design. (2013).
62. Payne, K. M. Investigations into the Effects of Water Exchange and the Structure of Lanthanide Chelates. (Portland State University, 2016).
63. Rust, L., Payne, K. M., Carniato, F., Botta, M. & Woods, M. Differences in the Relaxometric Properties of Regioisomeric Benzyl-DOTA Bifunctional Chelators: Implications for Molecular Imaging. *Bioconjugate Chem.* **30**, 1530–1538 (2019).

64. Webber, B. C. & Woods, M. The confluence of structure and dynamics in lanthanide(III) chelates: how dynamics help define structure in solution. *Dalton Trans.* **43**, 251–258 (2014).
65. Webber, B. C. *et al.* Analysis of the Relaxometric Properties of Extremely Rapidly Exchanging Gd³⁺ Chelates: Lessons from a Comparison of Four Isomeric Chelates. *Inorg. Chem.* [acs.inorgchem.0c00905](https://doi.org/10.1021/acs.inorgchem.0c00905) (2020) doi:10.1021/acs.inorgchem.0c00905.
66. Poole, R. A. *et al.* Identification of emissive lanthanide complexes suitable for cellular imaging that resist quenching by endogenous anti-oxidants. *Org. Biomol. Chem.* **5**, 2055–2062 (2007).
67. Kiefer, G. E. & Woods, M. Solid State and Solution Dynamics of Pyridine Based Tetraaza-Macrocyclic Lanthanide Chelates Possessing Phosphonate Ligating Functionality (Ln-PCTMB): Effect on Relaxometry and Optical Properties. *Inorg. Chem.* **48**, 11767–11778 (2009).
68. Dunand, F. A., Borel, A. & Merbach, A. E. How Does Internal Motion Influence the Relaxation of the Water Protons in LnIII-DOTA-like Complexes? *J. Am. Chem. Soc.* **124**, 710–716 (2002).
69. Woods, M. *et al.* Correlation of Water Exchange Rate with Isomeric Composition in Diastereoisomeric Gadolinium Complexes of Tetra(carboxyethyl)dota and Related Macrocyclic Ligands. *J. Am. Chem. Soc.* **122**, 9781–9792 (2000).
70. Woods, M., Payne, K. M., Valente, E. J., Kucera, B. E. & Young, V. G. Crystal Structures of DOTMA Chelates from Ce³⁺ to Yb³⁺: Evidence for a Continuum of Metal Ion Hydration States. *Chemistry – A European Journal* **25**, 9997–10005 (2019).

71. Avedano, S., Botta, M., Haigh, J. S., L. Longo, D. & Woods, M. Coupling Fast Water Exchange to Slow Molecular Tumbling in Gd³⁺ Chelates: Why Faster Is Not Always Better. *Inorg. Chem.* **52**, 8436–8450 (2013).
72. Slack, J. R. & Woods, M. The effect of regioisomerism on the coordination chemistry and CEST properties of lanthanide(III) NB-DOTA-tetraamide chelates. *J Biol Inorg Chem* **19**, 173–189 (2014).
73. Aime, S. *et al.* Relaxometric, Structural, and Dynamic NMR Studies of DOTA-like Ln (III) Complexes (Ln= La, Gd, Ho, Yb) Containing *ap*-Nitrophenyl Substituent. *Inorganic Chemistry* **35**, 2726–2736 (1996).
74. Raghunand, N. *et al.* Design, Synthesis, and Evaluation of 1,4,7,10-Tetraazacyclododecane-1,4,7-triacetic Acid Derived, Redox-Sensitive Contrast Agents for Magnetic Resonance Imaging. *J. Med. Chem.* **53**, 6747–6757 (2010).
75. Avedano, S., Botta, M., Haigh, J. S., L. Longo, D. & Woods, M. Coupling Fast Water Exchange to Slow Molecular Tumbling in Gd³⁺ Chelates: Why Faster Is Not Always Better. *Inorg. Chem.* **52**, 8436–8450 (2013).
76. Lim, B. *et al.* A metal-free and mild approach to 1, 3, 4-oxadiazol-2 (3 H)-ones via oxidative C–C bond cleavage using molecular oxygen. *Organic & biomolecular chemistry* **16**, 2105–2113 (2018).
77. Harpp, D. N., Bao, L. Q., Black, C. J., Gleason, J. G. & Smith, R. A. Efficient. α -halogenation of acyl chlorides by N-bromosuccinimide, N-chlorosuccinimide, and molecular iodine. *The Journal of Organic Chemistry* **40**, 3420–3427 (1975).

78. Galli, C. 'Cesium Ion Effect' and Macrocyclization. A Critical Review. *Organic Preparations and Procedures International* **24**, 285–307 (1992).
79. Woods, M., Kovacs, Z., Zhang, S. & Sherry, A. D. Towards the Rational Design of Magnetic Resonance Imaging Contrast Agents: Isolation of the Two Coordination Isomers of Lanthanide DOTA-Type Complexes. *Angewandte Chemie International Edition* **42**, 5889–5892 (2003).
80. Aime, S. *et al.* Conformational and Coordination Equilibria on DOTA Complexes of Lanthanide Metal Ions in Aqueous Solution Studied by ¹H-NMR Spectroscopy. *Inorg. Chem.* **36**, 2059–2068 (1997).
81. Tircso, G., Webber, B. C., Kucera, B. E., Young, V. G. & Woods, M. Analysis of the Conformational Behavior and Stability of the SAP and TSAP Isomers of Lanthanide(III) NB-DOTA-Type Chelates. *Inorg. Chem.* **50**, 7966–7979 (2011).
82. Dunand, F. A., Dickins, R. S., Parker, D. & Merbach, A. E. Towards Rational Design of Fast Water-Exchanging Gd(dota-Like) Contrast Agents? Importance of the M/m Ratio. *Chemistry – A European Journal* **7**, 5160–5167 (2001).
83. Accardo, A., Tesauro, D., Aloj, L., Pedone, C. & Morelli, G. Supramolecular aggregates containing lipophilic Gd(III) complexes as contrast agents in MRI. *Coordination Chemistry Reviews* **253**, 2193–2213 (2009).
84. Nicolle, G. M., Tóth, É., Eisenwiener, K.-P., Mäcke, H. R. & Merbach, A. E. From monomers to micelles: investigation of the parameters influencing proton relaxivity. *J Biol Inorg Chem* **7**, 757–769 (2002).

85. Skinner, P. J. *et al.* Conjugates of cyclodextrins with charged and neutral macrocyclic europium, terbium and gadolinium complexes: sensitised luminescence and relaxometric investigations and an example of supramolecular relaxivity enhancement. *J. Chem. Soc., Perkin Trans. 2* 1329–1338 (2000) doi:10.1039/B002207L.
86. Brittain, H. G. & Desreux, J. F. Luminescence and NMR Studies of the Conformational Isomers of Lanthanide Complexes with an Optically Active Polyaza Polycarboxylic Macrocyclic. *Inorg. Chem.* **23**, 4459–4466 (1984).
87. Kielar, F., Tei, L., Terreno, E. & Botta, M. Large Relaxivity Enhancement of Paramagnetic Lipid Nanoparticles by Restricting the Local Motions of the GdIII Chelates. *J. Am. Chem. Soc.* **132**, 7836–7837 (2010).
88. Aime, S., Botta, M., Ermondi, G., Fedeli, F. & Uggeri, F. Synthesis and NMRD studies of gadolinium(3+) complexes of macrocyclic polyamino polycarboxylic ligands bearing .beta.-benzyloxy-.alpha.-propionic residues. *Inorg. Chem.* **31**, 1100–1103 (1992).
89. Howard, J. A. K. *et al.* Structure and dynamics of all of the stereoisomers of europium complexes of tetra(carboxyethyl) derivatives of dota: ring inversion is decoupled from cooperative arm rotation in the RRRR and RRRS isomers. *Chem. Commun.* 1381–1382 (1998) doi:10.1039/a802847h.
90. Bari, L. D., Pintacuda, G. & Salvadori, P. Solution Equilibria in YbDOTMA, a Chiral Analogue of One of the Most Successful Contrast Agents for MRI, GdDOTA. *Eur. J. Inorg. Chem.* **8** (2000).

91. Aime, S. *et al.* Properties, Solution State Behavior, and Crystal Structures of Chelates of DOTMA. *Inorg. Chem.* **50**, 7955–7965 (2011).
92. Petit, Y., Sanner, C. & Larchevêque, M. A Convenient Synthesis of Enantiomerically Pure (2R,3S)- and (2S,3R)-3-Hydroxy-2-methylbutanoic Esters. *Synthesis* **1988**, 538–540 (1988).
93. Kim, H. S., Austin, J. & Hage, D. S. Identification of drug-binding sites on human serum albumin using affinity capillary electrophoresis and chemically modified proteins as buffer additives. *ELECTROPHORESIS* **23**, 956–963 (2002).
94. Vipond, J. *et al.* A Bridge to Coordination Isomer Selection in Lanthanide(III) DOTA-tetraamide Complexes. 12.
95. Kotek, J., Rudovský, J., Hermann, P. & Lukeš, I. Three in One: TSA, TSA', and SA Units in One Crystal Structure of a Yttrium(III) Complex with a Monophosphinated H₄ dota Analogue. *Inorg. Chem.* **45**, 3097–3102 (2006).
96. Lukeš, I., Kotek, J., Vojtíšek, P. & Hermann, P. Complexes of tetraazacycles bearing methylphosphinic/phosphonic acid pendant arms with copper(II), zinc(II) and lanthanides(III). A comparison with their acetic acid analogues. *Coordination Chemistry Reviews* **216–217**, 287–312 (2001).
97. Shannon, R. D. Revised effective ionic radii and systematic studies of interatomic distances in halides and chalcogenides. *Acta Crystallographica Section A* **32**, 751–767 (1976).
98. Rudolph, W. W. & Irmer, G. On the Hydration of the Rare Earth Ions in Aqueous Solution. *J Solution Chem* **49**, 316–331 (2020).

99. Howard, J. A. K. *et al.* Structure and dynamics of all of the stereoisomers of europium complexes of tetra(carboxyethyl) derivatives of dota: ring inversion is decoupled from cooperative arm rotation in the RRRR and RRRS isomers. *Chem. Commun.* **0**, 1381–1382 (1998).
100. Aime, S. *et al.* Conformational and Coordination Equilibria on DOTA Complexes of Lanthanide Metal Ions in Aqueous Solution Studied by ¹H-NMR Spectroscopy. *Inorg. Chem.* **36**, 2059–2068 (1997).
101. Weber, R. W., Boutin, R. H., Nedelman, M. A., Lister-James, J. & Dean, R. T. Enhanced kidney clearance with an ester-linked ^{99m}Tc-radiolabeled antibody Fab'-chelator conjugate. *Bioconjugate Chemistry* **1**, 431–437 (1990).
102. Cox, J. P. L. *et al.* Synthesis of C- and N-Functionalised Derivatives of 1,4,7-Triazacyclononane-1,4,7-triyltriacetic acid (NOTA), 1,4,7,10-Tetraazacyclododecane-1,4,7,10-tetrayltetra-acetic Acid (DOTA), and Diethylenetriaminepenta-acetic Acid (DTPA): Bifunctional Complexing Agents for the Derivatisation of Anti bodies. *J. CHEM. SOC. PERKIN TRANS.* **10** (1990).
103. Montalbetti, C. A. G. N. & Falque, V. Amide bond formation and peptide coupling. *Tetrahedron* **61**, 10827–10852 (2005).
104. Beija, M., Afonso, C. A. M. & Martinho, J. M. G. Synthesis and applications of Rhodamine derivatives as fluorescent probes. *Chem. Soc. Rev.* **38**, 2410–2433 (2009).
105. Dunand, F. A., Aime, S. & Merbach, A. E. First ¹⁷⁰NMR Observation of Coordinated Water on Both Isomers of [Eu(DOTAM)(H₂O)]³⁺: A Direct Access to

- Water Exchange and its Role in the Isomerization¹. *J. Am. Chem. Soc.* **122**, 1506–1512 (2000).
106. Aime, S. *et al.* NMR, Relaxometric, and Structural Studies of the Hydration and Exchange Dynamics of Cationic Lanthanide Complexes of Macrocyclic Tetraamide Ligands. *J. Am. Chem. Soc.* **121**, 5762–5771 (1999).
107. Ward, K. M., Aletras, A. H. & Balaban, R. S. A New Class of Contrast Agents for MRI Based on Proton Chemical Exchange Dependent Saturation Transfer (CEST). *Journal of Magnetic Resonance* **143**, 79–87 (2000).
108. Aime, S. *et al.* Paramagnetic Lanthanide(III) complexes as pH-sensitive chemical exchange saturation transfer (CEST) contrast agents for MRI applications. *Magn. Reson. Med.* **47**, 639–648 (2002).
109. Ratnakar, S. J., Woods, M., Lubag, A. J. M., Kovács, Z. & Sherry, A. D. Modulation of Water Exchange in Europium(III) DOTA–Tetraamide Complexes via Electronic Substituent Effects. *J. Am. Chem. Soc.* **130**, 6–7 (2008).
110. Lewis, M. M., Milne, M., Bartha, R. & Hudson, R. H. E. Dysprosium(III) and thulium(III) complexes of DO3A-monoanilides: an investigation of electronic effects on their relaxometric and amide-based PARACEST properties. *Can. J. Chem.* **93**, 244–252 (2015).
111. Carney, C. E. *et al.* Towards the Rational Design of MRI Contrast Agents: δ -Substitution of Lanthanide(III) NB-DOTA-Tetraamide Chelates Influences but Does Not Control Coordination Geometry. *Chem. Eur. J.* **17**, 10372–10378 (2011).

112. Miller, K. J. *et al.* The Population of SAP and TSAP Isomers in Cyclen-Based Lanthanide(III) Chelates Is Substantially Affected by Solvent. *Inorg Chem* **49**, 8662–8664 (2010).
113. Milne, M. *et al.* MRI ParaCEST agents that improve amide based pH measurements by limiting inner sphere water T2 exchange. *RSC Adv.* **4**, 1666–1674 (2013).
114. Basal, L. A. *et al.* Fluorinated Eu^{III}-based multimodal contrast agent for temperature- and redox-responsive magnetic resonance imaging. *Chem. Sci.* **8**, 8345–8350 (2017).
115. Webber, B. C. & Woods, M. Structural Analysis of Isomeric Europium(III) Chelates of NB-DOTMA. *Inorg. Chem.* **51**, 8576–8582 (2012).
116. Zhu, Q., Girish, A., Chattopadhyaya, S. & Yao, S. Q. Developing novel activity-based fluorescent probes that target different classes of proteases. *Chem. Commun.* 1512–1513 (2004) doi:10.1039/B404471A.
117. Hupfer, M. L. *et al.* Arylic versus Alkyllic—Hydrophobic Linkers Determine the Supramolecular Structure and Optoelectronic Properties of Tripodal Amphiphilic Push–Pull Thiazoles. *Langmuir* **35**, 2561–2570 (2019).
118. Kolluri, P. K. *et al.* Design, synthesis of novel (Z)-2-(3-(4-((3-benzyl-2,4-dioxothiazolidin-5-ylidene)methyl)-1-phenyl-1H-pyrazol-3-yl)phenoxy)-N-arylacetamide derivatives: Evaluation of cytotoxic activity and molecular docking studies. *Journal of Molecular Structure* **1202**, 127300 (2020).
119. Wang, C.-C., Zhou, J., Ma, Z.-W., Chen, X.-P. & Chen, Y.-J. Synthesis of spirobarbiturate-pyrrolidinones *via* a domino aza-Michael/S_N2 cyclization of

- barbiturate-derived alkenes with *N*-alkoxy α -haloamides. *Org. Biomol. Chem.* **17**, 9200–9208 (2019).
120. Liu, S., Pietryka, J., Ellars, C. E. & Edwards, D. S. Comparison of Yttrium and Indium Complexes of DOTA-BA and DOTA-MBA: Models for ^{90}Y - and ^{111}In -Labeled DOTA–Biomolecule Conjugates. *Bioconjugate Chem.* **13**, 902–913 (2002).
121. Catalytic Enantioselective Intramolecular C(sp³)–H Amination of 2-Azidoacetamides - Zhou - 2019 - Angewandte Chemie International Edition - Wiley Online Library. <https://onlinelibrary-wiley-com.proxy.lib.pdx.edu/doi/full/10.1002/anie.201811927>.

APPENDIX: CHAPTER 2 STERN-VOLMER LUMINESCENCE SPECTRA

A1.1. Stern-Volmer Emission Spectra for GdNB-DOTA Corner and Side

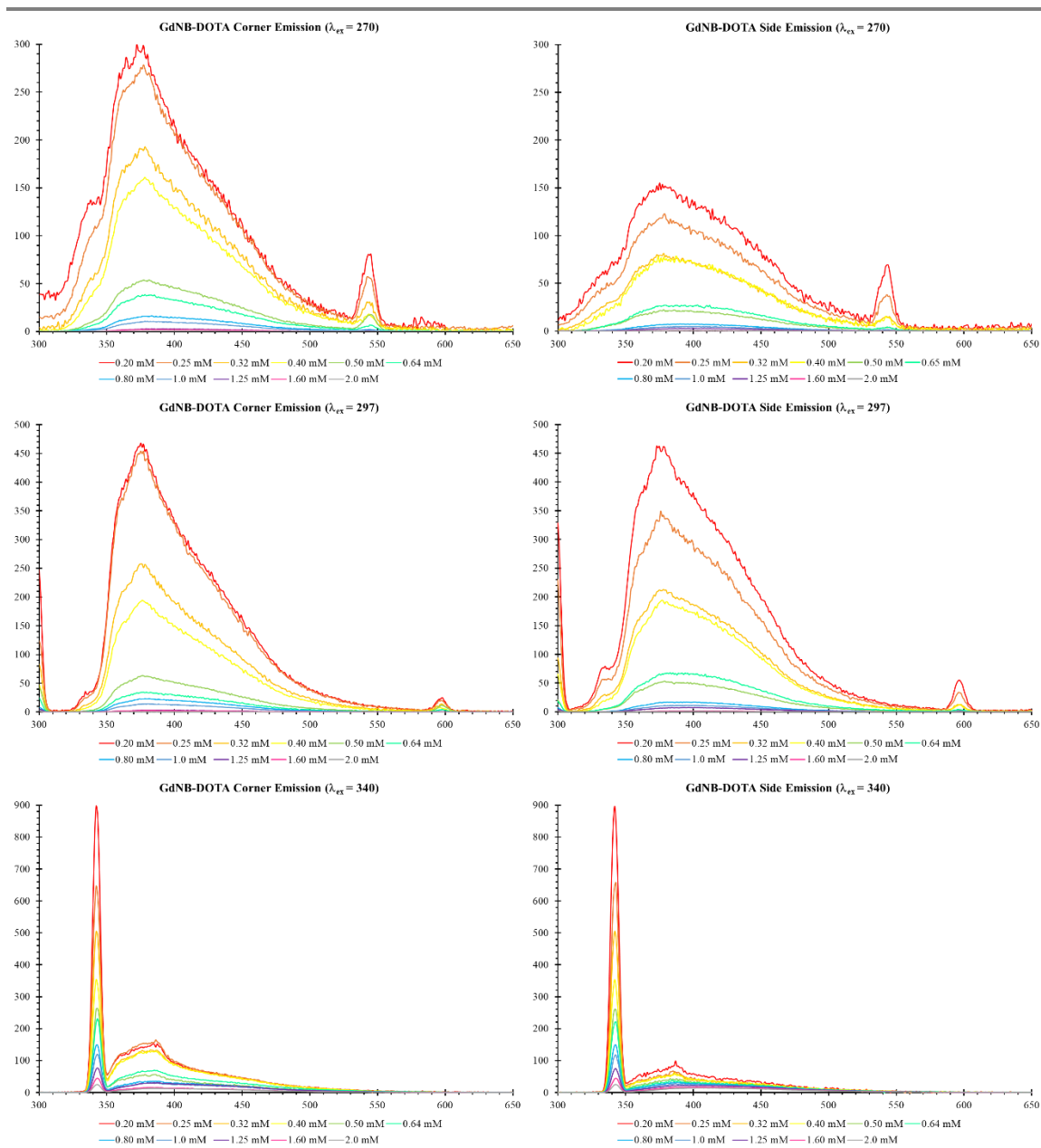


Figure A.1. Emission spectra at various concentrations for GdNB-DOTA Corner (left) and Side (right) at $\lambda_{ex} = 270$ nm (top), 297 nm (middle), and 340 nm (bottom).

A1.2. Stern-Volmer Excitation Spectra for GdNB-DOTA Corner and Side

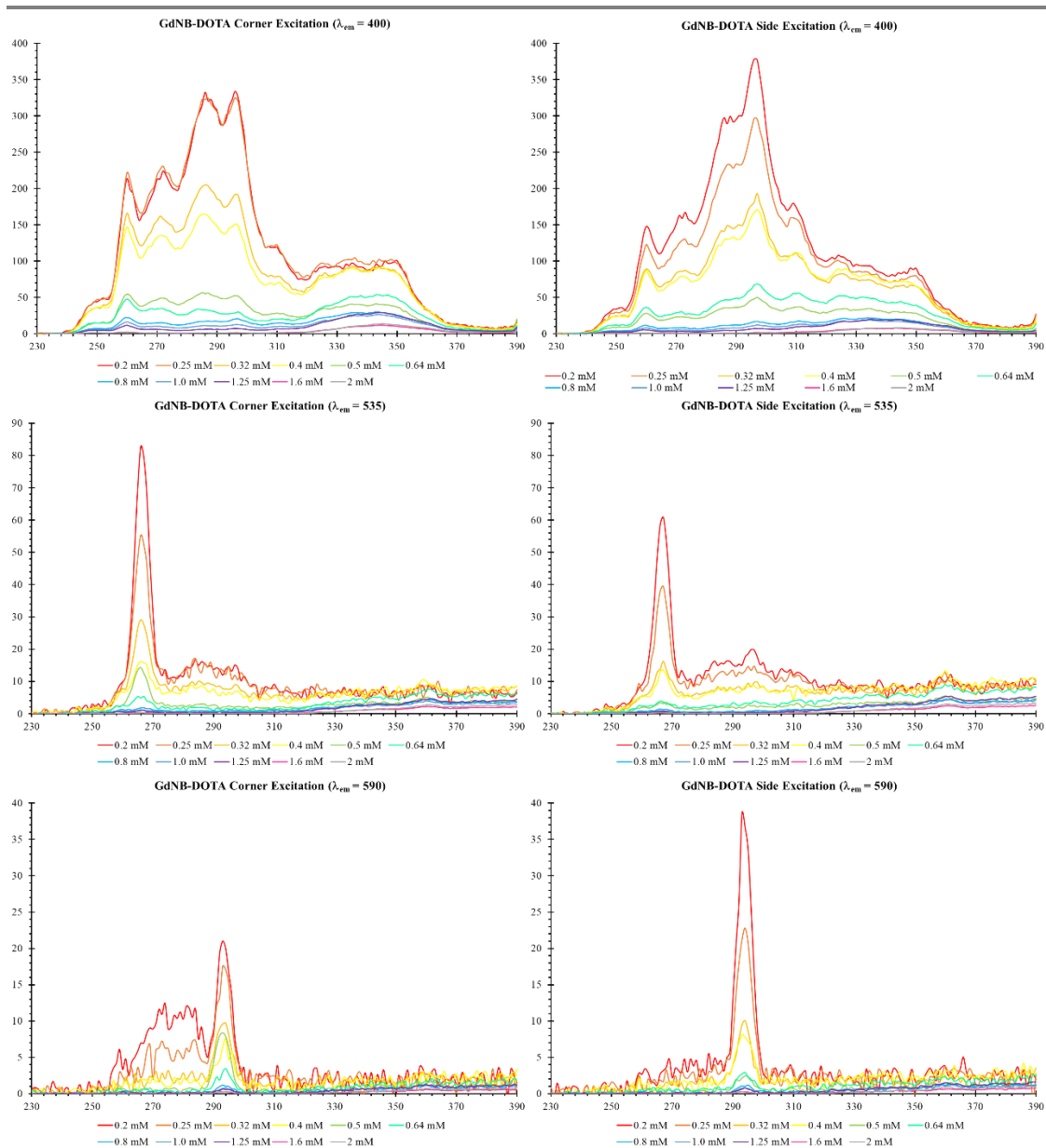


Figure A.2. Excitation spectra at various concentrations for GdNB-DOTA Corner (left) and Side (right) at $\lambda_{em} = 400$ nm (top), 535 nm (middle), and 590 nm (bottom).